Universidad de Valladolid

Escuela de Doctorado Universidad de Valladolid

PROGRAMA DE DOCTORADO EN FÍSICA

TESIS DOCTORAL:

STUDY OF THE THERMAL CONDUCTIVITY OF BULK AND MICRONIZED NANOCELLULAR POLYMERS

Presentada por Ismael Sánchez Calderón
para optar al grado de
Doctor por la Universidad de Valladolid

Dirigida por:
Prof. Dr. Miguel Ángel Rodríguez Pérez
Dr. Victoria Bernardo García

FINANCIACIÓN

Se agradece a la Junta de Catilla y León por el apoyo económico aportado para la realización de esta tesis doctoral a través de un contrato de formación predoctoral, de acuerdo a la Orden de 12 de diciembre de 2019, de la Consejería de Educación, por la que se convocan ayudas destinadas a financiar la contratación predoctoral de personal investigador, cofinanciadas por el Fondo Social Europeo (BOCyL de 23 de diciembre de 2019). Además, quiero agradecer la financiación recibida por el grupo CellMat, proveniente de los siguientes proyectos de investigación:

- POLIMEROS NANOCELULARES TRANSPARENTES Y AISLANTES TERMICOS: FABRICACION, CARACTERIZACION Y RELACION PROCESOESTRUCTURA- PROPIEDADES (RTI2018-098749-B-I00). Financiado por el Ministerio de Ciencia e Innovación, Programa Estatal de I+D+i Orientada a los Retos de la Sociedad.
- SUSTAINABLE PRODUCTION OF SUPER THERMAL INSULATING NANOCELLULAR POLYMERS WITH REDUCED THERMAL CONDUCTIVITY BY INCREASING PHONONS SCATTERING (TED2021-130965B-I00) Financiado por el Ministerio de Ciencia e Innovación, Proyectos estratégicos orientados transición ecológica y transición digital 2021.
- DESARROLLO DE SUPER AISLANTES TERMICOS BASADOS EN POLIMEROS NANOCELULARES Y BLOQUEDAORES DE LA RADACION INFRAROJA (PID2021-127108OB-I00). Financiado por el Ministerio de Ciencia e Innovación, Proyectos de Generación de Conocimiento 2021.
- HACIA LA PRODUCCION INDUSTRIAL DE POLIMEROS NANOCELULARES TRANSPARENTES. (PDC2022-133391-I00). Financiado por el Ministerio de Ciencia e Innovación, Proyectos I+D+i Pruebas de Concepto 2022.

FUNDING

Financial support from the Junta de Catilla y León according to the Orden de 12 de diciembre de 2019, de la Consejería de Educación, por la que se convocan ayudas destinadas a financiar la contratación predoctoral de personal investigador, cofinanciadas por el Fondo Social Europeo (BOCyL de 23 de diciembre de 2019) is gratefully acknowledged. In addition, financial assistance by CellMat group provided by the following research projects is also acknowledged:

- POLIMEROS NANOCELULARES TRANSPARENTES Y AISLANTES TERMICOS: FABRICACION, CARACTERIZACION Y RELACION PROCESOESTRUCTURA- PROPIEDADES (RTI2018-098749-B-I00). Funded by Ministerio de Ciencia e Innovación, Programa Estatal de I+D+i Orientada a los Retos de la Sociedad.
- SUSTAINABLE PRODUCTION OF SUPER THERMAL INSULATING NANOCELLULAR POLYMERS WITH REDUCED THERMAL CONDUCTIVITY BY INCREASING PHONONS SCATTERING (TED2021-130965B-I00) Funded by Ministerio de Ciencia e Innovación, Proyectos estratégicos orientados transición ecológica y transición digital 2021.
- DESARROLLO DE SUPER AISLANTES TERMICOS BASADOS EN POLIMEROS NANOCELULARES Y BLOQUEDAORES DE LA RADACION INFRAROJA (PID2021-127108OB-I00). Funded by Ministerio de Ciencia e Innovación, Proyectos de Generación de Conocimiento 2021.
- HACIA LA PRODUCCION INDUSTRIAL DE POLIMEROS NANOCELULARES TRANSPARENTES. (PDC2022-133391-I00). Funded by Ministerio de Ciencia e Innovación, Proyectos I+D+i Pruebas de Concepto 2022.

Contents

Resumen en Español

Chapter 1: Introduction

Chapter 2: State of the Art

Chapter 3: Materials & Methods

Chapter 4: Results

Chapter 5: Conclusions & Future Work

Resumen en Español

"Uno para todos y todos para uno."

Los tres mosqueteros

Alexandre Dumas

ÍNDICE

I. Introducción

I.I. Aislamiento térmico

Desde el principio de los tiempos el ser humano ha sido consciente de la importancia del aislamiento térmico (**Figura 1**)[1]. Por ejemplo, los primeros pueblos prehistóricos construían viviendas temporales utilizando pieles de animales, lana y productos relacionados con plantas. Más tarde, debido al estilo de vida asentado, surgió la necesidad de utilizar materiales más duraderos para la vivienda como la madera, la piedra o la tierra. Por ejemplo, utilizando la tierra como aislante, los egipcios se retiraban a la frescura de las cámaras subterráneas en los días calurosos[2]. Los historiadores creen que los antiguos griegos y romanos descubrieron el asbesto y le encontraron muchos usos debido a su resistencia al calor y al fuego[3]. Además, los primeros habitantes de España cubrían sus casas de piedra con corteza de corcho debido a su comportamiento aislante[4]. A medida que se desarrollaba la tecnología, también lo hacían las innovaciones. Así, con la introducción de la chimenea para proporcionar calor (artificial y controlado) en el interior de la vivienda estaba claro que el desafío no solo era cómo mantener el frío afuera sino también en cómo mantener el calor adentro[2].

Figura 1. Evolución del aislamiento térmico en viviendas.

Sin embargo, no fue hasta la llegada de la revolución industrial en el siglo XIX que se generalizó la aplicación de aislamientos térmicos de forma deliberada con objetivo comercial (**Figura 1**). En esos años, las técnicas de planificación y construcción cambiaron drásticamente, los sistemas estructurales no se planificaban de manera empírica sino con métodos de cálculo con la introducción de materiales de construcción como hierro fundido, estructuras de vidrio, hormigón y acero. Sin embargo, el aislamiento térmico proporcionado por estos materiales era muy inferior al de los materiales utilizados en ese momento (adobe o ladrillo), lo que generaba mayores pérdidas de calor y mayores demandas de calefacción[1]. Así, el ser humano comenzó a desarrollar sus propios

aislantes térmicos a partir de materiales naturales y artificiales: caña, lana mineral, fibra de vidrio, perlita expandida, polímeros celulares (como la espuma de poliestireno y la espuma de poliuretano), etc. (**Figura 2**). En particular, el desarrollo de los polímeros celulares (materiales bifásicos en los que una fase gaseosa se encuentra dispersa en una matriz polimérica continua) en la década de los 1940 provocó una gran revolución en el mercado de los materiales aislantes[1] debido a sus interesantes propiedades: ligereza, bajo coste, y baja conductividad térmica entre otros[5].

Figura 2. Algunos ejemplos de aislantes térmicos.

Hoy en día, encontrar nuevos materiales con mejores propiedades de aislamiento térmico sigue siendo una tarea obligatoria. Más del 16% de la energía mundial se destina a la climatización de edificios, por lo que el aislamiento térmico es un factor clave para reducir el consumo energético y las emisiones de CO_2 asociadas a la producción de energía[6,7]. Así, gobiernos como el de la Unión Europea han desarrollado marcos legislativos[8,9] para mejorar el rendimiento energético de los edificios. Existen dos caminos posibles para lograr este objetivo: aumentar el espesor de la capa aislante utilizando aislantes convencionales (como la lana mineral, la espuma de poliestireno, o la espuma de poliuretano), caracterizados por conductividades térmicas entre 25-60 mW/(m·K), o desarrollar nuevos superaislantes térmicos (como aerogeles o paneles de aislamiento al vacío (VIP)), caracterizados por conductividades térmicas mucho más bajas (4-16 mW/(m·K))[7,10–12]. Este último enfoque también ampliaría el área útil en los edificios ya que estos materiales brindan una mejor resistencia térmica con espesores reducidos.

En particular, en los últimos años, se ha afirmado repetidas ocasiones que los polímero nanocelulares (una nueva clase de polímeros celulares en la frontera de la ciencia de materiales y polímeros) podrían usarse potencialmente como un aislante térmico avanzado[13–15].

I.II. Polímeros nanocelulares

Desde la aparición de los primeros polímeros celulares en la década de los 1940, su desarrollo se ha centrado en mejorar su rendimiento. Como se muestra en la **Figura 3**, estos materiales se caracterizan por tamaños de celda de cientos de micras (polímeros celulares convencionales). Más tarde, a principios de la década de 1980, se produjeron los polímeros microcelulares (tamaños de celdas inferiores a 10 micras) en el Instituto Tecnológico de Massachusetts (MIT) (**Figura 3**)[16]. Los polímeros microcelulares mostraron propiedades mecánicas mejoradas en comparación con los polímeros celulares convencionales. Estos resultados sugirieron que se podría lograr una mayor mejora al reducir aún más el tamaño de celda, lo que dio lugar a los llamados polímeros nanocelulares (caracterizados por tamaños de células inferiores a 1 micrón) en la década de los 2000 (**Figura 3**). De hecho, los polímeros nanocelulares han mostrado propiedades prometedoras como reducción de la conductividad térmica a través de la fase gaseosa, transparencia, elevado área superficial y mejora de las propiedades mecánicas, entre otras[17–23]. Además, los polímeros nanocelulares, como muchos otros materiales celulares termoplásticos, también se caracterizan por su peso ligero, bajo costo y reciclabilidad. Por lo tanto, los polímeros nanocelulares presentan una combinación única de propiedades.

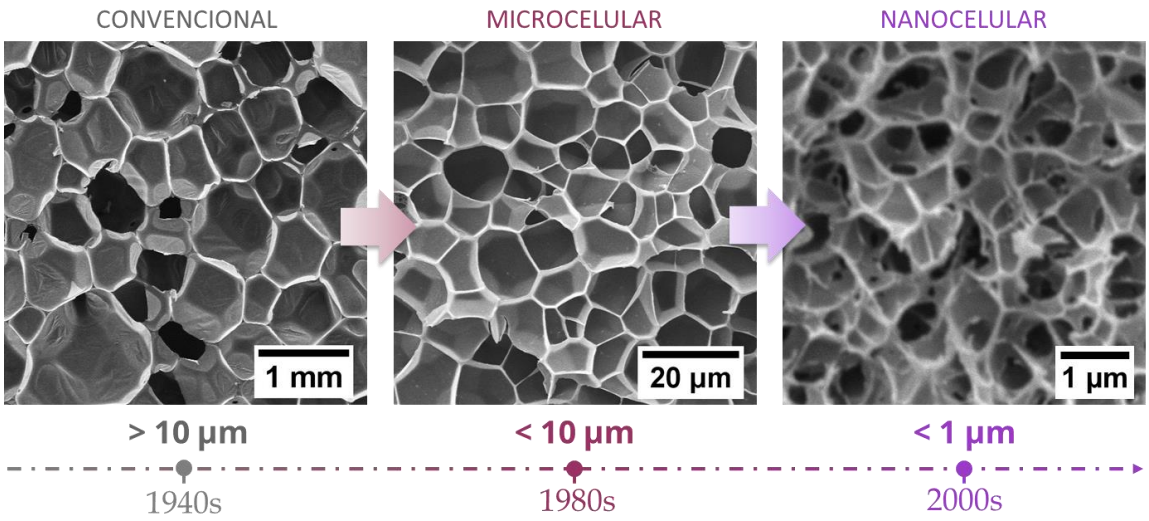

Figura 3. Evolución del tamaño de celda de los materiales celulares a lo largo del tiempo.

Esas propiedades excepcionales surgen como resultado de su tamaño de celda reducido, ya que las fases sólida y gaseosa están confinadas en la estructura nanocelular. Por un lado, la fase sólida está confinada en paredes celulares delgadas con espesores entre 20-60 nm, que son del mismo orden de magnitud que la longitud de la cadena del polímero[24,25]. Por otro lado, el gas está confinado en poros nanométricos. Cuando el tamaño de la celda se reduce a la nanoescala, las moléculas de gas chocan con mayor frecuencia con las paredes de las celdas que entre ellas, lo que reduce la transferencia de energía. Así, la contribución de la conducción a través de la fase gaseosa a la conductividad térmica total del material se ve drásticamente disminuida debido al llamado efecto Knudsen.[26].

Precisamente, la aparición del efecto Knudsen en polímeros nanocelulares[17,18] es la razón por la que estos materiales podrían ser potencialmente utilizados como aislantes térmicos avanzados al combinar bajas densidades y tamaños de celda nanométricos[13–15]. Sin embargo, hasta la fecha, faltan datos experimentales sobre la conductividad térmica total de los polímeros nanocelulares que demuestren el comportamiento de superaislante. Esto se debe a que la producción de polímeros nanocelulares sigue siendo un desafío[27], especialmente en el rango de baja densidad. Además, dado que los procesos de fabricación se limitan principalmente a la escala de laboratorio, la producción de muestras con dimensiones lo suficientemente grandes para su correcta caracterización también es una tarea compleja[28]. Así, solo unos pocos trabajos en la literatura recogen medidas de conductividad térmica de polímeros nanocelulares[17,29–33]. Sin embargo, la mayoría de estos resultados de conductividad térmica no son fiables, ya que han sido obtenidos utilizando una técnica transitoria para medir la conductividad térmica que permite medir muestras de pequeñas dimensiones pero cuya precisión para materiales aislantes térmicos no está clara[34–36].

Por estas razones, muchos autores han tratado de predecir teóricamente las propiedades térmicas de estos materiales[15,37–40] y, a pesar de las primeras predicciones[15], trabajos recientes[38–40] han demostrado que el mínimo de conductividad térmica que se puede alcanzar con estos materiales es superior a lo esperado para un aislante térmico avanzado. Esto se debe a que, a pesar de la reducción en la conducción a través de la fase gaseosa debido al efecto Knudsen, los otros dos mecanismos de transferencia de calor (radiación y conducción a través de la fase sólida) aumentan la conductividad térmica total.

La falta de conocimiento acerca de la conductividad térmica de los polímeros nanocelulares ha motivado el desarrollo de esta tesis, afrontando los retos que se muestran en la **Figura 4** para su aplicación como aislantes térmicos y persiguiendo los objetivos definidos en la Sección 3.

Figura 4. Retos en el campo de los polímeros nanocelulares para su aplicación como aislantes térmicos.

II. Marco de la tesis

Esta investigación se enmarca dentro de las actividades de investigación del Laboratorio de Materiales Celulares (CellMat)[41] perteneciente al Departamento de Física de la Materia Condensada de la Universidad de Valladolid. CellMat fue fundado en 1999 por el Prof. Dr. José Antonio de Saja y el Prof. Dr. Miguel Ángel Rodríguez-Pérez. CellMat nació como un laboratorio de caracterización de polímeros celulares comerciales, principalmente basados en poliolefinas. Desde un principio, la base de CellMat fue establecer la relación entre producción, estructura, propiedades y aplicaciones de los materiales celulares (tetraedro de materiales celulares) (**Figura 5**). Con la experiencia adquirida en los primeros años, en 2005, CellMat adquirió equipamiento para producir sus propios materiales celulares, dando un paso más en sus actividades de investigación. Otro objetivo clave de CellMat fue promover la transferencia de conocimiento y tecnología entre academia e industria como un factor crítico para el desarrollo industrial. Así, los investigadores de CellMat fundaron una empresa spin-off (CellMat Technologies S.L.) en 2012[42]. Actualmente, CellMat reúne más de 280 publicaciones científicas en JCR, 36 tesis doctorales defendidas, y su investigación se sustenta en cinco temas principales: polímeros nanocelulares[43–46], materiales celulares multifuncionales[47–50], nanocompuestos celulares[51,52], espumas de poliuretano[53,54] y materiales celulares bioplásticos[55,56]. En particular, esta tesis se enmarca en la línea de investigación de polímeros nanocelulares, siendo dirigida por el Prof. Dr. Miguel Ángel Rodríguez-Pérez, responsable de CellMat y CellMat Technologies S.L., y la Dra. Victoria Bernardo, líder del equipo de CellMat Technologies S.L.

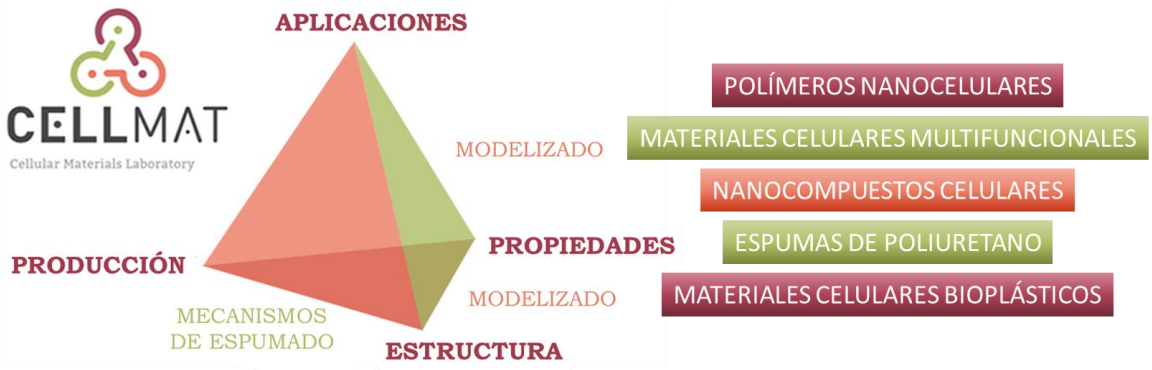

Figura 5. Base de las investigaciones de CellMat (tetraedro de materiales celulares), y líneas de investigación actuales.

La línea de investigación de los polímeros nanocelulares comenzó en 2014 con la tesis doctoral del Dr. Javier Pinto[45]. CellMat fue pionero en la producción de polímeros nanocelulares. Debido al gran interés en esta nueva clase de materiales cuatro tesis doctorales se han centrado en su estudio hasta la fecha, en particular las tesis doctorales de la Dra. Belén Notario[46], la Dra. Victoria Bernardo[43], la Dra. Judith Martín-de-León[44], y el Dr. Mikel Múgica[50]. Así, CellMat se ha convertido en un laboratorio de referencia en el campo de los polímeros nanocelulares. Por ejemplo,

CellMat demostró que la conducción a través de la fase gaseosa se reduce en este tipo de material debido a su tamaño de celda nanométrico (efecto Knudsen)[17], que si el tamaño de celda se reduce por debajo de 50 nm es posible producir polímeros nanocelulares transparentes[20,57], que los polímeros nanocelulares presentan propiedades mecánicas mejoradas[18,58], y que debido a su tamaño de celda reducido el coeficiente de extinción disminuye (mayor contribución de la radiación a la conductividad térmica total)[39].

El trabajo de investigación presentado en esta tesis doctoral se basa en la investigación previa y tiene como objetivo estudiar en profundidad la conductividad térmica de los polímeros nanocelulares y, a partir de ello, mejorar su aislamiento térmico. Además, esta investigación tiene como objetivo analizar el potencial de los polímeros nanocelulares para ser utilizados como núcleo (core) de VIPs.

III. Objetivos

La falta de conocimiento sobre la conductividad térmica de los polímeros nanocelulares ha motivado este trabajo. Esta investigación tiene un objetivo principal y tres metas secundarias (**Figura 6**). El objetivo principal es el **estudio de la conductividad térmica de polímeros nanocelulares**. Para lograr este fin, se fijan los siguientes objetivos secundarios:

- Medición de la conductividad térmica de polímeros nanocelulares con métodos de estado estacionario. Para lograr este objetivo se seguirán dos caminos. En primer lugar, desarrollar un método de estado estacionario que permita caracterizar la conductividad térmica de nuevos aislantes térmicos (como polímeros nanocelulares) desarrollados a escala de laboratorio (muestras de pequeñas dimensiones). En segundo lugar, fabricar muestras grandes para poder utilizar equipos de estado estacionario comerciales.
- Análisis de los mecanismos de transferencia de calor que tienen lugar en polímeros nanocelulares, evaluando su potencial y limitaciones. Esto se llevará a cabo combinando medidas experimentales (con datos fiables obtenidos por medio de técnicas de estado estacionario) y modelos analíticos.
- Mejora del aislamiento térmico proporcionado por los polímeros nanocelulares mediante una nueva ruta basada en la micronización. En esta tesis se desarrollará un nuevo material: un polvo de baja densidad formado por partículas micrométricas con celdas nanométricas en su interior. Para este nuevo material, también se estudiarán en detalle los mecanismos de transferencia de calor.

Figura 6. Objetivos generales de esta tesis.

Para lograr estos objetivos, se ha investigado la conductividad térmica de polimetilmetacrilato (PMMA) microcelular y nanocelular. Se ha elegido PMMA como matriz polimérica debido a su alta capacidad para producir materiales nanocelulares de baja densidad[20,25,59–62]. La metodología de la tesis se presenta en **Figura 7**. En primer lugar, se establecerá el método para medir la conductividad térmica en condiciones estacionarias. En segundo lugar, se estudiará la conductividad térmica, de polímeros nanocelulares en forma de placa basados en PMMA, tanto experimental como teóricamente para comprender los mecanismos de transferencia de calor. Luego, el material será micronizado para generar un nuevo material: un polvo nanocelular micronizado, que será estudiado en detalle. El análisis de este novedoso material también incluirá una caracterización detallada de la conductividad térmica del polvo y la posibilidad de compactar el material para generar prototipos para su uso como core de VIP, así como la optimización de la conductividad térmica mediante la adición de bloqueadores de infrarrojos.

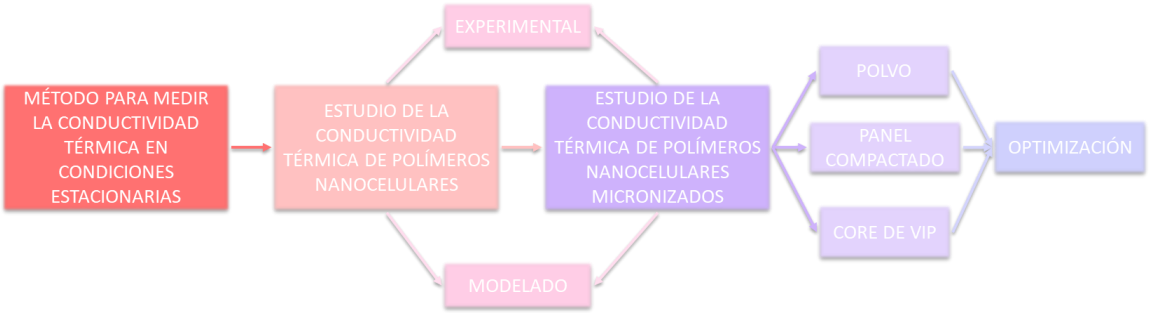

Figura 7. Metodología seguida en esta tesis.

Teniendo en cuenta los objetivos generales y la metodología de este trabajo, se han llevado a cabo las siguientes actividades:

1) Preparación de polímeros nanocelulares de baja densidad con grandes dimensiones adecuados para ser medidos en equipos de estado estacionario comerciales: Los equipos de estado estacionario comerciales requieren muestras con grandes dimensiones para las mediciones, pero la producción de tales especímenes de polímeros nanocelulares, especialmente en el rango de baja densidad, sigue siendo un reto. Esto se debe a que la producción de estos materiales está restringida a escala de laboratorio (pequeñas dimensiones). En esta tesis, enfrentamos este desafío al producir varias muestras

(caracterizadas por la misma densidad y estructura celular) que son apiladas para formar una muestra con dimensiones lo suficientemente grandes como para ser medida en equipos estado estacionario comerciales.

2) Caracterización de la conductividad térmica de muestras aislantes de pequeñas dimensiones: Las muestras aislantes producidas a escala de laboratorio (pequeñas dimensiones) se suelen caracterizar mediante técnicas transitorias, pero estos métodos no proporcionan datos fiables. Por lo tanto, esta tesis también tiene como objetivo desarrollar un método de estado estacionario para caracterizar adecuadamente la conductividad térmica de muestras aislantes de pequeñas dimensiones. El método desarrollado y su aplicabilidad a polímeros nanocelulares se muestran en el **Capítulo 3**
3) Análisis de la conductividad térmica del PMMA microcelular y nanocelular en forma de placa: Una vez medida la conductividad térmica del PMMA microcelular y nanocelular en forma de placa, el objetivo es estudiar los mecanismos de transferencia de calor para desarrollar un modelo capaz de predecir la conductividad térmica a partir de las características de las muestras (densidad y estructura celular). Los resultados de este estudio se muestran en el **Capítulo 4**. En cuanto a los parámetros clave del modelado, se establecen dos objetivos principales:
    a. Determinar experimentalmente el factor de estructura del sólido en polímeros nanocelulares de baja densidad. No hay datos confiables para este parámetro en la literatura. El factor de estructura del sólido es clave para comprender la conducción a través de la fase sólida y evaluar las diferencias entre los polímeros nanocelulares (estructura continua) y otros superaislantes (estructura discontinua).
    b. Determinar experimentalmente el coeficiente de extinción en polímeros nanocelulares de baja densidad, por primera vez, para cuantificar la contribución de la radiación y conocer las posibilidades de reducir este término.
4) Producción y caracterización de PMMA microcelular y nanocelular micronizado: se explorará la ruta de la micronización para mejorar aislamiento térmico proporcionado por los polímeros microcelulares y nanocelulares. Mediante la micronización se pretende transformar la estructura celular continua en una estructura discontinua, reduciendo así la contribución de la conducción a través de la fase sólida. Además, la micronización puede presentar algunas ventajas como la reducción de la densidad y de la radiación. Esto se debe a que las partículas van a estar rodeadas por aire y porque las partículas (o los huecos entre las partículas) pueden actuar como puntos de dispersión, respectivamente. Además, esta ruta puede permitir un escalado más fácil que la producción de muestras en forma de placa con grandes dimensiones. Este material es un sistema novedoso y una de las novedades clave de la presente tesis. Por tanto, el objetivo es estudiar en detalle los sistemas micronizados (densidad, contenido de celdas abiertas, estructura celular, empaque de

polvo, tamaño de partícula y conductividad térmica) y desarrollar un modelo capaz de predecir la conductividad térmica del material micronizado para comprender completamente los mecanismos de transferencia de calor en este novedoso material.

5) Fabricación y análisis de paneles compactados basados en PMMA microcelular y nanocelular micronizado: el objetivo es producir paneles compactados basados en PMMA microcelular y nanocelular micronizado para adquirir conocimientos sobre este nuevo enfoque. Para ello, se producirán paneles compactados y se caracterizará su conductividad térmica para desarrollar un modelo capaz de predecir la conductividad térmica de dichos sistemas y evaluar la contribución de cada mecanismo de transferencia de calor.
6) Evaluación del potencial de los paneles compactados como core de VIPs: Debido a su estructura abierta y porosa, las mediciones de conductividad térmica de los paneles compactados se realizarán a presión ambiente y al vacío, evaluando así el potencial de estos materiales para ser utilizados como core para paneles de aislamiento de vacío. Como paso final, nuestro objetivo es realizar una comparación de la conductividad térmica entre las muestras en forma de placa, las muestras micronizadas y los paneles compactados.
7) Optimización de los sistemas basados en PMMA microcelular y nanocelular micronizado mediante la adición de bloqueadores de infrarrojos: además de los otros beneficios, la micronización puede permitir una adición y dispersión más fácil de bloqueadores de infrarrojos en forma de polvo para reducir la contribución de la radiación. Esto se debe a que la dispersión de los bloqueadores de infrarrojos en la matriz polimérica antes de la etapa de espumado es un desafío ya que se requieren grandes cizalladuras durante el proceso de extrusión para evitar su aglomeración. Además, el proceso se vuelve más desafiante a medida que aumenta el porcentaje de bloqueadores de infrarrojos en la matriz polimérica. Por tanto, nuestro objetivo es estudiar el efecto de la adición de bloqueadores de infrarrojos en el material micronizado y en los paneles compactados.

IV. Estructura de la tesis

Esta tesis está escrita como un ***compendio de publicaciones***. En este trabajo se incluyen siete artículos científicos. De estos trabajos, cuatro de ellos ya han sido publicados, estando los otros tres pendientes de aceptación. Estos trabajos se incluyen en el **Capítulo 3** y en el **Capítulo 4**. Además, esta tesis cumple con los requisitos para obtener el título de **Doctor** con **Mención Internacional**. La estructura de los capítulos con sus correspondientes publicaciones científicas se presenta esquemáticamente en la **Figura 8**.

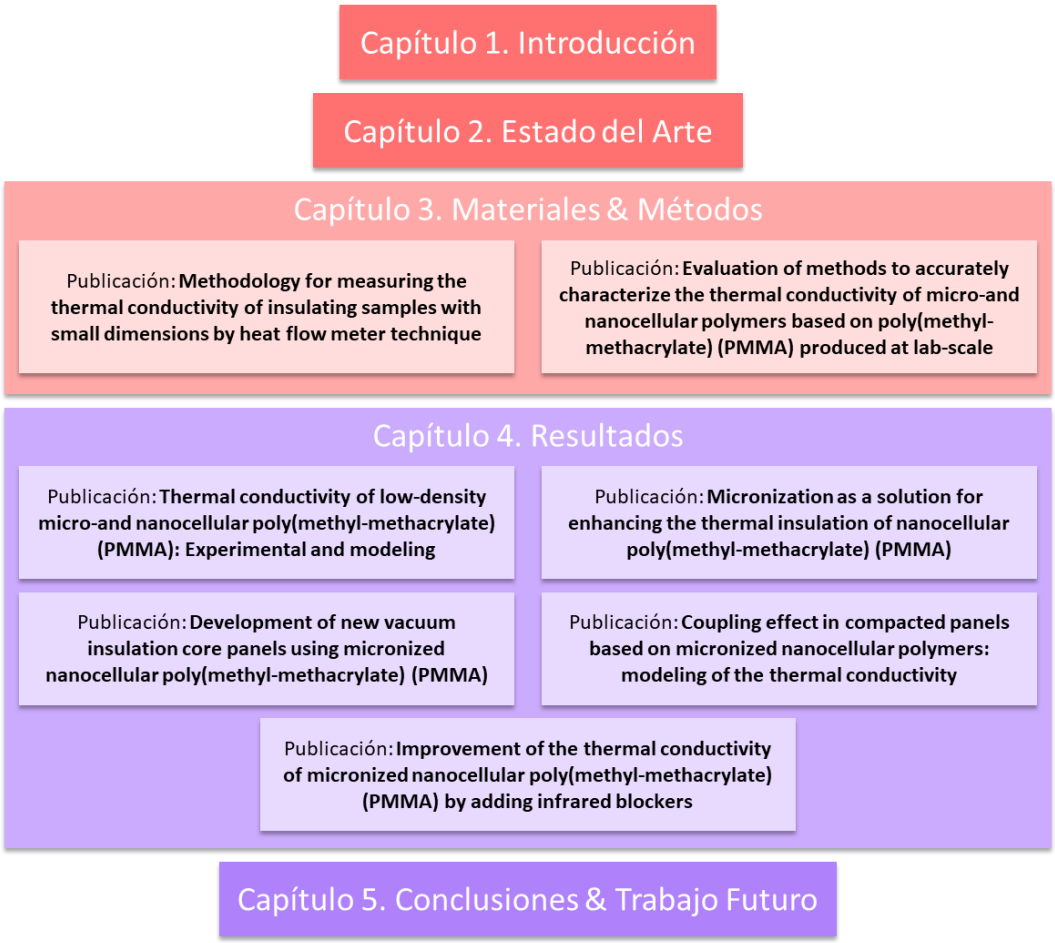

Figura 8. Estructura de la tesis: Resumen de los capítulos y publicaciones científicas.

El trabajo presentado en esta tesis está dividido en cinco capítulos que contienen la siguiente información.

Capítulo 1: Introducción. Este capítulo contiene una breve introducción al tema de investigación (los polímeros nanocelulares) y el marco de esta tesis dentro de CellMat. A esto le siguen los objetivos y una descripción general de la estructura de la tesis. Además, se presentan los artículos científicos, conferencias y otros trabajos relevantes derivados de esta investigación.

Capítulo 2: Estado del Arte. En primer lugar, este capítulo proporciona una descripción general de los polímeros nanocelulares con respecto a su producción, los parámetros clave para describir la estructura celular y sus propiedades. A continuación, se presenta un análisis detallado de los parámetros y las técnicas de caracterización de conductividad térmica de los polímeros nanocelulares. También se incluyen los datos de conductividad térmica de polímeros nanocelulares presentes en la literatura en función de los parámetros de estructura celular y la técnica utilizada. Estos datos son comparados con los principales aislantes térmicos utilizados en la actualidad. Finalmente, este capítulo incluye una revisión del estado del arte de los paneles de aislamiento al vacío (VIPs) debido al potencial de polímeros nanocelulares para ser utilizados como core de VIPs.

Capítulo 3: Materiales & Métodos. En este capítulo se describen las materias primas, las rutas de producción y las técnicas de caracterización utilizadas en esta investigación. Además, se incluyen dos publicaciones sobre el desarrollo y validación de una técnica para caracterizar adecuadamente la conductividad térmica de aislantes térmicos de pequeñas dimensiones, en particular para polímeros nanocelulares.

Capítulo 4: Resultados. En este capítulo se presentan los principales resultados de esta tesis recogidos en cinco publicaciones. Los artículos siguen una secuencia lógica, contando una historia sobre la caracterización experimental de la conductividad térmica de los sistemas nanocelulares, y su modelado y optimización para mejorar el aislamiento térmico proporcionado por estos materiales por medio de la micronización. En primer lugar, se presentan los resultados de polímeros microcelulares y nanocelulares de baja densidad en forma de placa. Luego, estos sistemas fueron micronizados, obteniendo un polvo caracterizado por partículas micrométricas con celdas nanométricas en su interior. Este material novedoso también se estudia en detalle. Posteriormente, el polvo es compactado obteniendo paneles que se pueden manipular. Los paneles compactados se estudian a presión ambiente y bajo vacío para evaluar su potencial para ser utilizados como core de VIP. Finalmente, los sistemas basados en polímeros microcelulares y nanocelulares micronizados son optimizadas mediante la adición de bloqueadores de infrarrojos para reducir el aporte de radiación.

Capítulo 5: Conclusiones & Trabajo Futuro. En este capítulo se presentan las principales conclusiones de esta investigación. Además, los resultados de conductividad térmica obtenidos en esta tesis se comparan con los datos de la literatura. Finalmente, se sugieren futuros temas de investigación relacionados con la optimización de los materiales producidos en este trabajo.

V. Publicaciones, patentes, conferencias y cursos

V.I. Publicaciones

Tabla 1 recoge todas las publicaciones relacionadas con esta tesis. Estas publicaciones se incluyen en el capítulo correspondiente. Por su parte, **Tabla 2** recoge otros trabajos científicos, relacionados con el campo de los polímeros microcelulares y nanocelulares, publicados durante el desarrollo de esta tesis y en los que el autor de esta tesis ha colaborado.

Tabla 1. Publicaciones en revistas internacionales incluidas en esta tesis.

Referencia de la publicación	Capítulo	Q/IF
I. Sánchez-Calderón, B. Merillas, V. Bernardo, M.Á. Rodríguez-Pérez **Methodology for measuring the thermal conductivity of insulating samples with small dimensions by heat flow meter technique** Journal of Thermal Analysis and Calorimetry 147 (2022) 12523–12533. https://doi.org/10.1007/s10973-022-11457-7	**3**	**Q1/4.755**

I. Sánchez-Calderón, Á. Sillero, F. Lizalde-Arroyo, V. Bernardo, J. Martín-de-León, M.Á. Rodríguez-Pérez **Evaluation of methods to accurately characterize the thermal conductivity of micro-and nanocellular polymers based on poly(methyl-methacrylate) (PMMA) produced at lab-scale** Polymer Testing 117 (2023) 107842. https://doi.org/10.1016/j.polymertesting.2022.107842	**3**	**Q1/4.931**
I. Sánchez-Calderón, V. Bernardo, J. Martín-de-León, M.Á. Rodríguez-Pérez **Thermal conductivity of low-density micro-and nanocellular poly(methyl-methacrylate) (PMMA): Experimental and modeling** Materials & Design 221 (2022) 110938. https://doi.org/10.1016/j.matdes.2022.110938	**4**	**Q1/9.417**
I. Sánchez-Calderón, V. Bernardo, D. Cuadra-Rodríguez, J. Martín-de-León, M.Á. Rodríguez-Pérez **Micronization as a solution for enhancing the thermal insulation of nanocellular poly(methyl-methacrylate) (PMMA)** Polymer (Guildf) 261 (2022) 125397. https://doi.org/10.1016/j.polymer.2022.125397	**4**	**Q1/4.432**
I. Sánchez-Calderón, V. Bernardo, F. Lizalde-Arroyo, J. Martín-de-León, M.Á. Rodríguez-Pérez **Development of new vacuum insulation core panels using micronized nanocellular poly(methyl-methacrylate) (PMMA)**	**4**	**-**
I. Sánchez-Calderón, V. Bernardo, F. Lizalde-Arroyo, J. Martín-de-León, M.Á. Rodríguez-Pérez **Coupling effect in compacted panels based on micronized nanocellular polymers: modeling of the thermal conductivity**	**4**	**-**
I. Sánchez-Calderón, V. Bernardo, F. Lizalde-Arroyo, J. Martín-de-León, M.Á. Rodríguez-Pérez **Improvement of the thermal conductivity of micronized nanocellular poly(methyl-methacrylate) (PMMA) by adding infrared blockers**	**4**	**-**

Tabla 2. Otras publicaciones.

Referencia de la publicación	**Q/IF**
I. Sánchez-Calderón, V. Bernardo, J. Martín-de-León, M.Á. Rodríguez-Pérez **Novel approach based on autoclave bead foaming to produce expanded polycarbonate (EPC) bead foams with microcellular structure and controlled crystallinity** Materials & Design. 212 (2021) 110200. https://doi.org/10.1016/j.matdes.2021.110200	**Q1/9.417**
I. Sánchez-Calderón, V. Bernardo, M. Santiago-Calvo, H. Naji, A. Saiani, M.Á. Rodríguez-Pérez **Effect of the molecular structure of TPU on the cellular structure of nanocellular polymers based on PMMA/TPU blends** Polymers (Basel). 13 (2021). https://doi.org/10.3390/polym13183055	**Q1/4.967**

V. Bernardo, J. Martin-de León, I. Sanchez-Calderon, E. Laguna-Gutiérrez, M.A. Rodríguez-Pérez **Nanocellular polymers with a gradient cellular structure based on poly(methyl methacrylate)/thermoplastic polyurethane blends produced by gas dissolution foaming** Macromolecular Materials and Engineering. 1900428 (2019) 1900428. https://doi.org/10.1002/mame.201900428	**Q1/3.853**

V.II. Patentes

Tabla 3 recoge las patentes publicadas durante el desarrollo de la tesis.

Tabla 3. Patentes.

Patentes
WO 2022/117642 A1: NANOCELLULAR EXPANDED POLYMER BEADS, METHOD OF MANUFACTURE AND USES. M. Múgica Izaguirre, V. Bernardo García, J. Martín de León, I. Sánchez Calderón, M.Á. Rodríguez Pérez.

V.III. Conferencias

Los resultados de esta tesis han sido presentados en varios congresos internacionales, como se presenta en **Tabla 4**.

Tabla 4. Contribuciones a conferencias internacionales.

Contribución a conferencia
12/10/2022 – 14/10/2022: CellMAT 2022. Organized by Deutsche Gesellschaft für Materialkunde e.V. / German Materials Society. Hybrid-Conference (Web participation). **A detailed study of the heat transfer mechanisms in micro-and nanocellular PMMA: modelling of the thermal conductivity** Ismael Sánchez Calderón; Victoria Bernardo García; Miguel Ángel Rodríguez Pérez *Comunicación oral*
11/04/2022 – 12/04/2022: IVIS 2021. Organized by Brunel University. London, United Kingdom. **Analysis of the suitability of using powdered micro and nanocellular polymers as core materials for VIP** Ismael Sánchez Calderón; Victoria Bernardo García; Miguel Ángel Rodríguez Pérez *Comunicación oral & artículo científico*
13/09/2021 – 16/09/2021: FOAMS 2021. Organized by SPE (Society of Plastics Engineers). Web-Conference. **Study of the Feasibility of Producing Expanded Polycarbonate Bead Foams (EPC) By Autoclave Bead Foaming** Ismael Sánchez Calderón; Victoria Bernardo García; Miguel Ángel Rodríguez Pérez *Comunicación oral & artículo científico*
07/10/2020 – 09/10/2020: CellMAT 2020. Organized by Deutsche Gesellschaft für Materialkunde e.V. / German Materials Society. Web-Conference. **Study of the thermal conductivity of powdered microcellular polymers based on PMMA** Ismael Sánchez Calderón; Victoria Bernardo García; Miguel Ángel Rodríguez Pérez *Póster*

02/10/2019 – 03/10/2019: FOAMS 2019. Organized by SPE (Society of Plastics Engineers). Valladolid, Spain.

Low-density PMMA/TPU nanocellular polymers with tuneable cellular structure by modifying the TPU chemistry and concentration

Ismael Sánchez Calderón; Victoria Bernardo García; Mercedes Santiago Calvo; Judith Martín de León; Miguel Ángel Rodríguez Pérez

Póster

24/10/2018 – 26/10/2018: CellMAT 2018. Organized by Deutsche Gesellschaft für Materialkunde e.V. / German Materials Society. Bad Staffelstein, Alemania.

Fabrication of low-density nanocellular polymers using PMMA/TPU blends

Victoria Bernardo Garcia; Judith Martín de León; Ismael Sánchez Calderón; Ester Laguna Gutiérrez; Miguel Ángel Rodríguez Pérez

Co-autor en comunicación oral

V.IV. Estancias de investigación, cursos y proyectos

Tabla 5, **Tabla 6, y Tabla 7** recogen las estancias de investigación en otras instituciones, los cursos realizados y otras actividades de investigación relacionadas con la participación en proyectos financiados durante el desarrollo de la tesis respectivamente.

Tabla 5. Estancias de investigación en otras instituciones.

Localización, fecha y tema
Universidad de Coimbra (Portugal) → Octubre 2022 – Enero 2023 Tema: **Preparation of super insulating materials by blending nanocellular PMMA powder and silica aerogels**

Tabla 6. Cursos que se han realizado durante la tesis.

Título, organizador, localización y fecha
Carnet radiológico Universidad de Valladolid – Valladolid, España, Febrero 2021

Tabla 7. Participación en proyectos con financiación.

FINANCIACIÓN PÚBLICA
POLIMEROS NANOCELULARES TRANSPARENTES Y AISLANTES TERMICOS: FABRICACION, CARACTERIZACION Y RELACION PROCESOESTRUCTURA- PROPIEDADES. Referencia: RTI2018-098749-B-I00, Ministerio de Ciencia e Innovación, Programa Estatal de I+D+i Orientada a los Retos de la Sociedad. 01/01/2019-30/09/2022. Presupuesto: 157300 €
SUSTAINABLE PRODUCTION OF SUPER THERMAL INSULATING NANOCELLULAR POLYMERS WITH REDUCED THERMAL CONDUCTIVITY BY INCREASING PHONONS SCATTERING. Referencia: TED2021-130965B-I00, Ministerio de Ciencia e Innovación, Proyectos estratégicos orientados transición ecológica y transición digital 2021. 01/01/2022-30/12/2022. Presupuesto: 146800 €
DESARROLLO DE SUPER AISLANTES TERMICOS BASADOS EN POLIMEROS NANOCELULARES Y BLOQUEDAORES DE LA RADACION INFRAROJA. Referencia: PID2021-127108OB-I00, Ministerio de Ciencia e Innovación, Proyectos de Generación de Conocimiento 2021. 01/09/2022-31/08/2025. Presupuesto: 205700 €
HACIA LA PRODUCCION INDUSTRIAL DE POLIMEROS NANOCELULARES TRANSPARENTES. Referencia: PDC2022-133391-I00, Ministerio de Ciencia e Innovación, Proyectos I+D+i Pruebas de Concepto 2022. 01/12/2022-31/12/2023. Presupuesto: 149500 €

FINANCIACIÓN PRIVADA
DESARROLLO DE ESTRATEGÍAS PARA FABRICAR POLÍMEROS NANOCELULARES EN PROCESOS INDUSTRIALES: EXTRUSIÓN Y PERLITAS EXPANDIDAS. Tipo de contrato: Artículo 83 Investigación, Financiado por CellMat Technologies S.L. 01/12/2014-30/12/2020. Presupuesto: 120000 €
EVALUACIÓN DE LA VIABILIDAD PARA PRODUCIR POLÍMEROS NANOCELULARES USANDO MUY ELEVADAS PRESIONES. Tipo de contrato: Artículo 83 Investigación, Financiado por HIPERBARIC, S.A, 19/02/2019-30/06/2020. Presupuesto: 50200 €
INVESTIGACIÓN DE TECNOLOGÍA DE ESPUMACIÓN DE POLÍMEROS NANOCELULARES (PROYECTO NCELL). Tipo de contrato: Artículo 83 Investigación, Financiado por HIPERBARIC, S.A, 18/03/2021-31/12/2022. Presupuesto: 65000 €
MICRONIZADO, COMPACTACIÓN Y CARACTERIZACIÓN DE PERLITAS NANOCELULARES EXPANDIDAS. Tipo de contrato: Artículo 83 Investigación, Financiado por CellMat Technologies S.L. 25/04/2021-31/07/2022. Presupuesto: 59000 €
FABRICACIÓN DE MATERIALES PRECURSORES Y CARACTERIZACIÓN DE LAS PROPIEDADES FÍSICAS DE POLÍMEROS NANOCELULARES. Tipo de contrato: Artículo 83 Investigación, Financiado por CellMat Technologies S.L. 25/04/2021-31/01/2023. Presupuesto: 58250 €

VI. Metodología del trabajo

En esta sección se describe la metodología de trabajo seguida en esta tesis doctoral.

VI.I. Materiales y producción

El material principal bajo estudio ha sido el polimetilmetacrilato (PMMA). El PMMA se caracteriza por su alta transparencia, alta resistencia al impacto y excelente aislamiento térmico y acústico. En lo que respecta a esta tesis, se utilizará como polímero de investigación debido a su alta afinidad por el CO_2 y su capacidad para producir materiales nanocelulares de baja densidad[20,25,59–62]. En esta tesis se empleado el grado de PMMA comercial 7H (ver el **Capítulo 3** Sección 3.1.1 para más información).

Por otra parte, para producir los materiales celulares se ha utilizado CO_2 (grado médico, 99% pureza).

Además, se han utilizado diferentes bloqueadores de infrarrojo como son el dióxido de titanio (TiO_2), las nanoplaquetas de grafito (GnP) y el carburo de silicio (SiC). Las características y distribuidores de los bloqueadores de infrarrojo empleados se detallan en el **Capítulo 3** Sección 3.1.3. Estos materiales tienen diferentes comportamientos de atenuación de la radiación infrarroja: las partículas de TiO_2 y SiC dispersan y absorben la radiación, mientras que las GnP reducen la transmisión infrarroja principalmente por absorción[31,63]. El estudio del efecto de la adición de los bloqueadores de infrarrojo a los materiales micronizados producidos en esta tesis se muestra en el **Capítulo 4** Sección 4.6.

VI.II. Producción

En esta tesis se han fabricado tres tipos de materiales celulares: materiales celulares en forma de placa, materiales celulares micronizados y paneles compactados. La **Figura 9** muestra el proceso seguido para la producción de los materiales.

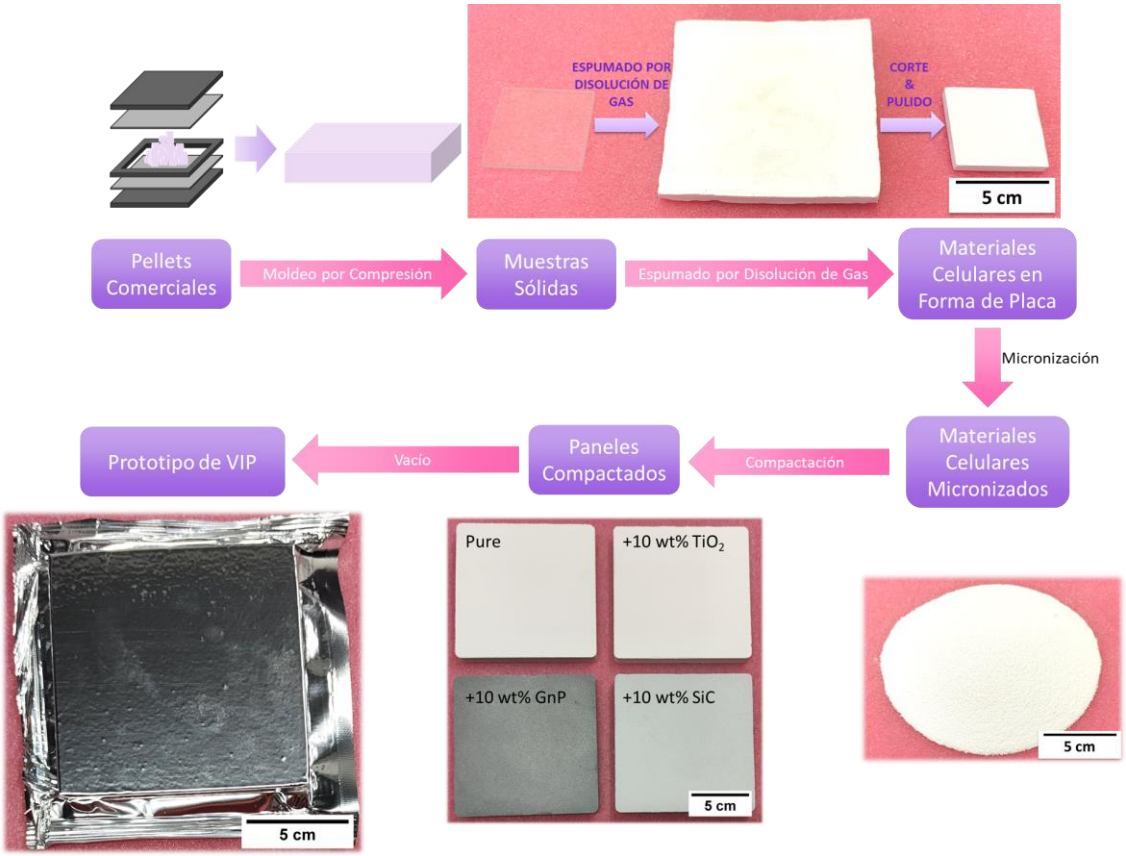

Figura 9. Proceso de producción seguido en esta tesis.

En primer lugar, a partir de los pellets comerciales de PMMA se han fabricado, por medio de la técnica conocida como moldeo por compresión, muestras sólidas de PMMA para su posterior espumado. Ver el **Capítulo 3** Sección 3.2.1 para más información acerca de la producción de las muestras sólidas.

A continuación, se han fabricado los materiales celulares en forma de placa a través del llamado espumado por disolución de gas. Para el estudio de la conductividad térmica de las placas de PMMA microcelular y nanocelular (**Capítulo 4** Sección 4.2) estos materiales fueron cortados y pulidos. El proceso de producción de los materiales celulares en forma de placa se detalla en el **Capítulo 3** Sección 3.2.2.

Una vez caracterizados, los materiales celulares en forma de placa han sido micronizados por medio de un molino batidor de rotor, obteniendo materiales celulares micronizados (ver el **Capítulo 3** Sección 3.2.3).

Finalmente, se han producido paneles compactados tras la compactación del material celular micronizado como se detalla en **Capítulo 3** Sección 3.2.4. Además, se han producido prototipos de VIPs tras realizar vacío a los paneles compactados (ver el **Capítulo 3** Sección 3.2.5 para más información acerca del proceso).

VI.III. Caracterización

Se han empleado diversas técnicas de caracterización en función del tipo de material como se muestra en la **Tabla 8**. En el **Capítulo 3** Sección 3.3 se detallan en profundidad las técnicas utilizadas.

Tabla 8. Técnicas de caracterización utilizadas en esta tesis para los diferentes tipos de materiales producidos.

Material & Caracterización	***Sólido***	***Material Celular en Forma de Placa***	***Material Celular Micronizado***	***Panel Compactado***
Densidad	Picnometría	Principio de Arquímedes	Densidad Aparente	Densidad Aparente
Estructura Celular	-	SEM	SEM	SEM
Contenido de Celda Abierta	-	Picnometría	Picnometría	-
Tamaño de Partícula	-	-	Tomografía de Rayos X Análisis de Imagen Difracción Láser	-
Conductividad Térmica	-	HFM TPS	HFM	HFM

- Sólido: Se midió la densidad mediante picnometría de gases.
- Material celular en forma de placa: La densidad fue obtenida mediante el principio de Arquímedes. Por otro lado, la estructura celular se caracterizó a través de microscopía electrónica de barrido (SEM). Además, contenido de celda abierta se obtuvo a través de picnometría de gases. Finalmente, se midió la conductividad térmica mediante métodos de estado estacionario, utilizado un conductivímetro medidor de flujo de calor (HFM), y de estado transitorio utilizando la técnica conocida como TPS.
- Material celular micronizado: La densidad fue obtenida mediante el método de densidad aparente rellenando un volumen conocido con cierta masa de material. Se utilizó microscopía electrónica de barrido (SEM) para visualizar las partículas y picnometría de gases para obtener el contenido de celda abierta. Además, se caracterizó el tamaño de polvo mediante diversas técnicas: tomografía de Rayos X, análisis de imagen y difracción láser. Por último, se utilizó un conductivímetro medidor de flujo de calor (HFM) para medir la conductividad térmica.
- Panel compactado: La densidad fue obtenida mediante el método de densidad aparente tras medir la masa y las dimensiones del panel compactado. Por otro lado, se utilizó microscopía electrónica de barrido (SEM) para visualizar las partículas tras el proceso de compactación. Finalmente, la conductividad térmica fue medida tanto a presión ambiente como a diferentes presiones de vacío mediante un conductivímetro medidor de flujo de calor (HFM). En el **Capítulo 3** Sección 3.3.5.1 se detalla el procedimiento para las mediciones en vacío.

VII. Principales resultados y conclusiones

Esta tesis ha investigado en detalle la conductividad térmica de polímeros nanocelulares. Los objetivos de la tesis se muestran esquemáticamente en la **Figura 10** junto con los principales logros relacionados con cada uno. Fue posible medir la conductividad térmica de polímeros nanocelulares utilizando técnicas confiables y usar los resultados para comprender en detalle los mecanismos de transferencia de calor en los materiales en forma de placa y modelar su conductividad térmica. Luego, se mejoró el aislamiento térmico proporcionado por los polímeros nanocelulares gracias a la principal novedad de esta tesis: la micronización de polímeros nanocelulares para dar lugar a un nuevo material, a partir del cual se pueden producir paneles compactados. Los materiales micronizados y compactados fueron estudiados en detalle para comprender también los mecanismos de transferencia de calor y desarrollar modelos para predecir su conductividad térmica. Se obtuvieron resultados bastante prometedores en los paneles compactados, con conductividades mínimas de 10.7 mW/(m·K) en vacío y tan bajas como 9.6 mW/(m·K) cuando se añadieron bloqueadores de infrarrojos.

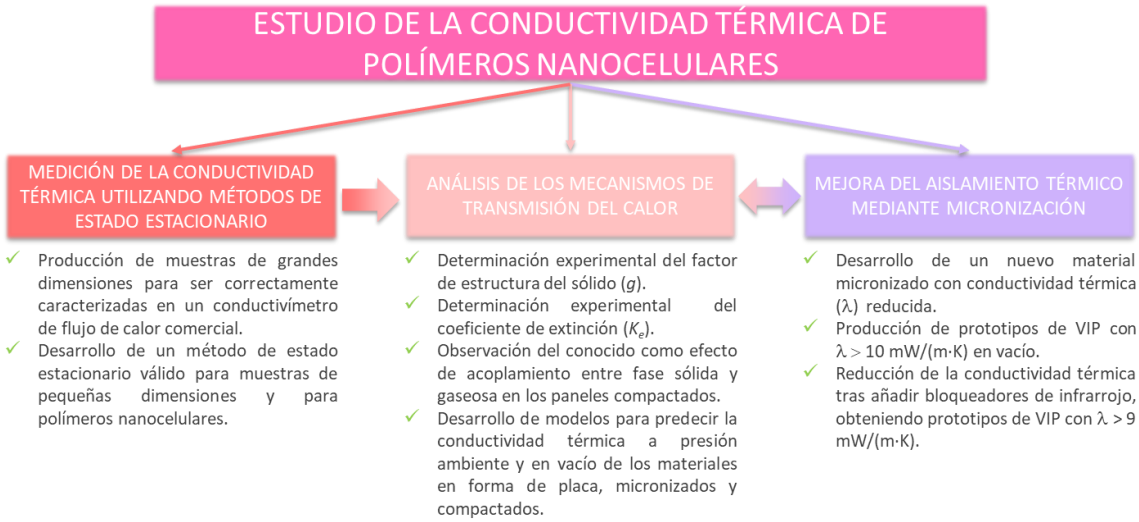

Figura 10. Objetivos y principales logros alcanzados en esta tesis.

Así, los resultados presentados en el **Capítulo 3** y el **Capítulo 4** han reportado varias conclusiones importantes en el campo de los polímeros nanocelulares. Las conclusiones principales se recogen en los siguientes párrafos:

VII.I. Polímeros nanocelulares en forma de placa: medida de la conductividad térmica

Muestras de polimetilmetacrilato (PMMA) microcelular y nanocelular de baja densidad (densidades relativas entre 0.09-0.18 y tamaños de celda entre 400-4000 nm) fueron producidas mediante espumado por disolución de gas utilizando CO_2 como agente espumante físico. Tras cortar y pulir las muestras se obtuvieron placas con dimensiones de 50×50×7 mm^3.

- Las muestras se apilaron formando un stack de grandes dimensiones (150×150×14 mm^3) para medir adecuadamente su conductividad térmica a diferentes temperaturas utilizando un conductivímetro de flujo de calor comercial (HFM) (**Capítulo 4** Sección 4.2). Las muestras fabricadas rellenan nuevas regiones en términos de densidad relativa - tamaño de celda - conductividad térmica con respecto al estado del arte[17,29–33,44,64] como se muestra en **Figura 11**. Conductividades térmicas entre 37.4-46.6 mW/(m·K) fueron obtenidas a 10 °C para las muestras en forma de placa. Es importante señalar que la mayoría de los datos de la literatura se obtienen de muestras de pequeñas dimensiones utilizando la técnica transitoria conocida como TPS, cuya precisión para caracterizar la conductividad térmica de los aislantes térmicos no está clara[34–36]. Entonces, los resultados obtenidos son uno de los pocos puntos de datos confiables en la literatura junto con las mediciones de estado estacionario obtenidas a través de conductivímetro de placa caliente protegida casero (GHP*) y sensores externos (ES).

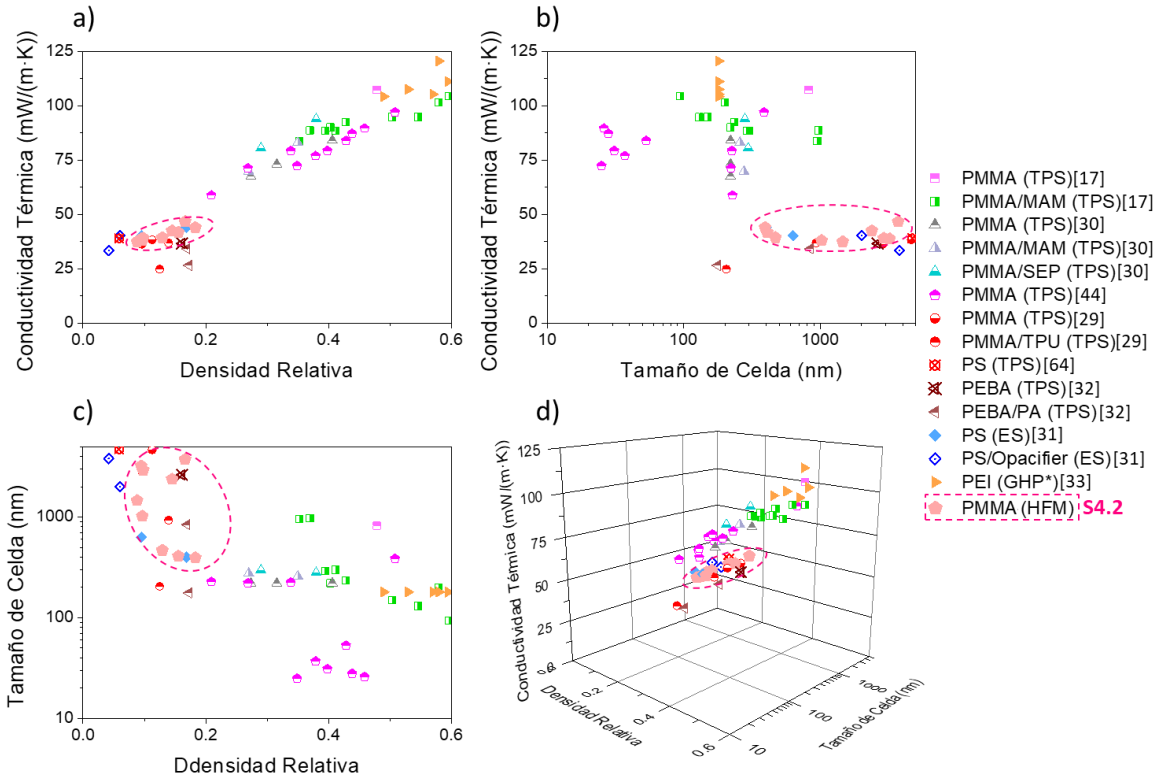

Figura 11. Conductividad térmica de polímeros nanocelulares en forma de placa (datos del estado del arte + resultados de esta tesis): a) conductividad térmica - densidad relativa, b) conductividad térmica - tamaño de celda, c) tamaño de celda - densidad relativa, y d) mapa 3D: conductividad térmica - tamaño de celda - densidad relativa.

- Paralelamente a las mediciones HFM de muestras grandes, se desarrollaron y validaron dos métodos de estado estacionario capaces de medir muestras de pequeñas dimensiones,

mostrando resultados precisos (**Figura 12**): el uso de una máscara de menor conductividad térmica (M) y el uso de sensores externos (ES) (**Capítulo 3** Sección 3.4 y Sección 3.5).

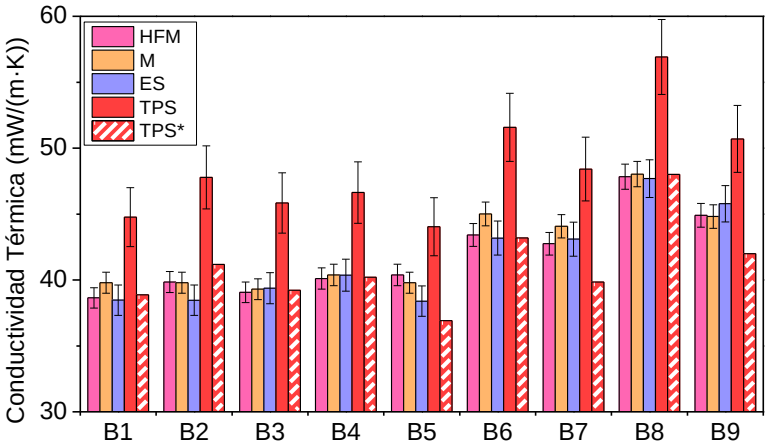

Figura 12. Conductividad térmica de PMMA nanocelular en forma de placa obtenida a través del conductivímetro de flujo de calor comercial (HFM), el método de máscara (M), el método de sensores externos (ES), el método TPS y aplicando la corrección TPS propuesta por Zheng et al.[35]. Extraído del **Capítulo 3** Sección 3.5.

- Método de máscara (M): La máscara llena el área del transductor de flujo de calor del HFM comercial que la muestra no puede cubrir. Por lo tanto, el flujo de calor total resultante en los transductores es la suma del flujo de calor a través de la muestra y la máscara. Este método permite medir de manera cómoda y precisa la conductividad térmica de pequeñas muestras aislantes utilizando un conductivímetro de flujo de calor convencional sin ninguna inversión adicional. Sin embargo, el principal inconveniente de este método es que la conductividad térmica de la máscara debe ser necesariamente inferior a la de la muestra para proporcionar resultados precisos. Este hecho puede complicar el uso de este método para muestras superaislantes como los aerogeles, caracterizados por conductividades térmicas de alrededor de 14 mW/(m·K)[65,66].
- Método de sensores externos (ES): el flujo de calor y la temperatura se miden en ambos lados de la muestra con sensores de flujo de calor externos y termopares, respectivamente. Además, se necesitan dos piezas de goma, colocadas entre la muestra y las placas del HFM, para minimizar las fluctuaciones del flujo de calor registrado. Esta metodología, desarrollada en esta tesis, ha sido descrita y validada para diferentes espumas convencionales (**Capítulo 3** Sección 3.4) y para polímeros nanocelulares (**Capítulo 3** Sección 3.5). En este caso hay que modificar el HFM convencional, pero la principal ventaja de este método es que se puede utilizar para cualquier tipo de material, incluso para superaislantes. De hecho, Merillas et al. [66–69] utilizan este método para medir la conductividad térmica de aerogeles caracterizados por conductividades térmicas tan bajas como 12 mW/(m·K).

- Finalmente, la conductividad térmica de las muestras en forma de placa también se midió a través de TPS, obteniendo altas desviaciones con respecto a las medidas de referencia (HFM), incluso cuando se aplica una corrección desarrollada por Zheng et al.[35] (TPS*) (**Capítulo 3** Sección 3.5), como se muestra en la **Figura 12**. Por lo tanto, el TPS, a pesar de permitir medir muestras con pequeñas dimensiones, no es una técnica confiable para caracterizar polímeros nanocelulares.

VII.II. Polímeros nanocelulares en forma de placa: modelado de la conductividad térmica

La conductividad térmica del PMMA microcelular y nanocelular en forma de placa se analizó en profundidad para estudiar la contribución de cada mecanismo de transferencia de calor (conducción a través de la fase sólida, conducción a través de la fase gaseosa y radiación) (**Capítulo 4** Sección 4.2).

- Los datos experimentales se utilizaron para calcular el factor de estructura del sólido (g) y el coeficiente de extinción (K_e) de los polímeros nanocelulares y conocer su comportamiento en estos novedosos sistemas:
    - Se introdujo un método novedoso para determinar g a partir de la pendiente de la conductividad térmica frente a la temperatura al cubo. Se obtuvieron g en torno a 0.89. Esos valores son altos en comparación con otros superaislantes térmicos como los aerogeles que presentan valores en torno a 0.05[70,71]. La razón de este diferente comportamiento está relacionada con la estructura de la fase sólida: los polímeros nanocelulares presentan una fase sólida continua, mientras que los aerogeles presentan una estructura discontinua caracterizada por partículas en contacto. Además, el aumento del factor de estructura del sólido en comparación con los materiales celulares convencionales de baja densidad (donde g oscila entre 1/3 y 2/3 para espumas de celdas abiertas y cerradas respectivamente[5]), puede estar asociado con un incremento de la conductividad térmica del polímero cuando está confinado en las paredes y aristas de la celda. Por lo tanto, en lugar de distribuirse aleatoriamente, las cadenas de polímero se orientan en la estructura, facilitando el transporte de fonones.
    - A partir del análisis de la conductividad térmica vs. La temperatura, se puede obtener el coeficiente de extinción (en el que se incluyen los mecanismos de absorción y dispersión de la radiación). Esta es la primera vez que se obtiene el coeficiente de extinción de polímeros nanocelulares basados en PMMA mediante mediciones de conductividad térmica. Así, se ha obtenido una ecuación empírica que relaciona el tamaño de celda y la densidad con el coeficiente de extinción. K_e disminuye a medida que se reduce el tamaño de la celda debido a la reducción de la dispersión de la radiación infrarroja por parte de las celdas. Estos resultados concuerdan con los

obtenidos, tanto a nivel teórico como experimental, para polímeros nanocelulares[39,40].

- Se desarrolló un modelo semiempírico capaz de predecir la conductividad térmica de PMMA microcelular y nanocelular de baja densidad. El modelo semiempírico depende únicamente de las propiedades de la espuma (densidad relativa y tamaño de celda) y las condiciones de la medida (temperatura y presión). El modelo permite comprender la influencia de cada parámetro en la conductividad total, así como las conductividades mínimas esperadas que se pueden alcanzar dependiendo de cómo se distribuyan las cadenas del polímero en la espuma. Una reducción del factor de estructura sólida g conduce a conductividades térmicas más bajas. Además, la región donde aparece el mínimo cambia. Por ejemplo, a presión ambiental y suponiendo g = 0.89, la conductividad térmica mínima prevista es de 34 mW/(m·K) para densidades relativas de 0.08 y tamaños de celda de alrededor de 140 nm. Mientras tanto, si se supone g = 0.3, la conductividad térmica mínima prevista es de 22 mW/(m·K) para densidades relativas de 0.18 y tamaños de celda de alrededor de 70 nm. A vacío máximo y suponiendo g = 0.89, el modelo predice conductividades térmicas mínimas superiores a 17 mW/(m·K) para PMMA nanocelular en forma de placa.

- En general, la conductividad térmica aumenta con la densidad. Sin embargo, cuando el tamaño de celda se reduce por debajo de la micra, el efecto Knudsen juega un papel clave, lo que lleva a una reducción drástica de la conducción a través de la fase de las celdas, disminuyendo la conductividad térmica general. Como contrapartida, la reducción del tamaño de celda por debajo de la micra implica un aumento de la radiación para espumas de baja densidad. Por lo tanto, existe un compromiso entre estos dos factores (densidad relativa y tamaño de celda) para producir un material óptimo con una conductividad térmica mínima (**Figura 13**).

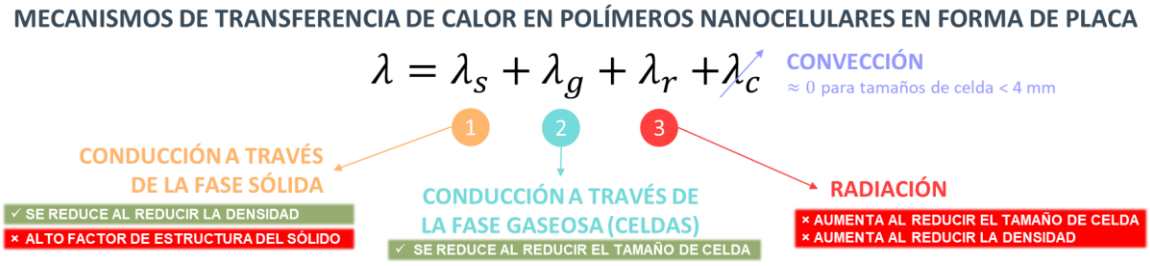

Figura 13. Mecanismos de transferencia de calor en polímeros nanocelulares en forma de placa.

VII.III. Sistemas micronizados basados en polímeros nanocelulares

Se exploró la micronización como una forma de mejorar el aislamiento térmico proporcionado por los polímeros nanocelulares al disminuir la conducción a través de la fase sólida, como una ruta

para escalar los polímeros nanocelulares y como un enfoque para facilitar la adición de bloqueadores de infrarrojos. Mediante la micronización es posible transformar la fase sólida continua de la estructura celular en una fase sólida discontinua con las nanoceldas dentro de partículas micrométricas. Se produjeron muestras micronizadas (M) (**Capítulo 4** Sección 4.3) y paneles compactaros (C) (**Capítulo 4** Sección 4.4) con dimensiones de 120×120×15 mm^3. Para la compactación se utilizó un molde con dimensiones similares a las de los materiales en forma de placa con el objetivo de poder comparar los resultados, pero el proceso también podría ser válido para moldes más grandes.

- En general, tras micronizar, la densidad (densidad aparente) se reduce debido a la presencia de huecos entre las partículas de polvo. Sin embargo, la densificación de las partículas de polvo durante el proceso de micronización podría conducir a densidades aparentes más altas. El aumento de densidad puede deberse a las fuerzas que intervienen en el proceso de molienda, es decir, el material puede comprimirse parcialmente y por tanto densificarse. La densificación es menor en muestras nanocelulares que en muestras microcelulares. Por tanto, los tamaños de celdas nanocelulares permiten un proceso de micronización más eficiente con menor densificación y una reducción significativa de la densidad.

- La micronización da como resultado partículas poliédricas donde la estructura celular es visible en la superficie de las partículas. Por lo tanto, el proceso de micronización mantiene la estructura celular y ayuda a interconectar la estructura celular, aumentando el contenido de celdas abiertas. Este es un factor clave para poder evacuar la estructura celular interna a la hora de producir paneles de aislamiento al vacío (VIP).

- La micronización permite obtener partículas de un tamaño aproximado de 100 µm (obtenido mediante análisis de imagen). El tamaño de las partículas depende del tamiz utilizado para la micronización. La distribución del tamaño de partículas es monomodal, pero cubre una amplia gama de tamaños de partículas.

- Es necesaria una densificación del 145% (bajo presión y temperatura) de la densidad aparente del material micronizado para obtener paneles compactados. La estructura nanocelular aún es visible en los paneles, lo que significa que el proceso de compactación no modifica significativamente la estructura y mantiene la interconectividad de las células.

- La micronización conduce a una reducción de la conductividad térmica debido a un cambio en los mecanismos de transferencia de calor debido a la discontinuidad de la fase sólida. Así, las muestras micronizadas (M) y los paneles compactados (C) presentan menor conductividad térmica a presión ambiente que los materiales en forma de placa (B), incluso presentando densidades más altas, como se muestra en la **Figura 14**.

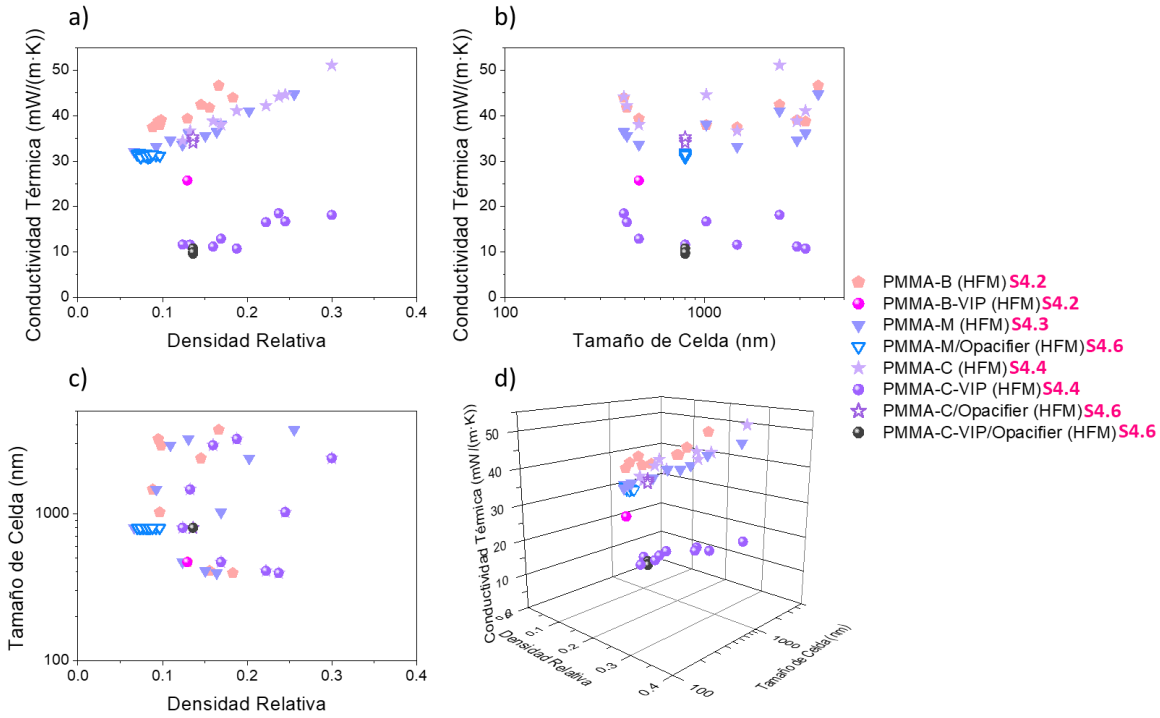

Figura 14. Conductividad térmica experimental de los materiales producidos en esta tesis (B-placas, M-micronizados, C-paneles compactados y VIP-paneles de aislamiento de vacío): a) conductividad térmica - densidad relativa, b) conductividad térmica - tamaño de celda, c) tamaño de celda – densidad relativa, y d) mapa 3D: conductividad térmica – tamaño de celda – densidad relativa.

- El estudio de las muestras micronizadas empleando un modelo simple, basado en los modelos habitualmente utilizados para describir los polímeros nanocelulares (**Capítulo 4** Sección 4.3), que incluye, en una primera aproximación, la conducción a través de la fase sólida, la conducción a través de las celdas, la conducción a través de los huecos y radiación mostró que:
  - El factor de estructura sólida se reduce en aproximadamente un 29% (de 0.89 a 0.63). Así, la conducción a través de la fase sólida disminuye gracias al proceso de micronización (las partículas de polvo actúan como resistencias térmicas adicionales).
  - El coeficiente de extinción aumenta ya que la presencia de partículas puede actuar como puntos de dispersión adicionales. Por lo tanto, la radiación térmica se reduce.

- Por otro lado, se ha observado que el comportamiento de la conductividad térmica en vacío (VIP) es diferente entre los materiales en forma de placa (B) y los paneles compactados (C) (**Capítulo 4** Sección 4.4), los cuales presentan menor conductividad térmica (casi la mitad, como se muestra en la **Figura 14**) y dos caídas de conductividad térmica (en lugar de una sola) (**Figura 15a**). Las caídas de conductividad térmica al evacuar el panel compactado corresponden al efecto Knudsen aplicado a la conducción a través de las celdas y al efecto

de acoplamiento, que depende del tamaño de celda y del tamaño de partícula respectivamente. Además, la reducción de la conductividad térmica en vacío fue mayor de lo esperado si solo se considera el efecto Knudsen. Por lo tanto, el estudio de los paneles compactados en vacío proporcionó nuevos conocimientos sobre los sistemas en polvo. Debido a la discontinuidad de la estructura, surge un nuevo mecanismo de transferencia de calor llamado efecto de acoplamiento. La conductividad térmica de acoplamiento tiene en cuenta la interacción entre las partículas del core y el gas en sistemas formados por partículas de contacto[72,73]. Este mecanismo adicional de transferencia de calor es insignificante para espumas con estructuras celulares continuas porque el efecto de acoplamiento es el resultado del flujo de calor de una partícula a otra a través de la fase gaseosa.

- Se desarrolló un modelo semiempírico capaz de predecir la conductividad térmica de paneles compactados basados en PMMA microcelular y nanocelular (**Capítulo 4** Sección 4.4). El modelo incluye conducción a través de la fase sólida, conducción a través de las celdas, radiación y efecto de acoplamiento. Debido al proceso de compactación, se considera que la fracción de vacíos era nula. El modelo presenta la principal novedad de considerar un sistema de partículas independientes para calcular los mecanismos de conducción. El modelo semiempírico depende únicamente de las propiedades del material compactado (densidad relativa aparente, tamaño de celda y tamaño de partícula) y las condiciones de medida (temperatura y presión). El modelo presenta una alta precisión para los paneles compactados a presiones ambientales, a vacío máximo y también a diferentes presiones de vacío, lo que permite analizar la contribución de cada mecanismo de transferencia de calor.
    - El modelo es único al introducir el concepto de asociación infinita de resistencias para cuantificar la conducción a través de las partículas de polvo. El modelo asume que la radiación en el panel compactado es como la de un material en forma de placa (la presencia de interfaces de partículas no crea superficies de dispersión adicionales para la radiación).
    - El modelo muestra que la reducción del factor de estructura sólida podría ser mayor a la esperada en base a los resultados del modelo simple utilizado para el material micronizado, disminuyendo de 0.89 a 0.33.
    - Se determinó el factor de acoplamiento (que depende de la densidad y la temperatura). El modelo muestra que el efecto de acoplamiento representa alrededor del 55% de la conductividad térmica total a presión ambiente.

- Para paneles compactados basados en polímeros nanocelulares, el modelo predice conductividades térmicas mínimas de 32.5 mW/(m·K) a presión ambiente y de 10 mW/(m·K) a vacío máximo.

- La **Figura 15** recoge una comparación entre muestras en forma de placa y paneles compactados de características similares (150 kg/m^3 y 500 nm de tamaño de celda, siendo 100 µm el tamaño de partícula del panel compactado) utilizando el modelo semiempírico desarrollado en esta tesis para cada sistema para hacer las predicciones. La **Figura 15a** muestra que el panel compactado presenta una conductividad térmica más baja a presión ambiente que la muestra en forma de placa (36.1 frente a 39.0 mW/(m·K) respectivamente); y tambien en vacío, donde la diferencia entre las dos conductividades es mucho mayor (11.8 frente a 24.2 mW/(m·K)). Mientras tanto, las **Figura 15b** y **15d** muestran que, debido a la micronización, la conducción a través de la fase sólida se reduce de 19.5 mW/(m·K) para la muestra en forma de placa a 7.1 mW/(m·K) para el panel compactado, lo que supone una reducción del aporte a conductividad térmica total de un 60% (del 50% al 20%). Asimismo, se observa que en los paneles compactados la contribución del efecto de acoplamiento representa más de la mitad de la conductividad térmica. La radiación es igual ya que ambos modelos utilizan la misma ecuación para determinarla.

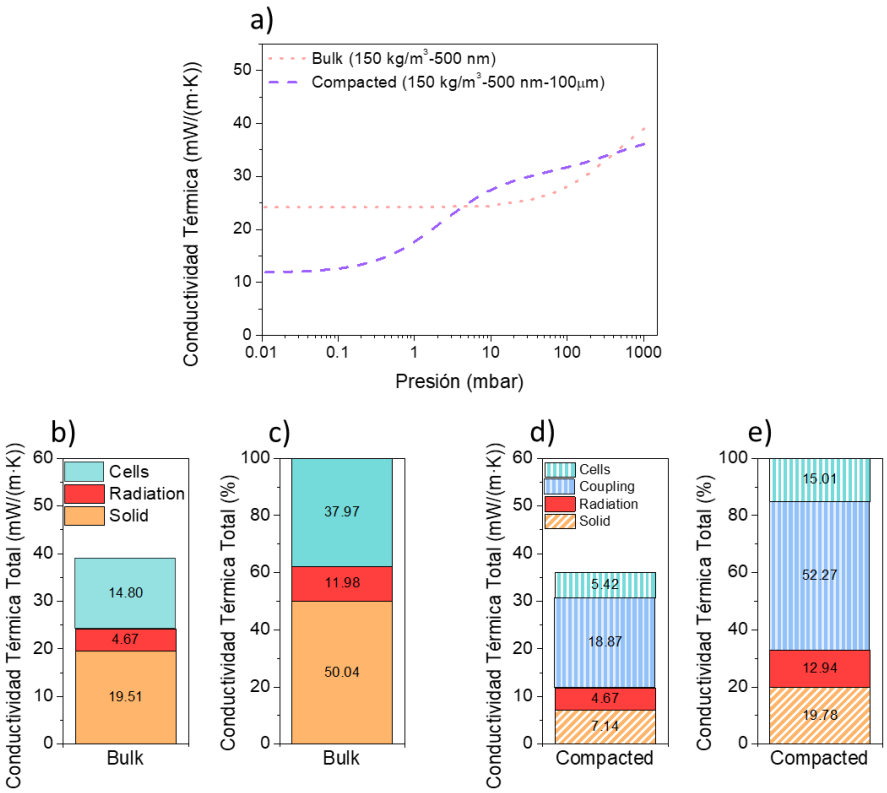

Figura 15. Comparación entre muestras en forma de placa y los paneles compactados de características similares (150 kg/m^3 y 500 nm de tamaño de celda, siendo el tamaño de partícula de la muestra compactada de 100 µm). a) Predicción de la conductividad térmica a 10ºC en función de

la presión de muestras en forma de placa y los paneles compactados según la ecuación obtenida en el **Capítulo 4** Sección 4.2 y en el **Capítulo 4** Sección 4.5 respectivamente. Contribución prevista de cada mecanismo a la conductividad térmica total del material en forma de placa en mW/(m·K) (b) y en % de la conductividad térmica total (c). Contribución prevista de cada mecanismo a la conductividad térmica total de los paneles compactados en mW/(m·K) (d) y en % de la conductividad térmica total (e).

- La micronización permite la introducción de bloqueadores de infrarrojos al hacer mezclas de polvo. La adición de bloqueadores de infrarrojo reduce la conductividad térmica, como se muestra en la **Figura 14**. Existe una cantidad de bloqueador de infrarrojo óptima que conduce a un mínimo de conductividad térmica debido a un compromiso entre reducir la radiación y aumentar la conducción a través de la fase sólida. Para paneles compactados de iguales características, en vacío, la adición de bloqueadores de infrarrojo redujo la conductividad térmica de 11.6 mW/(m·K) a 9.6 mW/(m·K) (**Capítulo 4** Sección 4.6).

Referencias

[1] D. Bozsaky, The historical development of thermal insulation materials, Period. Polytech. Archit. 41 (2010) 49. https://doi.org/10.3311/pp.ar.2010-2.02.

[2] Albert Farwell Bemis, The Evolving House, Cambridge, MA: Technology Press, 1933.

[3] R.T. Bynum, Insulation Handbook, McGraw-Hill Professional, 2000.

[4] P.D. Close, Thermal Insulation of Buildings, New York: Reinhold, 1947.

[5] N.C.. Hilyard, A. Cunningham, Low density cellular plastics Physical basis of behaviour, 1994. https://doi.org/10.1007/978-94-011-1256-7.

[6] J. Wernery, F. Mancebo, W.J. Malfait, M. O'Connor, B.P. Jelle, The economics of thermal superinsulation in buildings, Energy Build. 253 (2021) 111506. https://doi.org/10.1016/j.enbuild.2021.111506.

[7] M. Casini, Smart Buildings, 2016th ed., Elsevier, 2016. https://doi.org/10.1016/C2015-0-00182-4.

[8] Directive 2010/31/EU of the European Parliament and of the Council of 19 May 2010 on the energy performance of buildings, (n.d.).

[9] Directive 2012/27/EU of the European Parliament and of the Council of 25 October 2012 on energy efficiency, amending Directives 2009/125/EC and 2010/30/EU and repealing Directives 2004/8/EC and 2006/32/EC, (n.d.).

[10] W. Villasmil, L.J. Fischer, J. Worlitschek, A review and evaluation of thermal insulation materials and methods for thermal energy storage systems, Renew. Sustain. Energy Rev. 103 (2019) 71–84. https://doi.org/10.1016/j.rser.2018.12.040.

[11] S. Schiavoni, F. D'Alessandro, F. Bianchi, F. Asdrubali, Insulation materials for the building sector: A review and comparative analysis, Renew. Sustain. Energy Rev. 62 (2016) 988–1011. https://doi.org/10.1016/j.rser.2016.05.045.

[12] M. Casini, Advanced construction materials, in: Constr. 4.0, Elsevier, 2022: pp. 337–404. https://doi.org/10.1016/B978-0-12-821797-9.00005-2.

[13] S. Costeux, CO2-Blown nanocellular foams, J. Appl. Polym. Sci. 131 (2014). https://doi.org/10.1002/app.41293.

[14] S. Liu, J. Duvigneau, G.J. Vancso, Nanocellular polymer foams as promising high performance thermal insulation materials, Eur. Polym. J. 65 (2015) 33–45. https://doi.org/10.1016/j.eurpolymj.2015.01.039.

[15] C. Forest, P. Chaumont, P. Cassagnau, B. Swoboda, P. Sonntag, Polymer nano-foams for insulating applications

prepared from CO2 foaming, Prog. Polym. Sci. 41 (2015) 122–145. https://doi.org/10.1016/j.progpolymsci.2014.07.001.

[16] V. Kumar, N.P. Suh, A process for making microcellular thermoplastic parts, Polym. Eng. Sci. 30 (1990) 1323–1329. https://doi.org/10.1002/pen.760302010.

[17] B. Notario, J. Pinto, E. Solorzano, J.A. de Saja, M. Dumon, M.A. Rodríguez-Pérez, Experimental validation of the Knudsen effect in nanocellular polymeric foams, Polymer (Guildf). 56 (2015) 57–67. https://doi.org/10.1016/j.polymer.2014.10.006.

[18] B. Notario, J. Pinto, M.A. Rodriguez-Perez, Nanoporous polymeric materials: A new class of materials with enhanced properties, Prog. Mater. Sci. 78–79 (2016) 93–139. https://doi.org/10.1016/j.pmatsci.2016.02.002.

[19] B. Xiang, Y. Jia, Y. Lei, F. Zhang, J. He, T. Liu, S. Luo, Mechanical properties of microcellular and nanocellular silicone rubber foams obtained by supercritical carbon dioxide, Polym. J. 51 (2019) 559–568. https://doi.org/10.1038/s41428-019-0175-6.

[20] J. Martín-de León, V. Bernardo, M.Á. Rodríguez-Pérez, Key Production Parameters to Obtain Transparent Nanocellular PMMA, Macromol. Mater. Eng. 302 (2017) 1700343. https://doi.org/10.1002/mame.201700343.

[21] B. Notario, A. Ballesteros, J. Pinto, M.A. Rodríguez-Pérez, Nanoporous PMMA: A novel system with different acoustic properties, Mater. Lett. 168 (2016) 76–79. https://doi.org/10.1016/j.matlet.2016.01.037.

[22] B. Notario, J. Pinto, R. Verdejo, M.A. Rodríguez-Pérez, Dielectric behavior of porous PMMA: From the micrometer to the nanometer scale, Polymer (Guildf). 107 (2016) 302–305. https://doi.org/10.1016/j.polymer.2016.11.030.

[23] G.Q. Lu, X.S. Zhao, Nanoporous Materials - An Overview, in: Nanoporous Mater. Sci. Eng., Imperial College Press, 2004: pp. 1–13. https://doi.org/10.1142/9781860946561_0001.

[24] B. Notario, J. Pinto, M.A. Rodríguez-Pérez, Towards a new generation of polymeric foams: PMMA nanocellular foams with enhanced physical properties, Polymer (Guildf). 63 (2015) 116–126. https://doi.org/10.1016/j.polymer.2015.03.003.

[25] J. Martín-de León, V. Bernardo, M. Rodríguez-Pérez, Low Density Nanocellular Polymers Based on PMMA Produced by Gas Dissolution Foaming: Fabrication and Cellular Structure Characterization, Polymers (Basel). 8 (2016) 265. https://doi.org/10.3390/polym8070265.

[26] Z.-Y. Li, C.-Y. Zhu, X.-P. Zhao, A theoretical and numerical study on the gas-contributed thermal conductivity in aerogel, Int. J. Heat Mass Transf. 108 (2017) 1982–1990. https://doi.org/10.1016/j.ijheatmasstransfer.2017.01.051.

[27] J. Martín-de León, V. Bernardo, M. Rodríguez-Pérez, Nanocellular Polymers: The Challenge of Creating Cells in the Nanoscale, Materials (Basel). 12 (2019) 797. https://doi.org/10.3390/ma12050797.

[28] J. Martín-de León, V. Bernardo, P. Cimavilla-Román, S. Pérez-Tamarit, M.Á. Rodríguez-Pérez, Overcoming the Challenge of Producing Large and Flat Nanocellular Polymers: A Study with PMMA, Adv. Eng. Mater. 21 (2019). https://doi.org/10.1002/adem.201900148.

[29] G. Wang, J. Zhao, L.H. Mark, G. Wang, K. Yu, C. Wang, C.B. Park, G. Zhao, Ultra-tough and super thermal-insulation nanocellular PMMA/TPU, Chem. Eng. J. 325 (2017) 632–646. https://doi.org/10.1016/j.cej.2017.05.116.

[30] V. Bernardo, J. Martin-de Leon, J. Pinto, R. Verdejo, M.A. Rodriguez-Perez, Modeling the heat transfer by conduction of nanocellular polymers with bimodal cellular structures, Polymer (Guildf). 160 (2019) 126–137. https://doi.org/10.1016/j.polymer.2018.11.047.

[31] F. Almeida, H. Beyrichen, N. Dodamani, R. Caps, A. Müller, R. Oberhoffer, Thermal conductivity analysis of a new sub-micron sized polystyrene foam, J. Cell. Plast. 57 (2021) 493–515. https://doi.org/10.1177/0021955X20943101.

[32] J. Zhao, G. Wang, Z. Xu, A. Zhang, G. Dong, G. Zhao, C.B. Park, Ultra-elastic and super-insulating biomass

PEBA nanoporous foams achieved by combining in-situ fibrillation with microcellular foaming, J. CO2 Util. 57 (2022) 101891. https://doi.org/10.1016/j.jcou.2022.101891.

[33] C. Zhou, N. Vaccaro, S.S. Sundarram, W. Li, Fabrication and characterization of polyetherimide nanofoams using supercritical CO2, J. Cell. Plast. 48 (2012) 239–255. https://doi.org/10.1177/0021955X12437984.

[34] O. Almanza, M.A. Rodríguez-Pérez, J.A. De Saja, Applicability of the Transient Plane Source Method To Measure the Thermal Conductivity of Low-Density Polyethylene Foams, J. Polym. Sci. Part B Polym. Phys. 42 (2004) 1226–1234. https://doi.org/10.1002/polb.20005.

[35] Q. Zheng, S. Kaur, C. Dames, R.S. Prasher, Analysis and improvement of the hot disk transient plane source method for low thermal conductivity materials, Int. J. Heat Mass Transf. 151 (2020) 119331. https://doi.org/10.1016/j.ijheatmasstransfer.2020.119331.

[36] R.C. Kerschbaumer, S. Stieger, M. Gschwandl, T. Hutterer, M. Fasching, B. Lechner, L. Meinhart, J. Hildenbrandt, B. Schrittesser, P.F. Fuchs, G.R. Berger, W. Friesenbichler, Comparison of steady-state and transient thermal conductivity testing methods using different industrial rubber compounds, Polym. Test. 80 (2019) 106121. https://doi.org/10.1016/j.polymertesting.2019.106121.

[37] H. Yu, H. Zhang, J. Zhao, J. Liu, X. Xia, X. Wu, Thermal conductivity of micro/nano-porous polymers: Prediction models and applications, Front. Phys. 17 (2021). https://doi.org/10.1007/s11467-021-1107-4.

[38] G. Wang, C. Wang, J. Zhao, G. Wang, C.B. Park, G. Zhao, Modelling of thermal transport through a nanocellular polymer foam: Toward the generation of a new superinsulating material, Nanoscale. 9 (2017) 5996–6009. https://doi.org/10.1039/c7nr00327g.

[39] V. Bernardo, J. Martin-de Leon, J. Pinto, U. Schade, M.A. Rodriguez-Perez, On the interaction of infrared radiation and nanocellular polymers: First experimental determination of the extinction coefficient, Colloids Surfaces A Physicochem. Eng. Asp. 600 (2020). https://doi.org/10.1016/j.colsurfa.2020.124937.

[40] P. Buahom, C. Wang, M. Alshrah, G. Wang, P. Gong, M. Tran, C.B. Park, Wrong expectation of superinsulation behavior from largely-expanded nanocellular foams, Nanoscale. (2020). https://doi.org/10.1039/d0nr01927e.

[41] http://cellmat.es/, (n.d.).

[42] http://www.cellmattechnologies.com/en/, (n.d.).

[43] V. Bernardo, Production and Characterization of Nanocellular Polymers Based on Nanostructured PMMA Blends and PMMA Nanocomposites. (July 2019), n.d.

[44] J. Martin-de Leon, Understanding The Production Process Of Nanocellular Polymers Based On Pmma Driven By A Homogeneous Nucleation. (October 2019), n.d. https://pdfs.semanticscholar.org/a3d2/2c024e3c550652f34f510769ad3d84e6020d.pdf.

[45] J. Pinto, Fabrication and Characterization of Nanocellular Polymeric Materials from Nanostructured Polymers (May 2014), (n.d.).

[46] B. Notario, Fabrication and Characterization of the Physical Properties of Nanocellular Polymers: the Transition from the Micro to the Nanoscale (September 2016), (n.d.).

[47] E. López-González, Analysis of the Composition-Structure-Properties Relationship of Open-Cell Polyolefin-Based Foams With Tailored Levels of Gas-Phase Tortuosity (November 2019), n.d.

[48] C. Saiz-Arroyo, Fabricación de Materiales Celulares Mejorados Basados en Poliolefinas. Relación Procesado-Composición-Estructura-Propiedades (April 2012), (n.d.).

[49] M.Á. Rodríguez-Pérez, Propiedades Térmicas y Mecánicas de Espumas de Poliolefinas (March 1999), (n.d.).

[50] M. Múgica, Development of Cellular Low Density Expanded Beads. Formulation-Process-Structure Relationship (April 2022), (n.d.).

[51] H. Ventura, Development of New Composites Reinforced Lightweight Green Structures of Flax With Nonwoven Fibres (June 2017), (n.d.).

[52] A. Ballesteros, Understanding the Relationships Between Composition, Process, Cellular Structure and

Properties of Cellular Polymers Based on Blends of Polystyrene with Inorganic and Organic Nucleating Agents (April 2022), (n.d.).

[53] M. Santiago-Calvo, Synthesis, Foaming Kinetics and Physical Properties of Cellular Nanocomposites Based on Rigid Polyurethane (November 2019), n.d.

[54] P. Cimavilla-Román, Desing and Validation of Experimental Methods for Probing Foam Formation Dynamics and Structure. (Nobember 2022), (n.d.).

[55] L. Oliveira-Salmazo, Foaming Kinetics and Cellular Structure Control of Materials Based on Natural Rubber and Polyolefins (May 2015), n.d.

[56] A. López-Gil, Development of Environmentally Friendly Cellular Polymers for Packaging and Structural Applications. Study of the Relationship Cellular Structure-Mechanical Properties (January 2016), n.d.

[57] J. Martín-de León, J.L. Pura, V. Bernardo, M.Á. Rodríguez-Pérez, Transparent nanocellular PMMA: Characterization and modeling of the optical properties, Polymer (Guildf). 170 (2019) 16–23. https://doi.org/10.1016/j.polymer.2019.03.010.

[58] J. Martín-de León, F. Van Loock, V. Bernardo, N.A. Fleck, M.Á. Rodríguez-Pérez, The influence of cell size on the mechanical properties of nanocellular PMMA, Polymer (Guildf). 181 (2019) 121805. https://doi.org/10.1016/j.polymer.2019.121805.

[59] H. Guo, V. Kumar, Solid-state poly(methyl methacrylate) (PMMA) nanofoams. Part I: Low-temperature CO2 sorption, diffusion, and the depression in PMMA glass transition, Polymer (Guildf). 57 (2015) 157–163. https://doi.org/10.1016/j.polymer.2014.12.029.

[60] J. Pinto, J.A. Reglero-Ruiz, M. Dumon, M.A. Rodriguez-Perez, Temperature influence and CO2 transport in foaming processes of poly(methyl methacrylate)–block copolymer nanocellular and microcellular foams, J. Supercrit. Fluids. 94 (2014) 198–205. https://doi.org/10.1016/j.supflu.2014.07.021.

[61] V. Bernardo, J. Martin-de Leon, J. Pinto, T. Catelani, A. Athanassiou, M.A. Rodriguez-Perez, Low-density PMMA/MAM nanocellular polymers using low MAM contents: Production and characterization, Polymer (Guildf). 163 (2019) 115–124. https://doi.org/10.1016/j.polymer.2018.12.057.

[62] I. Sánchez-Calderón, V. Bernardo, M. Santiago-Calvo, H. Naji, A. Saiani, M.Á. Rodríguez-Pérez, Effect of the molecular structure of TPU on the cellular structure of nanocellular polymers based on PMMA/TPU blends, Polymers (Basel). 13 (2021). https://doi.org/10.3390/polym13183055.

[63] R. Caps, J. Fricke, Thermal conductivity of opacified powder filler materials for vacuum insulations, Int. J. Thermophys. 21 (2000) 445–452. https://doi.org/10.1023/A:1006691731253.

[64] P. Gong, P. Buahom, M.-P. Tran, M. Saniei, C.B. Park, P. Pötschke, Heat transfer in microcellular polystyrene/multi-walled carbon nanotube nanocomposite foams, Carbon N. Y. 93 (2015) 819–829. https://doi.org/10.1016/j.carbon.2015.06.003.

[65] B. Merillas, J.P. Vareda, J. Martín-de León, M.Á. Rodríguez-Pérez, L. Durães, Thermal Conductivity of Nanoporous Materials: Where Is the Limit?, Polymers (Basel). 14 (2022) 2556. https://doi.org/10.3390/polym14132556.

[66] B. Merillas, F. Villafañe, M.Á. Rodríguez-Pérez, Super-Insulating Transparent Polyisocyanurate-Polyurethane Aerogels: Analysis of Thermal Conductivity and Mechanical Properties, Nanomaterials. 12 (2022) 2409. https://doi.org/10.3390/nano12142409.

[67] B. Merillas, F. Villafañe, M.Á. Rodríguez-Pérez, Improving the Insulating Capacity of Polyurethane Foams through Polyurethane Aerogel Inclusion: From Insulation to Superinsulation, Nanomaterials. 12 (2022) 2232. https://doi.org/10.3390/nano12132232.

[68] B. Merillas, A. Lamy-Mendes, F. Villafañe, L. Durães, M.Á. Rodríguez-Pérez, Silica-Based Aerogel Composites Reinforced with Reticulated Polyurethane Foams: Thermal and Mechanical Properties, Gels. 8 (2022) 1–18. https://doi.org/10.3390/gels8070392.

[69] B. Merillas, A. Lamy-Mendes, F. Villafañe, L. Durães, M. Rodríguez-Pérez, Polyurethane foam scaffold for silica aerogels: effect of cell size on the mechanical properties and thermal insulation, Mater. Today Chem. 26 (2022). https://doi.org/10.1016/j.mtchem.2022.101257.

[70] P. Scheuerpflug, M. Hauck, J. Fricke, Thermal properties of silica aerogels between 1.4 and 330 K, J. Non. Cryst. Solids. 145 (1992) 196–201. https://doi.org/10.1016/S0022-3093(05)80455-7.

[71] L.W. Hrubesh, R.W. Pekala, Thermal properties of organic and inorganic aerogels, J. Mater. Res. 9 (1994) 731–738. https://doi.org/10.1557/JMR.1994.0731.

[72] S. Fantucci, A. Lorenzati, A. Capozzoli, M. Perino, Analysis of the temperature dependence of the thermal conductivity in Vacuum Insulation Panels, Energy Build. 183 (2019) 64–74. https://doi.org/10.1016/j.enbuild.2018.10.002.

[73] R. Baetens, B.P. Jelle, J.V. Thue, M.J. Tenpierik, S. Grynning, S. Uvsløkk, A. Gustavsen, Vacuum insulation panels for building applications: A review and beyond, Energy Build. 42 (2010) 147–172. https://doi.org/10.1016/j.enbuild.2009.09.005.

Chapter 1

Introduction

"I solemnly swear that I am up to no good."

Harry Potter

INDEX

1. Introduction

1.1. Introduction

1.1.1. Thermal insulation

Humans have been aware of the importance of thermal insulation in buildings since the beginning of the times (**Figure 1.1**)[1]. For instance, the first prehistoric peoples built temporary dwellings using animal furs, wool, and plant-related products, but their lifespan was limited. Later, because of the settled lifestyle, there was a need of using more durable materials for housing like wood, stone, or earth. For example, using the earth as an insulator, Egyptians retired to the coolness of subterranean chambers on hot days[2]. Historians believe that ancient Greeks and Romans discovered asbestos and found many uses for it because of its resistance to heat and fire[3]. Also, early inhabitants of Spain covered their stone houses with cork bark due to its insulation behavior[4]. As technology developed, so did innovations. With the introduction of the fireplace to provide controlled and artificial heat inside housing[2], it was clear that the challenge became not only how to keep cold out but also how to keep heat in.

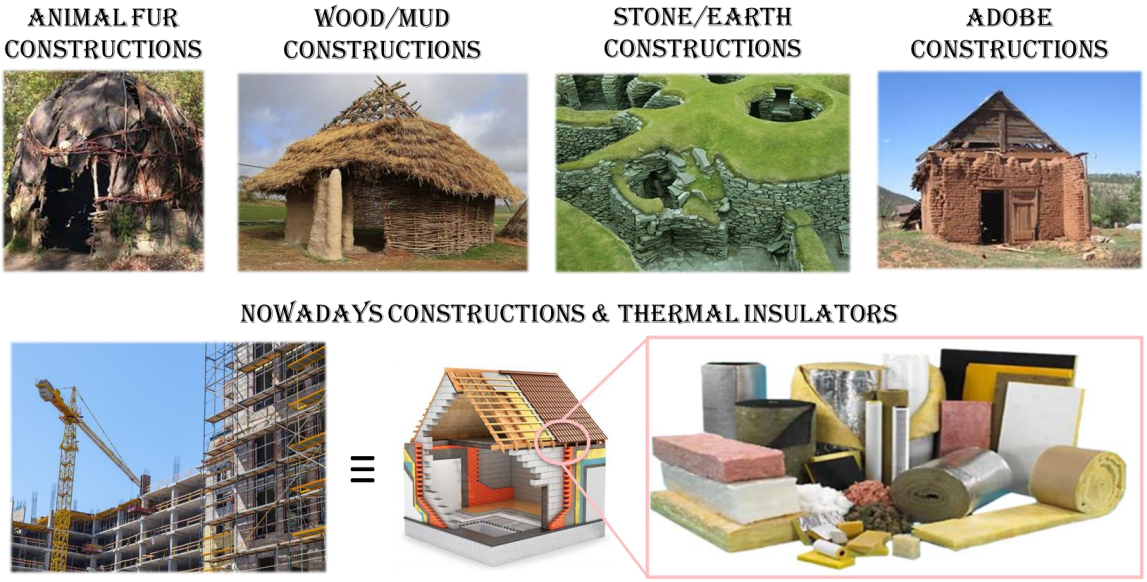

Figure 1.1. Evolution of thermal insulation on housing.

Nevertheless, it was not until the advent of the industrial revolution in the 19th century that deliberate commercial application of thermal insulations became mainstream (**Figure 1.1**). In those years, the techniques of planning and construction changed dramatically, the structural systems were planned not in empirical ways but on calculative methods with the introduction of building materials such as cast iron, glass structures, concrete, and steel. However, the thermal insulation behavior of those materials was much lower than the materials used at that time (adobe or bricks) resulting in greater heat losses and higher heating demands[1]. Thus, humans started developing their own thermal insulators from natural and artificial materials: reed, mineral wool, fiberglass,

expanded perlite, cellular polymers (like polystyrene foam and polyurethane foam), etc (**Figure 1.2**). Particularly, the development of cellular polymers (two-phase materials in which a gaseous phase is dispersed in a continuous polymer matrix) in the 1940s caused a huge revolution in the insulation materials' market[1] due to their exciting properties: lightweight, low-cost, and low thermal conductivity among others[5].

Figure 1.2. Some examples of thermal insulators.

Nowadays, finding new materials with enhanced thermal insulation properties is still a mandatory task. More than 16% of global energy is destined for building climatization, making thermal insulation a key factor to reduce energy consumption and the CO_2 emissions associated with energy production[6,7]. Thus, governments like the European Union had developed legislative frameworks[8,9] to boost energy performance in buildings. There are two possible routes to achieve this objective: increasing the thickness of the insulation layer using conventional insulators (such as mineral wool, polystyrene foam, polyurethane foam), characterized by thermal conductivities between 25-60 mW/(m·K), or developing new super thermal insulators (like aerogels or vacuum insulation panels (VIPs)), characterized by much lower thermal conductivities (4-16 mW/(m·K))[7,10–12]. This last approach would also extend the useful area in buildings since these materials provide better thermal resistance with reduced thickness.

Particularly, in recent years, it has been claimed several times that nanocellular polymer (a new class of cellular polymers in the frontier of materials and polymer science) could be potentially used as an advanced thermal insulator[13–15].

1.1.2. Nanocellular polymers

Since the appearance of the first cellular polymers in the 1940s their development has been focused on improving their performance. As shown in **Figure 1.3**, these materials were characterized by

cell sizes of hundreds of microns (conventional cellular polymers). Later on, microcellular polymers (cell sizes below 10 microns), were produced for the first time in the earlies 1980s at the Massachusetts Institute of Technology (MIT) (**Figure 1.3**)[16]. Microcellular polymers showed enhanced mechanical properties in comparison with conventional cellular polymers. These results suggested that further improvement could be reached by reducing even more cell size, giving rise to the so-called nanocellular polymers (characterized by cell sizes below 1 micron) in the 2000s (**Figure 1.3**). In fact, nanocellular polymers have shown promising properties such as thermal conductivity reduction through the gas phase, transparency, high surface area, and improved mechanical properties, among others[17–23]. Note that nanocellular polymers, like many other thermoplastic cellular materials, are also characterized by their lightweight, low cost, and recyclability. Therefore, nanocellular polymers present a unique combination of properties.

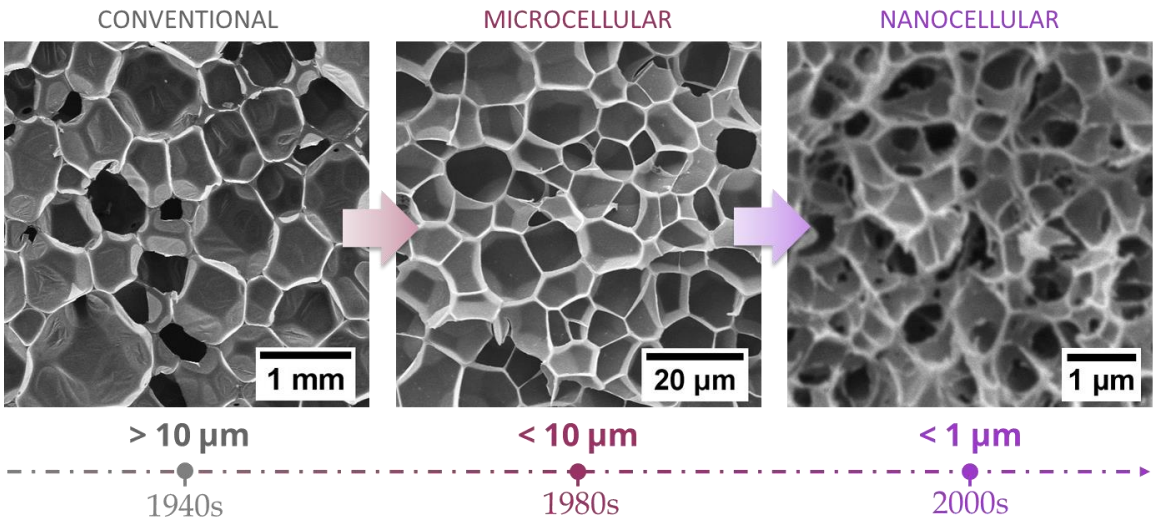

Figure 1.3. Evolution in the cell size of cellular materials over time.

Those outstanding properties arise as a result of their reduced cell size since the solid and gas phases are confined in the nanocellular structure. On the one hand, the solid phase is confined in thin cell walls with thicknesses between 20-60 nm, which are of the same order of magnitude as the polymer chain length[24,25]. On the other hand, the gas is confined in nanometric pores. When the cell size is reduced to the nanoscale the gas molecules collide more often with the cell walls than among them, reducing the energy transfer. Thus, the contribution of the conduction through the gas to the total thermal conductivity of the material is drastically decreased due to the so-called Knudsen effect[26].

Precisely, the appearance of the Knudsen effect in nanocellular polymers[17,18] is the reason why these materials could be potentially used as advanced thermal insulators when combining low-densities and nanometric cell sizes[13–15]. However, up to date, there is a lack of experimental data regarding the total thermal conductivity of nanocellular polymers that prove the super-insulator behavior. This is because the production of nanocellular polymers is still a challenge[27], especially

in the low-density range. Moreover, since fabrication processes are mainly limited to the lab scale, the production of samples with dimensions large enough for characterization is also a complex task[28]. Thus, only a few works in the literature collect the thermal conductivity of nanocellular polymers[17,29–33]. However, most of those thermal conductivity results are not reliable, since they have been obtained by using a transient technique to measure the thermal conductivity that allows measuring samples with small dimensions but its accuracy for thermal insulating materials is not clear [34–36].

For these reasons, many authors have tried to theoretically predict the thermal properties of these materials[15,37–40] and, despite the early predictions[15], recent works[38–40] have shown that the minimum thermal conductivity that can be reached with these materials is higher than expected for an advanced thermal insulator. This is because, despite the reduction in the gas conduction due to the Knudsen effect, the other two heat transfer mechanisms (radiation and conduction through the solid phase) increase the total thermal conductivity.

The lack of knowledge regarding the thermal conductivity of nanocellular polymers has encouraged to development of this thesis, facing the challenges shown in **Figure 1.4** for their application as thermal insulators, and pursuing the objectives defined in Section 1.3.

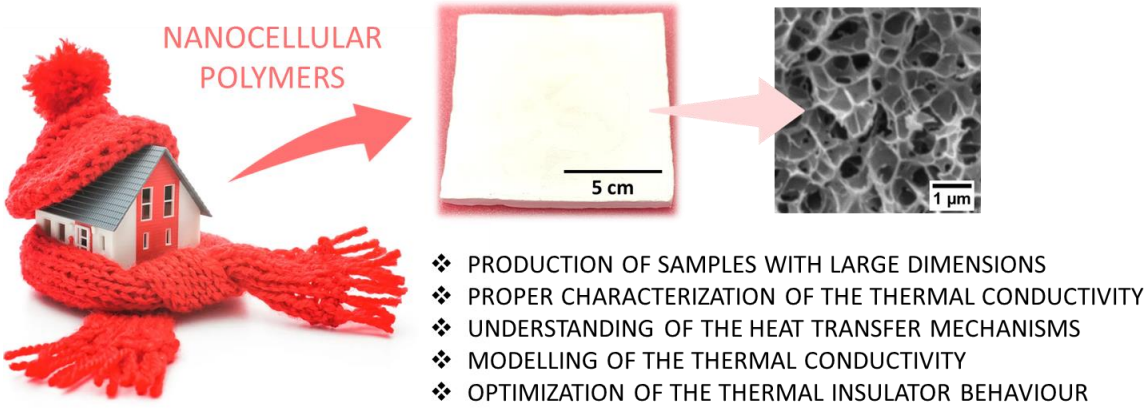

Figure 1.4. Challenges in the field of nanocellular polymers for their application as thermal insulators.

1.2. Framework of this thesis

This investigation is framed as part of the research activities of the Cellular Materials Laboratory (CellMat)[41] which belongs to the Condensed Matter Physics Department of the University of Valladolid. CellMat was founded in 1999 by Prof. Dr. José Antonio de Saja and Prof. Dr. Miguel Ángel Rodríguez-Pérez. CellMat started as a characterization laboratory for commercial cellular polymers, mainly based on polyolefins. From the beginning, the basis of CellMat was to establish the relationship between production, structure, properties, and applications of cellular materials (cellular materials tetrahedron) (**Figure 1.5**). With the expertise gained in the early years, in 2005,

CellMat acquired facilities to produce their own cellular materials, taking a step forward in their research activities. Another key goal of CellMat was to promote the transfer of knowledge and technology between academia and the industry, as a critical factor for industrial development. Thus, CellMat researchers founded a spin-off company (CellMat Technologies S.L.) in 2012[42]. Nowadays, CellMat gathers more than 280 scientific publications in JCR, 36 Ph.D. thesis, and its research is sustained in five main topics: nanocellular polymers[43–46], multifunctional cellular materials[47–50], cellular nanocomposites[51,52], polyurethane foams[53,54], and bioplastic cellular materials[55,56]. In particular, this thesis was supervised by Prof. Dr. Miguel Ángel Rodríguez-Pérez, head of the CellMat and CellMat Technologies S.L. and Dr. Victoria Bernardo, team leader of CellMat Technologies S.L., being framed within the nanocellular polymers research topic.

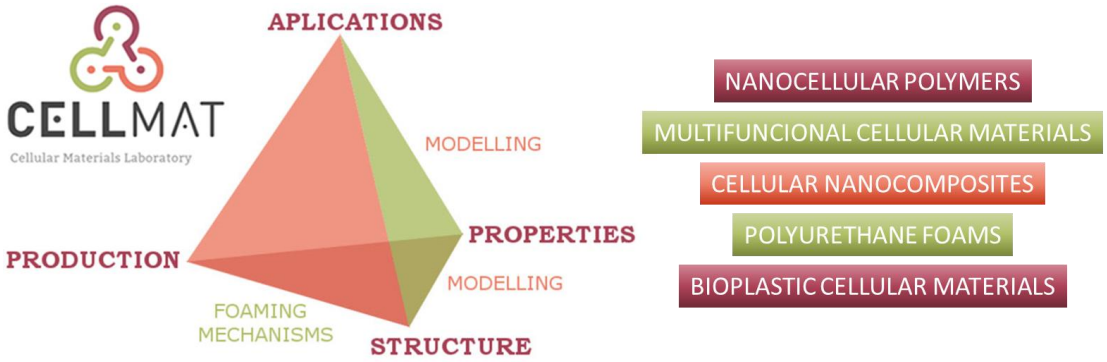

Figure 1.5. Basis of the investigations of CellMat (cellular materials tetrahedron), and current research lines.

The research topic of nanocellular polymers started back in 2014 with the Ph.D. thesis of Dr. Javier Pinto[45]. CellMat was pioneer in the production of nanocellular polymers and due to the great interest in this new class of materials, four more Ph.D. theses have been focused on their study, in particular the thesis of Dr. Belén Notario[46], Dr. Victoria Bernardo[43], Dr. Judith Martín-de-León[44], and Dr. Mikel Múgica[50]. Thus, CellMat has become a reference laboratory in the field of nanocellular polymers. For instance, CellMat proved that the conduction through the gas phase is reduced in this type of material due to their nanoscale cell size (Knudsen effect)[17], that if the cell size is reduced below 50 nm is possible to produce transparent nanocellular polymers[20,57], that nanocellular polymers present enhanced mechanical properties[18,58], and that due to their reduced cell size the extinction coefficient decreases (higher radiation contribution to the total thermal conductivity)[39].

The research work presented in this thesis is based on this previous research and aims to study deeply the thermal conductivity behavior of nanocellular polymers and, from that, enhance their thermal insulation behavior. Also, this research aims to analyze the potential of nanocellular polymers to be used as VIPs' core.

1.3. Objectives

The lack of knowledge regarding the thermal conductivity of nanocellular polymers has motivated this work. This investigation has one primary objective and three secondary goals (**Figure 1.6**). The main objective is the **study of the thermal conductivity of nanocellular polymers**. To achieve this goal, the following secondary objectives are fixed:

- Measuring the thermal conductivity of nanocellular polymers with steady-state methods. To achieve this goal, two routes will be followed. First, developing a steady-state method that allows characterizing the thermal conductivity of new thermal insulators (like nanocellular polymers) developed at lab-scale (samples with small dimensions). Second, fabricating large specimens to allow the use of conventional steady-state equipments.
- Understanding the heat transfer mechanisms taking place in nanocellular polymers, evaluating their potential and limitations. This will be conducted by combining experimental measurements (with reliable data obtained through steady-state techniques) and analytical modeling.
- Enhancing the thermal insulation behavior of nanocellular polymers by means of a new route based on micronization. A new material will be developed in this thesis: a low-density powder formed by micrometric particles with nanometric cells inside them. For this new material, the heat transfer mechanisms will be studied in detail too.

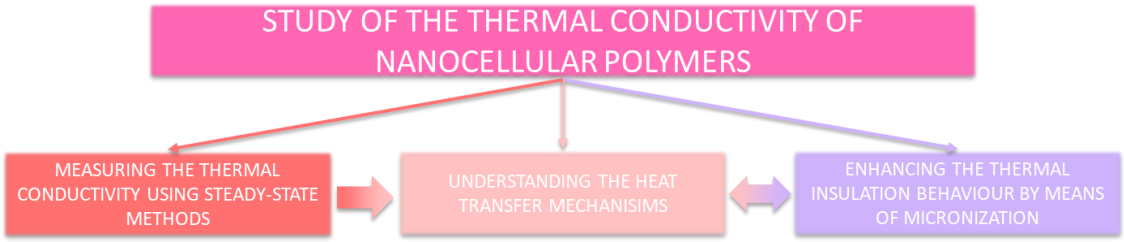

Figure 1.6. General objectives of this thesis.

To achieve these goals, the thermal conductivity of microcellular and nanocellular poly (methyl methacrylate) (PMMA) has been investigated. PMMA has been chosen as the polymer matrix due to its high ability to produce low-density nanocellular materials[20,25,59–62]. The methodology of the thesis is presented in **Figure 1.7**. First, the method for measuring the thermal conductivity in steady-state conditions will be established. Second, the thermal conductivity will be studied for bulk nanocellular polymers based on PMMA, both experimentally and theoretically, to understand the heat transfer mechanisms. Then, the material will be micronized to generate a new material: a micronized nanocelullar powder, which will be studied in detail. The analysis of this novel material will also include a detailed characterization of the thermal conductivity of the powder and the possibility of compacting the material to generate VIP core prototypes, as well as the optimization of the thermal conductivity by adding infrared blockers.

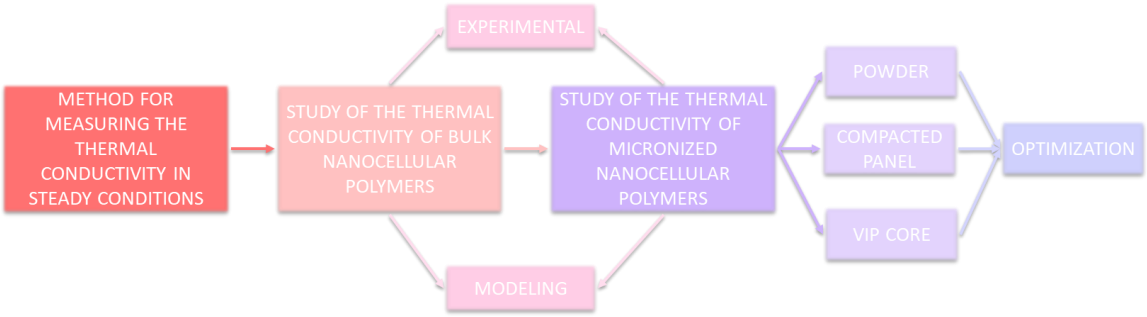

Figure 1.7. Methodology followed in this thesis.

Taking into account the general objectives and the methodology of this work, the following activities have been carried out:

1) Preparing low-density nanocellular polymers with large dimensions suitable to be measured in conventional steady-state machines: Commercial steady-state equipment requires samples with large dimensions for the measurements, but the production of such specimens of nanocellular polymers, especially in the low-density range, is still challenging. This is because the production of these materials is restricted to the lab-scale (small dimensions). In this thesis, we face this challenge by producing several samples (characterized by the same density and cellular structure) to form a stack with dimensions large enough to be measured in commercial steady-state equipment.
2) Characterizing the thermal conductivity of insulating samples with small dimensions: Insulating samples produced at lab-scale (small dimensions) are usually characterized using transient techniques, but these methods do not provide reliable data. Thus, this thesis also aims to develop a steady-state method to properly characterize the thermal conductivity of insulating samples with small dimensions. The method developed and its applicability to nanocellular polymers are shown in **Chapter 3**.
3) Analyzing the thermal conductivity of bulk microcellular and nanocellular PMMA: Once the thermal conductivity of bulk microcellular and nanocellular PMMA is measured, we aim to study the heat transfer mechanisms to develop a model able to predict the thermal conductivity from the samples' characteristics (density and cellular structure). The results of this study are shown in **Chapter 4**. Regarding the modeling key parameters, two main objectives are set:
    a. Determining experimentally the solid structure factor in low-density nanocellular polymers. There is no reliable data for this parameter in the literature. The solid structure factor is key to understanding the conduction through the solid phase and evaluating the differences between nanocellular polymers (continuous structure) and other super-insulators (discontinuous structure).

b. Determining experimentally the extinction coefficient in low-density nanocellular polymers, for the first time, to quantify the radiation contribution and learn about the possibilities to reduce this term.

4) Producing and characterizing micronized microcellular and nanocellular PMMA: We will explore the route of micronization to enhance the thermal insulator behavior of microcellular and nanocellular polymers. By means of micronization, we aim to transform the continuous cellular structure into a discontinuous structure, thus, reducing the contribution of the conduction of the solid phase. Furthermore, micronization may present some advantages like density and radiation reduction. This is because the powder particles may be surrounded by air and because the powder particles (or the voids between the powder particles) may act as scattering points respectively. Also, this route may allow an easier scale-up than the production of bulk samples with large dimensions. This material is a novel system and one of the key novelties of the present thesis. Then, we aim to study in detail the micronized systems (density, open cell content, cellular structure, powder packaging, particle size, and thermal conductivity) and to develop a model able to predict the thermal conductivity of the micronized material to fully understand the heat transfer mechanisms in this novel material.
5) Fabricating and analyzing self-standing compacted panels based on micronized microcellular and nanocellular PMMA: In order to obtain self-standing samples from the micronized microcellular and nanocellular PMMA we aim to produce compacted panels to gain knowledge about this novel approach. To do this, compacted panels will be produced, and their thermal conductivity will be characterized to develop a model able to predict the thermal conductivity of those systems and evaluate the contribution of each heat transfer mechanism.
6) Evaluating the performance of the compacted panels as VIP core materials: Due to their open and porous structure, the thermal conductivity measurements of the compacted panels will be performed at ambient pressure and at vacuum, thus evaluating the potential of these materials to be used as a core for vacuum insulation panels. As final step, we aim to perform a comparison of the thermal conductivity of bulk samples, micronized samples, and compacted panels.
7) Optimizing the performance of the panels by adding IR blockers: In addition to the other benefits, the micronization may allow an easier addition and dispersion of infrared blockers in the form of powder to reduce the radiation contribution. This is because the dispersion of the infrared blockers in the polymer matrix before foaming is a challenge because high shears are required during the extrusion process to avoid their agglomeration. Furthermore, the process becomes more challenging as the percentage of infrared blockers on the

polymer matrix increases. Then, we aim to study the effect of the addition of infrared blockers in the powder and in compacted panels obtained from this powder.

1.4. Structure of the thesis

This thesis is written as a ***compendium of publications***. Seven scientific papers are included in this work. From these papers, four of them have already been published, while the other three are still pending acceptance. These papers are included in **Chapter 3** and **Chapter 4**. Also, this thesis fulfills the requirements to obtain the degree of **Doctor in Philosophy (Ph. D)** with an **International Mention**. The structure of the chapters with their corresponding scientific publications is schematically presented in **Figure 1.8**.

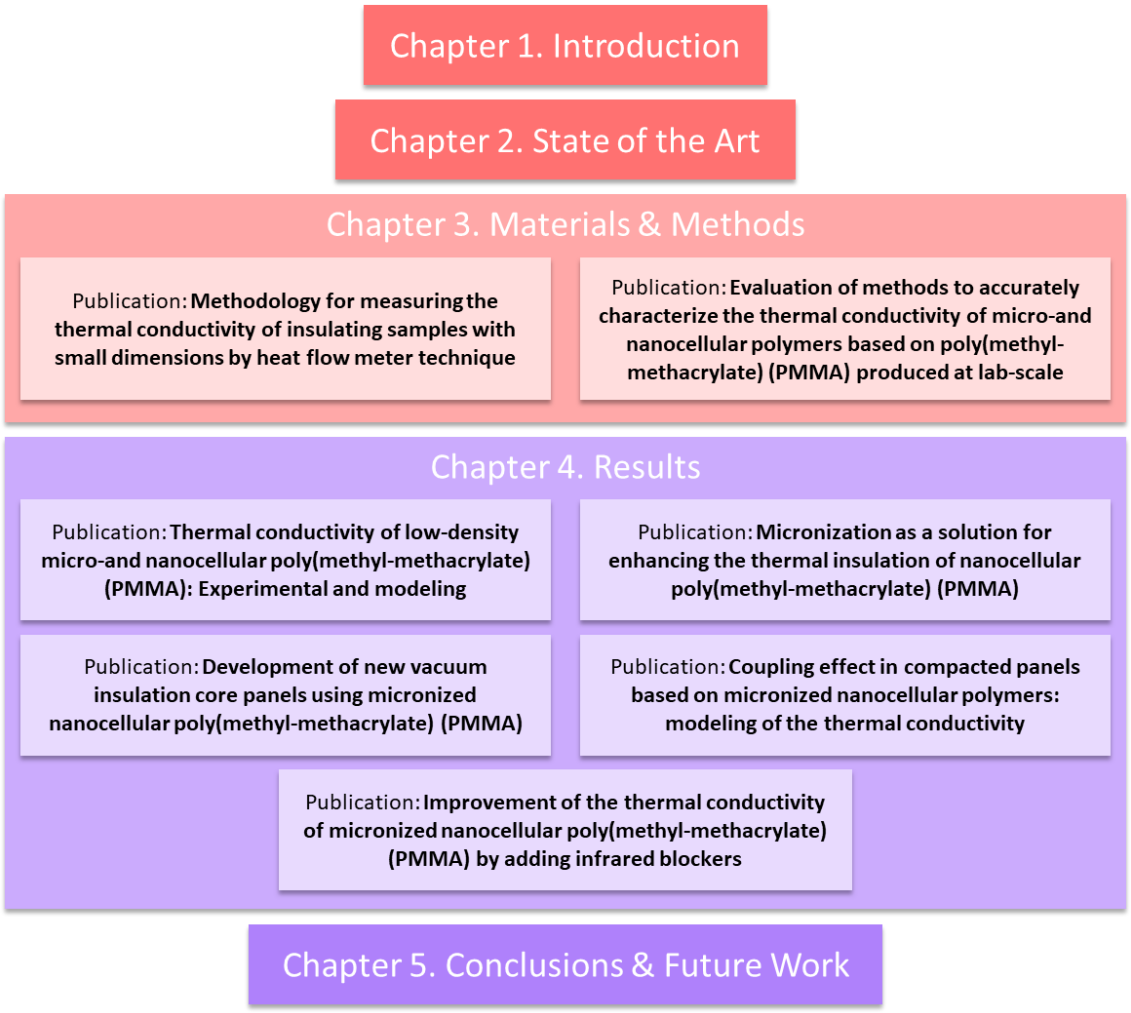

Figure 1.8. Structure of the thesis: Overview of the chapters and scientific publications.

The work presented in this thesis is divided into five chapters containing the following information.

Chapter 1: Introduction. This chapter presents a brief introduction to the research topic (nanocellular polymers) and the framework of this thesis within CellMat. This is followed by the objectives and an overview of the structure of the thesis. Also, a summary of the scientific articles, conferences, and other relevant works derived from this research are listed.

Chapter 2: State of the Art. First, this chapter provides an overview of nanocellular polymers regarding their production, the key parameters to describe the cellular structure, and their properties. Then, a detailed analysis of thermal conductivity parameters and characterization techniques of nanocellular polymers is presented. Thermal conductivity data from the literature as a function of the cellular structure parameters and the technique used to obtain those data is also included to compare the thermal conductivity behavior of nanocellular polymer with the main thermal insulators used nowadays. Furthermore, this chapter includes a revision of the state of the art of vacuum insulation panels (VIPs) due to the potential use of nanocellular polymers as VIPs core.

Chapter 3: Materials & Methods. This chapter describes the raw materials, production routes, and characterization techniques used in this research. Two publications are included regarding the development and validation of a technique to properly characterize the thermal conductivity of thermal insulators of small dimensions, particularly for nanocellular polymers.

Chapter 4: Results. Herein, the main results of this thesis are presented. Five publications are included. The papers follow a logical sequence, telling a story regarding the experimental characterization of the thermal conductivity of nanocellular systems, and its modeling and optimization to enhance their thermal insulating behavior by means of micronization. First, the results of bulk low-density of microcellular and nanocellular polymers are presented. Then, these systems were micronized, obtaining a powder characterized by micrometric particles with nanocells inside them. This novel material is also studied in detail. After that, the powder was compacted obtaining pieces that can be handled. The compacted panels are studied at ambient pressure and under vacuum to evaluate their potential to be used as cores for VIP. Finally, the formulations were optimized by adding infrared blockers, to reduce the radiation contribution.

Chapter 5: Conclusions and future work. This chapter presents the main conclusions of this research. Moreover, the thermal conductivity results obtained in this thesis are compared with the literature data. Finally, future research topics regarding further optimization of the materials produced in this work are suggested.

1.5. Publications, patents, conferences, and courses

1.5.1. Publications

Table 1.1 gathers all the publications related to this thesis. These publications are included in the corresponding chapter. Meanwhile, **Table 1.2** collects other scientific papers related to the field of microcellular and nanocellular polymers published during the development of this thesis in which the author of this thesis has collaborated.

Table 1.1. Publications in international journals included in this thesis.

Publication reference	Chapter	Q/IF
I. Sánchez-Calderón, B. Merillas, V. Bernardo, M.Á. Rodríguez-Pérez **Methodology for measuring the thermal conductivity of insulating samples with small dimensions by heat flow meter technique** Journal of Thermal Analysis and Calorimetry 147 (2022) 12523–12533. https://doi.org/10.1007/s10973-022-11457-7	**3**	**Q1/4.755**
I. Sánchez-Calderón, Á. Sillero, F. Lizalde-Arroyo, V. Bernardo, J. Martín-de-León, M.Á. Rodríguez-Pérez **Evaluation of methods to accurately characterize the thermal conductivity of micro-and nanocellular polymers based on poly(methyl-methacrylate) (PMMA) produced at lab-scale** Polymer Testing 117 (2023) 107842. https://doi.org/10.1016/j.polymertesting.2022.107842	**3**	**Q1/4.931**
I. Sánchez-Calderón, V. Bernardo, J. Martín-de-León, M.Á. Rodríguez-Pérez **Thermal conductivity of low-density micro-and nanocellular poly(methyl-methacrylate) (PMMA): Experimental and modeling** Materials & Design 221 (2022) 110938. https://doi.org/10.1016/j.matdes.2022.110938	**4**	**Q1/9.417**
I. Sánchez-Calderón, V. Bernardo, D. Cuadra-Rodríguez, J. Martín-de-León, M.Á. Rodríguez-Pérez **Micronization as a solution for enhancing the thermal insulation of nanocellular poly(methyl-methacrylate) (PMMA)** Polymer (Guildf) 261 (2022) 125397. https://doi.org/10.1016/j.polymer.2022.125397	**4**	**Q1/4.432**
I. Sánchez-Calderón, V. Bernardo, F. Lizalde-Arroyo, J. Martín-de-León, M.Á. Rodríguez-Pérez **Development of new vacuum insulation core panels using micronized nanocellular poly(methyl-methacrylate) (PMMA)**	**4**	**-**
I. Sánchez-Calderón, V. Bernardo, F. Lizalde-Arroyo, J. Martín-de-León, M.Á. Rodríguez-Pérez **Coupling effect in compacted panels based on micronized nanocellular polymers: modeling of the thermal conductivity**	**4**	**-**
I. Sánchez-Calderón, V. Bernardo, F. Lizalde-Arroyo, J. Martín-de-León, M.Á. Rodríguez-Pérez **Improvement of the thermal conductivity of micronized nanocellular poly(methyl-methacrylate) (PMMA) by adding infrared blockers**	**4**	**-**

Table 1.2. Other publications.

Publication reference	Q/IF
I. Sánchez-Calderón, V. Bernardo, J. Martín-de-León, M.Á. Rodríguez-Pérez **Novel approach based on autoclave bead foaming to produce expanded polycarbonate (EPC) bead foams with microcellular structure and controlled crystallinity** Materials & Design. 212 (2021) 110200. https://doi.org/10.1016/j.matdes.2021.110200	**Q1/9.417**

I. Sánchez-Calderón, V. Bernardo, M. Santiago-Calvo, H. Naji, A. Saiani, M.Á. Rodríguez-Pérez **Effect of the molecular structure of TPU on the cellular structure of nanocellular polymers based on PMMA/TPU blends** Polymers (Basel). 13 (2021). https://doi.org/10.3390/polym13183055	**Q1/4.967**
V. Bernardo, J. Martin-de Leon, I. Sanchez-Calderon, E. Laguna-Gutierrez, M.A. Rodriguez-Perez **Nanocellular polymers with a gradient cellular structure based on poly(methyl-methacrylate)/thermoplastic polyurethane blends produced by gas dissolution foaming** Macromolecular Materials and Engineering. 1900428 (2019) 1900428. https://doi.org/10.1002/mame.201900428	**Q1/3.853**

1.5.2. Patents

Table 1.3 summarizes the patents published during the development of the thesis.

Table 1.3. Patents.

Patents
WO 2022/117642 A1: NANOCELLULAR EXPANDED POLYMER BEADS, METHOD OF MANUFACTURE AND USES. M. Múgica Izaguirre, V. Bernardo García, J. Martín de León, I. Sánchez Calderón, M.Á. Rodríguez Pérez.

1.5.3. Conferences

The results of this thesis have been presented at several international conferences, as presented in **Table 1.4**.

Table 1.4. Contributions to international conferences.

Conference contributions
12/10/2022 – 14/10/2022: CellMAT 2022. Organized by Deutsche Gesellschaft für Materialkunde e.V. / German Materials Society. Hybrid-Conference (Web participation). **A detailed study of the heat transfer mechanisms in micro-and nanocellular PMMA: modelling of the thermal conductivity** Ismael Sánchez Calderón; Victoria Bernardo García; Miguel Ángel Rodríguez Pérez *Oral communication*
11/04/2022 – 12/04/2022: IVIS 2021. Organized by Brunel University. London, United Kingdom. **Analysis of the suitability of using powdered micro and nanocellular polymers as core materials for VIP** Ismael Sánchez Calderón; Victoria Bernardo García; Miguel Ángel Rodríguez Pérez *Oral communication & scientific paper*
13/09/2021 – 16/09/2021: FOAMS 2021. Organized by SPE (Society of Plastics Engineers). Web-Conference. **Study of the Feasibility of Producing Expanded Polycarbonate Bead Foams (EPC) By Autoclave Bead Foaming** Ismael Sánchez Calderón; Victoria Bernardo García; Miguel Ángel Rodríguez Pérez *Oral communication & scientific paper*

07/10/2020 – 09/10/2020: CellMAT 2020. Organized by Deutsche Gesellschaft für Materialkunde e.V. / German Materials Society. Web-Conference.

Study of the thermal conductivity of powdered microcellular polymers based on PMMA

Ismael Sánchez Calderón; Victoria Bernardo García; Miguel Ángel Rodríguez Pérez

Poster

02/10/2019 – 03/10/2019: FOAMS 2019. Organized by SPE (Society of Plastics Engineers). Valladolid, Spain.

Low-density PMMA/TPU nanocellular polymers with tuneable cellular structure by modifying the TPU chemistry and concentration

Ismael Sánchez Calderón; Victoria Bernardo García; Mercedes Santiago Calvo; Judith Martín de León; Miguel Ángel Rodríguez Pérez

Poster

24/10/2018 – 26/10/2018: CellMAT 2018. Organized by Deutsche Gesellschaft für Materialkunde e.V. / German Materials Society. Bad Staffelstein, Alemania.

Fabrication of low-density nanocellular polymers using PMMA/TPU blends

Victoria Bernardo Garcia; Judith Martín de León; Ismael Sánchez Calderón; Ester Laguna Gutiérrez; Miguel Ángel Rodríguez Pérez

Co-author in oral communication

1.5.4. Research stays, courses, and projects

Table 1.5, **Table 1.6, and Table 1.7** summarize the research stays in other institutions, the attended courses, and other research activities relating to funded projects during the development of the thesis respectively.

Table 1.5. Research stays in other institutions.

Location, time, and topic
University of Coimbra (Portugal) → October 2022 – January 2023 Topic: **Preparation of super insulating materials by blending nanocellular PMMA powder and silica aerogels**

Table 1.6. Attended courses during this thesis.

Title, organizer, location, and time
Carnet radiológico University of Valladolid – Valladolid, Spain, February 2021

Table 1.7. Participation in research-funded projects.

PUBLIC FUNDING
POLIMEROS NANOCELULARES TRANSPARENTES Y AISLANTES TERMICOS: FABRICACION, CARACTERIZACION Y RELACION PROCESOESTRUCTURA- PROPIEDADES. Reference: RTI2018-098749-B-I00, Ministerio de Ciencia e Innovación, Programa Estatal de I+D+i Orientada a los Retos de la Sociedad. 01/01/2019-30/09/2022. Budget: 157300 €
SUSTAINABLE PRODUCTION OF SUPER THERMAL INSULATING NANOCELLULAR POLYMERS WITH REDUCED THERMAL CONDUCTIVITY BY INCREASING PHONONS SCATTERING. Reference: TED2021-130965B-I00, Ministerio de Ciencia e Innovación, Proyectos Estratégicos Orientados a la Transición Ecológica y a la Transición Digital 2021. 01/01/2022-30/12/2022. Budget: 146800 €

DESARROLLO DE SUPER AISLANTES TERMICOS BASADOS EN POLIMEROS NANOCELULARES Y BLOQUEDAORES DE LA RADACION INFRAROJA. Reference: PID2021-127108OB-I00, Ministerio de Ciencia e Innovación, Proyectos de Generación de Conocimiento 2021. 01/09/2022-31/08/2025. Budget: 205700 €

HACIA LA PRODUCCION INDUSTRIAL DE POLIMEROS NANOCELULARES TRANSPARENTES. Reference: PDC2022-133391-I00, Ministerio de Ciencia e Innovación, Proyectos I+D+i Pruebas de Concepto 2022. 01/12/2022-31/12/2023. Budget: 149500 €

PRIVATE FUNDING

DESARROLLO DE ESTRATEGÍAS PARA FABRICAR POLÍMEROS NANOCELULARES EN PROCESOS INDUSTRIALES: EXTRUSIÓN Y PERLITAS EXPANDIDAS. Tipo de contrato: Artículo 83 Investigación, Funded by CellMat Technologies S.L. 01/12/2014-30/12/2020. Budget: 120000 €

EVALUACIÓN DE LA VIABILIDAD PARA PRODUCIR POLÍMEROS NANOCELULARES USANDO MUY ELEVADAS PRESIONES. Tipo de contrato: Artículo 83 Investigación, Funded by HIPERBARIC, S.A, 19/02/2019-30/06/2020. Budget: 50200 €

INVESTIGACIÓN DE TECNOLOGÍA DE ESPUMACIÓN DE POLÍMEROS NANOCELULARES (PROYECTO NCELL). Tipo de contrato: Artículo 83 Investigación, Funded by HIPERBARIC, S.A, 18/03/2021-31/12/2022. Budget: 65000 €

MICRONIZADO, COMPACTACIÓN Y CARACTERIZACIÓN DE PERLITAS NANOCELULARES EXPANDIDAS. Tipo de contrato: Artículo 83 Investigación, Funded by CellMat Technologies S.L. 25/04/2021-31/07/2022. Budget: 59000 €

FABRICACIÓN DE MATERIALES PRECURSORES Y CARACTERIZACIÓN DE LAS PROPIEDADES FÍSICAS DE POLÍMEROS NANOCELULARES. Tipo de contrato: Artículo 83 Investigación, Funded by CellMat Technologies S.L. 25/04/2021-31/01/2023. Budget: 58250 €

References

[1] D. Bozsaky, The historical development of thermal insulation materials, Period. Polytech. Archit. 41 (2010) 49. https://doi.org/10.3311/pp.ar.2010-2.02.

[2] Albert Farwell Bemis, The Evolving House, Cambridge, MA: Technology Press, 1933.

[3] R.T. Bynum, Insulation Handbook, McGraw-Hill Professional, 2000.

[4] P.D. Close, Thermal Insulation of Buildings, New York: Reinhold, 1947.

[5] N.C.. Hilyard, A. Cunningham, Low density cellular plastics Physical basis of behaviour, 1994. https://doi.org/10.1007/978-94-011-1256-7.

[6] J. Wernery, F. Mancebo, W.J. Malfait, M. O'Connor, B.P. Jelle, The economics of thermal superinsulation in buildings, Energy Build. 253 (2021) 111506. https://doi.org/10.1016/j.enbuild.2021.111506.

[7] M. Casini, Smart Buildings, 2016th ed., Elsevier, 2016. https://doi.org/10.1016/C2015-0-00182-4.

[8] Directive 2010/31/EU of the European Parliament and of the Council of 19 May 2010 on the energy performance of buildings, (n.d.).

[9] Directive 2012/27/EU of the European Parliament and of the Council of 25 October 2012 on energy efficiency, amending Directives 2009/125/EC and 2010/30/EU and repealing Directives 2004/8/EC and 2006/32/EC, (n.d.).

[10] W. Villasmil, L.J. Fischer, J. Worlitschek, A review and evaluation of thermal insulation materials and methods for thermal energy storage systems, Renew. Sustain. Energy Rev. 103 (2019) 71–84. https://doi.org/10.1016/j.rser.2018.12.040.

[11] S. Schiavoni, F. D'Alessandro, F. Bianchi, F. Asdrubali, Insulation materials for the building sector: A review and comparative analysis, Renew. Sustain. Energy Rev. 62 (2016) 988–1011. https://doi.org/10.1016/j.rser.2016.05.045.

[12] M. Casini, Advanced construction materials, in: Constr. 4.0, Elsevier, 2022: pp. 337–404. https://doi.org/10.1016/B978-0-12-821797-9.00005-2.

[13] S. Costeux, CO2-Blown nanocellular foams, J. Appl. Polym. Sci. 131 (2014). https://doi.org/10.1002/app.41293.

[14] S. Liu, J. Duvigneau, G.J. Vancso, Nanocellular polymer foams as promising high performance thermal

insulation materials, Eur. Polym. J. 65 (2015) 33–45. https://doi.org/10.1016/j.eurpolymj.2015.01.039.

[15] C. Forest, P. Chaumont, P. Cassagnau, B. Swoboda, P. Sonntag, Polymer nano-foams for insulating applications prepared from CO2 foaming, Prog. Polym. Sci. 41 (2015) 122–145. https://doi.org/10.1016/j.progpolymsci.2014.07.001.

[16] V. Kumar, N.P. Suh, A process for making microcellular thermoplastic parts, Polym. Eng. Sci. 30 (1990) 1323–1329. https://doi.org/10.1002/pen.760302010.

[17] B. Notario, J. Pinto, E. Solorzano, J.A. de Saja, M. Dumon, M.A. Rodríguez-Pérez, Experimental validation of the Knudsen effect in nanocellular polymeric foams, Polymer (Guildf). 56 (2015) 57–67. https://doi.org/10.1016/j.polymer.2014.10.006.

[18] B. Notario, J. Pinto, M.A. Rodriguez-Perez, Nanoporous polymeric materials: A new class of materials with enhanced properties, Prog. Mater. Sci. 78–79 (2016) 93–139. https://doi.org/10.1016/j.pmatsci.2016.02.002.

[19] B. Xiang, Y. Jia, Y. Lei, F. Zhang, J. He, T. Liu, S. Luo, Mechanical properties of microcellular and nanocellular silicone rubber foams obtained by supercritical carbon dioxide, Polym. J. 51 (2019) 559–568. https://doi.org/10.1038/s41428-019-0175-6.

[20] J. Martín-de León, V. Bernardo, M.Á. Rodríguez-Pérez, Key Production Parameters to Obtain Transparent Nanocellular PMMA, Macromol. Mater. Eng. 302 (2017) 1700343. https://doi.org/10.1002/mame.201700343.

[21] B. Notario, A. Ballesteros, J. Pinto, M.A. Rodríguez-Pérez, Nanoporous PMMA: A novel system with different acoustic properties, Mater. Lett. 168 (2016) 76–79. https://doi.org/10.1016/j.matlet.2016.01.037.

[22] B. Notario, J. Pinto, R. Verdejo, M.A. Rodríguez-Pérez, Dielectric behavior of porous PMMA: From the micrometer to the nanometer scale, Polymer (Guildf). 107 (2016) 302–305. https://doi.org/10.1016/j.polymer.2016.11.030.

[23] G.Q. Lu, X.S. Zhao, Nanoporous Materials - An Overview, in: Nanoporous Mater. Sci. Eng., Imperial College Press, 2004: pp. 1–13. https://doi.org/10.1142/9781860946561_0001.

[24] B. Notario, J. Pinto, M.A. Rodríguez-Pérez, Towards a new generation of polymeric foams: PMMA nanocellular foams with enhanced physical properties, Polymer (Guildf). 63 (2015) 116–126. https://doi.org/10.1016/j.polymer.2015.03.003.

[25] J. Martín-de León, V. Bernardo, M. Rodríguez-Pérez, Low Density Nanocellular Polymers Based on PMMA Produced by Gas Dissolution Foaming: Fabrication and Cellular Structure Characterization, Polymers (Basel). 8 (2016) 265. https://doi.org/10.3390/polym8070265.

[26] Z.-Y. Li, C.-Y. Zhu, X.-P. Zhao, A theoretical and numerical study on the gas-contributed thermal conductivity in aerogel, Int. J. Heat Mass Transf. 108 (2017) 1982–1990. https://doi.org/10.1016/j.ijheatmasstransfer.2017.01.051.

[27] J. Martín-de León, V. Bernardo, M. Rodríguez-Pérez, Nanocellular Polymers: The Challenge of Creating Cells in the Nanoscale, Materials (Basel). 12 (2019) 797. https://doi.org/10.3390/ma12050797.

[28] J. Martín-de León, V. Bernardo, P. Cimavilla-Román, S. Pérez-Tamarit, M.Á. Rodríguez-Pérez, Overcoming the Challenge of Producing Large and Flat Nanocellular Polymers: A Study with PMMA, Adv. Eng. Mater. 21 (2019). https://doi.org/10.1002/adem.201900148.

[29] G. Wang, J. Zhao, L.H. Mark, G. Wang, K. Yu, C. Wang, C.B. Park, G. Zhao, Ultra-tough and super thermal-insulation nanocellular PMMA/TPU, Chem. Eng. J. 325 (2017) 632–646. https://doi.org/10.1016/j.cej.2017.05.116.

[30] V. Bernardo, J. Martin-de Leon, J. Pinto, R. Verdejo, M.A. Rodriguez-Perez, Modeling the heat transfer by conduction of nanocellular polymers with bimodal cellular structures, Polymer (Guildf). 160 (2019) 126–137. https://doi.org/10.1016/j.polymer.2018.11.047.

[31] F. Almeida, H. Beyrichen, N. Dodamani, R. Caps, A. Müller, R. Oberhoffer, Thermal conductivity analysis of a new sub-micron sized polystyrene foam, J. Cell. Plast. 57 (2021) 493–515.

https://doi.org/10.1177/0021955X20943101.

[32] J. Zhao, G. Wang, Z. Xu, A. Zhang, G. Dong, G. Zhao, C.B. Park, Ultra-elastic and super-insulating biomass PEBA nanoporous foams achieved by combining in-situ fibrillation with microcellular foaming, J. CO2 Util. 57 (2022) 101891. https://doi.org/10.1016/j.jcou.2022.101891.

[33] C. Zhou, N. Vaccaro, S.S. Sundarram, W. Li, Fabrication and characterization of polyetherimide nanofoams using supercritical CO2, J. Cell. Plast. 48 (2012) 239–255. https://doi.org/10.1177/0021955X12437984.

[34] O. Almanza, M.A. Rodríguez-Pérez, J.A. De Saja, Applicability of the Transient Plane Source Method To Measure the Thermal Conductivity of Low-Density Polyethylene Foams, J. Polym. Sci. Part B Polym. Phys. 42 (2004) 1226–1234. https://doi.org/10.1002/polb.20005.

[35] Q. Zheng, S. Kaur, C. Dames, R.S. Prasher, Analysis and improvement of the hot disk transient plane source method for low thermal conductivity materials, Int. J. Heat Mass Transf. 151 (2020) 119331. https://doi.org/10.1016/j.ijheatmasstransfer.2020.119331.

[36] R.C. Kerschbaumer, S. Stieger, M. Gschwandl, T. Hutterer, M. Fasching, B. Lechner, L. Meinhart, J. Hildenbrandt, B. Schrittesser, P.F. Fuchs, G.R. Berger, W. Friesenbichler, Comparison of steady-state and transient thermal conductivity testing methods using different industrial rubber compounds, Polym. Test. 80 (2019) 106121. https://doi.org/10.1016/j.polymertesting.2019.106121.

[37] H. Yu, H. Zhang, J. Zhao, J. Liu, X. Xia, X. Wu, Thermal conductivity of micro/nano-porous polymers: Prediction models and applications, Front. Phys. 17 (2021). https://doi.org/10.1007/s11467-021-1107-4.

[38] G. Wang, C. Wang, J. Zhao, G. Wang, C.B. Park, G. Zhao, Modelling of thermal transport through a nanocellular polymer foam: Toward the generation of a new superinsulating material, Nanoscale. 9 (2017) 5996–6009. https://doi.org/10.1039/c7nr00327g.

[39] V. Bernardo, J. Martin-de Leon, J. Pinto, U. Schade, M.A. Rodriguez-Perez, On the interaction of infrared radiation and nanocellular polymers: First experimental determination of the extinction coefficient, Colloids Surfaces A Physicochem. Eng. Asp. 600 (2020). https://doi.org/10.1016/j.colsurfa.2020.124937.

[40] P. Buahom, C. Wang, M. Alshrah, G. Wang, P. Gong, M. Tran, C.B. Park, Wrong expectation of superinsulation behavior from largely-expanded nanocellular foams, Nanoscale. (2020). https://doi.org/10.1039/d0nr01927e.

[41] http://cellmat.es/, (n.d.).

[42] http://www.cellmattechnologies.com/en/, (n.d.).

[43] V. Bernardo, Production and Characterization of Nanocellular Polymers Based on Nanostructured PMMA Blends and PMMA Nanocomposites. (July 2019), n.d.

[44] J. Martin-de Leon, Understanding The Production Process Of Nanocellular Polymers Based On Pmma Driven By A Homogeneous Nucleation. (October 2019), n.d. https://pdfs.semanticscholar.org/a3d2/2c024e3c550652f34f510769ad3d84e6020d.pdf.

[45] J. Pinto, Fabrication and Characterization of Nanocellular Polymeric Materials from Nanostructured Polymers (May 2014), (n.d.).

[46] B. Notario, Fabrication and Characterization of the Physical Properties of Nanocellular Polymers: the Transition from the Micro to the Nanoscale (September 2016), (n.d.).

[47] E. López-González, Analysis of the Composition-Structure-Properties Relationship of Open-Cell Polyolefin-Based Foams With Tailored Levels of Gas-Phase Tortuosity (November 2019), n.d.

[48] C. Saiz-Arroyo, Fabricación de Materiales Celulares Mejorados Basados en Poliolefinas. Relación Procesado-Composición-Estructura-Propiedades (April 2012), (n.d.).

[49] M.Á. Rodríguez-Pérez, Propiedades Térmicas y Mecánicas de Espumas de Poliolefinas (March 1999), (n.d.).

[50] M. Múgica, Development of Cellular Low Density Expanded Beads. Formulation-Process-Structure Relationship (April 2022), (n.d.).

[51] H. Ventura, Development of New Composites Reinforced Lightweight Green Structures of Flax With Nonwoven

Fibres (June 2017), (n.d.).

[52] A. Ballesteros, Understanding the Relationships Between Composition, Process, Cellular Structure and Properties of Cellular Polymers Based on Blends of Polystyrene with Inorganic and Organic Nucleating Agents (April 2022), (n.d.).

[53] M. Santiago-Calvo, Synthesis, Foaming Kinetics and Physical Properties of Cellular Nanocomposites Based on Rigid Polyurethane (November 2019), n.d.

[54] P. Cimavilla-Román, Desing and Validation of Experimental Methods for Probing Foam Formation Dynamics and Structure. (Nobember 2022), (n.d.).

[55] L. Oliveira-Salmazo, Foaming Kinetics and Cellular Structure Control of Materials Based on Natural Rubber and Polyolefins (May 2015), n.d.

[56] A. López-Gil, Development of Environmentally Friendly Cellular Polymers for Packaging and Structural Applications. Study of the Relationship Cellular Structure-Mechanical Properties (January 2016), n.d.

[57] J. Martín-de León, J.L. Pura, V. Bernardo, M.Á. Rodríguez-Pérez, Transparent nanocellular PMMA: Characterization and modeling of the optical properties, Polymer (Guildf). 170 (2019) 16–23. https://doi.org/10.1016/j.polymer.2019.03.010.

[58] J. Martín-de León, F. Van Loock, V. Bernardo, N.A. Fleck, M.Á. Rodríguez-Pérez, The influence of cell size on the mechanical properties of nanocellular PMMA, Polymer (Guildf). 181 (2019) 121805. https://doi.org/10.1016/j.polymer.2019.121805.

[59] H. Guo, V. Kumar, Solid-state poly(methyl methacrylate) (PMMA) nanofoams. Part I: Low-temperature CO2 sorption, diffusion, and the depression in PMMA glass transition, Polymer (Guildf). 57 (2015) 157–163. https://doi.org/10.1016/j.polymer.2014.12.029.

[60] J. Pinto, J.A. Reglero-Ruiz, M. Dumon, M.A. Rodriguez-Perez, Temperature influence and CO2 transport in foaming processes of poly(methyl methacrylate)–block copolymer nanocellular and microcellular foams, J. Supercrit. Fluids. 94 (2014) 198–205. https://doi.org/10.1016/j.supflu.2014.07.021.

[61] V. Bernardo, J. Martin-de Leon, J. Pinto, T. Catelani, A. Athanassiou, M.A. Rodriguez-Perez, Low-density PMMA/MAM nanocellular polymers using low MAM contents: Production and characterization, Polymer (Guildf). 163 (2019) 115–124. https://doi.org/10.1016/j.polymer.2018.12.057.

[62] I. Sánchez-Calderón, V. Bernardo, M. Santiago-Calvo, H. Naji, A. Saiani, M.Á. Rodríguez-Pérez, Effect of the molecular structure of TPU on the cellular structure of nanocellular polymers based on PMMA/TPU blends, Polymers (Basel). 13 (2021). https://doi.org/10.3390/polym13183055.

Chapter 2

State of the Art

"You know nothing, Jon Snow."

Ygritte – GAME OF THRONES

INDEX

2. State of the Art

2.1. Nanocellular polymers

Nanocellular polymers are a new class of materials in the frontier of materials and polymer science characterized by cell sizes below 1 micron. They were developed in an attempt of improving the performance of microcellular polymers. Microcellular polymers, characterized by cell sizes below 10 microns, were produced for the first time in the earlies 1980s at the Massachusetts Institute of Technology (MIT)[1]. The enhanced mechanical properties of microcellular polymers in comparison with conventional cellular polymers allowed them to reach sectors where previously it was unthinkable to find cellular polymers. These results suggested that further improvement could be reached by reducing the cell size, giving rise to nanocellular polymers.

As a consequence of their reduced cell size, nanocellular polymers present a double confinement effect (**Figure 2.1**). On the one hand, the gas is confined in nanometric pores (**Figure 2.1a**). When the cell size reaches values around the mean free path of the gas molecules contained in the pores (70 nm for air molecules at atmospheric pressure and room temperature) the contribution of the conduction through the gas to the total thermal conductivity of the material is drastically decreased due to the Knudsen effect[2]. Knudsen effect is well-known to take place in nanocellular polymers [3,4]. On the other hand, the solid phase is also confined since the cell wall thickness (between 20-60 nm) are of the same order of magnitude as the polymer macromolecule length (**Figure 2.1b**)[5,6]. This effect can lead to significant changes in the behavior of the material, such as an increase of the glass transition temperature or improvements in the mechanical properties[5,7,8].

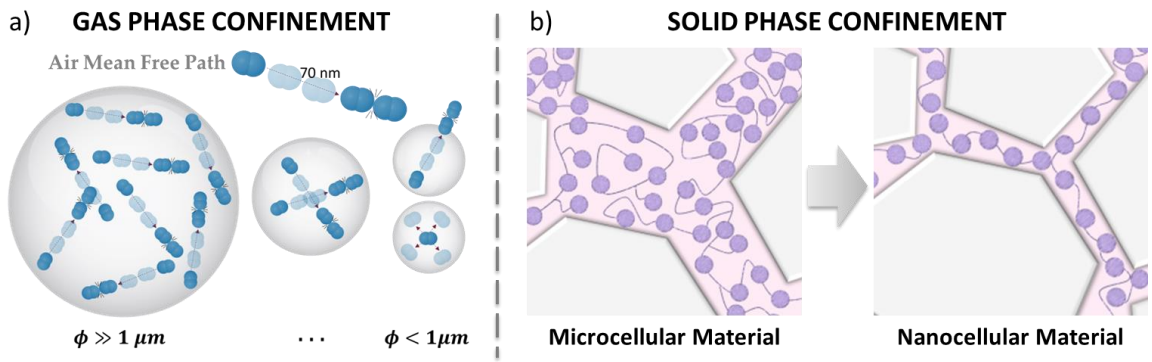

Figure 2.1. Scheme of the a) gas phase confinement and b) solid phase confinement (adapted from[9]).

Furthermore, it was proved that when the cell size is 10 times smaller than the light wavelength (visible light wavelength is centered around 500 nm), the material became partially transparent (i.e. the scattering of visible light is drastically reduced)[10,11]. This effect is due to the change of the scattering mechanism from Mie scattering to Rayleigh scattering when the cell size is reduced[11,12]. In addition, nanocellular materials with an interconnected cellular structure are

characterized by their high surface area, being suitable for their use as membranes for micro and ultrafiltration or in catalysis and sensors[13,14]. The reduction of the cell size can also result in the appearance of new or unexpected properties (electric, dielectric, or acoustic properties) in comparison with microcellular polymers[15,16]. Finally, nanocellular polymers, like many other thermoplastic cellular materials, are also characterized by their lightweight, low cost, and recyclability.

For all these reasons, in recent years, nanocellular polymers have aroused great interest in the scientific community. Depending on their cell size, nanocellular polymers can be applied in various applications (**Figure 2.2**). However, as it will be discussed subsequently, the production of these materials is still a challenge due to the difficulty of combining nanometric cell sizes with very low densities [17], and because the production of samples with large dimensions is also complex since fabrication processes are mainly limited to the lab-scale [18].

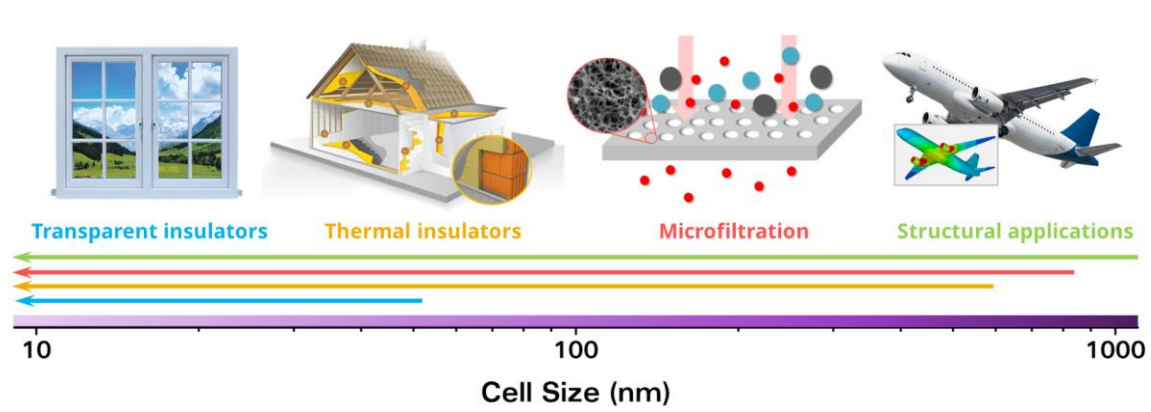

Figure 2.2. Scheme of some potential applications of nanocellular polymers depending on their cell size (adapted from[19]).

2.1.1. Structural parameters

The main parameter to describe a cellular polymer is its relative density (ρ_r). It is defined as the ratio between the density of the cellular material (ρ_f) and the density of the former solid (ρ_s) as shown in Equation (2.1).

$$\rho_r = \frac{\rho_f}{\rho_s} \tag{2.1}$$

The relative density of a nanocellular polymer can determine its range of application. For instance, high-density materials (relative densities above 0.6) are suitable for structural applications, meanwhile, low-density materials (relative densities below 0.2) would behave as thermal insulators.

It is also common to find the definition of porosity (V_f) or expansion ratio (ER) in the bibliography. The first one is defined as $V_f = 1 - \rho_r$ and accounts for the volume fraction of the gas phase, while the relative density is the fraction of solid phase. The second one accounts for the grade of volume

expansion that suffers the cellular polymer concerning the solid and it is defined as the inverse of the relative density ($ER = 1 / \rho_r$).

Another crucial descriptor in a cellular structure is the cell nucleation density (N_0), that is, the number of nucleation points in the solid material. Assuming that every nucleus in the solid material results in a cell, the cell nucleation density can be calculated from the cell density (N_v) (number of cells per unit of volume of the cellular material) according to Equation (2.2):

$$N_0 = \frac{N_v}{\rho_r} \tag{2.2}$$

To obtain a nanocellular polymer, cell nucleation densities higher than 10^{13} nuclei/cm^3 are needed. This is a considerable evolution from the previous materials, considering that in conventional cellular polymers N_0 is around 10^6 nuclei/cm^3, whereas microcellular polymers present cell nucleation densities in the order of 10^{10} nuclei/cm^3.

A further relevant parameter is the cell size (ϕ). As commented previously, the cell size of a nanocellular polymer is, in many cases, connected with its properties and possible applications. Both the cell size and the cell nucleation density can be calculated from image analysis of micrographs[20].

The three parameters described previously (relative density, cell nucleation density, and cell size) are theoretically correlated according to Equation (2.3)[1]. This relation implies that, for obtaining nanocellular polymers with very low relative densities, extremely high cell nucleation densities are required. For instance, to produce a nanocellular material with 100 nm of cell size and a relative density of 0.1, the cell nucleation density should be of the order of 10^{16} nuclei/cm^3.

$$N_0 = \frac{6}{\pi \phi^3}\left(\frac{1}{\rho_r} - 1\right) \tag{2.3}$$

The interconnectivity between the cells is also an important parameter connected with the possible applications of cellular polymers[13]. The percentage of open cells is defined as the volume fraction of interconnected cells, and it is known as open cell content (*OC*). Note that cells can be completely isolated (100% closed cell), totally connected by broken cell walls or the absence of cell walls (100% open cell), or intermediately connected (intermediate open cell content).

A detailed explanation of the methodology used to determine these parameters in this thesis can be found in **Chapter 3**.

2.1.2. Fabrication of nanocellular polymers by gas dissolution foaming

The production of nanocellular polymers requires specific technologies able to create a high density of nuclei that could grow into nanometric cells in the final stage. Nowadays, there are several

approaches to fabricate nanocellular polymers: phase separation techniques, template or imprinting methods, and foaming methods[3,21]. These first two approaches are mainly restricted to the fabrication of thin films, which is a limitation to the potential future applications of nanocellular polymers. Moreover, they usually require the use of organic solvents, which should be removed after the structure is obtained and could be potentially hazardous to the environment. For all these reasons, the last method, that is, the use of a foaming method is nowadays the most promising strategy to produce bulk nanocellular polymers using a scalable and environmentally friendly production route.

In particular, the gas dissolution foaming process using carbon dioxide (CO_2) as the physical blowing agent has been successfully used to obtain polymer-based nanocellular structures using a wide variety of polymer matrices[22–30]. The selection of CO_2 as the blowing agent is related to its excellent diffusion properties, especially in the supercritical state that can be easily reached at mild processing conditions (7.3 MPa and 31 ºC). Furthermore, this gas can be considered a green solvent that can be removed without using any pollutant compound, and that could be recycled in an industrial process[31]. In fact, CO_2 is considered today a sustainable alternative to other blowing agents used in the production of cellular polymers[32].

Gas dissolution foaming is a physical foaming process that consists of four stages: **saturation**, **depressurization**, **foaming**, and **stabilization** of the cellular structure (**Figure 2.3**). The gas dissolution foaming process takes place in an autoclave or pressure vessel where the blowing agent is supplied and kept at the desired conditions of pressure and temperature through a pressure controller and a heating/cooling system, respectively. In the next paragraphs, the physical phenomena occurring in each stage of the process are explained in detail. This process can be carried out in two different ways (the so-called one-step or two-step process), as will also be commented in the following description.

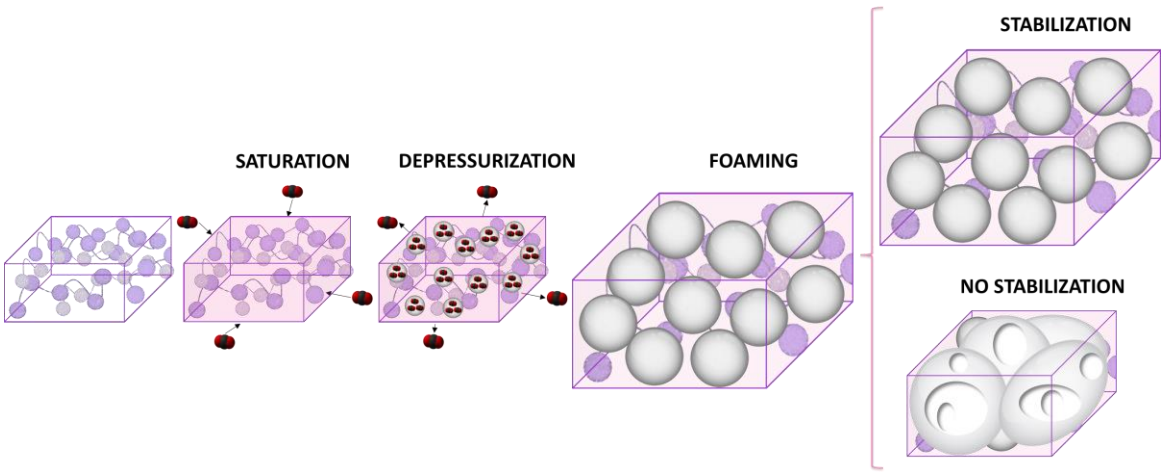

Figure 2.3. Evolution of a polymer sample under the gas dissolution foaming process (adapted from[9]).

The process starts with **saturation** (**Figure 2.3**). In this stage, the solid polymer is placed inside the autoclave under certain conditions of pressure (p_{sat}) and temperature (T_{sat}). Then, due to a concentration gradient, the gas starts to diffuse into the sample occupying the space between the polymer chains (free volume) and forming a homogeneous single-phase system of polymer-gas. For each pressure-temperature combination and every polymer matrix, there is a maximum amount of CO_2 that can be absorbed by the polymer, and that is called solubility. The time required to achieve this solubility, that is, the time to fully saturate the polymer (t_{sat}), is related to the polymer nature, the processing conditions, and size of the sample; and it is controlled by the diffusivity constant or diffusion coefficient[33–35]. During this stage, the CO_2 induces higher mobility to the polymer chains (plasticization) decreasing the glass transition temperature (T_g) when occupying the free volume[36–39]. The effective glass transition ($T_{g,eff}$) obtained after saturation will determine the optimum foaming route (one-step or two-step) that should be followed. This plasticization effect becomes more relevant in amorphous polymers since only the amorphous phase can uptake gas.

Once the sample is fully saturated the pressure is released (**depressurization**) (**Figure 2.3**). The pressure drop rate (v_{des}), that is, the velocity at which the gas leaves the pressure vessel, is a critical factor that might affect the later cellular structure. This is because the sudden decrease in pressure generates a thermodynamic instability that can result in a nucleation process.

When the pressure is released, the gas starts to diffuse from the surface out of the sample. As a result, the surface and some regions near the surface do not have any gas or the amount of gas is smaller than the critical value needed to create a cell. Then, a solid skin without any pores appears on the surface of the sample, as well as a transition region (with a variable amount of gas dissolved) from the solid skin to the homogeneous foamed core [40,41]. This transition region has cells with a different size to those of the homogeneous core. Once again, the diffusion velocity is controlled by a diffusion coefficient[22]. The sorption and desorption diffusion coefficients are in principle different, due to, among other effects, the different state of the polymer before and after the gas sorption.

If the saturation temperature is higher than the effective glass transition temperature of the polymer ($T_{sat} > T_{g,eff}$) after the CO_2 absorption, then the sample is in the rubber state and has enough mobility, so it would expand and foam immediately after the pressure release given that the depressurization does not induce an excessive cooling of the sample (one-step gas dissolution **foaming**)[42]. In these conditions, as the foaming takes place without any time delay, the solid skin should have a minimum thickness, and it is plausible to assume that the transition region between the core and the surface would also be small if the pressure drop rate is high enough.

Meanwhile, if $T_{sat} < T_{g,eff}$, or the depressurization induces cooling of the samples under the $T_{g,eff}$, then the sample is in the glassy state and an additional foaming step is required to expand the sample

(two-step gas dissolution **foaming**). Samples are introduced in a thermal bath (or any other heating system such as a hot plate press [18]) at a determined temperature (T_f) higher than the $T_{g,eff}$ during a certain time (t_f) for the foaming step. Then, the polymer chains acquire enough mobility, the gas diffuses from the nuclei to the cells and the expansion takes place. Both foaming temperature and foaming time must be controlled to ensure that the sample reaches the temperature homogeneously through all the volume and to further avoid undesired degeneration mechanisms or excessive growth of the cells. The time between the release of the pressure and the foaming step, the so-called desorption time (t_{des}), is an important parameter because during this time the gas is diffusing out of the sample, causing a gas concentration gradient inside the material which could lead to a gradient of the effective glass transition temperature, resulting in heterogeneous structures.

Finally, is essential to consider the fourth and last step, the **stabilization** of the cellular structure (**Figure 2.3**). As long as the temperature is higher than the effective glass transition of the polymer, the polymer chains have enough mobility to continue expanding the material. If this situation goes on too long, it can lead to degeneration mechanisms (coalescence, drainage, and/or coarsening) of the original cellular structure when the cell walls are broken, and many cells have joined together reducing the final number of cells and increasing its size (**Figure 2.3**). To prevent such phenomena, the cellular structure should be frozen, stopping further foaming, that means, at the end of the foaming process the material has to be cooled down at a temperature lower than $T_{g,eff}$.

Note that the final size of the foamed samples is determined by the autoclave dimensions and the maximum expansion that samples can achieve. As lab-scale autoclaves are relatively small, the size of the produced nanocellular polymers is also small. For instance, Martin de León et al.[18] produce large and flat nanocellular polymer parts with maximum dimensions of 100×100×6 mm^3 from solid sheets of 55×55×4 mm^3. Then, one specific challenge in the field of nanocellular polymers is the production of large specimens, first at lab-scale with conditions that could be extrapolated to the industrial scale.

Gas dissolution foaming is the method used in this research to fabricate nanocellular polymers. Specific details about the experimental conditions used and the characteristics of the set up can be found in **Chapter 3**.

2.1.2.1. Nucleation mechanisms

After depressurization, the polymer is in a supersaturated state. It means that the polymer no longer supports such an amount of gas because the solubility limit decreases at lower pressures or higher temperatures[43,44]. This thermodynamic instability (such as a pressure drop or a temperature increase) breaks the equilibrium between the gas and the polymer phases leading to, on the one hand, the diffusion of the gas outside of the polymer and, on the other hand, to phase separation.

This phase separation is governed in most of the foaming processes by the nucleation and growth mechanisms[45]. As previously commented, high cell nucleation rates are needed to produce nanocellular polymers, and the challenge becomes even more complicated in the range of low relative densities.

Two approaches can be followed according to the type of nucleation mechanism that takes place: homogeneous or heterogeneous nucleation. According to **homogeneous nucleation** theories[46], the activation energy (Gibbs energy barrier) necessary to generate a nucleus can be decreased by maximizing the amount of CO_2 uptake in a pure polymer. However, this requires the use of highly demanding processing conditions such as high pressures or low saturation temperatures, which complicates the possible production of low-density nanocellular polymers on a large scale[17]. Homogeneous nucleation has been proved to be able to generate nanocellular polymers with different systems such as poly(methyl-methacrylate) (PMMA)[6,10,23,45,47–51], polyetherimide (PEI)[25,52], polysulfone (PSU)[53], polyphenylsulfone (PPSU)[24,54], and polycarbonate (PC)[22], among others. In the homogeneous nucleation approach, the cellular structure can be tuned by modifying the saturation parameters (i.e., the amount of gas uptake) and/or the foaming conditions. The higher the gas uptake, the higher nucleation, resulting in smaller cells. This route was extensively studied for PMMA in the Ph.D. thesis of Judith Martín-de León[9].

Otherwise, the nucleation can be enhanced by taking advantage of the **heterogeneous nucleation** mechanism. In this case, the use of an immiscible second phase allows decreasing the Gibbs energy barrier in the interfaces between the matrix and the second phase, promoting a higher nucleation ratio[46]. To produce nanocellular polymers with this approach, nanoparticles (such as silica nanoparticles[55,56], sepiolites[57], carbon nanotubes[29,58], graphene[59,60], nanoclays[61–64], etc.) or nanostructured polymers blends [13,26,71–78,28,30,65–70] can be used as the second phase. This approach allows the production of nanocellular polymers using mild processing conditions. The cellular structure can be tuned by modifying the dispersion of the second phase. This route is extensively studied for PMMA nanocomposites in the Ph.D. thesis of Victoria Bernardo[19].

PMMA is one of the most interesting polymers to produce nanocellular polymers because of its high affinity to CO_2. For this reason, it has been selected to fabricate the nanocellular polymers to be studied in this thesis. Regarding the works that set the limits on the state of the art of the production of low-density nanocellular polymers based on PMMA, we can distinguish two different limits. On the one hand, Martin-de Leon et al. explored nanocellular polymers with extremely low cell sizes. They produced nanocellular PMMA via homogeneous nucleation using low saturation temperatures (from 0 to -32 ºC), different saturation pressures (from 6 to 20 MPa), and the use of PMMA with different viscosities, obtaining nanocellular PMMA with relative densities ranging

0.24 - 0.55 and cell sizes from 14 to 75 nm[10,48]. Meanwhile, for large cell sizes, Wang et al. by using the heterogeneous nucleation approach obtained nanocellular polymers with cell sizes around 205 nm and relative densities of 0.125 using thermoplastic polyurethane (TPU) as a nucleating agent in PMMA[70]. They use a saturation temperature of 25 ºC and a saturation pressure of 13.8 MPa.

2.1.3. Properties of nanocellular polymers

As a consequence of their reduced cell size, nanocellular polymers present a very interesting combination of properties[3,4,10,14,79]. For instance, as previously commented, it was proved that when the cell size is 10 times smaller than the light wavelength the material became transparent [10,11]. In addition, nanocellular materials with an interconnected cellular structure are characterized by their high surface area[13,14]. Also, the reduction of the cell size can lead to significant changes in the behavior of the material, such as an increase of the glass transition temperature or improvements in the mechanical properties[5,7,8] or the appearance of new or unexpected properties (electric, dielectric or acoustic properties) in comparison with microcellular polymers[15,16]. Furthermore, like many other thermoplastic cellular materials, they are characterized by their lightweight, low cost, and recyclability.

For the purposes of this thesis, the most interesting property of nanocellular polymers is the reduced conduction through the gas phase due to the Knudsen effect[2]. This effect was proved in 2014 for nanocellular polymers by Notario and co-workers[4]. Due to this reduction of one of the heat transfer mechanisms, it was claimed several times that nanocellular materials could be potentially used as advanced thermal insulators when combining low-densities and nanometric cell sizes, but no experimental data supported these claims[80–82]. In addition, there was a lack of understanding about the effect of the cell size in other heat transfer mechanisms, such as the conduction through the solid phase or the radiation term. Thus, one of the objectives of this thesis is to measure and study the thermal conductivity of microcellular and nanocellular polymers to identify their potential and limitations to be used as thermal insulating materials. In the next section, we focus our attention on this specific property.

2.2. Thermal conductivity

2.2.1. General description and methods

Thermal conductivity (λ) is an intensive physical property that describes heat transport through a material due to a temperature gradient. The units of thermal conductivity in the international system of units (SI) are W/(m·K). It is defined via Fourier's law of thermal conduction (Equation (2.4)). This equation states that the time rate of heat flux density through a material ($\vec{q}$) is proportional to the negative gradient of the temperature ($\vec{\nabla}T$), and λ is the parameter correlating both magnitudes. The heat flux density is defined as the time rate of heat transfer ($\partial\vec{Q}/\partial t$) per unit area ($A$) normal

to the direction of heat transfer (Equation (2.5)). It is a vector quantity since it has both direction and magnitude. According to the second law of thermodynamics, heat always flows in the direction towards the lower temperature. Regarding thermal conductivity, it is usually considered a scalar magnitude. Still, in some cases, it can vary with local position or direction (such as in anisotropic or heterogeneous materials). Insulating materials are characterized by a low thermal conductivity, in the range from 4 to 60 mW/(m·K)[83,84].

$$\vec{q} = -\lambda \vec{\nabla} T \tag{2.4}$$

$$\vec{q} = \frac{\frac{\partial \vec{Q}}{\partial t}}{A} \tag{2.5}$$

2.2.1.1. Parameters related to the thermal conductivity

Thermal conductivity is the main parameter to characterize insulation materials but in some works it is common to find other parameters to describe the insulation capability. These parameters, related to the thermal conductivity, are the thermal resistivity (R_λ), the thermal resistance of unit area (*R-Value*), and the heat transfer coefficient (*U-Value*).

Thermal resistivity (R_λ)

Thermal resistivity (R_λ) is an intensive property that represents the ability of a material to resist the flow of heat. It is the reciprocal of thermal conductivity and can be expressed according to Equation (2.6). Its unit is (m·K)/W.

$$R_\lambda = \frac{1}{\lambda} \tag{2.6}$$

Thermal resistance of unit area (R-Value)

Thermal resistance per unit area (*R-Value*) measures the material resistivity to heat flow at a specific thickness. Its unit is (m^2·K)/W. It is related to thermal conductivity or thermal resistivity according to Equation (2.7), where *d* is the thickness of the sample. The greater the *R-Value* of the material, the better the ability of the material to resist heat flow. This parameter together with the U-Value (explained below) are used for comparative purposes and are well-known parameters in the design of thermal envelopes in the bulling sector.

$$R\text{-}Value = R_\lambda \cdot d = \frac{d}{\lambda} \tag{2.7}$$

Heat transfer coefficient (U-Value)

The heat transfer coefficient (*U-Value*) represents the heat transfer through a material as a function of the temperature gradient between the sample thickness. The unit of the *U-Value* is W/(m^2·K) and

indicates the heat flow through an area of one square meter with a temperature difference of one Kelvin. It is the reciprocal of the R-value (Equation (2.8)). The lower the *U-Value* the higher the insulation capability. As said before, the *U* and *R-values* are commonly used in building and construction. For instance, achieving a *U-Value* of 0.2 W/(m²·K) is a typical requirement for building construction[85–89]. The required *U-Value* varies between roofs, walls, and floors, and also depends on the climate of the region. In cold climate regions, the required *U-value* is lower than in hot ones. To reduce the *U-value* there are two possible routes. On the one hand, increasing the thickness of the insulation layer using conventional insulation materials. However, this approach requires acquiring larger amounts of material, with implications for the environment and CO_2 emissions, with an increase in the cost, and also implies the reduction of the useful area in buildings. On the other hand, a promising approach goes through developing new thermal insulators with lower thermal conductivity. This alternative would allow not only save energy but also extend the useful area in buildings by obtaining the same insulation with reduced thickness.

$$U-Value = \frac{1}{R-Value} = \frac{\lambda}{d} \tag{2.8}$$

2.2.1.2. Thermal conductivity measurement techniques

When measuring the thermal conductivity, it is possible to distinguish between transient and steady-state techniques depending on how Equation (2.4) is solved. Both methods, either transient or steady-state, have advantages and limitations, and they are suitable for only a limited range of materials, depending on the thermal properties, sample configuration, and measuring temperature[90,91].

On the one hand, in transient or non-steady-state methods, the temperature distribution throughout the sample varies with time. In this case, solving the heat conduction equation is more complicated because it involves a time-dependent heat flow equation[92]. Among transient techniques, hot-disk Transient Plane Source (TPS) and laser flash methods (LFA) are commonly used[90]. Both methods are standardized according to ISO 22007-2[93] and ISO 22007-4[94] respectively. The TPS method consists of a sensor with the shape of a double spiral (**Figure 2.4a**). The sensor acts as a heat source as well as a temperature sensor. Thermal diffusivity and thermal conductivity are calculated by recording the sensor voltage and current variation after a pulse of certain power and time[95]. To achieve optimum contact between the sensor and the samples, the setup is compressed with an external load. Meanwhile, the LFA method consists of an energy pulse that is sent to the sample (**Figure 2.4b**). An infrared detector records the associated temperature rise at the rear surface of the sample. Then, the thermal diffusivity is calculated using the half-life period of the temperature rise[96]. After that, the thermal conductivity can be calculated by knowing the

material's specific heat capacity and density[97]. This method has the advantage of not involving temperature or heat-flow measurements for the determination of a thermal property.

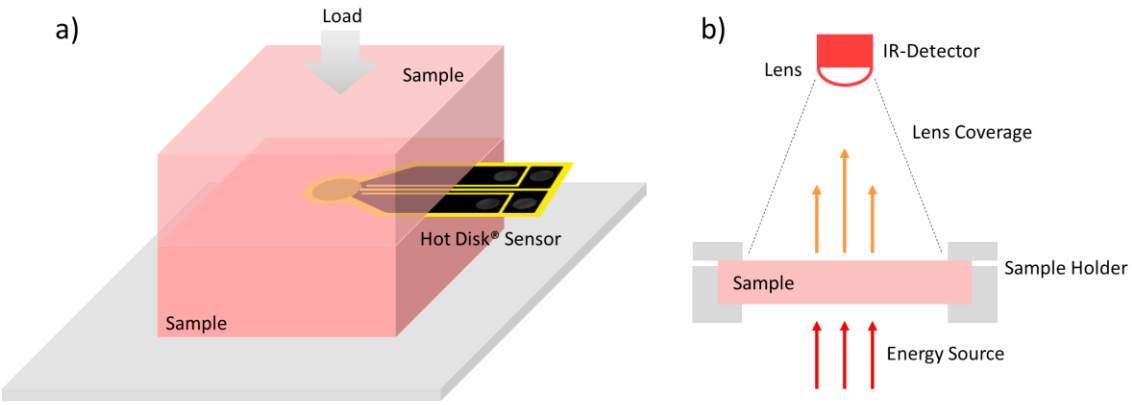

Figure 2.4. Scheme of a) TPS method and b) LFA method.

One interesting advantage of these transient techniques is that measurements can be performed in small samples; but, the accuracy of these methods for thermal insulating materials is not clear [97–99]. For instance, Almanza et al.[98] studied the thermal conductivity of polyethylene (PE) foams. Results showed that the values measured by TPS method follow the same trends as those measured by steady-state technique. However, the TPS values were approximately 20% higher than the reference (steady-state) values. In the work of Zheng et al.[99] it is proved that complex calculations are required to fit the TPS data to the values obtained in steady-state techniques. Therefore, since non-steady approaches are typically indirect (the thermal conductivity is obtained/calculated through measuring another property, not directly the heat flux), they are not the ideal techniques for characterizing insulating materials, characterized by very low thermal conductivities, in which any uncertainty can have a great effect[100].

On the other hand, in steady-state methods, a temperature difference that does not evolve with time is established; thus, the mathematics are simplified, turning the heat transfer problem into a one-dimensional problem (Equation (2.9)). A steady-state condition is attained when the heat flux through the sample thickness (d) per unit of area (A) is constant, i.e., the temperature at each point of the sample ($\Delta T = T_1 - T_2$) does not vary over time[90]. Among steady-state techniques, the guarded hot plate (GHP) and heat flow meter (HFM) methods are commonly used[90]. The GHP method (**Figure 2.5a**) is considered an absolute method because the heat flux is determined by measuring the power needed to keep the temperature of the hot plate constant[90,91]. In the GHP method, the sample is heated by an electrically heated plate (hot plate). The heat output corresponds to the electrical power supplied to the heating. The hot plate is embedded by a guard plate, which is separately tempered to the same temperature as the hot plate. There are two possible configurations. In the one-plate setup, the heat flow passes through one sample, while the top of the main heater acts as an insulating guard. Meanwhile, in the two-plate setup, the hot plate is

sandwiched between two samples of the same size as shown in (**Figure 2.5a**). On the contrary, the HFM (**Figure 2.5b**) is a comparative or relative method[90,91]. In this case, the heat flux is determined by measuring the voltage drop through an electrical resistor, a so-called sensor or heat flux transducer, which is previously calibrated. In the two steady-state techniques, the heat flows from a hot plate (at temperature T_1), throughout the sample, to a cold plate (at temperature $T_2<T_1$), establishing a temperature gradient.

$$q = -\lambda \frac{dT}{dx} \rightarrow q \int_{T_1}^{T_2} dT = -\lambda \int_0^d dx \rightarrow q(T_2 - T_1) = -\lambda d \rightarrow \lambda = \frac{q \cdot d}{T_1 - T_2} = \frac{Q \cdot d}{A \cdot \Delta T} \quad (2.9)$$

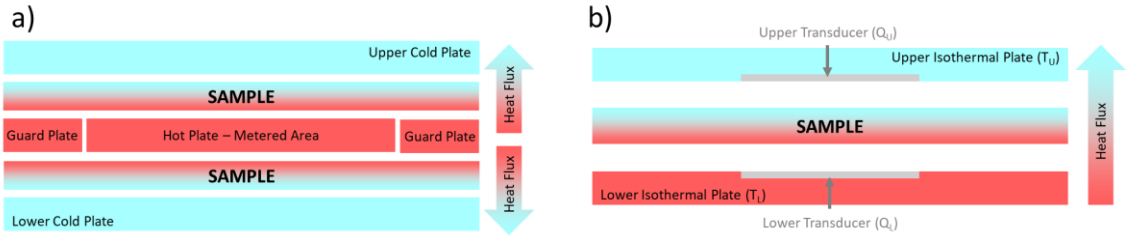

Figure 2.5. Scheme of a) GHP method and b) HFM method.

To obtain representative and comparable values of the thermal conductivity of insulating materials there are several international standards that rely on steady-state measurements[101–105]. For instance, ASTM C177[101], ISO 8302[102], or UNE-EN 12667[103] require measurements performed with hot plate meters, while ASTM C518[104] and ISO 8301[105] are prepared for measurements using heat flow meters.

When a new material for thermal insulation is developed at lab-scale, small prototypes are usually produced. This is the case of nanocellular polymers too: as commented before, the dimensions of these materials are limited when they are produced by the gas dissolution foaming process. To accurately characterize any new material with great potential for the thermal insulation market, such as nanocellular polymers or any others, steady-state measurements would be preferred because they provide more reliable and comparable results. However, at the lab-scale, the main problem of the steady-state techniques resides in the large samples that are needed to perform the measurements. As said before, steady-state machines are designed to fulfill the requirements of international standards, for which large samples are mandatory. Thus, researchers have been developing new methods to measure small-size samples[100,106–108]. For instance, Miller et al.[108] developed a hot-plate device to measure the thermal conductivity of small aerogel samples (20 mm diameter and 2.5 mm thickness) with conductivities on the order of that of air (around 26 mW/(m·K) at 20 ºC). Meanwhile, Jannot et al.[100,106,107] continuously improve a centered hot plate method to

finally measure centimeter size samples (15 mm diameter and 3-9 mm thickness) accurately. However, these devices are homemade methods with complex technical parts, complicating their scalability to other laboratories. Other researchers tuned their commercial heat flow meters[109] reducing the heat flux transducer area to measure disk samples with 20 mm diameter and 2–5 mm thickness. Finally, Almeida et al.[110] evaluate the thermal conductivity of disk-like samples of 60–100 mm diameter and 15–20 mm thickness with in-house built equipment based on two precision heat flux sensors. The equipment was made following the ASTM C518[104] standard as a guideline, however, they do not provide detailed information about the heat flux sensors characteristics and how to build the device for the measurements.

CHALLENGE

Therefore, to fully understand the potential of new insulation materials developed at lab-scale, such as nanocellular polymers, it is then mandatory to measure their properties using reliable and comparable steady-state measurements. To do so, large prototypes must be produced. Furthermore, new methods suitable for small specimens could be developed to allow a proper characterization of the thermal conductivity. These methods should rely on steady-state measurements to provide values comparable to those reported for standard insulating materials and must be easily implemented and used by the scientific community to provide comparable data.

This research aims at facing this challenge (see **Chapter 1** Section 1.3). First, by producing large prototypes suitable to be characterized with the conventional techniques. Second, by implementing methodologies to accurately characterize the thermal conductivity of nanocellular polymers. The developed solutions can be found in **Chapter 3**.

2.2.2. Thermal conductivity of nanocellular polymers

2.2.2.1. Heat transfer mechanisms

In a porous material, the total thermal conductivity (λ_t) can be described as a function of four different mechanisms: conduction through the solid phase (λ_s), conduction through the gas phase (λ_g), thermal radiation (λ_r), and convection within cells (λ_c), as shown in Equation (2.10)[111].

$$\lambda_t = \lambda_s + \lambda_g + \lambda_r + \lambda_c \tag{2.10}$$

However, the contribution of convection can be neglected when the cell sizes are lower than 4 mm [112–114]. For instance, Jeffreys [115] showed that the onset of convective flow in a fluid layer of thickness L_g, expansion coefficient α, kinematic viscosity ν, and thermal diffusivity κ will occur when the dimensionless parameter χ, given by Equation (2.11) is higher than 1709.5.

$$\chi = \frac{9.81\alpha(T_1 - T_2)L_g^3}{\kappa\nu} > 1790.5 \tag{2.11}$$

Where T_1 and T_2 ($T_2<T_1$) are the temperatures at the boundaries. Calculated values of χ for cellular materials with cells of 1 mm give values four orders of magnitude lower than the threshold value [115], indicating the lack of convective flow in these materials.

Conduction through the solid phase

Conduction through the solid phase depends on the solid volume fraction (X_s), on the conductivity of the solid matrix (λ'_s), and a structural factor g (Equation (2.12))[114]. In cellular polymers, the solid volume fraction corresponds to the relative density (ρ_r) (defined in Equation (2.1)).

$$\lambda_s = g\lambda'_s X_s = g\lambda'_s \rho_r \tag{2.12}$$

Regarding the conductivity of the solid matrix λ'_s, it depends on the polymer nature and the temperature. For instance, PS has a thermal conductivity between 120-185 mW/(m·K), while PMMA has a thermal conductivity between 170-215 mW/(m·K) at approximately 300 K[4,82,116–121]. As temperature increases, the thermal conductivity of the polymer increases[116,122]. This is because the energy carriers for thermal conduction in polymers are phonons. These phonons are particles obeying Bose-Einstein statistics and the thermal conductivity of a solid is determined by the phonon distribution which can be obtained by solving the Boltzmann equation (Equation (2.13))[116]. Where $C_i(\omega)d\omega$ is the heat capacity contribution of phonons of polarization i and frequency ω, $v_i(\omega)$ is the phonon velocity and $l_i(\omega)$ is the phonon free path. Equation (2.13) can be simplified by using the dominant phonon approximation, leading to Equation (2.14). This follows from the fact that, at any temperature T, the phonons which contribute significantly to the integral in Equation (2.13) have a frequency $\omega \approx 4k_BT/\hbar$ (where k_B is the Boltzmann constant and $\hbar$ the reduced Plank constant). Thus, the frequency dependence is converted to an equivalent temperature dependence and, after averaging over all polarizations Equation (2.14) is obtained. This is exactly the same expression obtained if the kinetic theory of gases is applied to a system of phonons[123].

$$\lambda'_s(T) = \frac{1}{3}\sum_i \int C_i(\omega)v_i(\omega)l_i(\omega)d\omega \tag{2.13}$$

$$\lambda'_s(T) = \frac{1}{3}C(T)v(T)l(T) \tag{2.14}$$

In conventional cellular polymers, the cell walls are several microns in thickness, so the polymer in the solid phase behaves like a bulk material and presents the same thermal conductivity that it should have in the solid form (before foaming). However, in nanocellular polymers the cell walls can be as thin as 20 nm, so the polymer macromolecules are confined within the cell walls[5,6]. Based on the increased tortuosity of the solid phase, one could expect a reduction of thermal conduction[4]. Nevertheless, as the polymer macromolecules get highly oriented in the thin cell

walls, an increment could also take occur. Orientation can be also expected in microcellular or conventional polymers because of the stretching of the cell wall during foaming.

According to the kinetic theory, the effective thermal conductivity of a thin polymer film at the skeleton (λ'_{s_eff}) can be calculated as stated in Equation (2.15), where l is the conventional mean free path of the phonons (that can be obtained from Equation (2.14)) and δ is the characteristic size of the polymer skeleton[124–128]. The solid skeleton of the nanocellular foams is composed of nanoscale cell walls and nanoscale struts. Thus, when going to the nanoscale, the characteristic size of the polymer skeleton decreases and can approximate to the mean free path of the phonons reducing the thermal conductivity through the solid phase according to Equation (2.15). This reduction of thermal conductivity is called size effect. However, the mean free path in polymers ranges from 0.1 to 10 nm[116,128], while the smallest cell wall thickness reported is 20 nm[6]. For PMMA at standard conditions, l is around 1 nm[116]. Then, size effect is not likely to occur in nanocellular PMMA, while in aerogels, which are formed by a discontinuous and smaller solid structure, this helps to significantly reduce conduction through the solid phase.

$$\lambda'_{s\_eff} = \lambda'_s \left(1 + \frac{4l}{3\delta}\right)^{-1} \tag{2.15}$$

Currently, it has not been established what is the thermal conductivity of a polymer when it is confined in a nanoscale thin film. For instance, Ma et al.[129] reported that thermal conductivity reduces as the thickness of ultra-thin amorphous PS films decreases using molecular dynamics simulations. Meanwhile, Kim et al.[130] reported experimentally that the thermal conductivity of ultra-thin amorphous PMMA films increases as the film thickness decreases, but they attributed that effect to a substrate effect in the measurement. Also, Zhang et al.[131] showed experimentally that the stretching of the polymer chain could increase the thermal conductivity in semicrystalline high-density polyethylene (HDPE). However, there are not direct measurements of the thermal conductivity of polymers that are forming a nanoscale porous structure like in the case of nanocellular polymers.

With respect to the solid structure factor (g), it is an efficiency-structural factor proposed by Glicksman[114]. For high-density foams, the g factor is 1, that is, the conduction through the solid is reduced to the same extent as the density after the foam is produced. However, for low-density foams, it has been proved that g can be lower than 1, that is, the conduction through the solid is lower than the expected value taking into account the density. For conventional foams with very low relative density ($\rho_r < 0.05$), a factor of 2/3 has been used when the cell walls are very thin and the cells have a polyhedral shape[114]. In this case, the polymer mass is the faces of the polyhedron, so if taking a hexahedron, four of the six faces (i.e., walls of a cell) are effective surfaces to the heat transfer (parallel to its direction), as shown in (**Figure 2.6a**). Meanwhile, if the fraction of mass in

the struts is also considered, g can have a minimum value of around 1/3 for materials with a high fraction of the solid phase in the struts[114]. This is because, the mass is localized on the edges (i.e., struts of a cell) of the hexahedron, so four of the twelve edges are effective surfaces to the heat transfer, as shown in **Figure 2.6b**. For microcellular and nanocellular polymers with medium/high relative densities (0.3–0.65), this factor was estimated to be in the range of 0.8–1[4,132,133]. However, information about the value of this structural factor is still scarce for these materials. In the low-density range, if only the structure is considered, one could expect g factors as those of conventional foams. Nonetheless, if the conductivity of the polymer increases because of the confinement and/or orientation of the polymer chains, this reduction can be hindered and not measurable. This is a quite challenging topic because it is very difficult to separate the possible modification of g due to changes in the cellular structure from the modifications due to a modification of the thermal conductivity of the polymeric matrix in the nanocellular polymer. For the purposes of this thesis, g is considered to contain all the information regarding the changes in the solid conduction, taking into account that the thermal conductivity of the polymer does not vary after the foaming process (when the polymer chains are located in the cell walls).

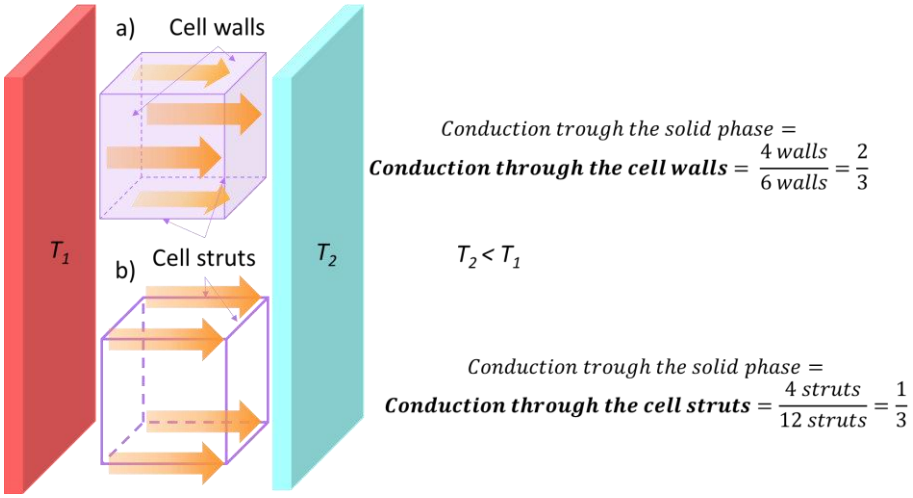

Figure 2.6. Conduction through the solid phase in low-density conventional foams with a) closed cells and b) open cells.

CHALLENGE

At the moment this thesis is presented, there are yet not reliable data about the behavior of the g factor for nanocellular polymers in the low-density range (relative density below 0.2). As stated before, it is challenging to measure the thermal conductivity of these materials, and this measurement is key to quantifying each heat transfer mechanism and evaluating the g factor. Thus, there is a need to determine g in nanocellular polymers and establish its dependency with the material's density.

In this work, this challenge is investigated with the aim of increasing the knowledge about the heat transfer mechanisms in nanocellular polymers (see **Chapter 4**).

From a theoretical perspective, there could be three possible scenarios. First, *g* can behave as in conventional cellular polymers, taking values between 1/3 and 2/3 in the low-density range. Another possibility is that *g* remains in the range of 0.8-1, as already measured in medium-density nanocellular polymers. In this case, the confinement of the polymer is limiting the conduction reduction expected by the low-density. Yet another option is to obtain very low *g* factors, as those measured in other nanoscale systems. For instance, this factor can take values as low as 0.05 for aerogels[120,134]. However, the structure of aerogels and nanocellular polymers is completely different. The main difference lays in the solid structure connectivity, which determines the phonon diffusion throughout the material[122]: while cellular materials present a continuous structure (**Figure 2.7a**), aerogels present a backbone structure with multiple contact points (**Figure 2.7b**), which minimizes conduction through the solid phase. As thermal conductivity depends on how the heat is transferred by the phonon diffusion through the material, increasing the number of contact points makes more difficult phonon diffusion, reducing the solid thermal conductivity and the solid structure factor (*g*).

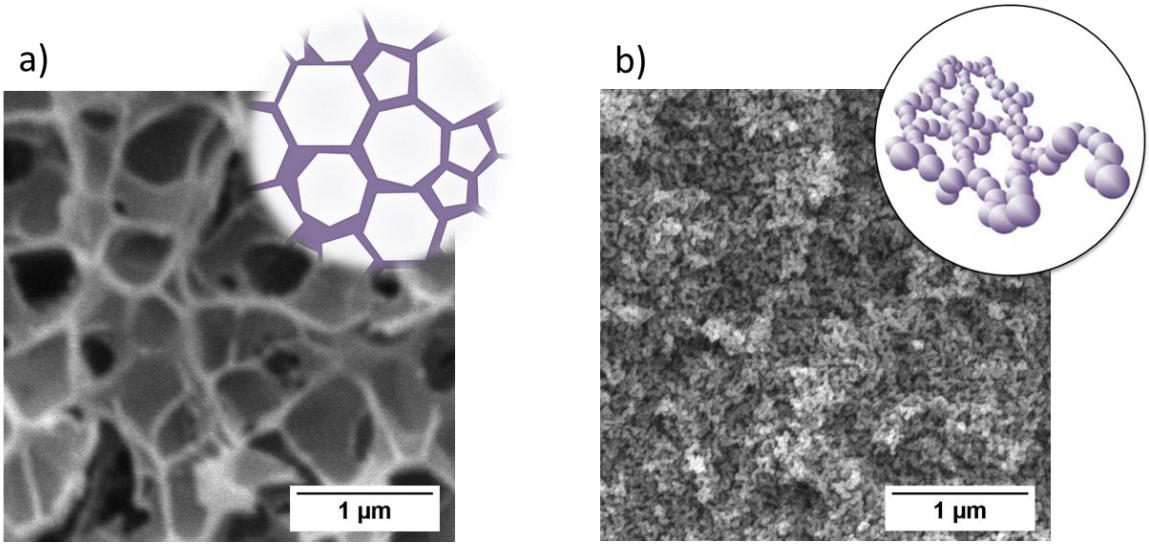

Figure 2.7. Scheme of the structure of a) nanocellular polymer (continuous structure), and b) aerogel (discontinuous structure).

Figure 2.8 shows the conduction through the solid phase according to Equation (2.12) as a function of the relative density for materials with different structure factors (1, 2/3, 1/3, and 0.05). The thermal conductivity of the solid (λ'_s) is taken as 180 mW/(m·K) (in the range of values for PMMA) for the predictions, which are focused on the medium density range. It is observed that as the solid structure factor is reduced, the conductivity decreases significantly. For instance, for a cellular material with 0.2 of relative density, the conduction through the solid phase is 36 mW/(m·K) if its solid structure factor is 1 (nanocellular polymer-like structure) but can be as low as 1.8 mW/(m·K) if the solid structure factor is 0.05 (aerogel-like structure). As stated before, there is still a need to figure out the solid structure factor of low-density nanocellular polymers (relative densities < 0.2).

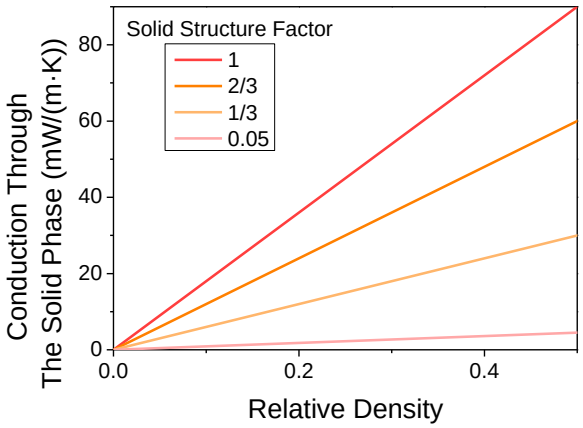

Figure 2.8. Conduction through the solid phase as a function of the relative density for materials with different solid structure factors. The thermal conductivity of the solid material for these calculations was taken as 180 mW/(m·K).

The solid structure factor is expressed in different ways in the literature. Assuming that the phonon diffusion model is valid, the solid thermal conductivity can also be obtained by Equation (2.16)[122,135], where v is the porous material longitudinal sound speed and v_s the solid material longitudinal sound speed. The solid structure factor can then be obtained by $g = v / v_s$. Note that the sound speed is related to the mechanical properties, so the solid thermal conductivity can be also estimated by measuring the mechanical properties[136].

$$\lambda_s = g\lambda'_s\rho_r = \frac{v}{v_s}\lambda'_s\rho_r \tag{2.16}$$

In other research works, a different approach is used to calculate the g factor taking into account the dependence of the sound speed with the relative density (Equation (2.17))[120]. This equation, also obtained by the percolating theory, is commonly used for aerogels where α range between 1.2-2 and C depends on the interconnectivity of the particles in aerogels (i.e. on the sound speed)[122,137]. For cellular materials α ≈ 1[110].

$$\lambda_s = \frac{v}{v_s}\lambda'_s\rho_r = C\rho_r{}^{\alpha} \tag{2.17}$$

Conduction through the gas phase

As shown in Equation (2.18) conduction through the gas phase depends on the gas volume fraction (X_g), and the thermal conductivity of the gas inside the cells λ'_g[138]. In cellular polymers, the gas volume fraction corresponds to the porosity (V_f) (calculated as $V_f = 1 - \rho_r$).

$$\lambda_g = \lambda'_g X_g = \lambda'_g V_f = \lambda'_g(1-\rho_r) \tag{2.18}$$

In nanocellular polymers, the appearance of the Knudsen effect reduces the contribution of the thermal conductivity of the gas phase with respect to the equation for conventional materials, as

experimentally proved by Notario et al.[4]. This effect implies that when the cell size is comparable to or smaller than the mean free path of the gas molecules (i.e. the average distance between collisions), they collide more often with the cell walls than among them, reducing the energy transfer[2]. Therefore, the conductivity of the gas inside the cells, λ'_g is reduced (see Equation (2.19)). It depends on the thermal conductivity of the free gas, that is, without being encapsulated in a cell, (λ'_{g0}) (which also depends on the temperature), the cell size (ϕ), the intrinsic parameter beta, and the mean free path of the gas molecules (l_g). According to the theory, Knudsen effect starts becoming relevant when the cell size is smaller than 100 times the mean free path, $\phi \leq 100\ l_g$[139]. At standard ambient temperature and pressure (25 ºC and 101325 Pa) the mean free path of the air is 70 nm. Then, Knusden effect takes place in nanocellular polymers filled with air at atmospheric pressure for $\phi \leq 7$ µm.

$$\lambda'_g = \frac{\lambda'_{g0}}{1 + \frac{2\beta l_g}{\phi}} \tag{2.19}$$

β is a dimensionless intrinsic parameter that considers the transfer of energy between the gas molecules and the solid structure. β value varies from 1.5 to 2 for argon and nitrogen[2]. There are several definitions for β in the literature, depending on different relations between the specific heat ratio (γ), the thermal accommodation coefficient (α), and the Prandtl number (Pr) [2,140–142]. In this work, we used Equation (2.20) to calculate this parameter[140]. The specific heat ratio is the relation between specific heat at constant pressure and specific heat at constant volume (c_p/c_v) and is 1.40 for air. On the other hand, the Prandtl number is a dimensionless parameter defined as the ratio of momentum diffusivity to thermal diffusivity (Pr = 0.713 for air). Based on this equation, β for air is 1.64[132,140].

$$\beta = \frac{2\gamma}{\gamma + 1}\frac{1}{Pr} \tag{2.20}$$

Meanwhile, the mean free path depends on the temperature (T), the pressure (p), and the molecule diameter (d_m) (3.6 Å for air[143]) as shown in Equation (2.21)[2], where R is the ideal gas constant and N_A the Avogadro's number. A scheme of the obtention of the mean free path is shown in **Figure 2.9**. If the gas molecules have diameter d, then the effective cross-section for collision can be modeled by using a circle of diameter $2d$ to represent the effective collision area of a molecule, A. Meanwhile, the "target" molecules are treated as a point of masses. In time t, the effective collision area would move at speed v creating the volume of interaction. The number of collisions can be estimated from the number of gas molecules that were in that volume, n_v (number of molecules per unit volume) multiplied by the volume. Then, the mean free path can be taken as the length of the path divided by the number of collisions and leads to Equation (2.21) after considering that the target molecules have an average velocity (n_v is calculated assuming ideal gas law). As seen in Equation (2.21), the mean free path rises as temperature increases and pressure decreases. While at standard ambient temperature and atmospheric pressure the mean free path in 70 nm for air, it

increases up to 7 mm when pressure decreases to 1 Pa (0.01 mbar). This means that Knudsen effect can take place for cell sizes as large as 7 mm at vacuum.

$$l_g = \frac{RT}{\sqrt{2}\pi d_m^2 N_A p} \tag{2.21}$$

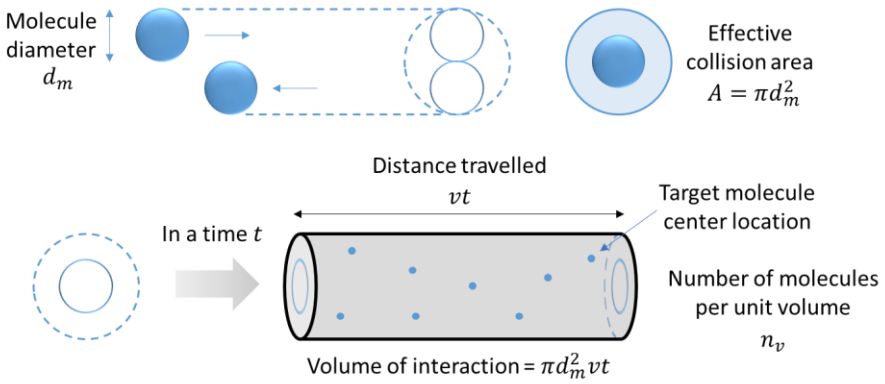

Figure 2.9. Scheme of the obtention of the free path (adapted from[144]).

So, the conduction through the gas phase can now be expressed in terms of the average cell size, the gas characteristics, the pressure, and the temperature, as given in Equation (2.22). As shown in **Figure 2.10**, at atmospheric pressure the predicted reduction starts becoming significant for cell sizes below the micron. Also, it is observed that as density is reduced the conduction through the gas phase increases because the amount of gas in the material is higher. However, thanks to the Knudsen effect, the differences in conduction through the gas phase at different densities are reduced when approaching the nanoscale.

$$\lambda_g = \lambda_g'(1-\rho_r) = \frac{\lambda'_{g0}(1-\rho_r)}{1+\frac{2\beta}{\phi}\frac{RT}{\sqrt{2}\pi d_m^2 N_A p}} \tag{2.22}$$

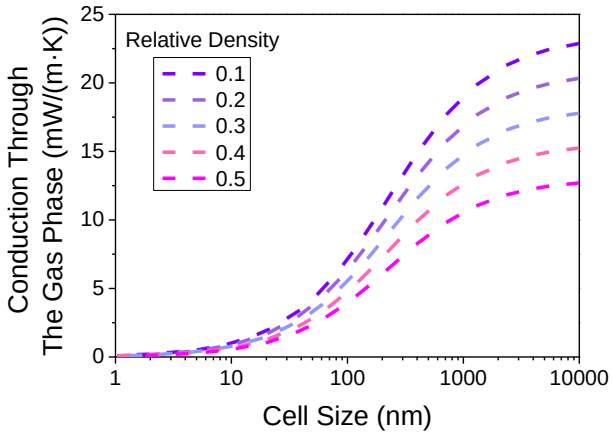

Figure 2.10. Conduction through the gas phase as a function of the average cell size considering the Knudsen effect for materials with different relative densities at ambient pressure. The gas assumed for the predictions is air.

Furthermore, since Equation (2.22) depends on the pressure, it is possible to obtain the dependence of the gas thermal conductivity inside the nanocellular polymer as a function of the pressure and the average cell size as shown in **Figure 2.11** for air. It is observed that, on the one hand, thanks to the Knudsen effect, when the cell size decreases the thermal conductivity at ambient pressure is reduced. On the other hand, when the pressure is reduced the thermal conductivity sharply decreases. Furthermore, as the cell size is reduced the required vacuum to fully evacuate is lower. This is the main principle of vacuum insulation panels (VIPs) wherein a highly open porous material is evacuated to low pressure (in the range of 0.01–10 mbar) [145].

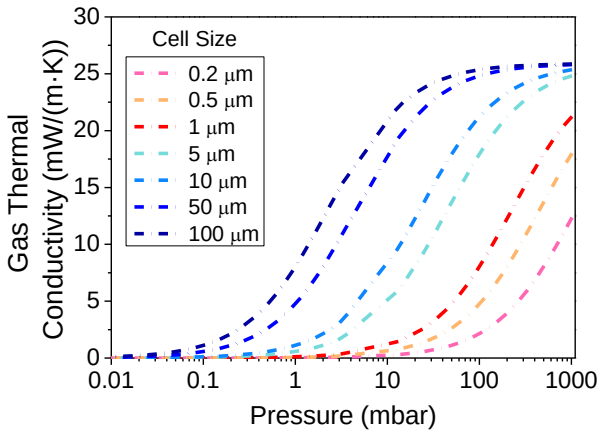

Figure 2.11. Gas thermal conductivity inside a cellular polymer as a function of the pressure and the average cell size of the porous material. The gas assumed for the predictions is air.

Finally, note that Equation (2.22) considers the average cell size, that is, it assumes that the nanocellular polymer presents a narrow and homogeneous cell size distribution. However, this is not always the case. Bimodal structures, with micrometric and nanometric cells, cannot be described with the current model, because the average cell size would neglect the contribution of the micrometric pores. Moreover, nanocellular structures with a wide cell size distribution also require a model that considers the variation of cell size, because every cell size would present a different contribution to the Knudsen effect. To study these kinds of systems, Bernardo et al.[132] developed a model based on the volume fraction (i.e., the porosity) that occupies each type of cell.

Radiation

Due to the fact of being at a certain temperature, materials emit, reflect, and absorb radiation. If we consider a black-body (a hypothetical body that completely absorbs all radiant energy falling upon it, reaches some equilibrium temperature, and then reemits that energy as quickly as it absorbs it), the spectral-energy distribution of emitted radiation (**Figure 2.12**) is given by Equation (2.23) (Planck radiation law)[146]. Where I is the spectral intensity, Λ is the wavelength, h is the Planck constant, c is the light speed, k_B is the Boltzmann constant, and T is the black-body temperature. The area under the curve corresponds to the emitted intensity in the wavelength range under

consideration. Also, note that the spectral distribution has always a maximum, the dependence of this wavelength maximum (Λ_{max}) with the temperature is given by Equation (2.24) (Wien displacement law). At ambient temperature (around 300 K), the maximum of emitted radiation is centered at approximately 10 μm (**Figure 2.12**), which corresponds to infrared radiation. That is, all bodies emit radiation in the infrared region of the electromagnetic spectrum, which corresponds to wavelengths from about 700 nanometers to 1 millimeter. In practice, real objects do not radiate with the intensity of a blackbody, having lower radiant power, but the range of emitted radiation predicted by this ideal theory is still valid.

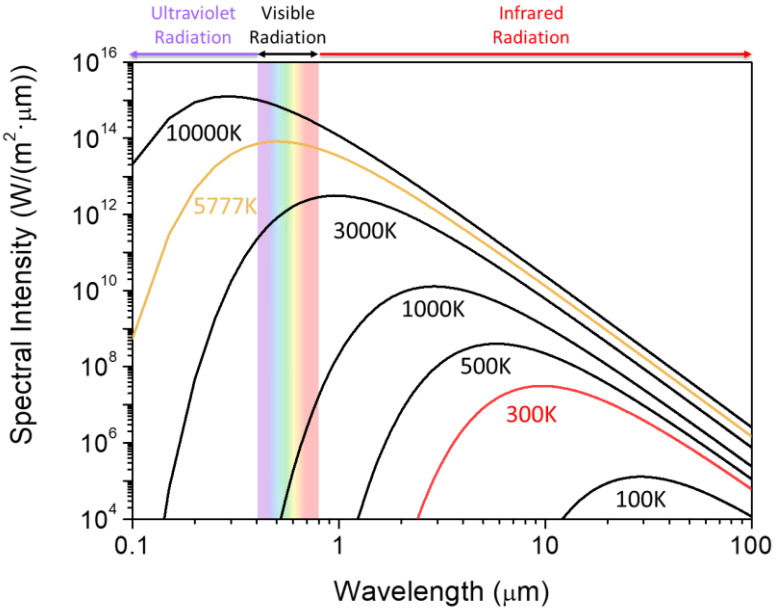

Figure 2.12. Black-body spectrum at different temperatures (5777 K is the sun's surface temperature).

$$I(\Lambda, T) = \frac{2\pi hc^2}{\Lambda^5} \frac{1}{exp\left(\frac{hc}{\Lambda k_B T}\right) - 1} \tag{2.23}$$

$$\Lambda_{max} = \frac{2897.8\ \mu m \cdot K}{T} \tag{2.24}$$

Then, the radiation contribution to the thermal conductivity (λ_r) of Equation (2.10) is related to infrared radiation. Within porous polymeric materials, radiation heat transfer is a diffusion-like process via scattering and absorption of infrared radiation. The scattering is caused by the cellular structure, while the solid fraction absorbs radiation. Polymers emit/absorb radiation in the so-called mid-infrared region (where wavelengths range from 2.5 to 25 μm). They absorb/emit at certain wavelengths that correspond to molecular movement vibrations[147]. The contribution of infrared radiation to the total thermal conductivity starts to become relevant when the relative density reaches values under 0.2 since at higher relative densities the high solid fraction absorbs a great amount of infrared radiation[112,120,137,148,149]. The radiative part of the thermal conductivity

in porous materials is given by Equation (2.25) (Rosseland approximation equation)[150], where σ is the Stefan-Boltzmann constant, n is the refractive index (considered equal to 1 for low-density cellular materials, and aerogels[120,151]), and K_e is the extinction coefficient of the porous material. Rosseland approximation is only valid for thick and homogeneous optical media (i.e., when the medium absorbs and scatters isotropically). The determination of the extinction coefficient of the porous material is essential to predict the radiation contribution.

$$\lambda_r = \frac{16n^2\sigma T^3}{3K_e} \tag{2.25}$$

For very-low-density cellular materials with cell sizes of hundreds of microns, Glicksman et al.[114,152,153] proposed an equation to obtain the effective extinction coefficient (Equation (2.26))[151]. The extinction coefficient is a sum of two contributions in this model. The first term depends on the relative density, the fraction of mass in the struts (f_s), and the cell size. The term 4.10 is a constant related to the cell geometry (taken as pentagonal dodecahedrons). This term is related to the scattering of the cellular structure. The extinction coefficient rises with the relative density and is increased when the cell size decreases because there are more cells per unit length in the same thickness (more scattering events). For cellular materials based on ethylene-vinyl acetate (EVA), polyethylene (PE), PS, and PMMA, f_s takes values between 0.1 - 0.4[151,154], whereas for PUR it takes values between 0.6 - 0.8[155]. As the fraction of mass in the struts increases the extinction coefficient rises, leading to lower radiation contribution. Meanwhile, the second term corresponds to the contribution of the absorption of the cell walls, being K_s the extinction coefficient of the solid polymer. This term depends on the fraction of mass in the cell walls (1-f_s) and the density too. Note that for very-low relative densities, this contribution is almost negligible.

$$K_e = K_G = \frac{4.10\sqrt{f_s\rho_r}}{\phi} + (1 - f_s)\rho_r K_s \tag{2.26}$$

For conventional foams, there are plenty of works calculating the extinction coefficient, both theoretically (using for instance Glicksman equations[114,151,152]) and experimentally (measuring transmittance to infrared radiation[151]). However, these theoretical models are not valid when the cell size is in the nanoscale since the cell size, cell struts, and cell walls (acting as scattering centers) are of the same order of magnitude or even lower than the infrared radiation wavelength. As the ratio between the scattering center and the wavelength decreases the scattering mechanisms change from optical to Mie and finally to Rayleigh[12,156–158]. For thermal infrared (average wavelength 10 microns), conventional foams are located in the optical region, while microcellular and nanocellular polymers are withing the Mie and Rayleigh scattering region. Therefore, Mie or Rayleigh scattering treatment may be used to deal with the electromagnetic interaction. In a general situation, the theory to describe the scattering process is the Mie theory

because it gives similar results to Rayleigh scattering theory (in the Rayleigh region) and to optical scattering in the geometric optic region[12,156,159,160].

Williams and Aldao also developed a model[161] able to predict the thermal radiation (Equation (2.27)). They modeled the polymer foam such as a set of *n* layers placed between two black-bodies at different temperatures. The number of layers is given by the relation of the polymer foam thickness (L), the cell size (ϕ), and the thickness of the polymer layer (δ) ($n=L/(\phi+\delta)$). Then, taking into account the net fraction of the radiation energy transmitted (T_N) through a single layer of thickness δ is possible to obtain the thermal radiation according to Equation (2.27).

$$\lambda_r = \frac{4\sigma T^3 L}{1+\left(\frac{L}{\phi}\right)\left(\frac{1}{T_N}-1\right)} \tag{2.27}$$

For nanocellular polymers, recent theoretical models proposed by Wang et al.[126] and Buahom et al.[156] assumed Mie scattering to deal with radiation. They showed that the contribution of radiation to the total thermal conductivity is more significant in a nanocellular polymer than in conventional or microcellular polymers due to a change in the scattering mechanism. For instance, in the Rayleigh scattering regime, the fraction of scattered radiation is reduced, and further, there is a strong dependency between the cell size, walls, and struts (acting as scattering centers) and the wavelength of the electromagnetic wave[162,163]. Experimentally, Bernardo et al.[160] proved a reduction of the scattered radiation in nanocellular polymers. They determined for the first time the scattering extinction coefficient for nanocellular PMMA by measuring the transmittance in the infrared region of microcellular and nanocellular PMMA (cell sizes from 14 nm to 20 μm) with a constant density of around 500 kg/m^3. A change in the relation between the scattering extinction coefficient and the cell size was observed for cell sizes around 1 μm (1/10 of the infrared wavelength at room temperature, which is centered at 10 microns). Therefore, they concluded that the scattering due to the cellular structure must be considered for larger cell sizes but it can be neglected for very small cell sizes (smaller than 200 nm). However, the density of the samples considered in that work was high, so the absorption contribution could not be measured.

In aerogels, such behavior is also usually reported. For instance, Heinemann et al.[164] did not observe differences between aerogels with different densities and the bulk material extinction coefficient, meaning that the scattering through the pores (characteristic pore size of 180 nm) is null. Meanwhile, Hrubesh et al.[120] claimed that the radiation contribution in aerogels was only associated with the absorption of the solid material, assuming that there is no scattering due to the reduced pore size. In those works, is usually to find Equation (2.28) to describe the radiation, which depends on the relative density and the extinction coefficient of the solid (i.e., scattering is neglected).

$$\lambda_r = \frac{16n^2\sigma T^3}{3\rho_r K_s} \tag{2.28}$$

CHALLENGE

Therefore, taking into account the results for aerogels, the previous theoretical works, and the experimental evidence, the radiation term in nanocellular polymers must be for sure different than that of conventional or microcellular polymers. However, up to date, there are not any works related to the experimental obtention of the extinction coefficient of low-density nanocellular polymers to prove the dependence with the cell size and the weight of the radiation term in the total thermal conductivity.

This thesis aims at deepening into this mechanism by measuring K_e of low-density nanocellular polymers for the first time (**Chapter 4**).

Finally, one interesting possibility to reduce the radiation contribution in cellular polymers is the addition of opacifiers or infrared radiation blockers (IR-blockers) to the polymer matrix. This is a well-known strategy for conventional cellular polymers[110,165] but this has not been studied for nanocellular polymers. An opacifier is a material that strongly absorbs or scatters infrared radiation, increasing the extinction coefficient and thus reducing heat transfer by radiation. Some examples of IR-blockers are used in the literature, such as carbon-based materials (multiwalled nanotubes, carbon black nanoparticles, graphite, graphene), titanium(IV) oxide (TiO_2), or aluminum oxide (Al_2O_3) [110,119,121,166,167].

CHALLENGE

The addition of IR-blockers in nanocellular polymers can modify the foaming process, affecting the cellular structure and even leading to higher densities[168]. The IR-blockers need to be in the nanometric range if they are incorporated into the solid formulation to prevent the appearance of large cells. In addition, the dispersion of the opacifiers in the polymer matrix before foaming is also a challenge because high shears are required during the extrusion process to avoid their agglomeration[168]. Furthermore, the process becomes more challenging as the percentage of IR-Blocker on the polymer matrix increases. Then, there is a need to find a way to introduce IR-blockers into nanocellular polymers in an easy way without affecting the cellular structure.

This is also one of the topics that would be covered in the present work (**Chapter 4**).

2.2.2.2. Research on the thermal conductivity of nanocellular polymers: theoretical works and experimental data

In the early years of the development of nanocellular polymers, it was claimed several times that they could be potentially used as advanced thermal insulators when combining low-densities and nanometric cell sizes, but no experimental data supported these claims[80–82]. Nowadays, the production and proper characterization of the thermal conductivity of these materials is still a

challenge due to the difficulty of combining nanometric cell sizes with very low densities[17], and because the production of samples with large dimensions is also complex since fabrication processes are mainly limited to the lab-scale[18]. For these reasons, many authors have tried to theoretically predict the thermal properties of these materials[82,126,156,160,169]. **Table 2.1** summarizes the hypothesis and predictions of the main theoretical models regarding the thermal conductivity of nanocellular polymers. For instance, Forest et al.[82] proposed an analytical model derived from aerogel studies. This model predicted thermal conductivities as low as 12 mW/(m·K) for nanocellular materials with relative densities between 0.1 - 0.2 and cell sizes around 100 nm at 27 ºC (300 K)[82]. Meanwhile, Wang et al.[126] mathematically modeled the thermal transport through a nanocellular polymer. Their model proposed that the contribution of the radiation term starts to be quite significant in nanocellular polymers with low densities. They predicted that the minimum conductivity that can be reached with these materials is not as low as expected (**Table 2.1**). Later, Bernardo and coworkers[160] proved that the transmittance of infrared radiation significantly increases when the cell size is reduced to the nanometric range. As a consequence, low-density nanocellular polymers combine low conduction through the gas phase with a high radiation contribution, leading to a compromise between cell size and density to obtain the best results. Finally, Buahom et al.[156] also developed a mathematical model to predict the thermal conductivity of microcellular and nanocellular polymer foams. They predicted the thermal conductivity of PS and PMMA foams with different relative densities and cell sizes. Particularly, they predicted a minimum of 37 mW/(m·K) for nanocellular PMMA with 0.1 of relative density and 100 nm of cell size at 27 ºC (300K)[156]. Both theoretical models[126,156] provided useful insights into the mechanisms acting during heat transfer in these materials. However, those models were only validated using medium and high-density samples.

Table 2.1. Theoretical models hypothesis and predictions regarding the thermal conductivity of nanocellular polymers.

Author	Conduction through the solid phase	Conduction through the gas phase	Radiation	Predictions at 300 K
Sundarram et al.[170] (2013) Finite element analysis and molecular dynamics simulation methods.	Finite Element Model (FEM) for microcellular polymers. Molecular Dynamics (MD) simulation for nanocellular polymers. Knudsen effect is included in MD simulations. $\lambda_g = \frac{\lambda'_{g0}(1-\rho_r)}{1+\frac{2\beta}{\phi}\frac{RT}{\sqrt{2}\pi d_m^2 N_A p}}$			15 mW/(m·K) for nanocellular PEI with relative density of 0.2 and 100 nm of cell size.
Forest et al.[82] (2015) Model derived from aerogels to predict the thermal conductivity of PS.	Empirical model from aerogels $\lambda_s = C\rho_r^{1.88}$	Knudsen effect $\lambda_g = \frac{\lambda'_{g0}(1-\rho_r)}{1+\frac{2\beta}{\phi}\frac{RT}{\sqrt{2}\pi d_m^2 N_A p}}$	Rosseland equation applied to aerogels $\lambda_r = \frac{16n^2\sigma T^3}{3\rho_r K_s}$ Where K_s is the extinction coefficient of the solid polymer	Minimum of 12 mW/(m·K) for nanocellular PS with relative densities between 0.1-0.2 and 100 nm of cell size, considering K_s=500 cm^{-1}.
Wang et al.[126] (2017) Association of resistances (solid in walls and struts and gas) to describe the conduction through the solid and gas phases.	Effective thermal conductivity of the solid that constitutes the cell walls and struts using the kinetic theory $\lambda'_{s\_eff} = \lambda'_s\left(1+\frac{l}{\delta}\right)^{-1}$	Knudsen effect $\lambda_g = \frac{\lambda'_{g0}(1-\rho_r)}{1+\frac{2\beta}{\phi}\frac{RT}{\sqrt{2}\pi d_m^2 N_A p}}$	Williams and Aldo equation using Mie theory to determine T_N $\lambda_r = \frac{4\sigma T^3 L}{1+\left(\frac{L}{\phi}\right)\left(\frac{1}{T_N}-1\right)}$	Minimum of around 25-35 mW/(m·K) for nanocellular polymers (100-1000 nm) with relative densities between 0.05 and 0.2, without considering high radiation absorption by the polymer.
Bernardo et al.[132] (2019) Association of cells depending on their cell size to describe bimodal cellular structures with medium/high densities.	$\lambda_s = g\lambda'_s\rho_r$ With g=1 obtained from experimental results	For cells larger than 7 µm: $\lambda_g = \lambda'_{g0}(1-\rho_r)$ For cells smaller than 7 µm: Knudsen effect $\lambda_g = \frac{\lambda'_{g0}(1-\rho_r)}{1+\frac{2\beta}{\phi}\frac{RT}{\sqrt{2}\pi d_m^2 N_A p}}$	Considered to be negligible because of the medium/high densities	32 mW/(m·K) for nanocellular PMMA with relative density of 0.2 and 100 nm of cell size.
Bernardo et al.[160] (2020) Model of the thermal conductivity including the radiation contribution using a semi-empirical equation.	$\lambda_s = g\lambda'_s\rho_r$ With g=2/3 assuming close-cell low-density foams	Knudsen effect $\lambda_g = \frac{\lambda'_{g0}(1-\rho_r)}{1+\frac{2\beta}{\phi}\frac{RT}{\sqrt{2}\pi d_m^2 N_A p}}$	Rosseland equation using a semi-empirical K_e $\lambda_r = \frac{16n^2\sigma T^3}{3K_e}$ $K_e = K_S\rho_r + A\left(\frac{6}{\pi\phi^3}(1-\rho_r)\right)^{1/3}\phi^B$ Where K_S is the extinction coefficient of the solid polymer, and A and B are constants	Minimum of 24 mW/(m·K) for nanocellular PMMA (0.05 of relative density and 70 nm) considering K_S=140 cm^{-1}. Minimum of 15 mW/(m·K) for nanocellular PMMA with relative densities between 0.02-0.03 and 50 nm of cell size, considering K_S=600 cm^{-1}.
Buahom et al.[156] (2020) Association of resistances (solid in walls and struts and gas) to describe the conduction through the solid and gas phases.	Effective thermal conductivity of the solid that constitutes the cell walls and struts using the kinetic theory $\lambda'_{s\_eff} = \lambda'_s\left(1+\frac{l}{\delta}\right)^{-1}$	Knudsen effect $\lambda_g = \frac{\lambda'_{g0}(1-\rho_r)}{1+\frac{2\beta}{\phi}\frac{RT}{\sqrt{2}\pi d_m^2 N_A p}}$	Rosseland equation using Mie theory to determine K_e $\lambda_r = \frac{16n^2\sigma T^3}{3K_e}$	Minimum of 37 mW/(m·K) for nanocellular PMMA (0.1 of relative density and 100 nm). Minimum of 48 mW/(m·K) for nanocellular PS (0.1 of relative density and 1000 nm).

Regarding experimental results of the thermal conductivity of nanocellular polymers, **Figure 2.13** collects all the experimental data points of the thermal conductivity of nanocellular polymers reported by the moment this research was finished. In the legend of this figure, the technique used to measure the thermal conductivity is included. Cell sizes up to 5 microns are included in this state review for the sake of comparison with the results of this thesis. It is observed that there is a lack of data because only a few works measure their thermal conductivity[4,9,30,52,70,110,119,132]. Furthermore, most of the results are measured by the Transient Plane Source method (TPS). As previously commented, TPS is a transient technique that allows measuring samples with small dimensions but its accuracy for thermal insulating materials is not clear [97–99].

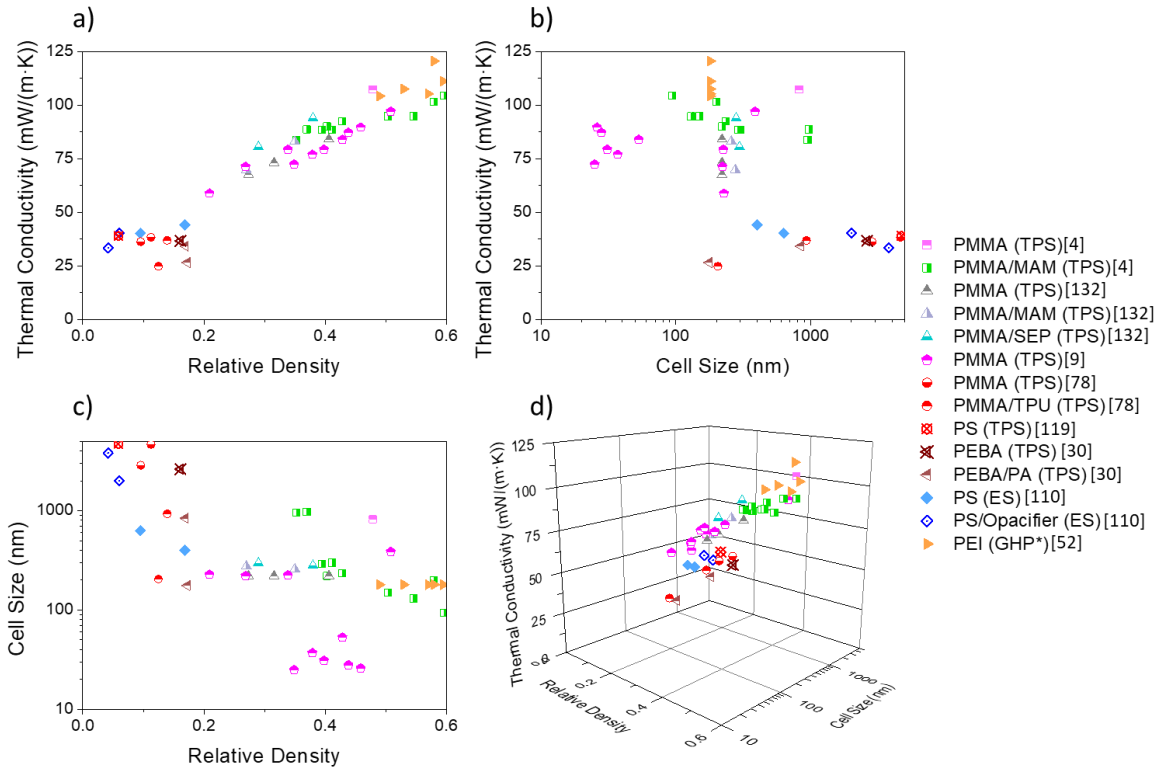

Figure 2.13. Experimental research on the thermal conductivity of nanocellular polymers: a) thermal conductivity – relative density, b) thermal conductivity – cell size, c) cell size – relative density, and d) Thermal conductivity – cell size – relative density 3D map.

For instance, Wang et al.[70] reported a super insulating nanocellular poly(methyl methacrylate)/thermoplastic polyurethane (PMMA/TPU) foam (24.8 mW/(m·K) of thermal conductivity) characterized by a relative density of 0.125 and 205 nm of cell size. Note that this value is below the air thermal conductivity, which is around 26 mW/(m·K) at 20 ºC. However, as already mentioned, the same authors theoretically predicted that such a low thermal conductivity cannot be reached for nanocellular PMMA[126,156]. The same research group also reported a polyether block amide/polyamide (PEBA/PA) foam with 26.5 mW/(m·K) (relative density of 0.17 and 180 nm of cell size)[30]. Apart from these results, there are no more data for low-density

nanocellular samples measured by TPS, but there are some data in the medium/high-density range. Notario et al.[4], Bernardo et al.[132] and Martin-de-León[9] studied samples with relative densities over 0.20. They obtained values of 60-100 mW/(m·K) for cell sizes between 20-1000 nm. Regarding the more reliable data (measured by a steady-state technique), Almeida et al.[110] studied the thermal conductivity of nanocellular polystyrene PS (relative density of 0.1 and 630 nm of cell size) obtaining 40.2 mW/(m·K). To measure the thermal conductivity, they employed a heat flow meter-based technique by using external sensors (ES) to measure the heat flux. Meanwhile, Zhou et al.[52] used a homemade guarded hot plate (GHP*) to study nanocellular polyetherimide (PEI) (relative density ranging 0.5-0.6 and cell sizes of around 45 nm), obtaining thermal conductivities between 105-120 mW/(m·K).

CHALLENGE

Therefore, the lack of thermal conductivity results regarding nanocellular polymers, particularly low-density range (**Figure 2.13**), with discrepancies between the steady-state measurements of Almeida et al.[110], the theoretical models of **Table 2.1**, and the TPS data, make it necessary to further study the thermal conductivity of low-density nanocellular polymers. Then, there is a need of:

- Thermal conductivity data measured using reliable techniques for thermal insulation materials.
- A model to correctly predict the experimental results and evaluate the potential and limitations of these novel materials.

This thesis aims at facing this challenge together with the development of the methodology to obtain these results (**Chapter 4** and **Chapter 3**, respectively).

Finally, based on the experimental and theoretical evidence, the question is now: are nanocellular polymers interesting to be used as thermal insulators? To answer this question, we need to understand the current state of the art of thermal insulating materials. Due to this, the next section seeks to provide a brief overview of the thermal insulators commonly used in the building sector.

2.2.3. Overview of thermal insulators

Currently, the materials commonly used in the building sector are characterized by thermal conductivities in the range from 4 to 60 mW/(m·K)[83,84,170,171]. Within the wide spectrum of thermal insulators, **Figure 2.14** shows a selection of the most frequently used materials in the building sector. The density of these materials is summarized in **Figure 2.15a**[84]**.** Derived from volcanic rock, expanded perlite is a natural, lightweight, inert, and fireproof rock. It shows conductivities around 46 mW/(m·K) and a density of 115 kg/m^3, being commonly used in cryogenic systems, mortars, and refractory elements. Meanwhile, recycled textile and mineral wool (which include rock or glass wool) are made of fibers. They are characterized by thermal conductivities ranging from 31 to 42 mW/(m·K) and they are usually employed in construction, their density range

is between 15-200 kg/m^3. Regarding the thermal insulators based on polymers, expanded polystyrene (EPS) and extruded polystyrene (XPS) are thermoplastic thermal insulators (can be recycled), whereas rigid polyurethane (PUR), polyisocyanurate (PIR), and phenolic foams are thermosets (obtained after a chemical reaction and cannot be recycled). They are conventional cellular polymers, presenting cell sizes larger than 10 µm, typically above 100 microns. EPS and XPS have thermal conductivities in the range of 31-38 mW/(m·K), whereas PUR, PIR and phenolic foams exhibit thermal conductivities from 24 to 35 mW/(m·K). This is because the gases within the cellular structure of these thermoset foams have lower thermal conductivity than that of the air. These gases tend to escape from the cellular structure via diffusion which leads to an aging process, increasing the thermal conductivity over time. EPS, XPS, PUR, and PIR present a density in the range of 25-35 kg/m^3 whereas phenolic foams density is usually higher (100 kg/m^3). Finally, aerogels and vacuum insulation panels (VIPs) are advanced super-insulators (thermal conductivity lower than that of air, which is around 26 mW/(m·K) at 20 ºC). These materials show conductivities of 10 mW/(m·K) and lower. Aerogels present a density in the range of 75 to 150 kg/m^3, meanwhile VIPs density is around 200 kg/m^3. They both are nanostructured materials usually silica-based. They arose with the aim of taking advantage of the Knudsen effect to reduce the gas contribution to the total thermal conductivity (**Figure 2.11**). Particularly, in VIPs, as it will explained in the next section, the conduction though the gas phase is null after evacuating an open porous material (core) placed inside a gas barrier envelope. Despite their good performance, the use of aerogels and VIPs is yet not widespread due to their high price and other technical reasons.

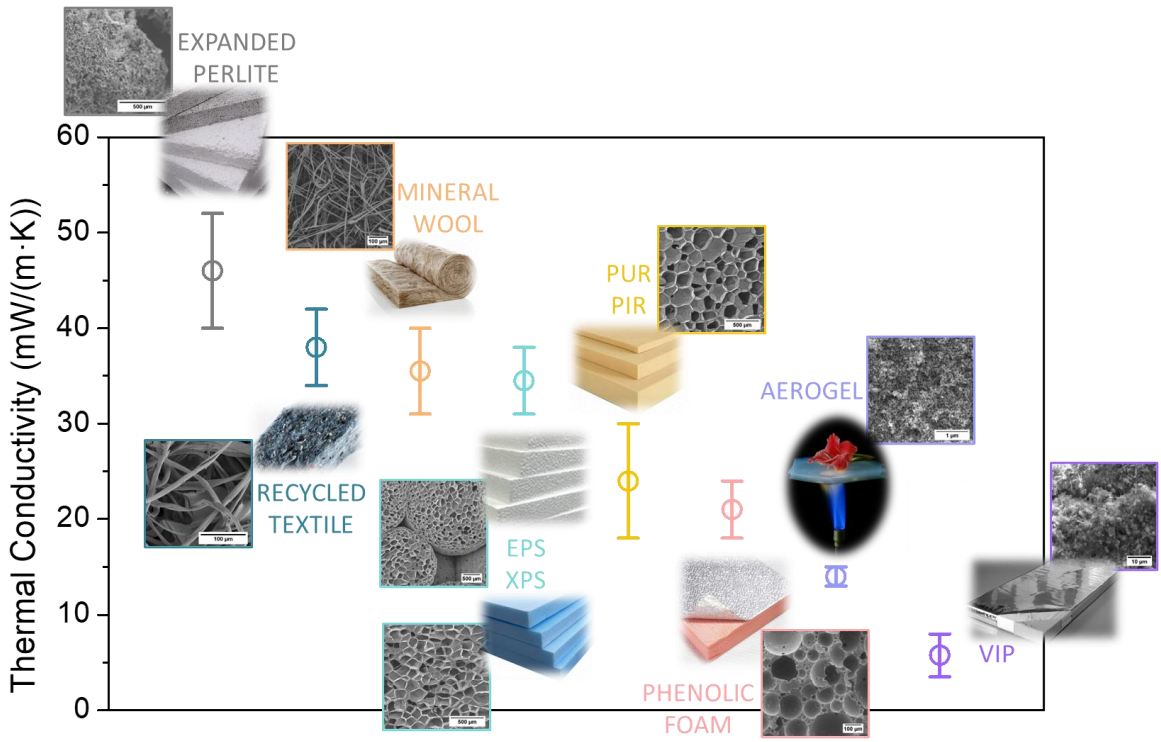

Figure 2.14. Thermal insulation performance of different thermal insulators.

Finally, a comparison of the necessary insulation thickness to achieve a *U-Value* of 0.2 W/(m²·K), is presented in **Figure 2.15b**. As previously commented, to reduce the *U-value* there are two possible routes: increasing the thickness of the insulation layer using conventional insulation materials or developing new thermal insulators with lower thermal conductivity. For instance, to achieve a *U-Value* of 0.2 W/(m²·K) the insulation thickness is 170 mm when using XPS (a conventional thermal insulator characterized by thermal conductivities in the range 31 to 38 mW/(m·K)). Meanwhile, if using an advance thermal super-insulator, like a VIP (thermal conductivity of 6 mW/(m·K)), the insulation thickness is reduced to 30 mm.

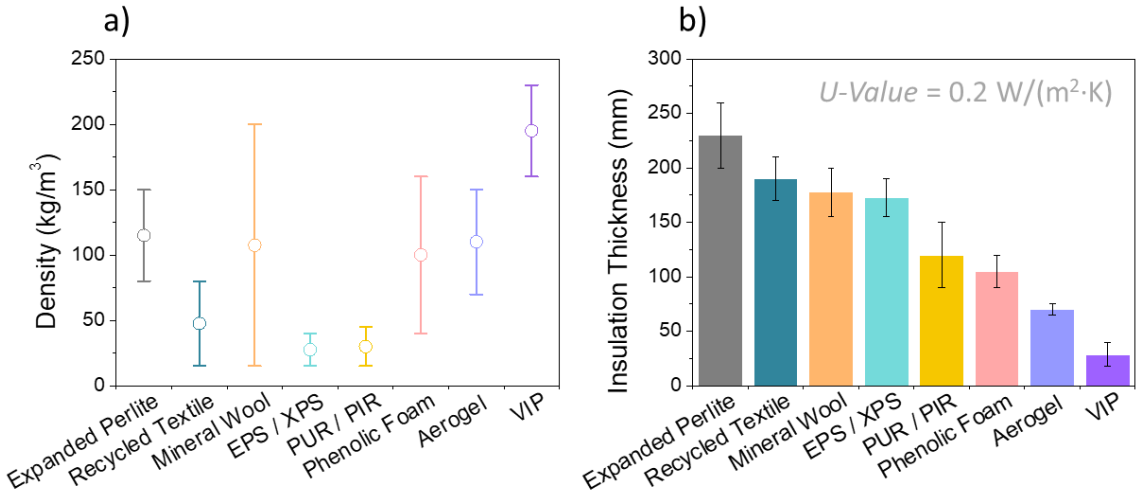

Figure 2.15. a) Density and b) insulation thickness to achieve a *U-Value* of 0.2 W/(m²·K) of different thermal insulators.

From this analysis of the current thermal insulation market, it can be concluded that aerogels and VIPs are the best materials, despite their higher density. The great performance is mainly due to two facts: they present a pore size in the nanoscale but also a discontinuous structure (**Figure 2.7b**). Nanocellular polymers are characterized by pore sizes in the range of these super-insulators and can be produced with similar density, but they present a continuous solid phase. Theoretical and experimental studies using steady-state measurements seem to point out that nanocellular polymers cannot reach the very low thermal conductivities of aerogels and VIPs. However, they do present Knudsen effect, their fabrication process is easier to scale-up than that of aerogels, and they allow producing cheaper and more sustainable materials.

Therefore, one of the main concepts of the present thesis arose from the analysis of the state of the art and the challenges identified so far in the field of nanocellular polymers: ***there is a chance to further boost the insulation performance of nanocellular polymers by creating a discontinuous solid phase. This can be achieved by milling the bulk nanocellular polymer and obtaining a micrometric powder that could be potentially used to generate VIP materials, the best thermal insulators currently in the market.***

In the following sections, VIPs are presented and the main features to characterize their structure and thermal conductivity are described.

2.3. Vacuum Insulation Panels (VIPs)

Vacuum insulation panels (VIPs) exhibit the lowest thermal conductivity in the market (as low as 4 mW/(m·K)) and represent one of the most promising high-performance thermal insulation materials[145]. A VIP can be described as an evacuated open porous material (core) placed inside a gas barrier envelope (**Figure 2.16**). In addition, a protective fleece is usually used to protect the core and improve handling in the case of compressed powders and fiber cores. Once the core is evacuated the envelope needs to be sealed to maintain the inner vacuum. As will be explained in the following sections, the thermal conductivity of vacuum insulation panels highly depends on the inner pressure. As pressure raise due to aging or puncturing the envelope, the thermal conductivity increases, so they are fragile materials that need special care during installation and use. This, together with their high cost and the thermal bridges that appear between two adjacent panels are the main drawbacks of VIPs. However, they are up to date the best super-insulators, showing thermal conductivities 9 times lower than mineral wool or conventional cellular polymers such as XPS (**Figure 2.14**).

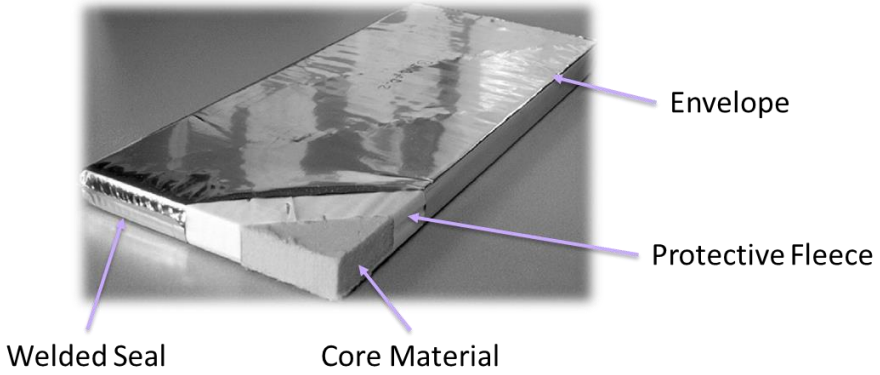

Figure 2.16. VIP scheme.

2.3.1. History of VIPs

In 1643, as a result of Evangelista Torricelli's theories of atmospheric pressure, the first vacuum atmosphere was obtained. However, the concept of vacuum thermal insulation was used for the first time in 1892 when Sir James Dewar first developed Dewar's flask to keep the gases cold enough to remain liquid. The first patent for vacuum insulation (German patent no. 516377) was granted by the German Reichspatentamt to O. Hemman of Sterchamolwerke, Dortmund in 1930[172]. This patent describes in a rather vague manner the advantages of a rubber-enclosed evacuated porous body[173]. The earliest precise idea of vacuum insulation panels was patented by Bovenkerk in 1955 (US Patent 2700633) in which a glass fiber core was enclosed into a welded steel foil[174]. Nanostructured cores were first described in the US Patent no. 3151365 from 1964, granted to the

inventors P.E. Glaser, A.G. Emslie, and W.A. Salmon of Arthur D. Little Company, Cambridge[175]. The development of VIP continued with experiments with different core materials and envelope techniques[173,176]. The first commercial use of vacuum insulation panels was in 1970 for its use in refrigerators, freezers, and cold shipping boxes. Meanwhile, in 1999 VIPs were first used for building applications[173]. The global vacuum insulation panel market reached a value of US$ 8.21 Billion in 2021 (around 16% of the thermal insulation market), and it is expected to reach a value of US$ 11.29 Billion by 2027, exhibiting a growth rate (CAGR) of 5.10% during 2022-2027[177,178].

2.3.2. VIPs core

The core is the inner part of a VIP as shown in **Figure 2.16**. It is fabricated from porous material and its function is to physically support the VIP envelope and provide superinsulation performance. By using porous materials such as open cell foams, powders, and fibers the heat transfer through the gas phase is suppressed when vacuum is applied, as previously commented. **Figure 2.17** shows the effect of the internal pressure on VIPs cores made of several materials. As previously commented when describing nanocellular polymers, the thermal conductivity reduction is significantly affected by effective pore size and the overall porosity of the core material. The effective pore size is equivalent to the cell size in cellular polymers, but due to the different configurations of the systems (fibers or aggregates of nanoparticles), the effective pore size is a useful parameter used by the researchers to characterize these materials, as it will be commented later. The materials usually used as core materials are based on fumed/precipitated silica (~200 kg/m^3), silica aerogel (~180 kg/m^3), glass fibers (~250 kg/m^3), and open cell rigid polyurethane foams (PUR) (~65 kg/m^3)[179]. The main drawback of open cell PUR and glass fiber cores is their large effective pore size (higher than 40 μm) requiring high vacuum (lower than 0.1 mbar) to reduce the thermal conductivity to very low values (**Figure 2.17**). However, glass fibers are usually used to reinforce the mechanical properties of fumed silica cores[179–181]. Regarding fumed silica and silica aerogel, the thermal transport through the gas phase is negligible for pressures lower than 50 mbar because of their small pore size (in the order of 20-100 nm) (effective pore size smaller than 500 nm)[110,179,182]. Precipitated silica is characterized by a slightly higher pore size than fumed silica but still provides good performance. Nevertheless, the main drawback of nanoscale silica materials is their high price[183,184].

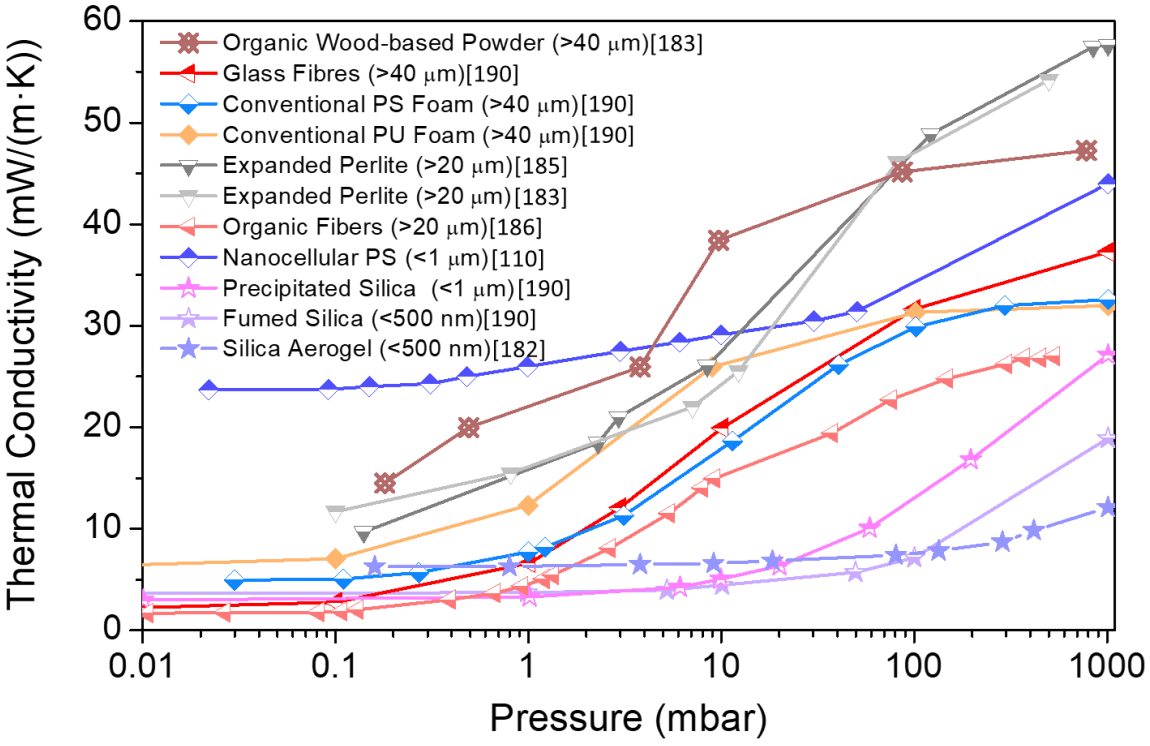

Figure 2.17. Effect of internal pressure on the thermal conductivity of several VIPs cores. Estimations of the effective pore size are also included.

Thus, the current research is focused on alternative low-cost core materials. For instance, Almeida et al.[183] studied expanded perlite and an organic wood-based powder. They obtained thermal conductivities around 60 mW/(m·K) at ambient pressure and 10 mW/(m·K) at 0.1 mbar for expanded perlite and thermal conductivities around 50 mW/(m·K) at ambient pressure and 15 mW/(m·K) at 0.1 mbar for the organic wood-based powder. Similar results were obtained by Verma et al.[185] for expanded perlite. However, the large effective pore size (higher than 20 μm) makes difficult its use as VIP core. Nemanič et al. used organic fibers to produce a core material obtaining thermal conductivities of 27 mW/(m·K) at ambient pressure and of 2 mW/(m·K) at 0.1 mbar[186]. Another interesting approach to reduce the core material cost is fabricating hybrid core materials by mixing fumed silica with low-cost materials (such as organic wood-based powder[183], hollow glass microspheres[187], rice husk ashes[188], and expanded perlite[183,189]). With this approach, intermediate results are obtained (following the rule of mixtures).

Nanocellular polymers have been also studied to be used as core materials for VIPs. Almeida et al.[110] produced nanocellular PS, but, despite the reduced cell size, the thermal conductivity results were worse than those obtained for conventional PS foam (**Figure 2.17**) due to the higher density (180 vs 44 kg/m^3). Also, note that despite presenting a similar density to that of fumed silica, the thermal conductivity at vacuum of the nanocellular PS is much higher (24 vs 4 mW/(m·K)). Then, the continuous cellular structure of nanocellular polymers leads to a larger contribution of the conduction through the solid phase, resulting in higher thermal conductivities

even under vacuum. This again points out the need of creating a discontinuous structure to reduce thermal conduction of these materials and allow their use as super-thermal insulators, such as core materials for VIPs.

2.3.3. VIPs envelope

The envelope is the external cover that contains the VIP core, protecting the VIP from air and water transmission and providing mechanical strength to withstand atmospheric pressure and handling stresses during transportation and installation. One of the major reasons why VIPs lose their thermal insulation performance during their lifetime is the permeation of air and water vapor through the VIP envelope. Therefore, the lifetime performance of VIPs highly depends on the gas barrier properties of the envelope. The key requirements for the development of a barrier envelope are[145,190,191]:

- Low permeation of water vapor transmission rate (WVTR) (below 10^{-2} g/(m^2·day)).
- Low air transmission rate (ATR) (below 10^{-2} cm^3/(m^2·day)).
- Sufficiently low thermal conductivity to avoid thermal bridges at the panel edges.
- Flexible and mechanically stable against handling stresses.

A typical VIP envelope (**Figure 2.18**) consists of three material layers, an outer protective layer, a barrier layer (which may be made up of several layers), and an inner sealing layer, each layer has a different function[179,191,192].

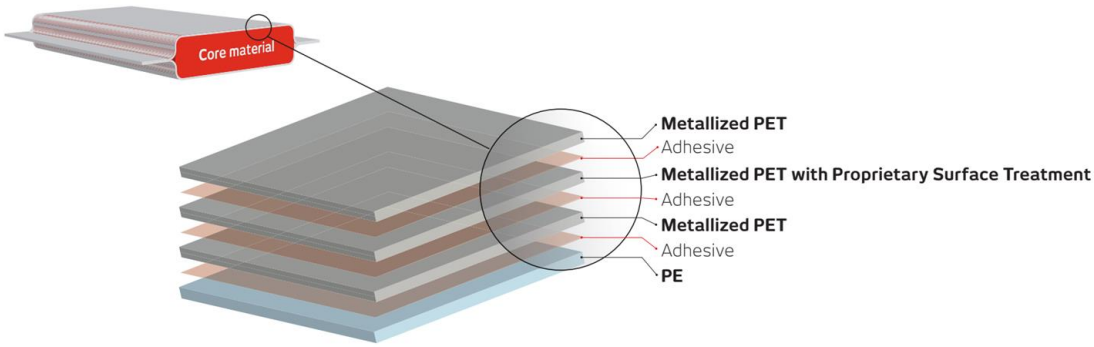

Figure 2.18. Scheme of the typical structure of a VIP envelope from[193].

The protective layer (outer layer) protects the VIP from environmental and handling stresses. Polyethylene terephthalate (PET) is usually used as a protective layer due to its low cost and good barrier properties (**Figure 2.19**). Meanwhile, the barrier layer (middle layer) protects the VIP against water vapor and air transmission through the envelope. This layer may be an aluminum foil with a thickness of up to 10 µm (AF) or a metalized multilayer laminate (MF). MFs have up to three aluminum-metalized PET or polypropylene (PP) sheets (the coating is performed with aluminum with a thickness of 20–100 nm) (**Figure 2.19**). The reduced total metal layer thickness of MFs compared to AFs leads to reduced thermal bridges when VIPs are installed. However, MFs

lead to faster moisture and air permeation through the VIP envelope. Hence, the thermal conductivity will increase much faster in VIPs with MF envelopes than with AF envelopes[145]. Proprietary Surfaces Treatments (PST) or the addition of a metalized ethylene vinyl alcohol copolymer (EVOH) layer are usually used to reduce the gas permeation, improving the behavior of MFs[193,194]. Polyurethane (PU) is employed as an adhesive between layers. Finally, the sealing layer (inner layer) seals the core material in the envelope and traditionally consists of low- or high-density polyethylene (LDPE or HDPE) (**Figure 2.19**). To seal the envelope, the film surfaces are heated by two hot bars under pressure to bond together the two layers of the envelope.

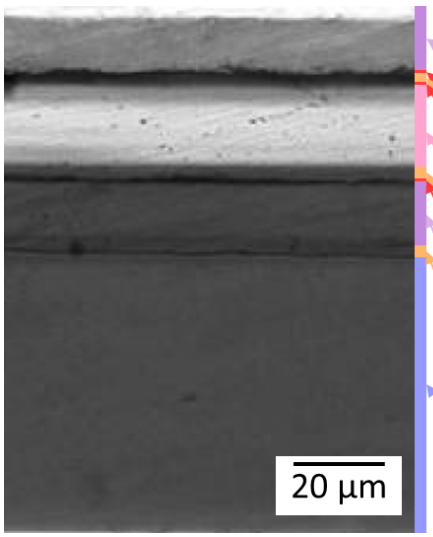

LAYER	MATERIAL	FUNCTION	THICKNESS	
1	PET	Protective Layer Substrate for 2	12 µm	PETmet
2	AL	Barrier Layer	30 nm	
3	PU	Adhesive	2 µm	
4	ALU	Barrier Layer	30 nm	PPmet
5	PP	Substrate for 4	18 µm	
6	PU	Adhesive	2 µm	
7	AL	Barrier Layer	30 nm	PETmet
8	PET	Substrate for 7	12 µm	
9	PU	Adhesive	2 µm	
10	LDPE	Sealing Layer	60 µm	

Figure 2.19. SEM visualization of a metalized multilayer laminate for use as a VIP envelope (adapted from[190]).

2.3.4. Thermal transport in VIPs

The overall thermal transport in VIPs (λ_t) can be described as a function of conduction through the solid phase (λ_s), conduction through the gas phase (λ_g), thermal radiation (λ_r), convection (λ_c), and coupling effect (λ_{coup}) as shown in Equation (2.29)[191].

$$\lambda_t = \lambda_s + \lambda_g + \lambda_r + \lambda_c + \lambda_{coup} \quad (2.29)$$

Since the core of VIPs can be considered as a porous material, the equation is similar to that presented for nanocellular polymers (Equation (2.10)) but includes the coupling effect, which is negligible for foams with a continuous solid phase[173,195–197]. In the next sections, the specific equations usually found in the literature to evaluate the different heat transport mechanisms in VIPs are presented.

Conduction through solid

Solid conduction is the dominant mode of heat transfer under evacuated conditions (**Figure 2.17**) in the core material since radiation is usually suppressed by the addition of IR-Blockers, as will be

discussed below. The equations presented for the conduction through the solid phase for nanocellular polymers (Equations (2.12), (2.16), and (2.17)) are also used for VIPs[110,191,196,198]. Normally, the contribution of the conduction through the solid phase in VIPs ranges between 1-5 mW/(m·K)[110,199]. Note that these values are far from the obtained by Almeida et al. for nanocellular PS (18 mW/(m·K))[110]. In the case of powders and fibers, it is very difficult to theoretically calculate the exact solid conduction due to the uneven particle size and the random arrangement. In those systems, the conduction through the solid phase is mainly determined by the size of the contact points between particles. Thus, many authors employ models based on the Hertz contact theory to calculate the solid thermal conductivity[138,197,199,200]. However, the contact resistance is not easy to characterize, depending on Poisson's ratio (v), Young's modulus (E), the radius of the particles, and the effective pressure load (p_{load}).

Conduction through gas

The conduction through the gas phase can be calculated using Equation (2.19) and Knudsen effect, observing the same effects for the pore size and the pressure dependencies. This is the main principle of vacuum insulation panels wherein a highly open porous material is evacuated to low pressure (in the range of 0.01–10 mbar). Therefore, due to the suppression of gas conduction when performing vacuum, the effective thermal conductivity of an evacuated porous material is highly reduced compared to its un-evacuated state. Furthermore, as the cell size is reduced, the required vacuum to fully evacuate is lower. For instance, as previously commented (**Figure 2.17**), fumed silica and silica aerogel are characterized by effective pore sizes smaller than 500 nm, requiring pressures around 50 mbar to be fully evacuated. Meanwhile, open cell PUR and glass fibers (effective pore size higher than 40 μm) require pressures of 0.1 mbar to be fully evacuated. Thus, nanoporous materials are preferred since in materials with large cell/pore sizes the vacuum required is too extreme, being more sensitive to pressure changes (aging).

Instead of using Equation (2.19) is usual to find Equation (2.30) in research papers concerning VIPs to characterize the thermal conductivity drop due to vacuum and the effective pore size (ϕ)[110,145,190,196,199–203]. $p_{1/2}$ is the gas pressure where the contribution of the gas phase is reduced to half, and it is related to the effective pore size according to Equation (2.31) at 300K[196]. Therefore, the Knudsen equation in this format is a useful tool to obtain the effective pore size by studying the material at different vacuums since the characterization of this parameter is quite difficult in powders and fibers.

$$\lambda_g = \frac{\lambda'_{g0}}{1 + \frac{p_{1/2}}{p}} \tag{2.30}$$

$$p_{1/2}(mbar) = \frac{230\ mbar}{\phi\ (\mu m)} \tag{2.31}$$

Radiation

Radiation in VIPs cores is usually high (higher than 4 mW/(m·K) at 300 K [110]), due to their low density (conventional foams) and their nanostructure (fumed silica and silica aerogels). The equation presented for the radiation for nanocellular polymers (Equation (2.25)) is also used for VIPs. In particular, silica-based materials present low extinction coefficients because silica is a weak absorber in the near infrared[198,204,205], leading to radiation contributions around 5 mW/(m·K) at 300 K.

Therefore, opacifiers are usually added to the core to reduce the radiation contribution to values of around 1 mW/(m·K) at 300 K[200,201,204]. Note that since most of the core materials are powders or fibers, the addition of IR-Blockers is easier than for bulk nanocellular polymers. Carbon black, graphite, titanium (IV) oxide (TiO_2), aluminum oxide (Al_2O_3), and silicon carbide (SiC) are usually used. Such materials have different attenuation behaviors, for instance, carbon-based opacifiers reduce radiation mainly by absorption, whereas TiO_2 or SiC particles scatter and absorb radiation[201]. The addition of opacifiers reduces by 1-3 mW/(m·K) the thermal conductivity of fumed silica core[201,206,207]. Note that opacifiers typically have high solid thermal conductivity, meaning that increasing the opacifier content will lead to higher conduction through the solid phase. However, an insufficient amount of opacifier will lead to a slight reduction of radiative conductivity. Hence, there is an optimum opacifier mass proportion to achieve a minimum thermal conductivity in VIPs cores [110]. Also, there is an optimum opacifier size to maximize the IR extinction which also depends on the temperature[208–210]. As the temperature increases, the optimal opacifier diameter reduces, hence, a smaller opacifier size is more appropriate at high temperatures[209–211]. For instance, Wang et al.[209] reported the optimum opacifier particle size for SiC is 6 μm for temperatures lower than 500 K, 5 μm for temperatures between 500-800 K, and 4 μm for temperatures higher than 800 K. Meanwhile for carbon black the optimum particle size vary from 4 to 2 μm when the temperature increases from 300 to 800 K[209].

Coupling effect

The coupling thermal conductivity takes into account the interaction between the core particles and the gas[145,212]. This term is well known in nanoporous systems consisting of contact particles and it can have a significant contribution to the total thermal conductivity at ambient pressure, as shown schematically in **Figure 2.20c**[196,198,213]. For instance, for powders consisting of hard grains the values of the coupling effect can range between 20-30 mW/(m·K) at atmospheric pressure [204]. This additional heat transfer mechanism is negligible for foams with continuous cellular structures because the coupling effect is a result of the heat flow from one solid particle to another through the gas phase (**Figure 2.20a**). In vacuum it is negligible due to the lack of gas molecules (**Figure 2.20b**). The coupling effect arises due to a shorter path for the heat flow from one particle

to the other through the gas phase (**Figure 2.20**) when the heat resistance between two solid phases is lower by passing through a gas phase than the solid path[197].

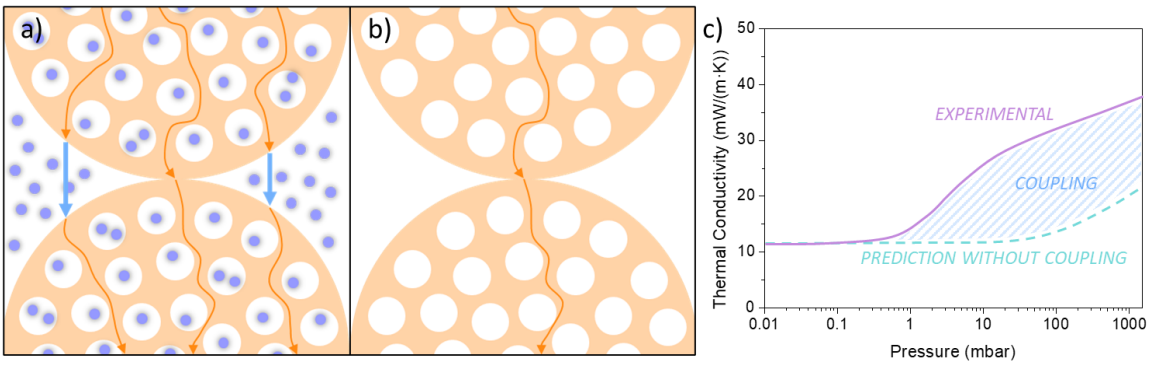

Figure 2.20. a) Scheme of the coupling effect at ambient pressure, where the structural thermal resistances are shorted by gas molecules (additional pathways occur), and b) scheme of solid-body conduction in porous powder materials at vacuum (adapted from[196]). c) Scheme of the effect of the coupling on the thermal conductivity as a function of pressure.

Some models to describe the coupling between the solid and gas phases have been proposed in most cases for silica aerogels[2,214]. In the simplest case, as proposed by Swimm et al.[195], it can be described as a series connection of thermal resistances between the solid (R_s) and the gas (R_g) phases (**Figure 2.21**). Using the general relation between the thermal resistance, the thermal conductivity and the thickness (Equation (2.7)), the following equation (Equation (2.32)) can be derived to describe the coupling. Where d_s and d_g are the thickness over which the heat is transferred within the solid and gas phases. The system is described in terms of a unit cell that contains all the information (the unit cell thickness is $d_{unit\ cell}$). In this model, all influencing parameters like the particle surface geometry near the area of particle-to-particle contact or the thermal conductivity of the solid are combined in one-factor *f*, which may be a function of the porosity of the material[197]. As the *f* factor is usually the only unknown parameter, it is obtained by solving the overall thermal conductivity equation and fitting the calculated data to the experimental data using the method of the least squares[197,213]. For instance, Sonnick et al.[197] obtained that f = -18.68 V_f + 17.94 (where V_f is the porosity, which ranges between 0.76 and 0.92) for a precipitated silica system. Therefore, f takes values from 3.74 to 0.75. Meanwhile, Swimm et al.[213] obtained f values of 1.73 to 2.25 for two organic aerogels (if doing a linear fit, f = - 26.00V_f + 22.01). Whereas Heinemann et al.[215] mentioned that for a bed of glass spheres f would be 7.

$$\lambda_{coup} = \frac{d_{unit\ cell}}{R_s + R_g} = \frac{d_s + d_g}{\frac{d_s}{\lambda_s} + \frac{d_g}{\lambda_g}} = \lambda_g \frac{\lambda_s (d_s + d_g)}{\lambda_g d_s + \lambda_s d_g} = \lambda_g \cdot f \qquad (2.32)$$

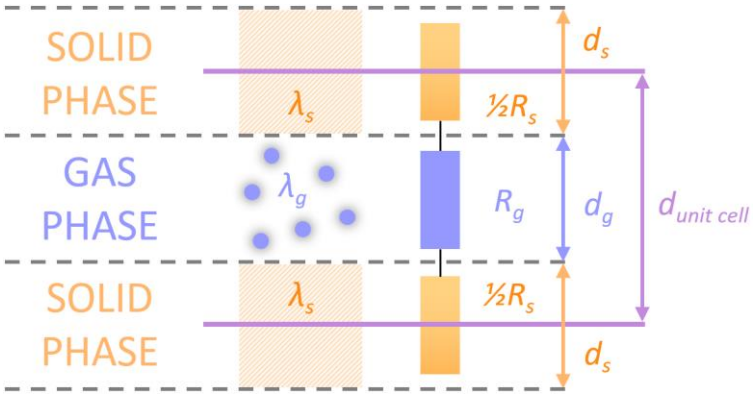

Figure 2.21. Simple resistance model to describe the coupling of solid and gas heat conduction (adapted from[195]). The violet lines indicate one unit cell.

2.3.5. Other effects affecting the thermal conductivity in VIP panels

There are other intrinsic effects affecting the thermal conductivity of VIPs, such as the thermal bridges through the envelope and the aging.

2.3.5.1. Thermal bridges

Thermal bridges, also known as linear thermal transmittance, occur at edges and corners of VIPs due to the higher thermal conductivity of the envelope with respect to the evacuated core, as shown schematically in **Figure 2.22a**[145,191]. Thermal bridges can be observed with infrared thermal imaging as shown in **Figure 2.22b**. Also, this technique allows the detection of damaged VIPs (**Figure 2.22b**). Due to this thermal bridge, the effective thermal conductivity (λ_{eff}) of the VIP is higher than the center-of-panel thermal conductivity (λ_{COP}) (Equation (2.33)).

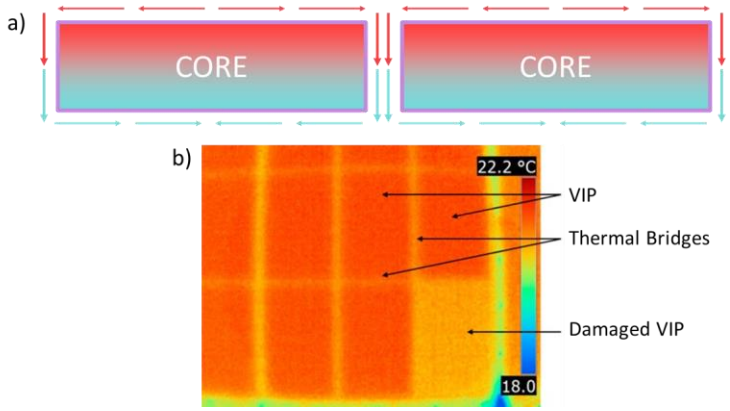

Figure 2.22. a) Scheme of thermal bridging in VIPs, and b) infrared thermal image of vacuum insulation panels (VIPs).

$$\lambda_{eff} = \lambda_{COP} + \Psi_{edge}\frac{P}{A} \tag{2.33}$$

λ_{COP} is given by Equation (2.29). The linear thermal transmittance (Ψ_{edge}) is a quantity describing the influence of a linear thermal bridge on the total heat flow. Ψ_{edge} depends on the panel (thickness

and thermal conductivity) and barrier film (thickness and thermal conductivity) properties. Note that depending on the envelope laminate layers and their thermal conductivity λ_{eff} may vary. Also, an increase in panel dimensions will lead to a decrease in the thermal bridging effect since the surface panel area (A) would be much higher than the perimeter (P).

2.3.5.2. Aging

The rise in thermal conductivity with time (aging) on VIPs depends on several factors[145,191,202]. As previously commented, the core properties (pore size) and the pressure play an important role in the VIP thermal conductivity (**Figure 2.11** and **Figure 2.17**). As the inner pressure increases, the thermal conductivity increases. The pressure at which the thermal conductivity sharply increases ($p_{1/2}$) increases as the pore size is reduced. Therefore, starting from the same inner pressure, the aging of VIPs made by materials with a smaller pore size (fumed silica or silica aerogels) would be slower than those cores characterized by large pore sizes (fibers or open cell PUR). Further, moisture inside the core material affects the thermal conductivity of VIPs. Both effects (an increase of pressure and moisture inside the VIPs) are determined by the barrier envelope properties for gas and water vapor, and the environmental conditions such as temperature and relative humidity.

Schwab et al.[216] developed an equation (Equation (2.34)) for predicting the thermal conductivity as a function of time for a fumed silica VIP core. They assumed the pressure and moisture contributions to be in a parallel resistance network. Therefore, the initial thermal conductivity was limited to only solid and radiative conductivity (λ_{evac}), whereas the thermal conductivity due to an increase in gas pressure ($p(t)$) and water content ($X_w(t)$) over time was added to calculate the time-dependent thermal conductivity. In Equation (2.34) b is the sorption isotherm constant.

$$\lambda(t) = \lambda_{evac} + \frac{\lambda'_{g0}}{1 + \frac{p_{1/2}}{p(t)}} + b \cdot X_w(t) \tag{2.34}$$

Therefore, the main drawback of VIPs is that their thermal conductivity increases over time due to a pressure rise. To counteract this effect and increase the expected service life of VIPs there are two possible routes. On the one hand, one possibility is the addition of desiccants (such as calcium oxide) and getters (like zeolites, activated carbon or metal alloys) to the core[179]. Desiccants are made of highly hygroscopic materials and work by entrapping moisture. Meanwhile, getters are highly porous structures with large surfaces and act by attracting and bonding with permeating gases to maintain a low pressure inside the panel. These materials will maintain the pressure inside the core until their capacity is reached. On the other hand, the solution is based on improving the VIPs' envelope and of course, as discussed before, a good way to improve the aging behavior is working with nanoporous cores in which the pressure needed to reach very low conductivities is higher.

References

[1] V. Kumar, N.P. Suh, A process for making microcellular thermoplastic parts, Polym. Eng. Sci. 30 (1990) 1323–1329. https://doi.org/10.1002/pen.760302010.

[2] Z.-Y. Li, C.-Y. Zhu, X.-P. Zhao, A theoretical and numerical study on the gas-contributed thermal conductivity in aerogel, Int. J. Heat Mass Transf. 108 (2017) 1982–1990. https://doi.org/10.1016/j.ijheatmasstransfer.2017.01.051.

[3] B. Notario, J. Pinto, M.A. Rodriguez-Perez, Nanoporous polymeric materials: A new class of materials with enhanced properties, Prog. Mater. Sci. 78–79 (2016) 93–139. https://doi.org/10.1016/j.pmatsci.2016.02.002.

[4] B. Notario, J. Pinto, E. Solorzano, J.A. de Saja, M. Dumon, M.A. Rodríguez-Pérez, Experimental validation of the Knudsen effect in nanocellular polymeric foams, Polymer (Guildf). 56 (2015) 57–67. https://doi.org/10.1016/j.polymer.2014.10.006.

[5] B. Notario, J. Pinto, M.A. Rodríguez-Pérez, Towards a new generation of polymeric foams: PMMA nanocellular foams with enhanced physical properties, Polymer (Guildf). 63 (2015) 116–126. https://doi.org/10.1016/j.polymer.2015.03.003.

[6] J. Martín-de León, V. Bernardo, M. Rodríguez-Pérez, Low Density Nanocellular Polymers Based on PMMA Produced by Gas Dissolution Foaming: Fabrication and Cellular Structure Characterization, Polymers (Basel). 8 (2016) 265. https://doi.org/10.3390/polym8070265.

[7] J. Pinto, B. Notario, R. Verdejo, M. Dumon, S. Costeux, M.A. Rodriguez-Perez, Molecular confinement of solid and gaseous phases of self-standing bulk nanoporous polymers inducing enhanced and unexpected physical properties, Polymer (Guildf). 113 (2017) 27–33. https://doi.org/10.1016/j.polymer.2017.02.046.

[8] J. Martín-de León, F. Van Loock, V. Bernardo, N.A. Fleck, M.Á. Rodríguez-Pérez, The influence of cell size on the mechanical properties of nanocellular PMMA, Polymer (Guildf). 181 (2019) 121805. https://doi.org/10.1016/j.polymer.2019.121805.

[9] J. Martin-de Leon, Understanding The Production Process Of Nanocellular Polymers Based On Pmma Driven By A Homogeneous Nucleation. (October 2019), n.d. https://pdfs.semanticscholar.org/a3d2/2c024e3c550652f34f510769ad3d84e6020d.pdf.

[10] J. Martín-de León, V. Bernardo, M.Á. Rodríguez-Pérez, Key Production Parameters to Obtain Transparent Nanocellular PMMA, Macromol. Mater. Eng. 302 (2017) 1700343. https://doi.org/10.1002/mame.201700343.

[11] J. Martín-de León, J.L. Pura, V. Bernardo, M.Á. Rodríguez-Pérez, Transparent nanocellular PMMA: Characterization and modeling of the optical properties, Polymer (Guildf). 170 (2019) 16–23. https://doi.org/10.1016/j.polymer.2019.03.010.

[12] A.J. Cox, A.J. DeWeerd, J. Linden, An experiment to measure Mie and Rayleigh total scattering cross sections, Am. J. Phys. 70 (2002) 620–625. https://doi.org/10.1119/1.1466815.

[13] J. Pinto, M. Dumon, M.A. Rodriguez-Perez, R. Garcia, C. Dietz, Block Copolymers Self-Assembly Allows Obtaining Tunable Micro or Nanoporous Membranes or Depth Filters Based on PMMA; Fabrication Method and Nanostructures, J. Phys. Chem. C. 118 (2014) 4656–4663. https://doi.org/10.1021/jp409803u.

[14] G.Q. Lu, X.S. Zhao, Nanoporous Materials - An Overview, in: Nanoporous Mater. Sci. Eng., Imperial College Press, 2004: pp. 1–13. https://doi.org/10.1142/9781860946561_0001.

[15] B. Notario, A. Ballesteros, J. Pinto, M.A. Rodríguez-Pérez, Nanoporous PMMA: A novel system with different acoustic properties, Mater. Lett. 168 (2016) 76–79. https://doi.org/10.1016/j.matlet.2016.01.037.

[16] B. Notario, J. Pinto, R. Verdejo, M.A. Rodríguez-Pérez, Dielectric behavior of porous PMMA: From the micrometer to the nanometer scale, Polymer (Guildf). 107 (2016) 302–305. https://doi.org/10.1016/j.polymer.2016.11.030.

[17] J. Martín-de León, V. Bernardo, M. Rodríguez-Pérez, Nanocellular Polymers: The Challenge of Creating Cells

in the Nanoscale, Materials (Basel). 12 (2019) 797. https://doi.org/10.3390/ma12050797.

[18] J. Martín-de León, V. Bernardo, P. Cimavilla-Román, S. Pérez-Tamarit, M.Á. Rodríguez-Pérez, Overcoming the Challenge of Producing Large and Flat Nanocellular Polymers: A Study with PMMA, Adv. Eng. Mater. 21 (2019). https://doi.org/10.1002/adem.201900148.

[19] V. Bernardo, Production and Characterization of Nanocellular Polymers Based on Nanostructured PMMA Blends and PMMA Nanocomposites. (July 2019), n.d.

[20] J. Pinto, E. Solórzano, M.A. Rodriguez-Perez, J.A. de Saja, Characterization of the cellular structure based on user-interactive image analysis procedures, J. Cell. Plast. 49 (2013) 555–575. https://doi.org/10.1177/0021955X13503847.

[21] H. Hentze, M. Antonietti, Porous polymers and resins for biotechnological and biomedical applications, Handb. Porous Solids. 90 (2002) 27–53. https://doi.org/https://doi.org/10.1016/S1389-0352(01)00046-0.

[22] H. Guo, V. Kumar, Some thermodynamic and kinetic low-temperature properties of the PC-CO2 system and morphological characteristics of solid-state PC nanofoams produced with liquid CO2, Polymer (Guildf). 56 (2015) 46–56. https://doi.org/10.1016/j.polymer.2014.09.061.

[23] H. Guo, A. Nicolae, V. Kumar, Solid-state poly(methyl methacrylate) (PMMA) nanofoams. Part II: Low-temperature solid-state process space using CO2 and the resulting morphologies, Polymer (Guildf). 70 (2015) 231–241. https://doi.org/10.1016/j.polymer.2015.06.031.

[24] V. Bernardo, J. Martín-De León, M.A.A. Rodríguez-Pérez, Production and characterization of nanocellular polyphenylsulfone foams, Mater. Lett. 178 (2016) 155–158. https://doi.org/10.1016/j.matlet.2016.05.002.

[25] D. Miller, P. Chatchaisucha, V. Kumar, Microcellular and nanocellular solid-state polyetherimide (PEI) foams using sub-critical carbon dioxide I. Processing and structure, Polymer (Guildf). 50 (2009) 5576–5584. https://doi.org/10.1016/j.polymer.2009.09.020.

[26] G. Wang, G. Zhao, L. Zhang, Y. Mu, C.B. Park, Lightweight and tough nanocellular PP/PTFE nanocomposite foams with defect-free surfaces obtained using in situ nanofibrillation and nanocellular injection molding, Chem. Eng. J. 350 (2018) 1–11. https://doi.org/10.1016/j.cej.2018.05.161.

[27] J. Ni, K. Yu, H. Zhou, J. Mi, S. Chen, X. Wang, Morphological evolution of PLA foam from microcellular to nanocellular induced by cold crystallization assisted by supercritical CO2, J. Supercrit. Fluids. 158 (2020) 104719. https://doi.org/10.1016/j.supflu.2019.104719.

[28] I. Sánchez-Calderón, V. Bernardo, M. Santiago-Calvo, H. Naji, A. Saiani, M.Á. Rodríguez-Pérez, Effect of the molecular structure of TPU on the cellular structure of nanocellular polymers based on PMMA/TPU blends, Polymers (Basel). 13 (2021). https://doi.org/10.3390/polym13183055.

[29] G. Wang, J. Zhao, C. Ge, G. Zhao, C.B. Park, Nanocellular poly(ether-block-amide)/MWCNT nanocomposite films fabricated by stretching-assisted microcellular foaming for high-performance EMI shielding applications, J. Mater. Chem. C. 9 (2021) 1245–1258. https://doi.org/10.1039/d0tc04099a.

[30] J. Zhao, G. Wang, Z. Xu, A. Zhang, G. Dong, G. Zhao, C.B. Park, Ultra-elastic and super-insulating biomass PEBA nanoporous foams achieved by combining in-situ fibrillation with microcellular foaming, J. CO2 Util. 57 (2022) 101891. https://doi.org/10.1016/j.jcou.2022.101891.

[31] S.L. Wells, J. Desimone, CO2 technology platform: An important tool for environmental problem solving, Angew. Chemie - Int. Ed. 40 (2001) 518–527. https://doi.org/10.1002/1521-3773(20010202)40:3<518::AID-ANIE518>3.0.CO;2-4.

[32] L.J.M. Jacobs, M.F. Kemmere, J.T.F. Keurentjes, Sustainable polymer foaming using high pressure carbon dioxide: A review on fundamentals, processes and applications, Green Chem. 10 (2008) 731–73. https://doi.org/10.1039/b801895b.

[33] F. Rindfleisch, T.P. DiNoia, M.A. McHugh, Solubility of polymers and copolymers in supercritical CO2, J. Phys. Chem. 100 (1996) 15581–15587. https://doi.org/10.1021/jp9615823.

[34] K.F. Webb, A.S. Teja, Solubility and diffusion of carbon dioxide in polymers, Fluid Phase Equilib. 158–160 (1999) 1029–1034. https://doi.org/10.1016/s0378-3812(99)00153-3.

[35] M.L. O'Neill, Q. Cao, M. Fang, K.P. Johnston, S.P. Wilkinson, C.D. Smith, J.L. Kerschner, S.H. Jureller, Solubility of homopolymers and copolymers in carbon dioxide, Ind. Eng. Chem. Res. 37 (1998) 3067–3079. https://doi.org/10.1021/ie980010x.

[36] J.E. Weller, V. Kumar, Solid-State Microcellular Polycarbonate Foams. I. The Steady-State Process Space Using Subcritical Carbon Dioxide, Polym. Eng. Sci. (2010). https://doi.org/10.1002/pen.

[37] Y. Dong Hwang, S. Woon Cha, The relationship between gas absorption and the glass transition temperature in a batch microcellular foaming process, Polym. Test. 21 (2002) 269–275. https://doi.org/10.1016/S0142-9418(01)00081-2.

[38] P. Alessi, A. Cortesi, I. Kikic, F. Vecchione, Plasticization of polymers with supercritical carbon dioxide: Experimental determination of glass-transition temperatures, J. Appl. Polym. Sci. 88 (2003) 2189–2193. https://doi.org/10.1002/app.11881.

[39] D.C. Rodríguez, D. Carrascal, E. Solórzano, M.A.R. Pérez, J. Pinto, Analysis of the retrograde behavior in PMMA-CO2 systems by measuring the (effective) glass transition temperature using refractive index variations, J. Supercrit. Fluids. 170 (2021). https://doi.org/10.1016/j.supflu.2020.105159.

[40] J. Pinto, S. Pardo, E. Solórzano, M.A. Rodríguez-Pérez, M. Dumon, J. a. de Saja, Solid Skin Characterization of PMMA/MAM Foams Fabricated by Gas Dissolution Foaming over a Range of Pressures, Defect Diffus. Forum. 326–328 (2012) 434–439. https://doi.org/10.4028/www.scientific.net/DDF.326-328.434.

[41] V. Kumar, J.E. Weller, A model for the unfoamed skin on microcellular foams, Polym. Eng. Sci. 34 (1994) 169–173. https://doi.org/10.1002/pen.760340302.

[42] J.A. Reglero Ruiz, P. Viot, M. Dumon, Microcellular foaming of polymethylmethacrylate in a batch supercritical CO2 process: Effect of microstructure on compression behavior, J. Appl. Polym. Sci. 118 (2010) 320–331. https://doi.org/10.1002/app.32351.

[43] P.L. Durrill, R.G. Griskey, Diffusion and solution of gases in thermally softened or molten polymers: Part I. Development of technique and determination of data, AIChE J. 12 (1966) 1147–1151. https://doi.org/10.1002/aic.690120619.

[44] W.W. Brandt, Model Calculation of the Temperature Dependence of Small Molecule Diffusion in High Polymers, J. Phys. Chem. 63 (1959) 1080–1085. https://doi.org/10.1021/j150577a012.

[45] S. Costeux, I. Khan, S.P. Bunker, H.K. Jeon, Experimental study and modeling of nanofoams formation from single phase acrylic copolymers, J. Cell. Plast. 51 (2015) 197–221. https://doi.org/10.1177/0021955X14531972.

[46] V.I. Kalikmanov, Nucleation Theory, Springer. (2013).

[47] Z. Zhang, Y.P. Handa, An in situ study of plasticization of polymers by high-pressure gases, J. Polym. Sci. Part B Polym. Phys. 36 (1998) 977–982. https://doi.org/10.1002/(SICI)1099-0488(19980430)36:6<977::AID-POLB5>3.0.CO;2-D.

[48] J. Martín-de León, V. Bernardo, E. Laguna-Gutiérrez, M.Á. Rodríguez-Pérez, Influence of the viscosity of poly(methyl methacrylate) on the cellular structure of nanocellular materials, Polym. Int. 69 (2020) 72–83. https://doi.org/10.1002/pi.5920.

[49] J. Martín-De León, V. Bernardo, M.Á. Rodriguez-Perez, Cyclic gas dissolution foaming as an approach for simultaneously reducing cell size and relative density in nanocellular pmma, Polymers (Basel). 13 (2021). https://doi.org/10.3390/polym13142383.

[50] J. Martín-de León, M. Jiménez, J.L. Pura, V. Bernardo, M.A. Rodriguez-Pérez, Easy-way production of highly transparent nanocellular polymers films, Polymer (Guildf). 236 (2021) 124298. https://doi.org/10.1016/j.polymer.2021.124298.

[51] S.K. Yeh, Z.E. Liao, K.C. Wang, Y.T. Ho, V. Kurniawan, P.C. Tseng, T.W. Tseng, Effect of molecular weight

to the structure of nanocellular foams: Phase separation approach, Polymer (Guildf). 191 (2020) 122275. https://doi.org/10.1016/j.polymer.2020.122275.

[52] C. Zhou, N. Vaccaro, S.S. Sundarram, W. Li, Fabrication and characterization of polyetherimide nanofoams using supercritical CO2, J. Cell. Plast. 48 (2012) 239–255. https://doi.org/10.1177/0021955X12437984.

[53] H. Guo, A. Nicolae, V. Kumar, Solid-state microcellular and nanocellular polysulfone foams, J. Polym. Sci. Part B Polym. Phys. 53 (2015) 975–985. https://doi.org/10.1002/polb.23719.

[54] H. Guo, A. Nicolae, V. Kumar, Fabrication of High Temperature Polyphenylsulfone Nanofoams Using High Pressure Liquid Carbon Dioxide, Cell. Polym. 35 (2016) 119–142. https://doi.org/10.1177/026248931603500302.

[55] S. Liu, R. Eijkelenkamp, J. Duvigneau, G.J. Vancso, Silica-Assisted Nucleation of Polymer Foam Cells with Nanoscopic Dimensions: Impact of Particle Size, Line Tension, and Surface Functionality, ACS Appl. Mater. Interfaces. 9 (2017) 37929–37940. https://doi.org/10.1021/acsami.7b11248.

[56] S. Costeux, L. Zhu, Low density thermoplastic nanofoams nucleated by nanoparticles, Polymer (Guildf). 54 (2013) 2785–2795. https://doi.org/10.1016/j.polymer.2013.03.052.

[57] V. Bernardo, J. Martín-de León, E. Laguna-Gutiérrez, M.Á. Rodríguez-Pérez, PMMA-sepiolite nanocomposites as new promising materials for the production of nanocellular polymers, Eur. Polym. J. 96 (2017) 10–26. https://doi.org/10.1016/j.eurpolymj.2017.09.002.

[58] A. Ameli, M. Nofar, C.B. Park, P. Pötschke, G. Rizvi, Polypropylene/carbon nanotube nano/microcellular structures with high dielectric permittivity, low dielectric loss, and low percolation threshold, Carbon N. Y. 71 (2014) 206–217. https://doi.org/10.1016/j.carbon.2014.01.031.

[59] S.P. Xiao, H.X. Huang, Generation of nanocellular TPU/reduced graphene oxide nanocomposite foams with high cell density by manipulating viscoelasticity, Polymer (Guildf). 183 (2019) 121879. https://doi.org/10.1016/j.polymer.2019.121879.

[60] V. Goodarzi, M. Fasihi, H. Garmabi, M. Ohshima, K. Taki, M. Reza Saeb, Microstructure, mechanical and electrical characterizations of bimodal and nanocellular polypropylene/graphene nanoplatelet composite foams, Mater. Today Commun. 25 (2020) 101447. https://doi.org/10.1016/j.mtcomm.2020.101447.

[61] C. Zeng, X. Han, L.J. Lee, K.W. Koelling, D.L. Tomasko, Polymer-Clay Nanocomposite Foams Prepared Using Carbon Dioxide, Adv. Mater. 15 (2003) 1743–1747. https://doi.org/10.1002/adma.200305065.

[62] Y.H. Lee, C.B. Park, K.I.H. Wang, M.H. Lee, HDPE-clay nanocomposite foams blown with supercritical CO2, J. Cell. Plast. 41 (2005) 487–502. https://doi.org/10.1177/0021955X05056964.

[63] S.-K. Yeh, Y.-C. Liu, W.-Z. Wu, K.-C. Chang, W.-J. Guo, S.-F. Wang, Thermoplastic polyurethane/clay nanocomposite foam made by batch foaming, J. Cell. Plast. 49 (2013) 119–130. https://doi.org/10.1177/0021955X13477432.

[64] Y. Ito, M. Yamashita, M. Okamoto, Foam processing and cellular structure of polycarbonate-based nanocomposites, Macromol. Mater. Eng. 291 (2006) 773–783. https://doi.org/10.1002/mame.200600075.

[65] J.A. Reglero Ruiz, E. Cloutet, M. Dumon, Investigation of the Nanocellular Foaming of Polystyrene in Supercritical CO2 by Adding a CO2-Philic Perfluorinated Block Copolymer, J. Appl. Polym. Sci. (2012). https://doi.org/10.1002/app.

[66] J. Pinto, M. Dumon, M. Pedros, J. Reglero, M.A. Rodriguez-Perez, Nanocellular CO2 foaming of PMMA assisted by block copolymer nanostructuration, Chem. Eng. J. 243 (2014) 428–435. https://doi.org/10.1016/j.cej.2014.01.021.

[67] C. Forest, P. Chaumont, P. Cassagnau, B. Swoboda, P. Sonntag, CO2 nano-foaming of nanostructured PMMA, Polymer (Guildf). 58 (2015) 76–87. https://doi.org/10.1016/j.polymer.2014.12.048.

[68] V. Bernardo, J. Martin-de Leon, E. Laguna-Gutierrez, T. Catelani, J. Pinto, A. Athanassiou, M.A. Rodriguez-Perez, Understanding the role of MAM molecular weight in the production of PMMA/MAM nanocellular

polymers, Polymer (Guildf). 153 (2018) 262–270. https://doi.org/10.1016/j.polymer.2018.08.022.

[69] V. Bernardo, J. Martin-de Leon, J. Pinto, T. Catelani, A. Athanassiou, M.A. Rodriguez-Perez, Low-density PMMA/MAM nanocellular polymers using low MAM contents: Production and characterization, Polymer (Guildf). 163 (2019) 115–124. https://doi.org/10.1016/j.polymer.2018.12.057.

[70] G. Wang, J. Zhao, L.H. Mark, G. Wang, K. Yu, C. Wang, C.B. Park, G. Zhao, Ultra-tough and super thermal-insulation nanocellular PMMA/TPU, Chem. Eng. J. 325 (2017) 632–646. https://doi.org/10.1016/j.cej.2017.05.116.

[71] V. Bernardo, J. Martin-de Leon, I. Sanchez-Calderon, E. Laguna-Gutierrez, M.A. Rodriguez-Perez, Nanocellular Polymers with a Gradient Cellular Structure Based on Poly(methyl methacrylate)/Thermoplastic Polyurethane Blends Produced by Gas Dissolution Foaming, Macromol. Mater. Eng. 1900428 (2019) 1900428. https://doi.org/10.1002/mame.201900428.

[72] N.M. Demewoz, S.K. Yeh, Fabrication and characterization of low-density nanocellular foam based on PMMA/TPU blends, Polymer (Guildf). 240 (2022) 124493. https://doi.org/10.1016/j.polymer.2021.124493.

[73] T. Nemoto, J. Takagi, M. Ohshima, Nanoscale cellular foams from a poly(propylene)-rubber blend, 293 (2008) 991–998. https://doi.org/10.1002/mame.200800184.

[74] T. Nemoto, J. Takagi, M. Ohshima, Control of bubble size and location in nano-/microscale cellular poly(propylene)/rubber blend foams, 293 (2008) 574–580. https://doi.org/10.1002/mame.200800015.

[75] T. Nemoto, J. Takagi, M. Ohshima, Nanocellular Foams—Cell Structure Difference Between Immiscible and Miscible PEEK/PEI Polymer Blends, Polym. Eng. Sci. 50 (2010) 2408–2416. https://doi.org/10.1002/pen.21766.

[76] T. Otsuka, K. Taki, M. Ohshima, Nanocellular Foams of PS/PMMA Polymer Blends, Macromol. Mater. Eng. 293 (2008) 78–82. https://doi.org/10.1002/mame.200700257.

[77] H. Yokoyama, K. Sugiyama, Nanocellular structures in block copolymers with CO2-philic blocks using CO2 as a blowing agent: Crossover from micro- to nanocellular structures with depressurization temperature, Macromolecules. 38 (2005) 10516–10522. https://doi.org/10.1021/ma051757j.

[78] Z. Shi, X. Ma, G. Zhao, G. Wang, L. Zhang, B. Li, Fabrication of high porosity Nanocellular polymer foams based on PMMA/PVDF blends, Mater. Des. 195 (2020). https://doi.org/10.1016/j.matdes.2020.109002.

[79] B. Xiang, Y. Jia, Y. Lei, F. Zhang, J. He, T. Liu, S. Luo, Mechanical properties of microcellular and nanocellular silicone rubber foams obtained by supercritical carbon dioxide, Polym. J. 51 (2019) 559–568. https://doi.org/10.1038/s41428-019-0175-6.

[80] S. Costeux, CO2-Blown nanocellular foams, J. Appl. Polym. Sci. 131 (2014). https://doi.org/10.1002/app.41293.

[81] S. Liu, J. Duvigneau, G.J. Vancso, Nanocellular polymer foams as promising high performance thermal insulation materials, Eur. Polym. J. 65 (2015) 33–45. https://doi.org/10.1016/j.eurpolymj.2015.01.039.

[82] C. Forest, P. Chaumont, P. Cassagnau, B. Swoboda, P. Sonntag, Polymer nano-foams for insulating applications prepared from CO2 foaming, Prog. Polym. Sci. 41 (2015) 122–145. https://doi.org/10.1016/j.progpolymsci.2014.07.001.

[83] W. Villasmil, L.J. Fischer, J. Worlitschek, A review and evaluation of thermal insulation materials and methods for thermal energy storage systems, Renew. Sustain. Energy Rev. 103 (2019) 71–84. https://doi.org/10.1016/j.rser.2018.12.040.

[84] S. Schiavoni, F. D'Alessandro, F. Bianchi, F. Asdrubali, Insulation materials for the building sector: A review and comparative analysis, Renew. Sustain. Energy Rev. 62 (2016) 988–1011. https://doi.org/10.1016/j.rser.2016.05.045.

[85] C. Moore, S. Shrestha, S. Gokarakonda, Building energy standards and labelling in Europe, (2019).

[86] F. Garzia, R. Pernetti, T. Weiss, D. Venus, A. Knotzer, M. Thouvenot, B. Berggren, CRAVEzero - D2.1: Report on EU implementation of nZEBs, (2018) 1-.38. http://www.cravezero.eu/wp-

content/uploads/2018/07/CRAVEzero_D21_Report-of-EU-implementation-of-nZEBs.pdf.

[87] K. Ahmed, M. Carlier, C. Feldmann, J. Kurnitski, A New Method for Contrasting Energy Performance and Near-Zero Energy Building Requirements in Different Climates and Countries, Energies. 11 (2018) 1334. https://doi.org/10.3390/en11061334.

[88] B. López-Mesa, M. Monzón-Chavarrías, A. Espinosa-Fernández, Energy Retrofit of Social Housing with Cultural Value in Spain: Analysis of Strategies Conserving the Original Image vs. Coordinating Its Modification, Sustainability. 12 (2020) 5579. https://doi.org/10.3390/su12145579.

[89] European Insulation Manufacturers Association (eurima): U-values for better energy performance of buildings, (n.d.).

[90] N. Yüksel, The Review of Some Commonly Used Methods and Techniques to Measure the Thermal Conductivity of Insulation Materials, in: Insul. Mater. Context Sustain., 2016. https://doi.org/http://dx.doi.org/10.5772/64157.

[91] D. Zhao, X. Qian, X. Gu, S.A. Jajja, R. Yang, Measurement techniques for thermal conductivity and interfacial thermal conductance of bulk and thin film materials, J. Electron. Packag. Trans. ASME. 138 (2016) 1–19. https://doi.org/10.1115/1.4034605.

[92] D. Kraemer, G. Chen, A simple differential steady-state method to measure the thermal conductivity of solid bulk materials with high accuracy, Rev. Sci. Instrum. 85 (2014). https://doi.org/10.1063/1.4865111.

[93] ISO 22007-2:2022 Plastics - Determination of thermal conductivity and thermal diffusivity - Part 2: Transient plane heat source (hot disc) method, (2022).

[94] ISO 22007-4:2017 Plastics — Determination of thermal conductivity and thermal diffusivity — Part 4: Laser flash method, (2017).

[95] O. Almanza, M.A. Rodríguez-Pérez, J.A. de Saja, Measurement of the thermal diffusivity and specific heat capacity of polyethylene foams using the transient plane source technique, Polym. Int. 53 (2004) 2038–2044. https://doi.org/10.1002/pi.1624.

[96] W.J. Parker, R.J. Jenkins, C.P. Butler, G.L. Abbott, Flash Method of Determining Thermal Diffusivity, Heat Capacity, and Thermal Conductivity, J. Appl. Phys. 32 (1961) 1679–1684. https://doi.org/10.1063/1.1728417.

[97] R.C. Kerschbaumer, S. Stieger, M. Gschwandl, T. Hutterer, M. Fasching, B. Lechner, L. Meinhart, J. Hildenbrandt, B. Schrittesser, P.F. Fuchs, G.R. Berger, W. Friesenbichler, Comparison of steady-state and transient thermal conductivity testing methods using different industrial rubber compounds, Polym. Test. 80 (2019) 106121. https://doi.org/10.1016/j.polymertesting.2019.106121.

[98] O. Almanza, M.A. Rodríguez-Pérez, J.A. De Saja, Applicability of the Transient Plane Source Method To Measure the Thermal Conductivity of Low-Density Polyethylene Foams, J. Polym. Sci. Part B Polym. Phys. 42 (2004) 1226–1234. https://doi.org/10.1002/polb.20005.

[99] Q. Zheng, S. Kaur, C. Dames, R.S. Prasher, Analysis and improvement of the hot disk transient plane source method for low thermal conductivity materials, Int. J. Heat Mass Transf. 151 (2020) 119331. https://doi.org/10.1016/j.ijheatmasstransfer.2020.119331.

[100] Y. Jannot, A. Degiovanni, V. Grigorova-Moutiers, J. Godefroy, A passive guard for low thermal conductivity measurement of small samples by the hot plate method, Meas. Sci. Technol. 28 (2017). https://doi.org/10.1088/1361-6501/28/1/015008.

[101] ASTM C177 Standard Test Method for Steady-State Heat Flux Measurements and Thermal Transmission Properties by Means of the Guarded-Hot-Plate Apparatus, (1997).

[102] ISO 8302 Thermal insulation - Determination of steady-state thermal resistance and related properties - Guarded hot plate apparatus, (1991). https://standards.iteh.ai/catalog/standards/sist/11594d7b-fd5c-45d7-816b-8e35f1df4d95/iso-4832-1991.

[103] UNE-EN 12667:2001 Thermal performance of building materials and products. Determination of thermal

resistance by means of guarded hot plate and heat flow meter methods. Products of high and medium thermal resistance., (2002).

[104] ASTM C518 Standard Test Method for Steady-State Thermal Transmission Properties by Means of the Heat Flow Meter Apparatus, (2017).

[105] ISO 8301 Thermal insulation - Determination of steady-state thermal resistance and related properties - Heat flow meter, (1991).

[106] Y. Jannot, V. Felix, A. Degiovanni, A centered hot plate method for measurement of thermal properties of thin insulating materials, Meas. Sci. Technol. 21 (2010). https://doi.org/10.1088/0957-0233/21/3/035106.

[107] Y. Jannot, S. Schaefer, A. Degiovanni, J. Bianchin, V. Fierro, A. Celzard, A new method for measuring the thermal conductivity of small insulating samples, Rev. Sci. Instrum. 90 (2019). https://doi.org/10.1063/1.5065562.

[108] R.A. Miller, M.A. Kuczmarski, Method for measuring thermal conductivity of small highly insulating specimens, J. Test. Eval. 38 (2010). https://doi.org/10.1520/JTE102474.

[109] N. Diascorn, S. Calas, H. Sallée, P. Achard, A. Rigacci, Polyurethane aerogels synthesis for thermal insulation - textural, thermal and mechanical properties, J. Supercrit. Fluids. 106 (2015) 76–84. https://doi.org/10.1016/j.supflu.2015.05.012.

[110] F. Almeida, H. Beyrichen, N. Dodamani, R. Caps, A. Müller, R. Oberhoffer, Thermal conductivity analysis of a new sub-micron sized polystyrene foam, J. Cell. Plast. 57 (2021) 493–515. https://doi.org/10.1177/0021955X20943101.

[111] L.J. Gibson, M.F. Ashby, Cellular Solids: Structure and Properties, Cambridge Univ. Press Cambridge. (1997).

[112] M. Alvarez-Lainez, M.A. Rodriguez-Perez, J.A. De Saja, Thermal Conductivity of Open-Cell Polyolefin Foams, J. Polym. Sci. Part B Polym. Phys. 46 (2008) 212–221.

[113] P.G. Collishaw, J.R.G. Evans, An assessment of expressions for the apparent thermal conductivity of cellular materials, J. Mater. Sci. 29 (1994) 486–498. https://doi.org/10.1007/BF01162512.

[114] N.C.. Hilyard, A. Cunningham, Low density cellular plastics Physical basis of behaviour, 1994. https://doi.org/10.1007/978-94-011-1256-7.

[115] H. Jeffreys, Some cases of instability in fluid motion, Proc. R. Soc. London. Ser. A, Contain. Pap. a Math. Phys. Character. 118 (1928) 195–208. https://doi.org/10.1098/rspa.1928.0045.

[116] C.L. Choy, Thermal Conductivity of Polymers, Polymer (Guildf). 18 (1977) 984–1004.

[117] W.N. Dos Santos, J.A. De Sousa, R. Gregorio, Thermal conductivity behaviour of polymers around glass transition and crystalline melting temperatures, Polym. Test. 32 (2013) 987–994. https://doi.org/10.1016/j.polymertesting.2013.05.007.

[118] N.R. Pradhan, G.S. Iannacchione, Thermal properties and glass transition in PMMA + SWCNT composites, J. Phys. D. Appl. Phys. 43 (2010). https://doi.org/10.1088/0022-3727/43/30/305403.

[119] P. Gong, P. Buahom, M.-P. Tran, M. Saniei, C.B. Park, P. Pötschke, Heat transfer in microcellular polystyrene/multi-walled carbon nanotube nanocomposite foams, Carbon N. Y. 93 (2015) 819–829. https://doi.org/10.1016/j.carbon.2015.06.003.

[120] L.W. Hrubesh, R.W. Pekala, Thermal properties of organic and inorganic aerogels, J. Mater. Res. 9 (1994) 731–738. https://doi.org/10.1557/JMR.1994.0731.

[121] C. V. Vo, F. Bunge, J. Duffy, L. Hood, Advances in thermal insulation of extruded polystyrene foams, Cell. Polym. 30 (2011) 137–156. https://doi.org/https://doi.org/10.1177/026248931103000303.

[122] H. Ebert, Thermal Properties of Aerogels, in: Aerogels Handb., 2011: pp. 537–564. https://doi.org/10.1007/978-1-4419-7589-8.

[123] C. Kittel, Introduction to solid state physics, John Wiley & Sons, Inc., New York, 1976.

[124] Z.M. Zhang, Nano/Microscale Heat Transfer, Springer International Publishing, Cham, 2020.

https://doi.org/10.1007/978-3-030-45039-7.

[125] J. Lee, J. Lim, P. Yang, Ballistic Phonon Transport in Holey Silicon, Nano Lett. 15 (2015) 3273–3279. https://doi.org/10.1021/acs.nanolett.5b00495.

[126] G. Wang, C. Wang, J. Zhao, G. Wang, C.B. Park, G. Zhao, Modelling of thermal transport through a nanocellular polymer foam: Toward the generation of a new superinsulating material, Nanoscale. 9 (2017) 5996–6009. https://doi.org/10.1039/c7nr00327g.

[127] J. Kaiser, T. Feng, J. Maassen, X. Wang, X. Ruan, M. Lundstrom, Thermal transport at the nanoscale: A Fourier's law vs. phonon Boltzmann equation study, J. Appl. Phys. 121 (2017) 044302. https://doi.org/10.1063/1.4974872.

[128] T. Feng, J. He, A. Rai, D. Hun, J. Liu, S.S. Shrestha, Size Effects in the Thermal Conductivity of Amorphous Polymers, Phys. Rev. Appl. 14 (2020) 044023. https://doi.org/10.1103/PhysRevApplied.14.044023.

[129] H. Ma, Z. Tian, Effects of polymer chain confinement on thermal conductivity of ultrathin amorphous polystyrene films, Appl. Phys. Lett. 107 (2015). https://doi.org/10.1063/1.4929426.

[130] I. Kim, M.G. Burzo, P.L. Komarov, P.E. Raad, Thermal conductivity measurements of ultra-thin amorphous poly(methyl methacrylate) (PMMA) films, ASME Int. Mech. Eng. Congr. Expo. Proc. 8 C (2013). https://doi.org/10.1115/IMECE2013-66507.

[131] R.C. Zhang, Z. Huang, D. Sun, D. Ji, M. Zhong, D. Zang, J.Z. Xu, Y. Wan, A. Lu, New insights into thermal conductivity of uniaxially stretched high density polyethylene films, Polymer (Guildf). 154 (2018) 42–47. https://doi.org/10.1016/j.polymer.2018.08.078.

[132] V. Bernardo, J. Martin-de Leon, J. Pinto, R. Verdejo, M.A. Rodriguez-Perez, Modeling the heat transfer by conduction of nanocellular polymers with bimodal cellular structures, Polymer (Guildf). 160 (2019) 126–137. https://doi.org/10.1016/j.polymer.2018.11.047.

[133] M. Saadatfar, C.H. Arns, M.A. Knackstedt, T. Senden, Mechanical and transport properties of polymeric foams derived from 3D images, Colloids Surfaces A Physicochem. Eng. Asp. 263 (2005) 284–289. https://doi.org/10.1016/j.colsurfa.2004.12.040.

[134] P. Scheuerpflug, M. Hauck, J. Fricke, Thermal properties of silica aerogels between 1.4 and 330 K, J. Non. Cryst. Solids. 145 (1992) 196–201. https://doi.org/10.1016/S0022-3093(05)80455-7.

[135] J. Fricke, E. Hümmer, H.-J. Morper, P. Scheuerpflug, Thermal Properties Of Silica Aerogels, Le J. Phys. Colloq. 24 (1989) C4-87-C4-97. https://doi.org/10.1051/jphyscol:1989414.

[136] J. Fricke, Aerogels, in: Springer Proc. Phys. 6, 1985.

[137] X. Lu, R. Caps, J. Fricke, C.T. Alviso, R.W. Pekala, Correlation between structure and thermal conductivity of organic aerogels, J. Non. Cryst. Solids. 188 (1995) 226–234. https://doi.org/10.1016/0022-3093(95)00191-3.

[138] J. Fricke, Thermal Transport in Porous Superinsulations, (1986) 94–103. https://doi.org/10.1007/978-3-642-93313-4_11.

[139] J. Nassios, Kinetic theory of rarefied gas flows with modern applications, Austms.Org.Au. (2006). https://www.austms.org.au/Publ/Gazette/2013/Mar13/Nassios.pdf.

[140] S. Song, M.M. Yovanovich, F.O. Goodman, Thermal gap conductance of conforming surfaces in contact, J. Heat Transfer. 115 (1993) 533–540. https://doi.org/10.1115/1.2910719.

[141] Y.L. He, T. Xie, Advances of thermal conductivity models of nanoscale silica aerogel insulation material, Appl. Therm. Eng. 81 (2015) 28–50. https://doi.org/10.1016/j.applthermaleng.2015.02.013.

[142] S. Sonnick, L. Erlbeck, M. Meier, H. Nirschl, M. Rädle, Methodical selection of thermal conductivity models for porous silica-based media with variation of gas type and pressure, Int. J. Heat Mass Transf. 187 (2022). https://doi.org/10.1016/j.ijheatmasstransfer.2022.122519.

[143] S.E. Kentish, C.A. Scholes, G.W. Stevens, Carbon Dioxide Separation through Polymeric Membrane Systems for Flue Gas Applications, Recent Patents Chem. Eng. 1 (2008) 52–66. https://doi.org/10.2174/1874478810801010052.

[144] http://hyperphysics.phy-astr.gsu.edu/hbase/Kinetic/menfre.html, (n.d.).

[145] R. Baetens, B.P. Jelle, J.V. Thue, M.J. Tenpierik, S. Grynning, S. Uvsløkk, A. Gustavsen, Vacuum insulation panels for building applications: A review and beyond, Energy Build. 42 (2010) 147–172. https://doi.org/10.1016/j.enbuild.2009.09.005.

[146] G. Barton, The Quantum Theory of Light, Phys. Bull. 25 (1974) 103–104. https://doi.org/10.1088/0031-9112/25/3/025.

[147] A. Ramírez-Hernández, C. Aguilar-Flores, A. Aparicio-Saguilán, Fingerprint analysis of FTIR spectra of polymers containing vinyl acetate, DYNA. 86 (2019) 198–205. https://doi.org/10.15446/dyna.v86n209.77513.

[148] E. Solórzano, M.A. Rodriguez-Perez, J. Lázaro, J.A. de Saja, Influence of Solid Phase Conductivity and Cellular Structure on the Heat Transfer Mechanisms of Cellular Materials: Diverse Case Studies, Adv. Eng. Mater. 11 (2009) 818–824. https://doi.org/10.1002/adem.200900138.

[149] O.A. Almanza, M.A. Rodríguez-Pérez, J.A. De Saja, Prediction of the radiation term in the thermal conductivity of crosslinked closed cell polyolefin foams, J. Polym. Sci. Part B Polym. Phys. 38 (2000) 993–1004. https://doi.org/10.1002/(SICI)1099-0488(20000401)38:7<993::AID-POLB10>3.0.CO;2-J.

[150] R. Siegel, J.R. Howell, Thermal Radiation Heat Transfer, Taylor & Francis. London, 1992.

[151] R.A. Campo-Arnáiz, M.A. Rodríguez-Pérez, B. Calvo, J.A. De Saja, Extinction coefficient of polyolefin foams, J. Polym. Sci. Part B Polym. Phys. 43 (2005) 1608–1617. https://doi.org/10.1002/polb.20435.

[152] L. Glicksman, M. Schuetz, M. Sinofsky, Radiation heat transfer in foam insulation, Int. J. Heat Mass Transf. 30 (1987) 187–197. https://doi.org/10.1016/0017-9310(87)90071-8.

[153] L.R. Glicksman, M. Torpey, Factors Governing Heat Transfer through Closed Cell Foam Insulation, J. Therm. Insul. 12 (1989) 257–269. https://doi.org/10.1177/109719638901200403.

[154] A. Kaemmerlen, C. Vo, F. Asllanaj, G. Jeandel, D. Baillis, Radiative properties of extruded polystyrene foams: Predictive model and experimental results, J. Quant. Spectrosc. Radiat. Transf. 111 (2010) 865–877. https://doi.org/10.1016/j.jqsrt.2009.11.018.

[155] S. Estravís, J. Tirado-Mediavilla, M. Santiago-Calvo, J.L. Ruiz-Herrero, F. Villafañe, M.Á. Rodríguez-Pérez, Rigid polyurethane foams with infused nanoclays: Relationship between cellular structure and thermal conductivity, Eur. Polym. J. 80 (2016) 1–15. https://doi.org/10.1016/j.eurpolymj.2016.04.026.

[156] P. Buahom, C. Wang, M. Alshrah, G. Wang, P. Gong, M. Tran, C.B. Park, Wrong expectation of superinsulation behavior from largely-expanded nanocellular foams, Nanoscale. (2020). https://doi.org/10.1039/d0nr01927e.

[157] C.F. Bohren, D.R. Huffman, Absorption and Scattering of Light by Small Particles, Wiley, 1998. https://doi.org/10.1002/9783527618156.

[158] H.J. Li, Y.W. Kiang, Radar and Inverse Scattering, Elsevier Inc., 2005. https://doi.org/10.1016/B978-012170960-0/50047-5.

[159] Lord Rayleigh, X. On the electromagnetic theory of light, London, Edinburgh, Dublin Philos. Mag. J. Sci. 12 (1881) 81–101. https://doi.org/10.1080/14786448108627074.

[160] V. Bernardo, J. Martin-de Leon, J. Pinto, U. Schade, M.A. Rodriguez-Perez, On the interaction of infrared radiation and nanocellular polymers: First experimental determination of the extinction coefficient, Colloids Surfaces A Physicochem. Eng. Asp. 600 (2020). https://doi.org/10.1016/j.colsurfa.2020.124937.

[161] R.J.J. Williams, C.M. Aldao, Thermal conductivity of plastic foams, Polym. Eng. Sci. 23 (1983) 293–298. https://doi.org/10.1002/pen.760230602.

[162] J. Wang, D. Petit, S. Ren, Transparent thermal insulation silica aerogels, Nanoscale Adv. 2 (2020) 5504–5515. https://doi.org/10.1039/d0na00655f.

[163] B. Merillas, J. Martín-De León, F. Villafañe, M.A. Rodríguez-Pérez, Transparent Polyisocyanurate-Polyurethane-Based Aerogels: Key Aspects on the Synthesis and Their Porous Structures, ACS Appl. Polym. Mater. (2021). https://doi.org/10.1021/acsapm.1c00712.

[164] U. Heinemann, R. Caps, J. Fricke, Radiation-conduction interaction : An investigation on silica aerogels, Int. J. Heat Mass Transf. 39 (1996) 2115–2130. https://doi.org/10.1016/0017-9310(95)00313-4.

[165] P. Buahom, P. Gong, C. Wang, H. Yu, J. Liu, C.B. Park, Carbon as a solution for nanocellular foam superinsulation, Carbon N. Y. 189 (2022) 319–338. https://doi.org/10.1016/j.carbon.2021.11.041.

[166] P. Gong, G. Wang, M.P. Tran, P. Buahom, S. Zhai, G. Li, C.B. Park, Advanced bimodal polystyrene/multi-walled carbon nanotube nanocomposite foams for thermal insulation, Carbon N. Y. 120 (2017) 1–10. https://doi.org/10.1016/j.carbon.2017.05.029.

[167] T. Li, G. Zhao, G. Wang, L. Zhang, J. Hou, Thermal-Insulation, Electrical, and Mechanical Properties of Highly-Expanded PMMA/MWCNT Nanocomposite Foams Fabricated by Supercritical CO2 Foaming, Macromol. Mater. Eng. 304 (2019) 1–14. https://doi.org/10.1002/mame.201800789.

[168] Y. Li, Z. Chen, C. Zeng, Poly(Methyl Methacrylate) (PMMA) Nanocomposite Foams, in: Polym. Nanocomposite Foam., 2018.

[169] H. Yu, H. Zhang, J. Zhao, J. Liu, X. Xia, X. Wu, Thermal conductivity of micro/nano-porous polymers: Prediction models and applications, Front. Phys. 17 (2021). https://doi.org/10.1007/s11467-021-1107-4.

[170] M. Casini, Smart Buildings, 2016th ed., Elsevier, 2016. https://doi.org/10.1016/C2015-0-00182-4.

[171] M. Casini, Advanced construction materials, in: Constr. 4.0, Elsevier, 2022: pp. 337–404. https://doi.org/10.1016/B978-0-12-821797-9.00005-2.

[172] Hemman O, German Patent Nr.516377, (1930)., (n.d.).

[173] J. Fricke, U. Heinemann, H.P. Ebert, Vacuum insulation panels-From research to market, Vacuum. 82 (2008) 680–690. https://doi.org/10.1016/j.vacuum.2007.10.014.

[174] Bovenkerk HP. Insulating structure and method of forming same. US patent 2700633, (1955)., (n.d.).

[175] Glaser PE, Emslie AG, Salmon WA. Insulation material and structures containing same. US patent no. 3151365, (1964)., (n.d.).

[176] J. Kośny, D.W. Yarbrough, eds., Thermal Insulation and Radiation Control Technologies for Buildings, Springer International Publishing, 2022. https://doi.org/10.1007/978-3-030-98693-3.

[177] https://www.imarcgroup.com/vacuum-insulation-panel-market, (n.d.).

[178] https://www.futuremarketinsights.com/reports/thermal-insulation-material-market, (n.d.).

[179] S.E. Kalnæs, B.P. Jelle, Vacuum insulation panel products: A state-of-the-art review and future research pathways, Appl. Energy. 116 (2014) 355–375. https://doi.org/10.1016/j.apenergy.2013.11.032.

[180] H. Abe, I. Abe, K. Sato, M. Naito, Dry powder processing of fibrous fumed silica compacts for thermal insulation, J. Am. Ceram. Soc. 88 (2005) 1359–1361. https://doi.org/10.1111/j.1551-2916.2005.00317.x.

[181] X. Tang, Y. Yu, Preparation of fumed silica compacts for thermal insulation using wet processing method, Int. J. Appl. Ceram. Technol. 15 (2018) 232–236. https://doi.org/10.1111/ijac.12791.

[182] X. Lu, M.C. Arduini-Schuster, J. Kuhn, O. Nilsson, J. Fricke, R.W. Pekala, Thermal conductivity of monolithic organic aerogels, Science (80-.). 255 (1992) 971–972. https://doi.org/10.1126/science.255.5047.971.

[183] F.A. Almeida, J. Corker, N. Ferreira, M.A. Neto, M. Fan, H. Beyrichen, R. Caps, Alternative low cost based core systems for vacuum insulation panels, Cienc. e Tecnol. Dos Mater. 29 (2017) e151–e156. https://doi.org/10.1016/j.ctmat.2016.10.002.

[184] B. Chang, L. Zhong, M. Akinc, Low cost composites for vacuum insulation core material, Vacuum. 131 (2016) 120–126. https://doi.org/10.1016/j.vacuum.2016.05.027.

[185] S. Verma, H. Singh, Predicting the conductive heat transfer through evacuated perlite based vacuum insulation panels, Int. J. Therm. Sci. 171 (2022) 107245. https://doi.org/10.1016/j.ijthermalsci.2021.107245.

[186] V. Nemanič, M. Žumer, New organic fiber-based core material for vacuum thermal insulation, Energy Build. 90 (2015) 137–141. https://doi.org/10.1016/j.enbuild.2015.01.012.

[187] C. Li, B. Li, N. Pan, Z. Chen, M.U. Saeed, T. Xu, Y. Yang, Thermo-physical properties of polyester fiber

reinforced fumed silica/hollow glass microsphere composite core and resulted vacuum insulation panel, Energy Build. 125 (2016) 298–309. https://doi.org/10.1016/j.enbuild.2016.05.013.

[188] C.-D. Li, M.-U. Saeed, N. Pan, Z.-F. Chen, T.-Z. Xu, Fabrication and characterization of low-cost and green vacuum insulation panels with fumed silica/rice husk ash hybrid core material, Mater. Des. 107 (2016) 440–449. https://doi.org/10.1016/j.matdes.2016.06.071.

[189] M. Alam, H. Singh, S. Brunner, C. Naziris, Experimental characterisation and evaluation of the thermo-physical properties of expanded perlite—Fumed silica composite for effective vacuum insulation panel (VIP) core, Energy Build. 69 (2014) 442–450. https://doi.org/10.1016/j.enbuild.2013.11.027.

[190] H. Simmler, U. Heinemann, H. Schwab, D. Quénard, E. Kücükpinar-niarchos, C. Stramm, Vacuum Insulation Panels. Study on VIP-components and Panels for Service Life Prediction of VIP in Building Applications (Subtask A), (2005).

[191] M. Alam, H. Singh, M.C. Limbachiya, Vacuum insulation panels (vips) for building construction industry - a review of the contemporary developments and future directions, Appl. Energy. 88 (2011) 3592–3602. https://doi.org/10.1016/j.apenergy.2011.04.040.

[192] E. Wegger, B.P. Jelle, E. Sveipe, S. Grynning, A. Gustavsen, R. Baetens, J.V. Thue, Aging effects on thermal properties and service life of vacuum insulation panels, J. Build. Phys. 35 (2011) 128–167. https://doi.org/10.1177/1744259111398635.

[193] https://hanita.averydennison.com/na/en/home/products/ultra-high-barrier-laminates/vip- laminates.html, (n.d.).

[194] K. Araki, W. Echigoya, T. Tsuruga, D. Kamoto, S. Matsuoka, Optimization of Multilayer Laminated Film and Absorbent of Vacuum Insulation Panel for Use at High Temperature, Seikei-Kakou. 20 (2008) 58–66. https://doi.org/10.4325/seikeikakou.20.58.

[195] K. Swimm, S. Vidi, G. Reichenauer, H.P. Ebert, Coupling of gaseous and solid thermal conduction in porous solids, J. Non. Cryst. Solids. 456 (2017) 114–124. https://doi.org/10.1016/j.jnoncrysol.2016.11.012.

[196] T. Beikircher, M. Demharter, Heat transport in evacuated perlite powders for super-insulated long-term storages up to 300 °c, J. Heat Transfer. 135 (2013) 1–11. https://doi.org/10.1115/1.4023351.

[197] S. Sonnick, M. Meier, J. Ross-Jones, L. Erlbeck, I. Medina, H. Nirschl, M. Rädle, Correlation of pore size distribution with thermal conductivity of precipitated silica and experimental determination of the coupling effect, Appl. Therm. Eng. 150 (2019) 1037–1045. https://doi.org/10.1016/j.applthermaleng.2019.01.074.

[198] M. Bouquerel, T. Duforestel, D. Baillis, G. Rusaouen, Heat transfer modeling in vacuum insulation panels containing nanoporous silicas - A review, Energy Build. 54 (2012) 320–336. https://doi.org/10.1016/j.enbuild.2012.07.034.

[199] J.S. Kwon, C.H. Jang, H. Jung, T.H. Song, Effective thermal conductivity of various filling materials for vacuum insulation panels, Int. J. Heat Mass Transf. 52 (2009) 5525–5532. https://doi.org/10.1016/j.ijheatmasstransfer.2009.06.029.

[200] H. Singh, M. Geisler, F. Menzel, Experimental investigations into thermal transport phenomena in vacuum insulation panels (VIPs) using fumed silica cores, Energy Build. 107 (2015) 76–83. https://doi.org/10.1016/j.enbuild.2015.08.004.

[201] R. Caps, J. Fricke, Thermal conductivity of opacified powder filler materials for vacuum insulations, Int. J. Thermophys. 21 (2000) 445–452. https://doi.org/10.1023/A:1006691731253.

[202] S. Verma, H. Singh, Vacuum insulation panels for refrigerators, Int. J. Refrig. 112 (2020) 215–228. https://doi.org/10.1016/j.ijrefrig.2019.12.007.

[203] R. Caps, U. Heinemann, M. Ehrmanntraut, J. Fricke, Evacuated insulation panels filled with pyrogenic silica powders: Properties and applications, High Temp. - High Press. 33 (2001) 151–156. https://doi.org/10.1068/htwu70.

[204] J. Fricke, H. Schwab, U. Heinemann, Vacuum Insulation Panels – Exciting Thermal Properties and Most

Challenging Applications, Int. J. Thermophys. 27 (2006) 1123–1139. https://doi.org/10.1007/s10765-006-0106-6.

[205] T. Rettelbach, J. Säuberlich, S. Korder, J. Fricke, Thermal conductivity of silica aerogel powders at temperatures from 10 to 275 K, J. Non. Cryst. Solids. 186 (1995) 278–284. https://doi.org/10.1016/0022-3093(95)00051-8.

[206] M. Davraz, M. Koru, H.C. Bayrakçi, Y. Yusufoğlu, O. Ipek, The effect of opacifier properties on thermal conductivity of vacuum insulation panel with fumed silica, J. Therm. Anal. Calorim. 142 (2020) 1377–1386. https://doi.org/10.1007/s10973-020-09277-8.

[207] M. Davraz, H.C. Bayrakci, Performance properties of vacuum insulation panels produced with various filling materials, Sci. Eng. Compos. Mater. 21 (2014) 521–527. https://doi.org/10.1515/secm-2013-0162.

[208] V. Napp, R. Caps, H. Ebert, Optimization of the Thermal Radiation Extinction of Silicon Carbide in a Silica Powder Matrix, J. Therm. Anal. Calorim. 56 (1999) 77–85. https://doi.org/10.1023/A:1010131324100.

[209] X.D. Wang, D. Sun, Y.Y. Duan, Z.J. Hu, Radiative characteristics of opacifier-loaded silica aerogel composites, J. Non. Cryst. Solids. 375 (2013) 31–39. https://doi.org/10.1016/j.jnoncrysol.2013.04.058.

[210] C.-Y. Zhu, Z.-Y. Li, H.-Q. Pang, N. Pan, Design and optimization of core/shell structures as highly efficient opacifiers for silica aerogels as high-temperature thermal insulation, Int. J. Therm. Sci. 133 (2018) 206–215. https://doi.org/10.1016/j.ijthermalsci.2018.07.032.

[211] J. Feng, D. Chen, W. Ni, S. Yang, Z. Hu, Study of IR absorption properties of fumed silica-opacifier composites, J. Non. Cryst. Solids. 356 (2010) 480–483. https://doi.org/10.1016/j.jnoncrysol.2009.12.015.

[212] S. Fantucci, A. Lorenzati, A. Capozzoli, M. Perino, Analysis of the temperature dependence of the thermal conductivity in Vacuum Insulation Panels, Energy Build. 183 (2019) 64–74. https://doi.org/10.1016/j.enbuild.2018.10.002.

[213] K. Swimm, G. Reichenauer, S. Vidi, H.P. Ebert, Impact of thermal coupling effects on the effective thermal conductivity of aerogels, J. Sol-Gel Sci. Technol. 84 (2017) 466–474. https://doi.org/10.1007/s10971-017-4437-5.

[214] C. Bi, G.H. Tang, Z.J. Hu, Heat conduction modeling in 3-D ordered structures for prediction of aerogel thermal conductivity, Int. J. Heat Mass Transf. 73 (2014) 103–109. https://doi.org/10.1016/j.ijheatmasstransfer.2014.01.058.

[215] U. Heinemann, J. Hetfleisch, R. Caps, J. Kuhn, J. Fricke, Evacuable Guarded Hot Plate for Thermal Conductivity Measurements between-200°C and 800°C, in: Adv. Therm. Insul. Proc. Eurotherm Semin. No.44At Rio Tinto - Port., 1995.

[216] H. Schwab, U. Heinemann, A. Beck, H.-P. Ebert, J. Fricke, Prediction of Service Life for Vacuum Insulation Panels with Fumed Silica Kernel and Foil Cover, J. Therm. Envel. Build. Sci. 28 (2005) 357–374. https://doi.org/10.1177/1097196305051894.

Chapter 3

Materials & Methods

"Do… or do not. There is not try."

Jedi Master Yoda – STAR WARS

INDEX

3. Materials & Methods

3.1. Materials

3.1.1. Poly(methyl-methacrylate) (PMMA)

Poly (methyl methacrylate) (PMMA) is the polymer selected to be used in this thesis. PMMA is an amorphous thermoplastic obtained from the polymerization of methyl methacrylate (**Figure 3.1**).

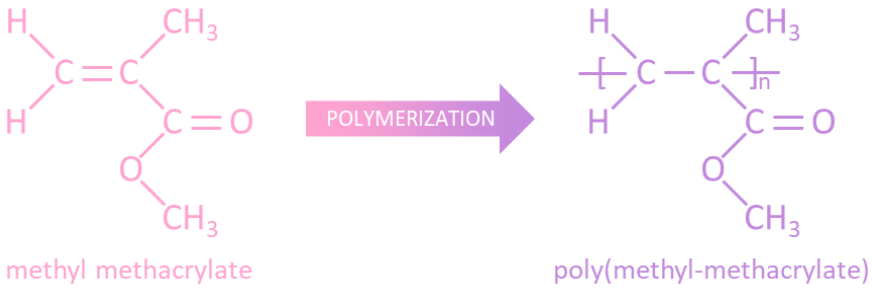

Figure 3.1. PMMA polymerization and chemical structure of PMMA.

PMMA is characterized by its high transparency, impact resistance, and excellent thermal and acoustic insulation. However, as far as this thesis concerns, it will be used as a research polymer due to its high CO_2 affinity and ability to produce low-density nanocellular materials[1–6].

In this thesis, a commercial PMMA grade (PLEXIGLAS® 7H) was used to produce microcellular and nanocellular polymers by gas dissolution foaming. The material was kindly supplied by Röhm GmbH in the form of pellets. This PMMA is characterized by a density of 1190 kg/m^3, a melt flow index (MFI) of 0.77 g/10 min (measured at 230 ºC and 2.16 kg) and a glass transition temperature (T_g) of 110.4 ºC measured by DSC (model DSC3+, Mettler) using a heating cycle performed between 20 °C and 160 °C at 10 °C/min (first cycle).

3.1.2. Carbon dioxide (CO_2)

Medical grade of carbon dioxide (CO_2) with 99.9% of purity was selected as the blowing agent for the gas dissolution foaming experiments.

3.1.3. Infrared blockers

An infrared blocker (IR-Blocker) or opacifier is a material that strongly absorbs or scatters infrared radiation. Three different types of IR-Blockers were used in this thesis: titanium dioxide (TiO_2) supplied by Riedel-de Haën (product code: 14027), graphite nanoplatelets (GnP) PLAT7 provided by Avanzare, and silicon carbide (SiC) F1000 supplied by Navarro SiC. These materials have different attenuation behaviors: TiO_2 and SiC powder particles both scatter and absorb radiation, meanwhile, GnP reduces the infrared transmission mainly by absorption[7,8]. The study of the effect of the addition of opacifiers to the materials produced in this thesis is shown in **Chapter 4** Section 4.6.

Figure 3.2 shows the appearance of the powders and their particles, whereas **Table 1** summarizes the particle size of the IR-Blockers (from the technical datasheets). As observed in **Figure 3.2**, TiO_2 is a white powder of spherical particles, GnP is a black powder of laminar shape particles, and SiC is a gray powder of polyhedral particles.

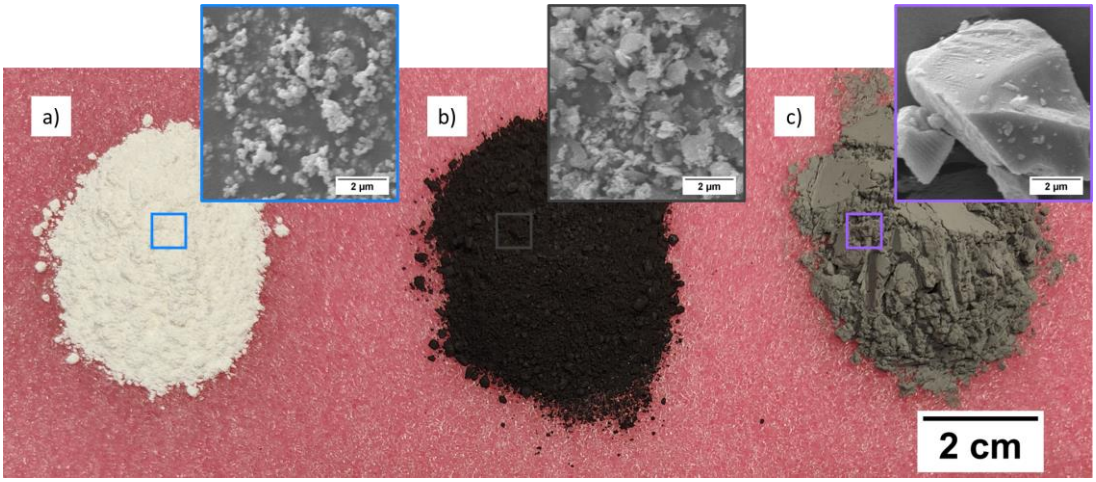

Figure 3.2. Photographs and SEM micrographs of the IR-blockers used in this thesis: a) TiO_2, b) GnP, and c) SiC.

Table 1. Particle size of the IR-blockers used in this thesis.

IR-Blocker	Particle Size
TiO_2	100-150 nm of diameter
GnP	7 µm of lateral size 2-3 nm of thickness
SiC	5 µm of diameter

3.2. Production methods

3.2.1. Solid samples production

Solid sheets of 4 mm in thickness were prepared by compression molding using a hot/cold plate hydraulic press provided by Talleres Remtex (Barcelona, Spain) (**Figure 3.3**). First, the commercial pellets were dried at 80 °C for at least 12 hours in a vacuum drying oven (model VacioTem TV, JP Selecta) at 150 mbar to remove the moisture. Second, the necessary amount of pellets was weighed and placed inside a mold (dimensions of 155×75×4 mm^3). Afterward, the mold is placed on the hot plate, and the polymer is heated at 250°C for 9 min without applying any pressure. During these 9 minutes, the polymer softens due to the selected temperature, which is higher than its T_g. Then, 20 tons are applied for one additional minute, allowing the softened PMMA to acquire the shape of the mold. Finally, the samples were cooled down to room temperature under the same pressure using the cold plate.

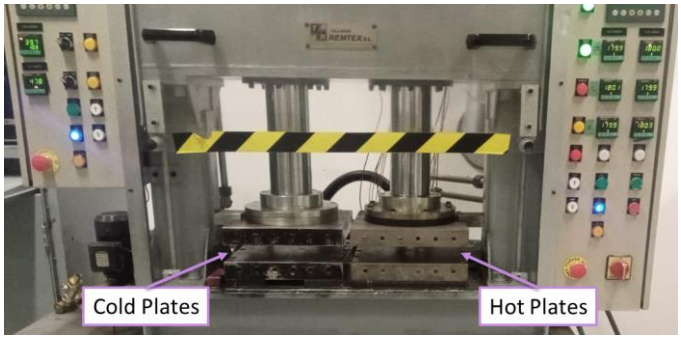

Figure 3.3. Hot and cold plates press.

The PMMA sheets were cut with a band sawing machine (model LB1200F, Makita) into samples with dimensions of 50×50×4 mm^3 to perform the foaming experiments.

3.2.2. Cellular materials production

Foaming experiments were performed in a high-pressure vessel (model PARR 4681, Parr Instruments Company) with a capacity of 1 liter, capable of operating at a maximum temperature of 350 °C and a maximum pressure of 41 MPa. An accurate pressure pump controller (model SFT-10, Supercritical Fluid Technologies Inc.) controls automatically the pressure to keep the desired value. The vessel is equipped with a clamp heater of 1200 W, and its temperature is controlled via a CAL 3300 temperature controller. With this setup (**Figure 3.4**) foaming experiments were performed using a two-step gas dissolution foaming process[9]. Extensive details about this process and the physical mechanisms involved in it can be found in **Chapter 2**.

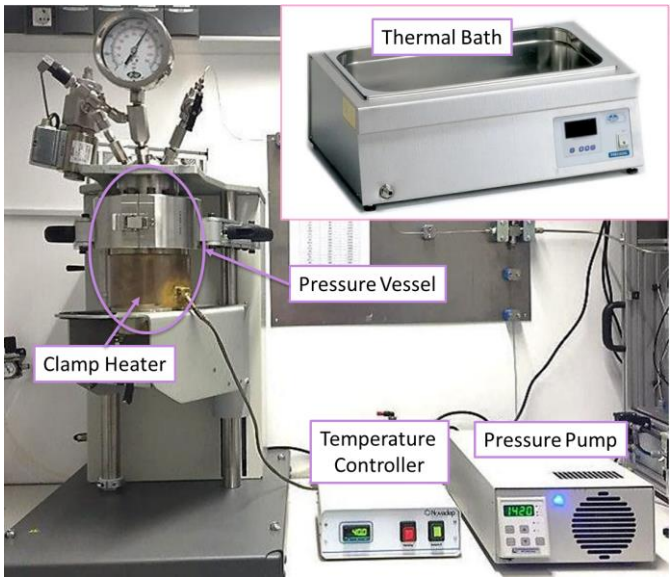

Figure 3.4. Set-up for the foaming experiments.

Samples were first introduced in the pressure vessel for the saturation stage. A collection of foamed samples with different cell sizes and densities was obtained by varying the saturation and foaming conditions. Saturation temperature varied from 25 to 45 °C, whereas saturation pressure varied

between 30-31 MPa. The saturation time was 20 h. This time is enough to ensure that the PMMA samples are fully saturated[10]. After saturation, the pressure was abruptly released. The pressure drop rate was of about 100 MPa/s during the first instants of the pressure drop[11]. Then, samples were removed from the pressure vessel and immersed in a water bath (model 6001222, J.P. Selecta) at 90 °C. The foaming time varied between 1 and 5 min.

Note that, under these saturation conditions, the effective glass transition temperature of PMMA after the gas absorption is below room temperature[10], so samples start to expand immediately after the release of pressure. Nevertheless, this expansion is clearly smaller than that taking place when the samples are introduced in the thermal bath at 90 ºC.

From the foamed samples (**Figure 3.5**), samples with dimensions of 50×50 mm^2 were cut using a band sawing machine (model LB1200F, Makita). Then, the solid skin was removed using a polisher (LaboPOl2-LaboForce3, Struers) to obtain a homogeneous sample to perform an accurate study of the influence of the density and cell size on thermal conductivity. The thickness of the final samples after polishing was 7 mm.

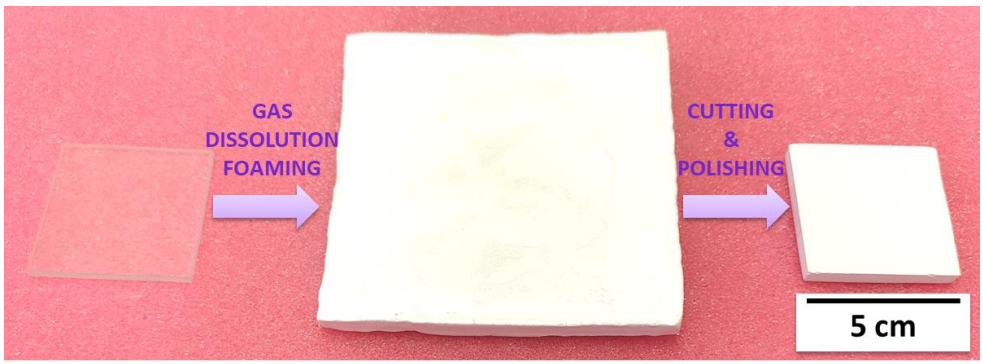

Figure 3.5. From left to right: PMMA solid precursor, cellular material obtained after the foaming experiment, and 50×50×7 mm^3 specimen obtained after cutting and polishing the cellular material.

3.2.3. Micronized cellular materials production

The bulk nanocellular samples were pre-grinded in a grinding machine (550 W of power) and then micronized using a rotor beater mill SR 300 (Retsch). For both processes, the samples were immersed in liquid nitrogen for at least 5 min to brittle them and preserve the cellular structure during milling. The grinding time was 15 s. The objective of the pre-grinding is to obtain particles smaller than 5×5×5 mm^3 able to be dosed in the rotor beater mill. The rotor beater mill speed was set at 10000 rpm, and the cold material was dosed every 15 s in small quantities to prevent excessive heating of the system. The sieve used to micronize the samples was a trapezoid stainless sieve with holes of 350 µm size. The sieve determines the maximum size of the powder particles but the friction during the rotation together with the cryogenic cooling may result in smaller particles as seen later. The processing conditions were optimized to prevent the collapse of the foam structure.

After the milling process, the resultant materials were homogeneous powders with micrometric particles characterized by an inner porosity (**Figure 3.6**).

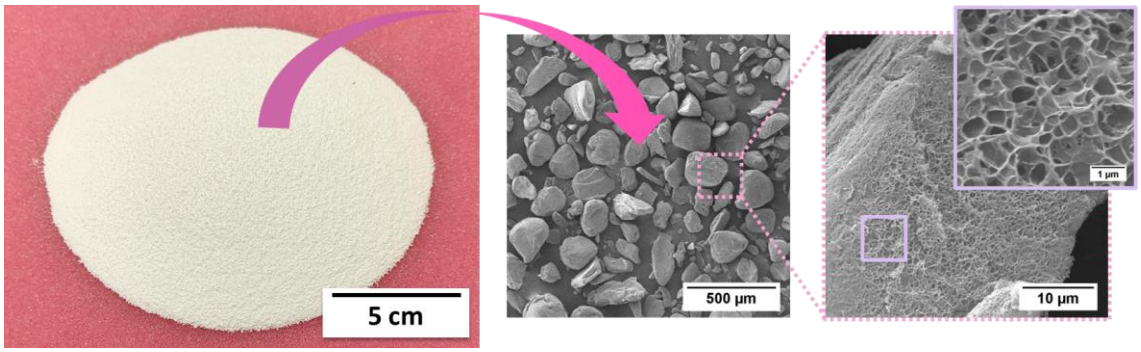

Figure 3.6. Micronized cellular material.

3.2.4. Compacted panels production

The micronized cellular materials were compacted using a hot plate hydraulic press with accurate control provided by Talleres Remtex (Barcelona, Spain). First, the micronized cellular materials were dried at 60 °C for 30 min in a forced-air high-temperature oven (model 2001405, JP Selecta). Second, the necessary amount of powder was weighed and placed inside a mold (dimensions of 120×120×15 mm^3). The target apparent density of the compacted samples presented in **Chapter 4** Section 4.4 is 145% of the apparent density of the micronized material. Meanwhile, the samples presented in section **Chapter 4** Section 4.6 are densified to a certain density (densification higher than 145% for some of the samples) to properly compare their thermal conductivity. Afterward, the mold is placed on the press under 20 tons at 80 ºC for 30 min. Finally, the sample is removed from the mold obtaining the self-standing compacted panel which is stable and can be handled (**Figure 3.7**).

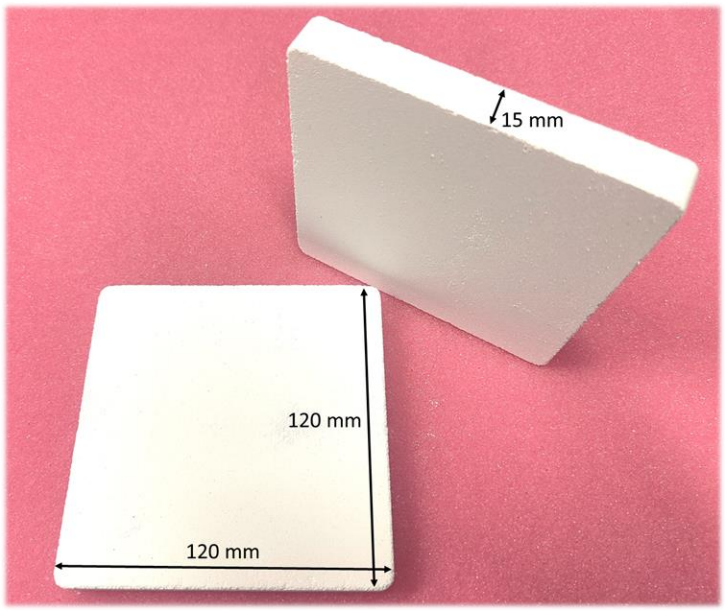

Figure 3.7. Compacted panels.

3.2.5. VIP prototype production

To produce VIPs prototypes (**Figure 3.8**), a set-up consisting of a vacuum pump (RV3, Edwards), a vacuum valve (VAC VALVE 425, Matva), a heat sealing tong (HPL WSZ 300, Hawo), and a vacuum bag (Pack-lab) was used. The vacuum pump allows an ultimate pressure of 0.002 mbar. First, the material is wrapped in fleece (**Figure 3.8b**) and then introduced in a vacuum bag with a composition of 12 µm of metalized PET and 80 µm of PE (sealant) (**Figure 3.8c**). The vacuum bag is connected to the vacuum pump through a vacuum valve and different accessories. Once the material is inside the vacuum bag the borders are sealed isolating the interior of the exterior. Finally, the pump is connected. After 2 days of performing vacuum to assure full evacuation of the gas inside the material (**Figure 3.8d**), the prototype is isolated from the vacuum valve by sealing the envelope in the region between them, obtaining a VIP prototype (**Figure 3.8e**).

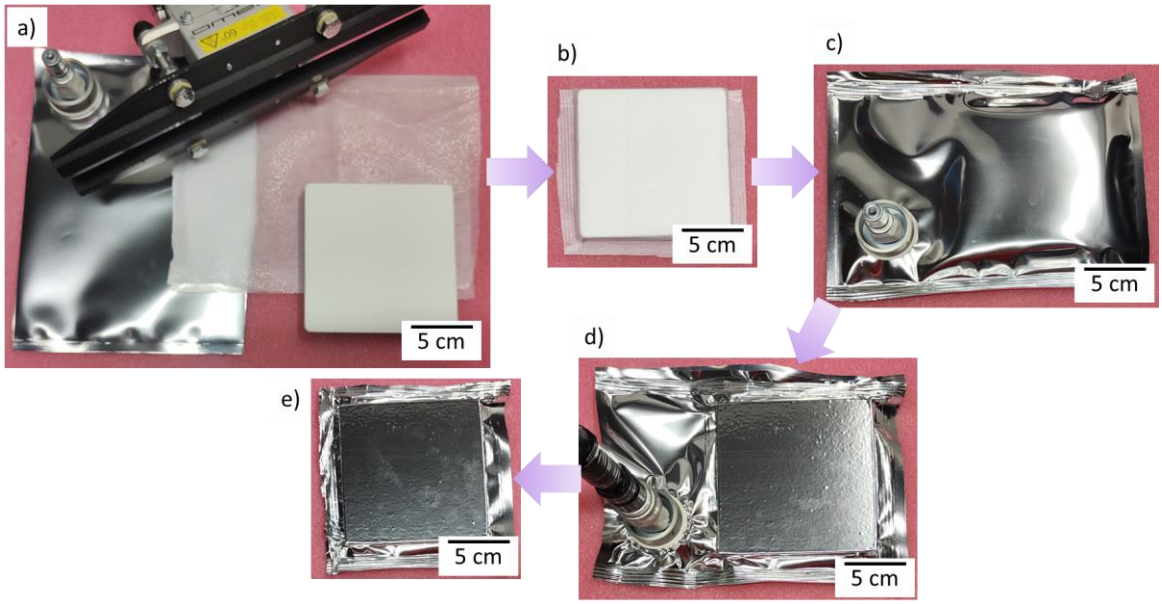

Figure 3.8. VIP prototype production: a) heat sealing tong, vacuum valve, vacuum bag, fleece, and compacted panel, b) compacted panel wrapped in fleece, c) compacted panel wrapped on fleece introduced in the vacuum bag and sealing, d) vacuum is applied, and e) final VIP prototype.

3.3. Characterization methods

Table 2 present a scheme of the characterization techniques used for each type of material (solid, bulk cellular material, micronized cellular material, and compacted panel). In the following sections, the characterization of each parameter for each material is detailed.

Table 2. Characterization techniques used in this thesis for the different types of material.

Material & Characterization	*Solid*	*Bulk Cellular Material*	*Micronized Cellular Material*	*Compacted Panel*
Density	Pycnometer	Archimedes' Principle	Apparent Density	Apparent Density
Cellular Structure	-	Scanning Electron Microscope	Scanning Electron Microscope	Scanning Electron Microscope
Open Cell Content	-	Pycnometer	Pycnometer	-
Particle Size	-	-	X-Ray Tomography Image Analysis Laser Diffraction	-
Thermal Conductivity	-	Heat Flow Meter Transient Plane Source	Heat Flow Meter	Heat Flow Meter

3.3.1. Density

3.3.1.1. Solid

The density of the solid PMMA (ρ) was measured with a gas pycnometer model AccuPyc II 1340 from Micromeritics according to ISO 12154[12]. The pycnometer provides the volume of the solid samples with high precision and calculates the density once the mass is given by the user. The density of the solid samples was determined using nitrogen (N_2) at a pressure of 19.5 psig and performing at least five measurements to obtain an accurate average value of the density.

3.3.1.2. Bulk cellular material

The density of the polished bulk cellular materials ($\rho_{\_B}$) was obtained according to ISO 1183-1[13] using the water-displacement method based on Archimedes' principle. A density determination kit for an AT261 Mettler-Toledo balance was used.

3.3.1.3. Micronized cellular material

When a material is micronized, it is now formed by micrometric particles surrounded by air voids (**Figure 3.9**). The powder is characterized by its apparent density (ρ_{app_M}). ρ_{app_M} was obtained according to ISO 60[14], by filling a known volume (V) with a given mass (m) and screeding ($\rho_{app\_M} = m / V$).

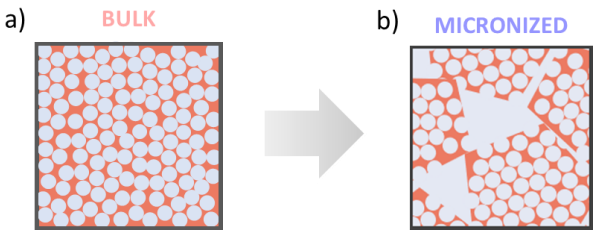

Figure 3.9. Scheme of a) bulk material and b) micronized material.

Assuming that each particle is characterized by a density ($\rho_{particle\_M}$), it is possible to define a packaging factor, F, calculated as Equation (3.1). Note that if the powder particles suffer some type

of densification during the milling process their density may be higher than the density of the initial bulk material ($\rho_{particle\_M} \geq \rho_{\_B}$).

$$F = \frac{\rho_{app\_M}}{\rho_{particle\_M}} \tag{3.1}$$

This packaging factor accounts for the fraction of the powder that is occupied by the particles (and not the voids), that is, the fraction of foamed particles in the powder. For random packaging of non-spherical particles, packaging factors as high as 0.77 are expected[15,16]. The experimental packaging factor can be obtained through X-Ray tomography (see Section 3.3.4.1).

3.3.1.4. Compacted panel

The apparent density of the compacted panel (ρ_{app_C}) was obtained according to UNE-EN 1602[17] by measuring the geometric volume (V) and the mass (m) of the piece ($\rho_{app\_C} = m / V$). Due to the compaction process, the powder particles suffer some densification resulting in a higher density ($\rho_{particle\_C}$)

3.3.2. Open Cell content (OC)

The open cell content (OC) of the materials was obtained according to ISO 4590[18] through Equation (3.2), using a gas pycnometer (model AccuPyc II 1340, Micromeritics). The gas used was N_2.

$$OC\ (\%) = \frac{V - V_{pyc}}{V(1 - \rho_r)} \cdot 100 \tag{3.2}$$

Where V is the geometric volume and V_{pyc} is the volume obtained from the pycnometric measurement. V_{pyc} was determined by using a pressure of 19.5 psig. The gas used was N_2.

3.3.2.1. Bulk cellular material

For the cellular materials, the geometric volume (V) was determined from the cellular material density (measured by the water-displacement method as explained in Section 3.3.1.1) and its mass (measured with an AT261 Mettler-Toledo balance) as $V = m / \rho_{\_B}$.

3.3.2.2. Micronized cellular material

For the micronized cellular materials, V is calculated after dividing the weight of the total amount of powder particles introduced in the pycnometer (measured with an AT261 Mettler-Toledo balance) between the density of the powder particles ($V = m / \rho_{particle\_M}$).

3.3.3. Cellular structure

3.3.3.1. Bulk cellular material

The cellular structure was analyzed using a Scanning Electron Microscope (FlexSEM 1000 VP-SEM). Samples were cooled in liquid nitrogen and fractured to maintain the cellular structure for the microscopic visualization. They were also coated with gold using a sputter coater (model SCD 005, Balzers Union). Several parameters were measured to obtain a complete analysis of the cellular structure. A tool based on ImageJ/FIJI[19] was used to obtain the average cell size in 3D (ϕ_{3D}), the cell size distribution, and the standard deviation coefficient (SD) (a correction factor of 1.273[19] was applied to the 2D values measured in the SEM micrograph to obtain the 3D values). The normalized standard deviation coefficient (SD/ϕ_{3D}) was calculated as an indicator of the homogeneity of the cellular structure. **Figure 3.10** shows an example of the process to produce a binary image from a regular SEM image.

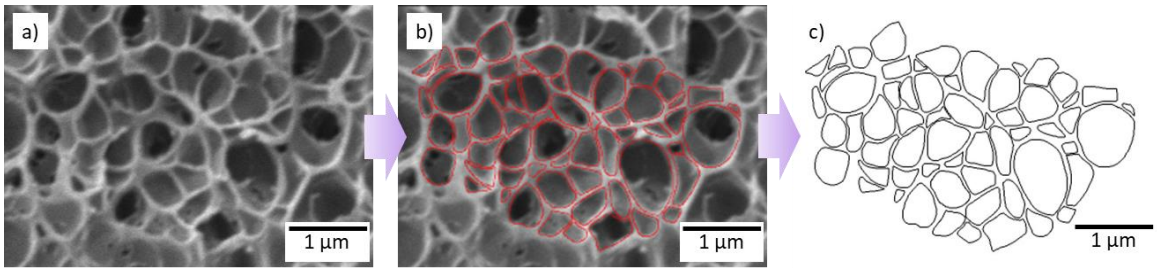

Figure 3.10. Example of image processing: a) original SEM image, b) manual standing out of the cells, and c) binary mask for image analysis.

Cell density (N_v) was determined using Kumar's theoretical approximation[20] (Equation (3.3)), where A is the analyzed area and n is the number of cells in that area. Finally, cell nucleation density (N_0) was determined (Equation (3.4)). More than 1000 cells per reference material were analyzed.

$$N_v = \left(\frac{n}{A}\right)^{3/2} \tag{3.3}$$

$$N_0 = \frac{N_v}{\rho_r} \tag{3.4}$$

3.3.3.2. Micronized cellular material

Scanning Electron Microscope (FlexSEM 1000 VP-SEM) was also used to visualize the surface of the micrometric particles and evaluate the effect of the micronization process on the cellular structure. The powders were also coated with gold using a sputter coater (model SCD 005, Balzers Union) to allow the visualization.

3.3.3.3. Compacted panel

Scanning Electron Microscope (FlexSEM 1000 VP-SEM) was used to visualize the surface of the compacted panel and the micrometric particles after the compaction process. The powders were coated with gold using a sputter coater (model SCD 005, Balzers Union) to allow the visualization.

3.3.4. Particle size

3.3.4.1. X-ray tomography

The particle size distribution of the micronized material was studied using a laboratory X-ray tomography setup [21–23]. The set-up consists of an X-ray microfocus source (Hamamatsu) with a maximum output power of 20 W (spot size: 5 μm, voltage: 20–100 kV, current:0–200 μA). Emitted X-rays form a cone beam of 39°, allowing up to obtain 20 times magnification in the experiments. The transmitted X-ray intensity is collected with a high-sensitivity flat panel connected to a frame grabber (Dalsa-Coreco), which records the projected images. The detector is composed of a matrix of 2240×2344 pixels, each with a size of 50 μm.

A Kapton cylinder of around 5 mm of diameter and 10 mm in height was used to hold the powder. Kapton is transparent to X-ray radiation allowing the acquisition of images of the powder inside the cylinder. The linear stage was placed in a position so that the pixel size was 3 μm. The tube voltage, current, exposure time, and rotation step were set to 55 kV, 170 μA, 1 s, and 0.3º. To enhance the contrast in the reconstructed images, each projection was the result of integrating three consecutive images. Once all the projections were acquired, the reconstruction process of the tomogram was carried out using the Octopus server/client reconstruction package[24] by reconstructing 1800 slices (equivalent to 5.4 mm in height). Due to the spatial resolution of the tomographic system (3 μm), the reconstructed slices (**Figure 3.11a**) can be used to analyze the volume occupied by the powder particles and the voids between the particles with respect to the total volume. With this aim, the slices were binarized using the software ImageJ/FIJI (**Figure 3.11b**). Once binarized, the particles are characterized by white pixels, whereas the void's pixels are black. Therefore, the number of white pixels regarding the total is the volume fraction of foamed particles, or in other words, the experimental packaging factor (*F*) (Equation (3.1)).

The local thickness analysis ImageJ/FIJI tool was used to study the powder particle size distribution (**Figure 3.11c**) and the void size distribution (**Figure 3.11d**). The void size is the size of the air regions that appear between the powder particles. By definition, the local thickness is the diameter of the largest sphere that fits inside the object and contains the point. Thus, this tool associates a thickness value (represented by a determined color) to each pixel. Hence, each pixel is characterized by a color that is related to a distance. From the color distribution, the desired distribution in percentage of number (%number) of either the particle size (**Figure 3.11e**) or the void size (**Figure**

3.11f) can be obtained. Also, it is possible to calculate the average particle size (D_T) and the average void size (V_T). D_T is obtained by performing the arithmetic mean (Equation (3.5)), where d_i is the distance associated to each pixel, and p is the total amount of pixels. V_T is calculated in the same way. Note that this technique assumes spherical particles.

$$D_T = \frac{\sum_{i=1}^{p} d_i}{p} \tag{3.5}$$

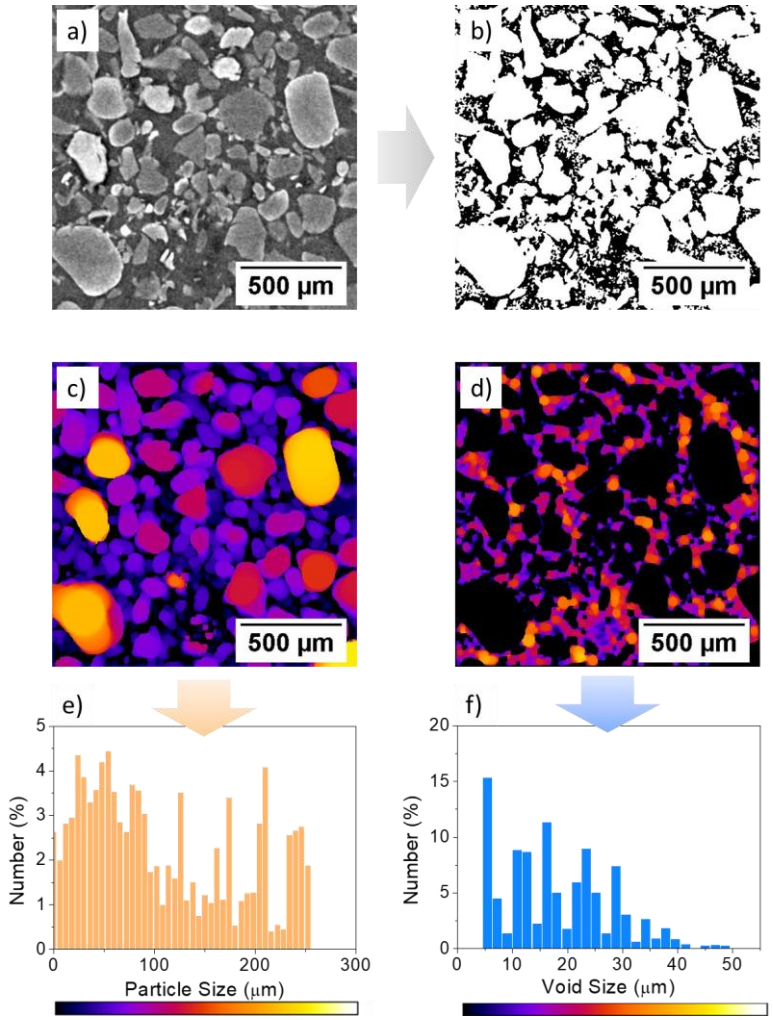

Figure 3.11. a) Raw X-ray tomography slice, b) binarized X-ray tomography slice (in white the powder particles and in black the voids), c) powder particles local thickness map slice, d) voids local thickness map slice, e) particle size distribution, and f) void size distribution.

3.3.4.2. Image analysis (Autocell)

The particle size distribution was also studied using an image analysis tool (Autocell) developed by CellMat Technologies S.L. (Valladolid, Spain) to characterize the cellular structure of different types of foamed samples. The tool allows obtaining accurate results quickly and cheaply. Details about the methodology, characteristics, and advantages of Autocell can be found in[25]. In this work, Autocell is used to characterize the particle size distribution (**Figure 3.12**). First, the powder

is dispersed on a contrasting background to take a picture with a small portable benchtop optical microscope (**Figure 3.12a**). This setup allows measuring accurately particles larger than 15 µm. Then, the image is analyzed with Autocell. The software selects the powder particles (**Figure 3.12b**) and creates a mask (**Figure 3.12c**) which is used to obtain the particle size distribution. More than 800 particles are analyzed. This technique assumes spherical particles and gives the powder particles size distribution in percentage of number (%number), from which it is possible to calculate the average particle size (D_{IA}). D_{IA} is obtained by performing the arithmetic mean (Equation (3.6)), where D_i is the particle size of each measured particle and n is the total amount of particles.

$$D_{IA} = \frac{\sum_{i=1}^{n} D_i}{n} \tag{3.6}$$

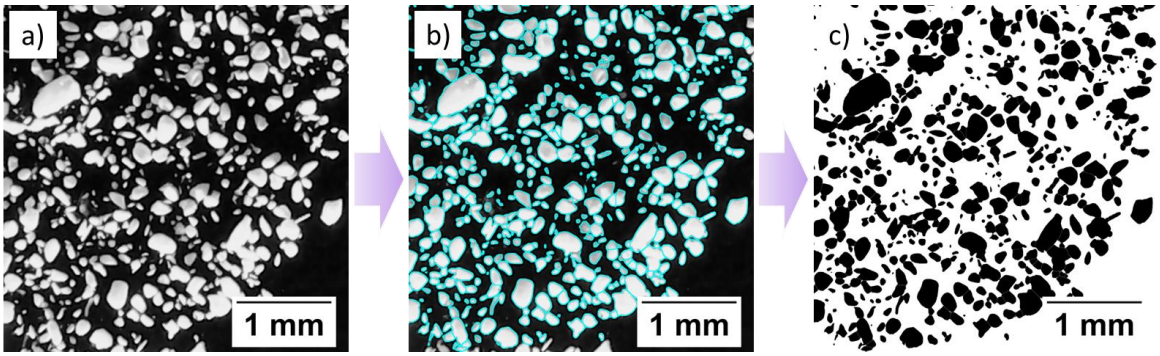

Figure 3.12. Methodology of Autocell: a) raw image, b) selection of particles on the raw image, and c) mask to be analyzed.

3.3.4.3. Laser Diffraction (LD)

Moreover, laser diffraction measurements were performed to study the particle size distribution according to ISO 13320[26]. Laser diffraction allows measuring particles between 40 nm and 2000 µm. Experiments were carried out at CENIEH (Burgos, Spain) using a LS13 320 Particle Size Analyzer (Beckman Coulter). The powder particles are dispersed for one minute in ethanol with ultrasounds. Then, they are analyzed in the ULM module. This technique assumes spherical particles and provides the particle size distribution in percentage of volume (%volume), from which it is possible to calculate the average particle size (D_{LD}). Note that in volume distributions, the larger particles have a higher weight than the smaller ones. D_{LD} is provided by the analysis software, and it is obtained through Equation (3.7). This equation gives the mean particle size (De Brouckere's mean diameter) of a distribution weighted by the volume.

$$D_{LD} = \frac{\sum_{i=1}^{m} f_i D_i^4}{\sum_{i=1}^{m} f_i D_i^3} \tag{3.7}$$

Where f_i is the frequency of occurrence of particles in size class i (there are m classes) in %volume, having a mean diameter D_i. Note that Equation (3.7) multiplies the volume of each class by its frequency and associated size, and divides by the total volume to calculate the mean particle size.

3.3.5. Thermal conductivity

3.3.5.1. Heat Flow Meter (HFM) (Steady-state)

Steady-state thermal conductivity measurements were carried out using a thermal heat flow meter model FOX 200 or FOX 314 (TA Instruments / LaserComp, Inc.), which measures according to ASTM C518 and ISO 8301[27,28]. For the measurements, the sample (polished cellular material, micronized cellular material, or compacted panel) was placed between the two plates, promoting a temperature gradient through the material thickness. Measurements were performed at 10, 20, 30, and 40 ºC. The temperature gradient (ΔT) was set to 20 ºC in every case (i.e., for the measurement at 10 ºC, the temperature goes from 0 ºC in the upper isothermal plate to 20 ºC in the lower one). The active area of the FOX 200 heat flux transducers is 75×75 mm^2, whereas the active area of the FOX 314 heat flux transducers is 100×100 mm^2. The absolute thermal conductivity accuracy for these devices is 2%.

For the measurements under vacuum, a set-up consisting of a vacuum pump (RV3, Edwards), a vacuum controller (VacuuSelect + VV-B15C electrovalve + Pirani VacuuWiew extend sensor, Vacuubrand), a vacuum valve (VAC VALVE 425, Matva), and a vacuum bag (Pack-lab) has been used (**Figure 3.13**). The vacuum pump allows an ultimate pressure of 0.002 mbar. The vacuum controller consists of a device (VacuuSelect) that allows to set and control the desired pressure by connecting the electrovalve and the Pirani sensor. The VV-B15C electrovalve opens until the set pressure is reached and once the desired pressure is reached the electrovalve closes. If the pressure increases over the set value, the electrovalve opens again. The pressure is measured with the Pirani VacuuWiew extend sensor (able to measure pressures from ambient pressure to 0.001 mbar).

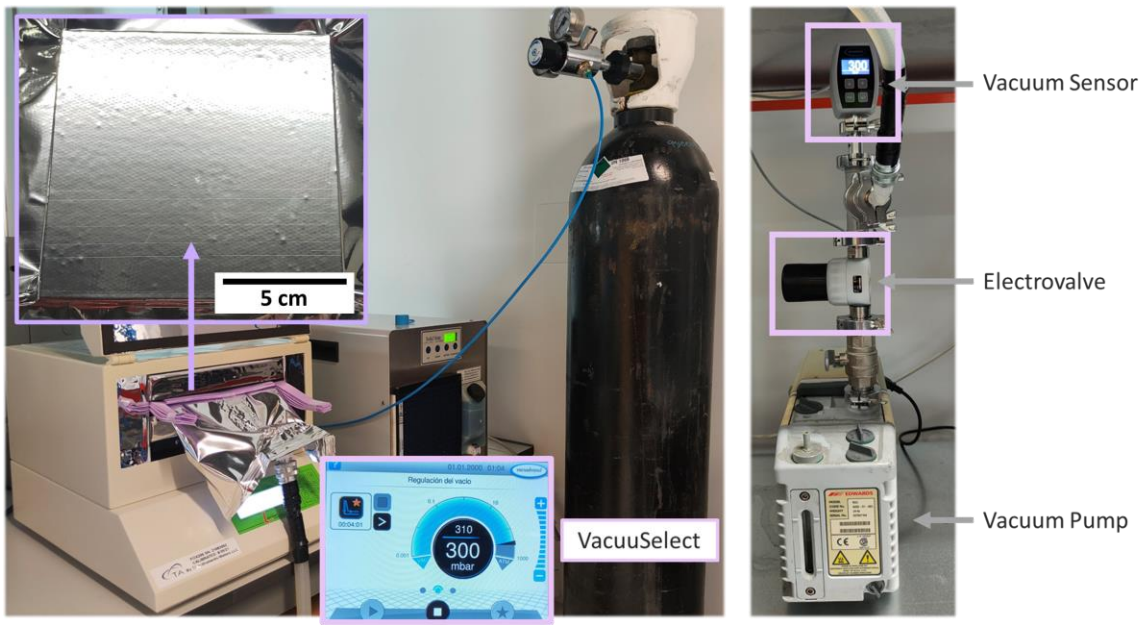

Figure 3.13. Set-up for measuring the thermal conductivity at different vacuum pressures.

The material to be measured under vacuum (either the bulk nanocellular samples or the VIP prototypes) is prepared as explained in Section 3.2.5 (**Figure 3.8**) but without removing the vacuum valve. The pump is connected to this valve and the vacuum inside can be controlled. To fill the remaining volume EVA foam strips were used as a mask to avoid convection.

For the measures at different pressures, a stabilization time of at least 2 hours was used once the desired pressure is reached. Meanwhile, for the measurement at maximum vacuum, the stabilization time was 2 days.

All of the samples of this work were prepared with dimensions large enough to be measured with the heat flow meter FOX 200. However, the fabrication of large prototypes is quite challenging in the case of nanocellular polymers, as already seen in **Chapter 2**. For this reason, in this thesis, we also investigated the possibility of measuring smaller prototypes with a new methodology specially designed for this purpose. The research in these measurement methodologies leads to two papers:

- Development of the external sensor method (Section 3.4): In this first paper, entitled ***"Methodology for measuring the thermal conductivity of insulating samples with small dimensions by heat flow meter technique"***, we developed and validated the technique using conventional insulators and one heat flux sensor placed on the cold plate. This paper was published in the **Journal of Thermal Analysis and Calorimetry** in 2022 (I. Sánchez-Calderón, B. Merillas, V. Bernardo, M.Á. Rodríguez-Pérez, Methodology for measuring the thermal conductivity of insulating samples with small dimensions by heat flow meter technique, J. Therm. Anal. Calorim. (2022). https://doi.org/10.1007/s10973-022-11457-7). The paper can be found at the end of this chapter in Section 3.4, where all the details about the setup and the validation of the model with commercial foams are explained in detail. Section 3.3.5.2 includes a brief overview of the experimental setup.

- Validation and optimization of the method to measure the thermal conductivity of small nanocellular polymers (Section 3.5): In this second paper, entitled ***"Evaluation of methods to accurately characterize the thermal conductivity of micro-and nanocellular polymers based on poly(methyl-methacrylate) (PMMA) produced at lab-scale"***, we study the validity of the method for microcellular and nanocellular PMMA (materials produced in **Chapter 4** (Section 4.2)) and compare the results with other steady-state and transient techniques, such as hot-disk transient plane source (TPS), extensively used in the literature to measure nanocellular polymers, as seen in **Chapter 2** (**Figure 2.13**). TPS is briefly explained below (section 3.3.5.3). This paper was published in **Polymer Testing** in 2022 (I. Sánchez-Calderón, Á. Sillero, F. Lizalde-Arroyo, V. Bernardo, J. Martín-de-León, M.Á. Rodríguez-Pérez, Evaluation of methods to accurately characterize the thermal conductivity of micro-and nanocellular polymers based on poly(methyl-methacrylate)

(PMMA) produced at lab-scale, Polym. Test. 117 (2023) 107842. https://doi.org/10.1016/j.polymertesting.2022.107842). For this work, the method was optimized, by using two heat flux sensors (each one placed on each plate) and the dataloggers that provide the higher resolution. The paper with all the details can be found at the end of this chapter in Section 3.5.

3.3.5.2. External heat flux sensors (Steady-state)

Heat flux sensors gSKIN®-XP 27 9C (greenTEG AG) and data loggers gSKIN® DLOG-4218 and DLOG-4219 (greenTEG AG) were used to create the set up to measure the thermal conductivity of small prototypes. The relative error of the flux measured is 3%. The combination of the sensor with DLOG-4219 provides a lower range of measurement than with DLOG-4218 (±120 vs. ±1100 W/m^2) but a higher resolution (0.09 vs 0.87 W/m^2). Sensor dimensions are 10×10 mm^2 with a thickness of 0.5 mm. The temperature range of the sensor is from -50 ºC to 150 ºC. The sensor is calibrated under steady-state conditions with a method that is oriented towards ISO8301[29]. To calculate the sensitivity of the sensor at temperature (T_s) Equation (3.8) is used, where S_0 and S_c are correction factors. Equation (3.8) and the correction factors are provided by greenTEG AG. The sensor temperature is obtained from a thermocouple which is connected to a PicoLog to register the temperature over time. Silicone rubbers are also used to assemble the set-up (**Figure 3.14**) and to minimize the fluctuations of the heat flux measurement.

$$S(T) = S_0 + (T_s - 22.5) \cdot S_c \tag{3.8}$$

The heat flux per unit area is finally calculated using the following formula (Equation (3.9)), where U is the sensor output voltage in μV.

$$q = \frac{Q}{A} = \frac{U}{S} \tag{3.9}$$

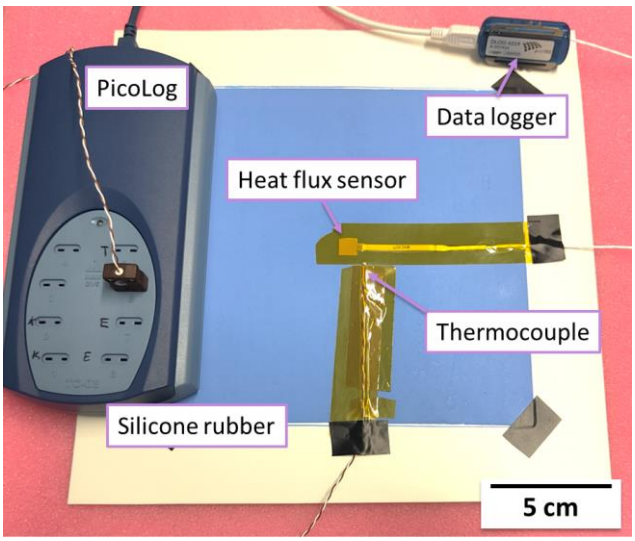

Figure 3.14. External heat flux sensors set-up.

The method for measuring the thermal conductivity of samples with small dimensions using external heat flux sensors is presented in Section 3.4. Four different thermal insulators (extruded polystyrene (XPS), expanded polystyrene (EPS), rigid polyurethane (PUR), and foamed polyethylene (PE)) were used to validate the developed methodology by performing measurements in the heat flow meter with and without the external sensor. From these results, a calibration curve that relates both methods was calculated. Further, the effect of the sample size was studied to explore the limits of the technique. Results show that the self-developed method is an accurate procedure to determine the thermal conductivity of samples with small dimensions (50×50 mm^2) via a steady-state condition.

Then, to validate this method for nanocellular polymers the thermal conductivity of the polished cellular materials described in Section 3.2.2 was determined with this setup and the results were compared to those of the conventional heat flow meter (Section 3.5). In addition, the samples were also measured using TPS as a comparative technique usually used in the literature.

3.3.5.3. Hot-disk transient plane source (TPS) (Transient)

As discussed in **Chapter 2** Sections 2.2.1.2 and 2.2.2.2 hot-disk transient hot plate (TPS) is a transient technique usually used to characterize insulating materials developed at lab-scale, because it allows measuring samples with small dimensions. However, despite it provides good trends (being useful for comparing samples with similar characteristics) the accuracy of its results is not clear[30–32]. For instance, TPS has been widely used to characterize nanocellular polymers[33–36]. To check the validity of TPS for nanocellular polymers, the thermal conductivity of the polished cellular materials was also determined using a hot-disk transient plane source thermal (TPS) constant analyzer model 2500 S (Hot Disk). TPS measures according to ASTM D 5930 and ISO 22007:2[37,38]. The accuracy of this equipment is 5%. The thermal conductivity measurement was carried out at room temperature (20 ± 2 °C). A disk-shaped TPS kapton-sensor (code 5501) with a diameter of 6.4 mm was used in all measurements. The sensor was placed between the two stacks of samples (**Figure 3.15**). The power output and test duration were 10 mW and 80 s, respectively. The measurement was performed at least 3 times for each sample to calculate an average value.

The results obtained with TPS are presented in Section 3.5. TPS provides thermal conductivity results with a high deviation (higher than 15%) from the reference value (HFM). In our measurements, the values are always high than those measured by the HFM. Those results are improved by applying the correction proposed by Zheng et al.[31], however, for the nanocellular samples, the deviations are still high. These results support that TPS might not be accurate to characterize the thermal conductivity of low-thermal conductivity materials and, in particular, for nanocellular polymers based on PMMA.

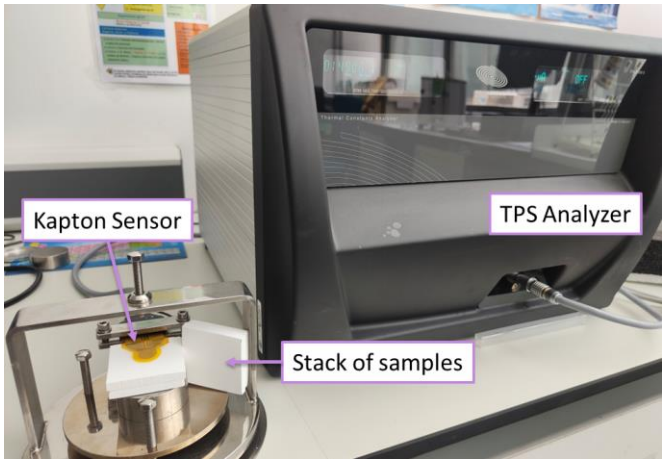

Figure 3.15. TPS measurements set-up.

References

[1] H. Guo, V. Kumar, Solid-state poly(methyl methacrylate) (PMMA) nanofoams. Part I: Low-temperature CO2 sorption, diffusion, and the depression in PMMA glass transition, Polymer (Guildf). 57 (2015) 157–163. https://doi.org/10.1016/j.polymer.2014.12.029.

[2] J. Pinto, J.A. Reglero-Ruiz, M. Dumon, M.A. Rodriguez-Perez, Temperature influence and CO2 transport in foaming processes of poly(methyl methacrylate)–block copolymer nanocellular and microcellular foams, J. Supercrit. Fluids. 94 (2014) 198–205. https://doi.org/10.1016/j.supflu.2014.07.021.

[3] J. Martín-de León, V. Bernardo, M.Á. Rodríguez-Pérez, Key Production Parameters to Obtain Transparent Nanocellular PMMA, Macromol. Mater. Eng. 302 (2017) 1700343. https://doi.org/10.1002/mame.201700343.

[4] V. Bernardo, J. Martin-de Leon, J. Pinto, T. Catelani, A. Athanassiou, M.A. Rodriguez-Perez, Low-density PMMA/MAM nanocellular polymers using low MAM contents: Production and characterization, Polymer (Guildf). 163 (2019) 115–124. https://doi.org/10.1016/j.polymer.2018.12.057.

[5] J. Martín-de León, V. Bernardo, M. Rodríguez-Pérez, Low Density Nanocellular Polymers Based on PMMA Produced by Gas Dissolution Foaming: Fabrication and Cellular Structure Characterization, Polymers (Basel). 8 (2016) 265. https://doi.org/10.3390/polym8070265.

[6] I. Sánchez-Calderón, V. Bernardo, M. Santiago-Calvo, H. Naji, A. Saiani, M.Á. Rodríguez-Pérez, Effect of the molecular structure of TPU on the cellular structure of nanocellular polymers based on PMMA/TPU blends, Polymers (Basel). 13 (2021). https://doi.org/10.3390/polym13183055.

[7] R. Caps, J. Fricke, Thermal conductivity of opacified powder filler materials for vacuum insulations, Int. J. Thermophys. 21 (2000) 445–452. https://doi.org/10.1023/A:1006691731253.

[8] F. Almeida, H. Beyrichen, N. Dodamani, R. Caps, A. Müller, R. Oberhoffer, Thermal conductivity analysis of a new sub-micron sized polystyrene foam, J. Cell. Plast. 57 (2021) 493–515. https://doi.org/10.1177/0021955X20943101.

[9] V. Kumar, N.P. Suh, A process for making microcellular thermoplastic parts, Polym. Eng. Sci. 30 (1990) 1323–1329. https://doi.org/10.1002/pen.760302010.

[10] J. Pinto, M. Dumon, M. Pedros, J. Reglero, M.A. Rodriguez-Perez, Nanocellular CO2 foaming of PMMA assisted by block copolymer nanostructuration, Chem. Eng. J. 243 (2014) 428–435. https://doi.org/10.1016/j.cej.2014.01.021.

[11] V. Bernardo, Production and Characterization of Nanocellular Polymers Based on Nanostructured PMMA Blends and PMMA Nanocomposites. (July 2019), n.d.

[12] ISO 12154 Determination of density by volumetric displacement — Skeleton density by gas pycnometry, (2014).

[13] UNE-EN ISO 1183-1:2019 Plásticos. Métodos para determinar la densidad de plásticos no celulares. Parte 1: Método de inmersión, método del picnómetro líquido y método de valoración., (2019).

[14] ISO 60:1977 Plastics — Determination of apparent density of material that can be poured from a specified funnel, (1977).

[15] X. Chateau, Particle packing and the rheology of concrete, in: Underst. Rheol. Concr., Elsevier, 2012: pp. 117–143. https://doi.org/10.1533/9780857095282.2.117.

[16] A. Averardi, C. Cola, S.E. Zeltmann, N. Gupta, Effect of particle size distribution on the packing of powder beds: A critical discussion relevant to additive manufacturing, Mater. Today Commun. 24 (2020) 100964. https://doi.org/10.1016/j.mtcomm.2020.100964.

[17] UNE-EN 1602:2013 Thermal insulating products for building applications. Determination of the apparent density., (n.d.).

[18] ISO 4590:2016 Rigid cellular plastics — Determination of the volume percentage of open cells and of closed cells, (2016).

[19] J. Pinto, E. Solórzano, M.A. Rodriguez-Perez, J.A. de Saja, Characterization of the cellular structure based on user-interactive image analysis procedures, J. Cell. Plast. 49 (2013) 555–575. https://doi.org/10.1177/0021955X13503847.

[20] V. Kumar, Process synthesis for manufacturing microcellular thermoplastic parts, Massachusetts Inst. Technol. (1988).

[21] E. Solórzano, J. Pinto, S. Pardo, F. Garcia-Moreno, M.A. Rodriguez-Perez, Application of a microfocus X-ray imaging apparatus to the study of cellular polymers, Polym. Test. 32 (2013) 321–329. https://doi.org/10.1016/j.polymertesting.2012.11.016.

[22] A. Ballesteros, E. Laguna-Gutierrez, P. Cimavilla-Roman, M.L. Puertas, A. Esteban-Cubillo, J. Santaren, M.A. Rodriguez-Perez, Influence of the dispersion of Nanoclays on the cellular structure of foams based on polystyrene, J. Appl. Polym. Sci. 138 (2021) 1–19. https://doi.org/10.1002/app.51373.

[23] P. Cimavilla-Román, S. Pérez-Tamarit, S. Barroso-Solares, J. Pinto, M.Á. Rodríguez-Pérez, Sub-pixel Tomographic Methods for Characterizing the Solid Architecture of Foams, Microsc. Microanal. (2022) 1–12. https://doi.org/10.1017/s1431927622000447.

[24] M. Dierick, B. Masschaele, L. Van Hoorebeke, Octopus, a fast and user-friendly tomographic reconstruction package developed in LabView, Meas. Sci. Technol. 15 (2004) 1366–1370. https://doi.org/10.1088/0957-0233/15/7/020.

[25] http://www.cellmattechnologies.com/en/software-and-methodology-for-the-characterization- of-cellular-structures/, (n.d.).

[26] ISO 13320:2020 Particle size analysis — Laser diffraction methods, (2020).

[27] ASTM C518 Standard Test Method for Steady-State Thermal Transmission Properties by Means of the Heat Flow Meter Apparatus, (2017).

[28] ISO 8301 Thermal insulation - Determination of steady-state thermal resistance and related properties - Heat flow meter, (1991).

[29] E.S. Schwyter, T. Helbling, W. Glatz, C. Hierold, Fully automated measurement setup for non-destructive characterization of thermoelectric materials near room temperature, Rev. Sci. Instrum. 83 (2012). https://doi.org/10.1063/1.4737880.

[30] O. Almanza, M.A. Rodríguez-Pérez, J.A. De Saja, Applicability of the Transient Plane Source Method To Measure the Thermal Conductivity of Low-Density Polyethylene Foams, J. Polym. Sci. Part B Polym. Phys. 42 (2004) 1226–1234. https://doi.org/10.1002/polb.20005.

[31] Q. Zheng, S. Kaur, C. Dames, R.S. Prasher, Analysis and improvement of the hot disk transient plane source method for low thermal conductivity materials, Int. J. Heat Mass Transf. 151 (2020) 119331.

https://doi.org/10.1016/j.ijheatmasstransfer.2020.119331.

[32] R.C. Kerschbaumer, S. Stieger, M. Gschwandl, T. Hutterer, M. Fasching, B. Lechner, L. Meinhart, J. Hildenbrandt, B. Schrittesser, P.F. Fuchs, G.R. Berger, W. Friesenbichler, Comparison of steady-state and transient thermal conductivity testing methods using different industrial rubber compounds, Polym. Test. 80 (2019) 106121. https://doi.org/10.1016/j.polymertesting.2019.106121.

[33] B. Notario, J. Pinto, E. Solorzano, J.A. de Saja, M. Dumon, M.A. Rodríguez-Pérez, Experimental validation of the Knudsen effect in nanocellular polymeric foams, Polymer (Guildf). 56 (2015) 57–67. https://doi.org/10.1016/j.polymer.2014.10.006.

[34] G. Wang, J. Zhao, L.H. Mark, G. Wang, K. Yu, C. Wang, C.B. Park, G. Zhao, Ultra-tough and super thermal-insulation nanocellular PMMA/TPU, Chem. Eng. J. 325 (2017) 632–646. https://doi.org/10.1016/j.cej.2017.05.116.

[35] V. Bernardo, J. Martin-de Leon, J. Pinto, R. Verdejo, M.A. Rodriguez-Perez, Modeling the heat transfer by conduction of nanocellular polymers with bimodal cellular structures, Polymer (Guildf). 160 (2019) 126–137. https://doi.org/10.1016/j.polymer.2018.11.047.

[36] J. Zhao, G. Wang, Z. Xu, A. Zhang, G. Dong, G. Zhao, C.B. Park, Ultra-elastic and super-insulating biomass PEBA nanoporous foams achieved by combining in-situ fibrillation with microcellular foaming, J. CO2 Util. 57 (2022) 101891. https://doi.org/10.1016/j.jcou.2022.101891.

[37] ASTM D 5930 Standard Test Method for Thermal Conductivity of Plastics by Means of a Transient Line-Source Technique, (2017).

[38] ISO 22007-2:2022 Plastics - Determination of thermal conductivity and thermal diffusivity - Part 2: Transient plane heat source (hot disc) method, (2022).

3.4. Methodology for measuring the thermal conductivity of insulating samples with small dimensions by heat flow meter technique

Ismael Sánchez-Calderón[1], Beatriz Merillas[1], Victoria Bernardo[2], Miguel Ángel Rodríguez-Pérez[1,3].

[1]*Cellular Materials Laboratory (CellMat), Condensed Matter Physics Department, University of Valladolid, Campus Miguel Delibes, Paseo de Belén 7, 47011 Valladolid, Spain.*

[2]*CellMat Technologies S.L. Paseo de Belén 9-A, 47011, Valladolid, Spain.*

[3]*BioEcoUVA Research Institute on Bioeconomy, University of Valladolid, 47011, Valladolid, Spain*

Corresponding author: Ismael Sánchez-Calderón (ismaelsc@fmc.uva.es)

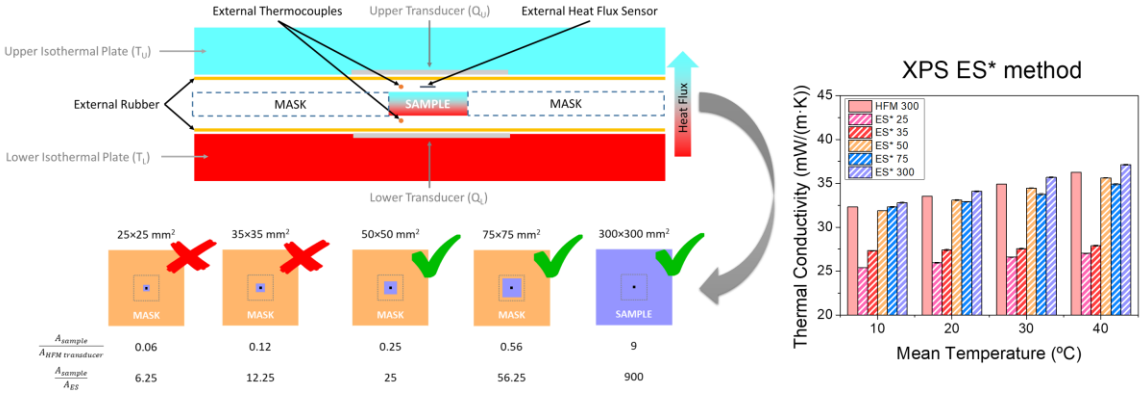

ABSTRACT

Nowadays, developing advanced, highly insulating materials for minimizing heat losses in buildings is of utmost relevance. Thus, there is a constant research activity focused on developing new and enhanced solutions for thermal insulation. However, characterizing the behavior of new thermal insulation materials, usually produced at lab-scale with small dimensions, by a steady-state approach is a challenge. The reason is that commercial heat flow meters require large samples (hundred on mm side) to provide accurate results of thermal conductivity because they are based on international standards. In this work, a new methodology to measure the thermal conductivity of small prototypes of thermal insulating materials (as low as 50×50 mm^2) is developed by using an external heat flow sensor placed into a standard heat flow meter apparatus. Four different thermal insulators were used to validate the developed methodology by performing measurements in the heat flow meter with and without the external sensor. From these results, a calibration curve that relates both methods was calculated. Further, the effect of the sample size was studied to explore the limits of the technique. Results show that the self-developed method is an accurate procedure to determine the thermal conductivity of samples with small dimensions via a steady-state condition.

Keywords: thermal conductivity, heat flux, heat flux sensor, heat flow meter, thermal insulator.

Published in: Journal of Thermal Analysis and Calorimetry 147 (2022) 12523–12533.

DOI: 10.1007/s10973-022-11457-7

3.5. Evaluation of methods to accurately characterize the thermal conductivity of micro-and nanocellular polymers based on poly(methyl-methacrylate) (PMMA) produced at lab-scale

Ismael Sánchez-Calderón[1], Ángel Sillero[1], Félix Lizalde-Arroyo[1], Victoria Bernardo[2], Judith Martín-de-León[1], Miguel Ángel Rodríguez-Pérez[1,3].

[1]*CellMat Laboratory. Campus Miguel Delibes. Faculty of Science. Condensed Matter Physics Department. University of Valladolid, Paseo de Belén 7, 47011, Valladolid, Spain.*

[2]*CellMat Technologies S.L., Paseo de Belén 9-A, 47011, Valladolid, Spain.*

[3]*BioEcoUVA Research Institute on Bioeconomy, University of Valladolid, 47011, Valladolid, Spain.*

Corresponding author: Ismael Sánchez-Calderón (ismaelsc@fmc.uva.es)

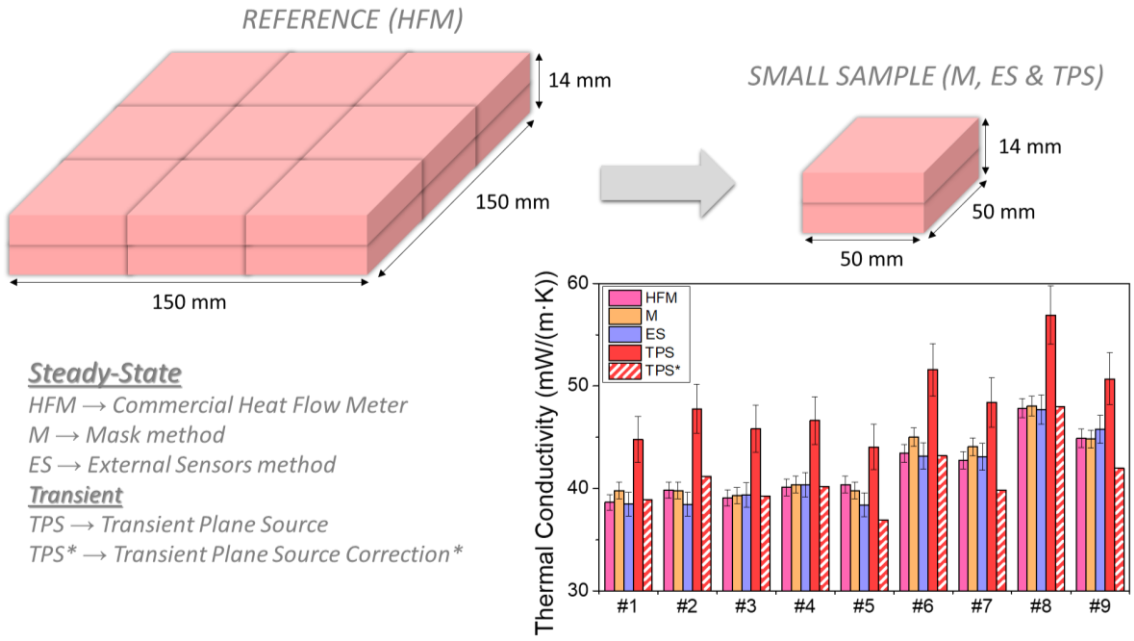

ABSTRACT

The characterization of the thermal conductivity of new and enhanced thermal insulators developed at lab-scale is a challenge. The small dimensions of the prototypes make impossible the use of the conventional techniques because steady-state methods require large samples. Furthermore, the accuracy of transient methods to measure the thermal conductivity is not clear. In this work, we compare four different approaches to measure the thermal conductivity of small prototypes of nanocellular poly(methyl-methacrylate) (PMMA). Both steady-state and transient techniques are used. Results show that the transient plane source method is not suitable for the characterization of these materials (the deviation from the steady-state methods is on average higher than 15%). In addition, two different approaches for measuring the thermal conductivity of small samples via a steady-state technique are proposed and validated.

Keywords: nanocellular polymers, thermal conductivity, steady-state, transient.

Published in: Polymer Testing 117 (2023) 107842.

DOI: 10.1016/j.polymertesting.2022.107842

Chapter 4

Results

"Yippee-ki-yay."

Detective John McClain – **DIE HARD**

INDEX

4. Results

4.1. Introduction

This chapter contains the main results obtained in this thesis besides those already presented in **Chapter 3** (Sections 3.4 and 3.5). The results contained in this chapter cover most of the objectives of the thesis, as it is schematically presented in the graphical abstract of **Figure 4.1**. The graphical abstract includes the section where each result is going to be discussed. Meanwhile, **Figure 4.2** is a flowchart that summarizes the contents of each section.

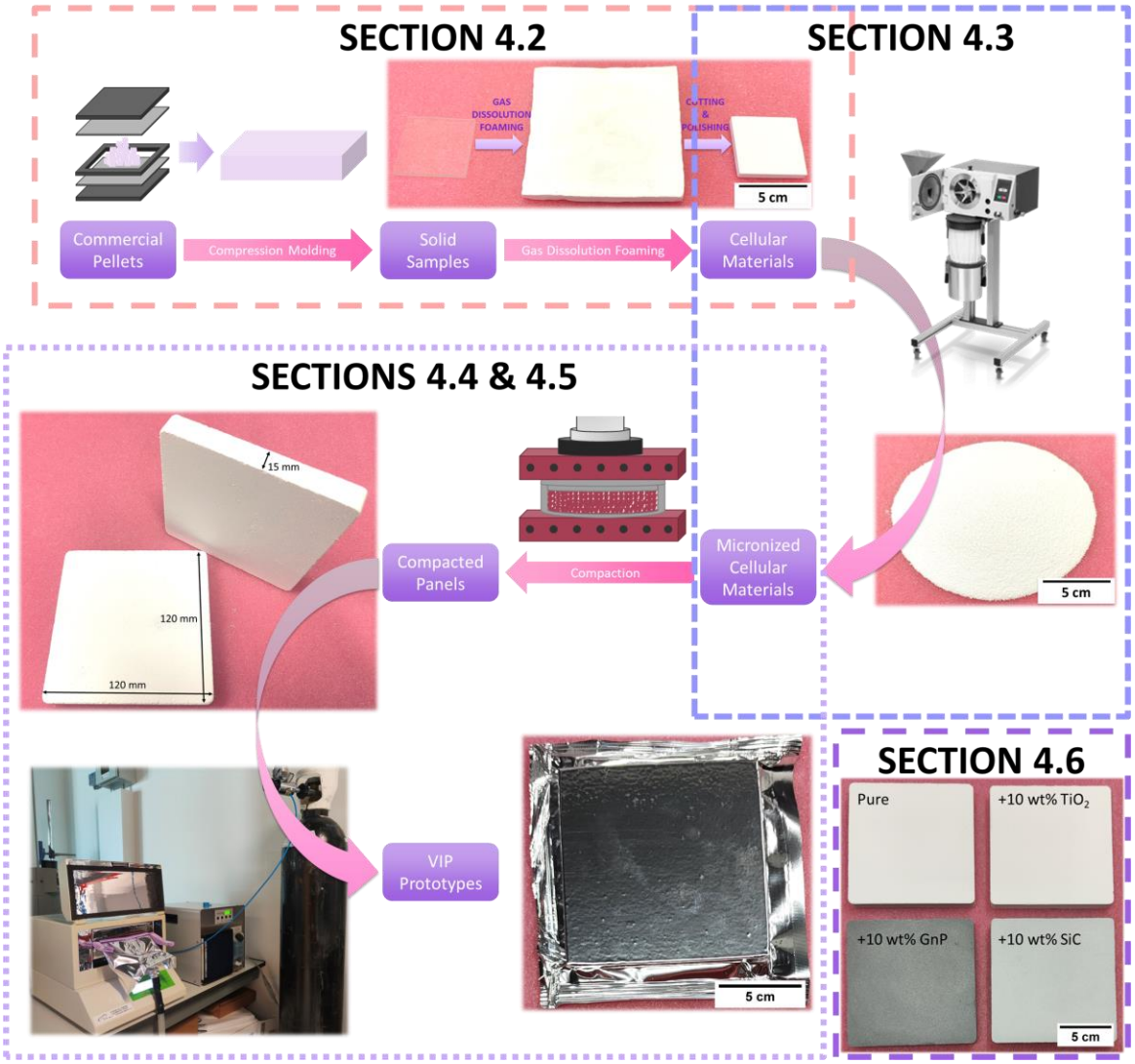

Figure 4.1. Graphical abstract of **Chapter 4** contents.

Section 4.2 includes the results concerning the characterization of the thermal conductivity of bulk nanocellular polymers collected in a publication entitled ***"Thermal conductivity of low-density micro-and nanocellular poly(methyl-methacrylate) (PMMA): Experimental and modeling"***. In this work, a collection of microcellular and nanocellular samples was prepared by gas dissolution foaming with densities ranging 100-200 kg/m^3 and cell sizes between 400–4000 nm. The challenge

of measuring large samples was overcome by staking several samples with the same characteristics (cell size and relative density). Samples of total dimensions 150×150×14 mm^3 were produced and their thermal conductivity was properly measured using a commercial heat flow meter (steady-state technique). The results obtained were taken as reference in **Chapter 3** Section 3.5 to validate the external sensor method as a steady-state technique able to measure accurately the thermal conductivity of nanocellular polymers with small dimensions. Using a methodology developed in this work, it was possible to calculate the solid structure factor and the effective extinction coefficient of the materials using only thermal conductivity measurements. While the structure factor *g* was found to be almost constant (around 0.89), the extinction coefficient showed a clear dependency with the density and the cell size, decreasing as the cell size decreases. This was the first time the extinction coefficient of nanocellular PMMA is calculated using experimental results of the thermal conductivity. Finally, a semiempirical model able to accurately predict the experimental thermal conductivity was developed. Using the model, predictions were made observing that the minimum thermal conductivity that can be reached with nanocellular polymers was around 34 mW/(m·K) at 10 ºC. A strong effect of the structure factor *g* was also observed. This paper was published in **Materials & Design** in 2022 (I. Sánchez-Calderón, V. Bernardo, J. Martín-de-León, M.Á. Rodríguez-Pérez, Thermal conductivity of low-density micro-and nanocellular poly(methyl-methacrylate) (PMMA): Experimental and modeling, Mater. Des. 221 (2022) 110938. https://doi.org/10.1016/j.matdes.2022.110938).

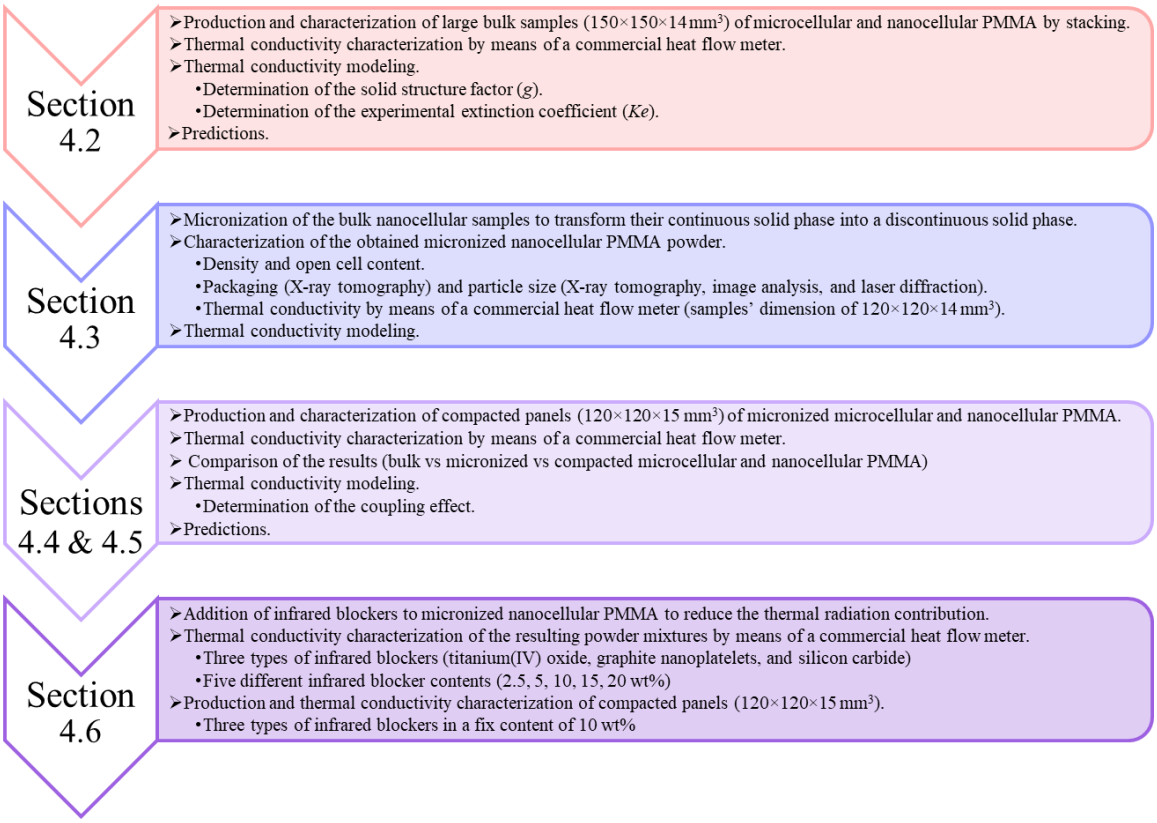

Figure 4.2. Flowchart of **Chapter 4** contents.

In Section 4.3 the nanocellular PMMA bulk samples produced in Section 4.2 were micronized to transform their continuous cellular structure into a discontinuous solid phase with the nanocells inside the micrometric particles. The characterization of the nanocellular powder is collected in a publication entitled ***"Micronization as a solution for enhancing the thermal insulation of nanocellular poly(methyl-methacrylate) (PMMA)"***. This paper set the basis for the detailed characterization of micronized microcellular and nanocellular polymers: apparent density, void fraction, size of the particles, etc. In addition, the thermal conductivity of the powder was measured. The objective of micronization was to reduce the thermal conductivity through the solid phase by generating an aerogel-like structure. Thus, the contact points between the powder particles may act as additional thermal resistances. The results of this work prove that after milling it is possible to obtain open cell nanoporous PMMA powders with thermal conductivity below that of the bulk nanocellular polymers (15% reduction). The reduction is not only due to a density decrease, but a result of the new structure of the powder material. The analysis shows that the solid structural factor decreases about 29% after micronization, probably due to the transition from a continuous cellular structure (bulk sample) to a discontinuous structure (powder material) where the contact points between the powder particles act as additional thermal resistances. Furthermore, the presence of micrometric voids seems to increase the radiation scattering, leading to a higher extinction coefficient and, therefore, reducing thermal radiation in comparison to the bulk samples. This work was published in **Polymer** in 2022 (I. Sánchez-Calderón, V. Bernardo, D. Cuadra-Rodríguez, J. Martín-de-León, M.Á. Rodríguez-Pérez, Micronization as a solution for enhancing the thermal insulation of nanocellular poly(methyl-methacrylate) (PMMA), Polymer (Guildf). 261 (2022) 125397. https://doi.org/10.1016/j.polymer.2022.125397).

Sections 4.4 and 4.5 are the natural continuation of the work presented in the previous sections (Sections 4.2 and 4.3). Section 4.4 collects the paper entitled ***"Development of new vacuum insulation core panels using micronized nanocellular poly(methyl-methacrylate) (PMMA)"*** which is pending for publication. In this work, the micronized microcellular and nanocellular PMMA powders were compacted to obtain self-standing compacted panels. The thermal conductivity of the produced samples was characterized at ambient pressure and under vacuum. Thermal conductivities between 37 and 51 mW/(m·K) were obtained at ambient pressure, while very low thermal conductivities ranging 11-18 mW/(m·K) were achieved at vacuum. When vacuuming an unexpected and large reduction of the thermal conductivity was observed, being associated with a coupling effect between the micronized particles and the air surrounding the particles. Then, it was proved that these compacted materials could be interesting candidates to be used as core in vacuum insulation panels (VIPs) since they show their best performance under vacuum. Meanwhile, Section 4.5 collects the paper entitled ***"Coupling effect in compacted panels based on micronized nanocellular polymers: modeling of the thermal conductivity"*** which is

pending for publication. In this work, the contribution of the coupling effect was determined and a model to predict the thermal conductivity was developed. The model is based on an infinite association of resistances (i.e., powder particles) to describe the thermal conduction through the solid and gas phases, plus the radiation and the coupling effect. Furthermore, a comparison between the predicted thermal conductivity between the bulk and micronized microcellular and nanocellular polymers based on PMMA is presented, showing that the micronized systems may be interesting for their use as a core for VIPs.

Finally, Section 4.6 is about the optimization of the materials by adding infrared blockers. The advantage of the micronized material is that other particles can be added directly to the powder, without compromising the inner cellular structure or the density. This paper entitled ***"Improvement of the thermal conductivity of micronized nanocellular poly(methyl-methacrylate) (PMMA) by adding infrared blockers"*** is pending for publication. In this work, a way to further enhance the thermal insulation behavior is analyzed through the addition of infrared blockers to micronized nanocellular PMMA for reducing the thermal radiation contribution. Three different opacifiers (titanium(IV) oxide, graphene nanoplatelets, and silicon carbide) were used in different contents (2.5, 5, 10, 15, and 20 wt%). The addition of infrared blockers allows reducing around 4% (1.2 mW/(m·K)) the thermal conductivity in comparison with the sample without opacifiers. It was observed that for each infrared blocker, there is an optimum mass proportion to achieve a minimum thermal conductivity. Compacted panels were also produced and studied under vacuum. When extracting the gas phase under vacuum, the thermal conductivity sharply decreases from 34.0 to 9.6 mW/(m·K) for the sample containing 10 wt% of SiC, which is 2 mW/(m·K) lower than the thermal conductivity of the reference powder (without IR-blockers). These results are quite interesting since the improvements are obtained even with densities 10% higher than the reference sample, confirming that the opacified compacted panels as potential candidates to be used as alternative, low-cost, and eco-friendly VIP cores.

4.2. Thermal conductivity of low-density micro-and nanocellular poly(methyl-methacrylate) (PMMA): experimental and modeling

Ismael Sánchez-Calderón[1], Victoria Bernardo[2], Judith Martín-de-León[1], Miguel Ángel Rodríguez-Pérez[1,3].

[1]*CellMat Laboratory. Campus Miguel Delibes. Faculty of Science. Condensed Matter Physics Department. University of Valladolid, Paseo de Belén 7, 47011, Valladolid, Spain.*

[2]*CellMat Technologies S.L., Paseo de Belén 9-A, 47011, Valladolid, Spain.*

[3]*BioEcoUVA Research Institute on Bioeconomy, University of Valladolid, 47011, Valladolid, Spain.*

Corresponding author: Ismael Sánchez-Calderón (ismaelsc@fmc.uva.es)

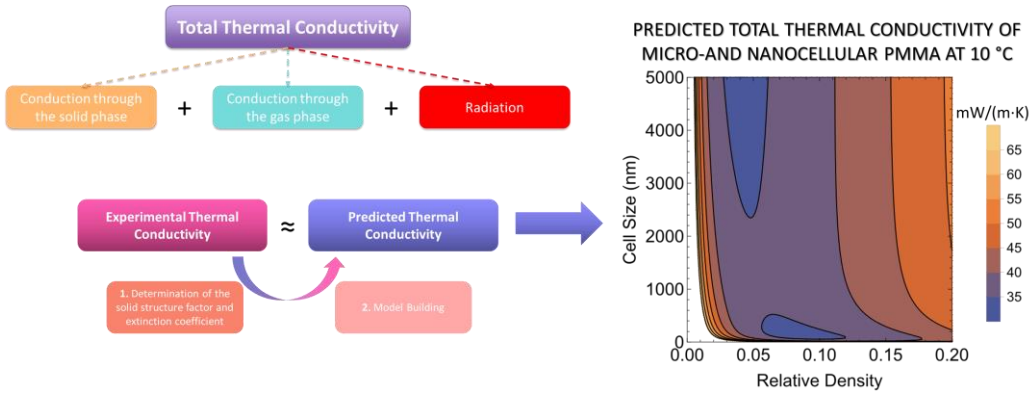

ABSTRACT

Nowadays, finding new materials with enhanced thermal insulation properties has become a mandatory task to reduce energy consumption and CO_2 emissions. In recent years, nanocellular polymers have aroused great attention due to their very interesting combination of properties, which include reduced conduction through the gas phase thanks to the Knudsen effect.

There are plenty of theoretical works hypothesizing the thermal insulation performance of nanocellular polymers. However, there is a lack of experimental results, especially at low densities. In the present work, the thermal conductivity of low-density microcellular and nanocellular poly(methyl-methacrylate) (PMMA) was measured to evaluate the different heat transfer mechanisms acting on these structures. PMMA foamed sheets with relative densities ranging from 0.09 to 0.18 and cell sizes between 400-4000 nm were produced by gas dissolution foaming using CO_2 as a physical blowing agent. Samples were measured at various temperatures, resulting in thermal conductivities between 37.4 and 46.6 mW/(m·K) at 10 ºC. Experimental results have been analyzed to build a semi-empirical model able to predict the thermal conductivity and each heat transfer mechanism contribution. To do this, a novel method to determine the solid structure factor from the slope of the thermal conductivity versus the temperature curve is introduced.

Keywords: thermal conductivity, poly(methyl-methacrylate), microcellular polymer, nanocellular polymer, conduction, radiation.

Published in: Materials & Design 221 (2022) 110938.

DOI: 10.1016/j.matdes.2022.110938

4.3. Micronization as a solution for enhancing the thermal insulation of nanocellular poly(methyl-methacrylate) (PMMA)

Ismael Sánchez-Calderón[1], Victoria Bernardo[2], Daniel Cuadra-Rodríguez[1], Judith Martín-de-León[1], Miguel Ángel Rodríguez-Pérez[1,3].

[1]*CellMat Laboratory. Campus Miguel Delibes. Faculty of Science. Condensed Matter Physics Department. University of Valladolid, Paseo de Belén 7, 47011, Valladolid, Spain.*

[2]*CellMat Technologies S.L., Paseo de Belén 9-A, 47011, Valladolid, Spain.*

[3]*BioEcoUVA Research Institute on Bioeconomy, University of Valladolid, 47011, Valladolid, Spain.*

Corresponding author: Ismael Sánchez-Calderón (ismaelsc@fmc.uva.es)

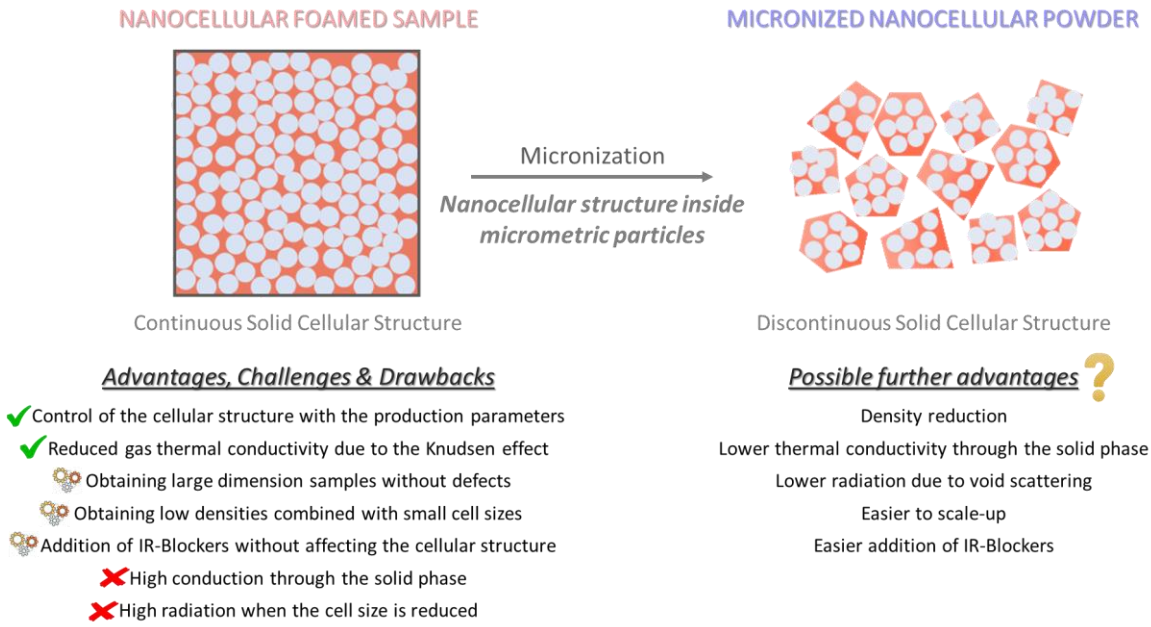

ABSTRACT

This work shows a route to reduce the thermal conductivity of nanocellular poly(methyl-methacrylate) (PMMA). This approach is based on micronizing to replace the continuous solid phase by a discontinuous one. PMMA powders with densities of 147-195 kg/m^3, formed by particles of 100 microns with nanometric cells inside them, are produced by milling. Micronization allows increasing the overall porosity maintaining the cell size. Results prove that after milling it is possible to obtain open cell nanoporous PMMA powders with thermal conductivity below that of the bulk materials (15% reduction). The reduction is not only due to a density decrease, but a result of the new structure of the powder material. The discontinuity of the solid phase and the increase in radiation extinction are the key factors allowing this improvement. This route is confirmed as a promising alternative to enhance the performance of nanocellular polymers.

Keywords: thermal conductivity, poly(methyl-methacrylate), nanocellular powder.

Published in: Polymer (Guildf) 261 (2022) 125397.

DOI: 10.1016/j.polymer.2022.125397

4.4. Development of new vacuum insulation core panels using micronized nanocellular poly(methyl-methacrylate) (PMMA)

Ismael Sánchez-Calderón[1], Victoria Bernardo[2], Félix Lizalde-Arroyo[1], Judith Martín-de-León[1], Miguel Ángel Rodríguez-Pérez[1,3].

[1]*CellMat Laboratory. Campus Miguel Delibes. Faculty of Science. Condensed Matter Physics Department. University of Valladolid, Paseo de Belén 7, 47011, Valladolid, Spain.*

[2]*CellMat Technologies S.L., Paseo de Belén 9-A, 47011, Valladolid, Spain.*

[3]*BioEcoUVA Research Institute on Bioeconomy, University of Valladolid, 47011, Valladolid, Spain.*

Corresponding author: Ismael Sánchez-Calderón (ismaelsc@fmc.uva.es)

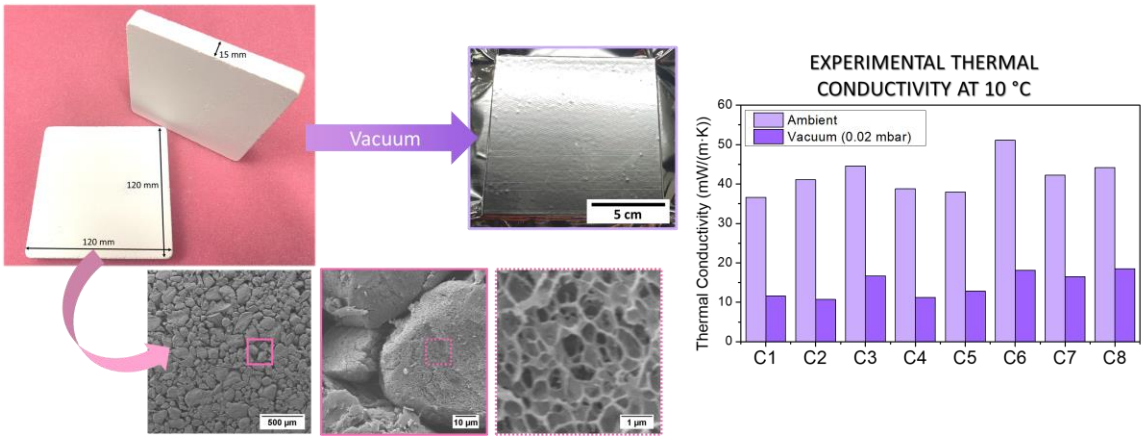

ABSTRACT

Thanks to their unique structure, nanocellular polymers can be micronized to generate a powdered material formed by micrometric particles with nanocells inside them. Due to the discontinuous structure, micronized nanocellular polymers present a significant reduction of thermal conductivity in comparison with their bulk counterparts. In this work, we produce and analyze insulating panels by compacting micronized microcellular and nanocellular poly(methyl-methacrylate) (PMMA). The compacted materials are self-standing and characterized by densities from 160 to 360 kg/m^3, cell sizes between 400-4000 nm, and thermal conductivities between 37 and 51 mW/(m·K) at ambient pressure. When the panels are subjected to vacuum conditions, very low thermal conductivities are achieved, ranging 11-18 mW/(m·K), identifying these materials as promising candidates for vacuum insulation. The mechanisms allowing this significant reduction in the thermal conductivity are discussed.

Keywords: Thermal conductivity, poly(methyl-methacrylate), thermal insulation, compacted micronized microcellular polymer, compacted micronized nanocellular polymer, coupling effect.

1. Introduction

Nowadays, Nowadays, finding new materials with enhanced thermal insulation properties has become a mandatory task to accomplish the new legislative frameworks developed by the governments[1,2] to boost energy performance, especially in the building sector[3]. The reason is that building climatization is responsible for around 40% of the energy used in buildings[3–5], and this demand could further increase as the global population is expected to grow[6]. Therefore, enhancing the thermal insulation performance of buildings is a key factor to reduce energy consumption and CO_2 emissions. There are two possible routes to achieve this objective[7]: increasing the thickness of the insulation layer using conventional insulators such as polymeric foams, characterized by thermal conductivities between 25-60 mW/(m·K), or using super thermal insulators based on silica like aerogels or vacuum insulation panels (VIPs), characterized by much lower thermal conductivities (4-16 mW/(m·K))[3,8–10]. This second approach would also extend the useful area in buildings since these materials provide better insulation with reduced thickness. However, up to today, their use is not widespread in the building sector due to their high price[11–14] and, in the case of silica aerogels, their poor mechanical properties that limit their applications[15]. Thus, the current research on silica aerogels is focused on improving their mechanical properties by mixing the silica inorganic networks with organic polymers or fiber networks, or directly producing organic aerogels[14–17], but their price is still high due to the complicated manufacturing process. Meanwhile, the research on VIPs is focused on alternative low-cost core materials[11,18–20] or fabricating hybrid core materials[11,21–23] to replace the current silica cores (fumed/precipitated silica or silica aerogel). The core is the inner part of a VIP, fabricated from a porous material, whose function is to physically support the VIP envelope and provide superinsulation performance. By using porous materials with an interconnected structure such as open cell foams, powders, and fibers the heat transfer through the gas phase is suppressed when vacuum is applied, achieving super-insulating thermal conductivities (thermal conductivities lower than 25 mW/(m·K)). Meanwhile, nanosilica is mostly used because it allows a further reduction of the solid conduction thanks to the nanoscale and discontinuous structure of the silica, while at the same time, it allows a greater reduction of the gas conduction at lower vacuum pressures thanks to the very small cell sizes in the nanoscale that promote the Knudsen effect[8,24–26].

Nanocellular polymers, characterized by cell sizes below the micron, present interesting characteristics to be maybe used for replacing the silica cores of VIPs. These materials are proven to show reduced thermal conduction through the gas phase due to the Knudsen effect, among other interesting properties[27–33]. There are some preliminary works about the use of these materials as potential core materials for VIPs. For instance, Almeida et al.[18] produced bulk nanocellular PS plates with a density of 177 kg/m^3. Nevertheless, despite the reduced cell size (400 nm), the thermal conductivity results (44 mW/(m·K) at ambient pressure and 24 mW/(m·K) under vacuum) were not

promising for VIP applications. Also, in our previous work[7], we produce bulk nanocellular PMMA plates (density 154 kg/m^3 and cell size of 470 nm) and studied its behavior at ambient pressure (39 mW/(m·K)) and at vacuum (25 mW/(m·K)). Again, looking at these results, nanocellular polymers may not be good candidates to be used as eco-friendly and low-cost alternative VIPs core because the thermal conductivities obtained both at ambient pressure and under vacuum are still too high.

Recently, it has been proved that by means of micronization, it is possible to enhance the thermal insulation behavior of nanocellular PMMA[34]. Micronization allows transforming the continuous solid phase of the bulk nanocellular polymers into a discontinuous solid phase formed by micrometric particles with nanoscale cells inside them. The new material shows a reduced density by maintaining the cellular structure, while the thermal conductivity decreases at ambient pressure. This strategy allows reducing the conduction through the solid phase by creating additional thermal resistances between the powder particles, and also reducing the radiation contribution because the micrometric voids between the powder particles act as scattering points for infrared radiation.

In the present work, we move one step forward by using the micronized nanocellular material to fabricate insulating panels that could be used as core materials for VIPs. A collection of microcellular and nanocellular polymers based on PMMA are micronized and then compacted forming self-standing panels with dimensions of 120×120×15 mm^3. The compacted panels show densities ranging from 160 to 360 kg/m^3 and cell sizes between 400-4000 nm and their thermal conductivity is measured using a heat flow meter (steady-state method) at ambient pressure and at different vacuum pressures.

2. Experimental

2.1. Materials and sample preparation

Microcellular and nanocellular materials based on PMMA were produced by gas dissolution foaming. The PMMA grade used was PLEXIGLAS® 7H kindly supplied by Röhm GmbH. This PMMA presents a density of 1190 kg/m^3, a melt flow index of 0.77 g/10 min (measured at 230 ºC and 2.16 kg), and a glass transition temperature of 110.4 ºC measured by DSC (model DSC3+, Mettler). Details of the procedure to produce and characterize these samples can be found elsewhere[7]. The main features of these bulk samples (in following denoted as B), density (ρ_B), cell size (ϕ_{3D_B}), normalized standard deviation of the cell size (SD/ϕ_{3D_B}), open cell content (OC_B), and thermal conductivity (λ_B) at 10 ºC are collected in **Table 1**. These bulk samples are numbered as a function of their density which ranges between 105 and 218 kg/m^3. Samples #5, #7, and #8 are nanocellular (cell size below 1 micron).

The bulk nanocellular samples were micronized. After the milling process, the resultant materials were homogeneous powders formed by micrometric particles. Details of the procedure to produce

and characterize these samples can be found in our previous work[34]. The main features of these micronized samples (in following denoted as M), apparent density (ρ_{app_M}), particle density ($\rho_{particle\_M}$), particle size obtained through image analysis (D_M), normalized standard deviation of the cell size (D_M/ϕ_{3D_B}), open cell content (OC_M), and thermal conductivity (λ_M) at 10 ºC) are also collected in **Table 1**. The particle density has been calculated from the apparent density according to Equation (S1) (**Supporting Information Section S1**) assuming the same fraction of particles in all the powders (packaging factor of 0.76). In all the materials the density of the powder particles is higher than the density of the bulk material, meaning that there is some densification during the milling process. The difference is greater in the microcellular samples. However, despite the densification, the cellular structure seems to not be modified after the micronization, as shown in **Supporting information Section S2 Figure S2**. Furthermore, the thermal conductivity is in general lower in the micronized material, despite the higher apparent density in many materials. This reduction is attributed to a decrease in the solid conduction caused by the discontinuity of the structure as well as a reduction of the radiation contribution. Finally, it is observed that after micronization, the open cell content of the samples increases to values over 80%, achieving interconnected structures suitable for vacuum evacuation.

Table 1. Density, cell size, normalized standard deviation of the cell size, open cell content, and thermal conductivity at 10 ºC of the bulk and micronized samples. Apparent density, particle density, particle size, normalized standard deviation of the particle size, open cell, and thermal conductivity at 10ºC of the micronized materials.

	Bulk					Micronized					
Sample	ρ_B (kg/m^3)	ϕ_{3D_B} (nm)	SD/ϕ_{3D_B}	OC_B (%)	λ_B at 10 °C (mW/(m·K))	ρ_{app_M} (kg/m^3)	$\rho_{particle\_M}$ (kg/m^3)	D_M (μm)	SD/D_M	OC_M (%)	λ_M at 10 °C (mW/(m·K))
1	105±12	1459	0.41	6±1	37.4	110±2	145	77	0.68	87±1	33.2
2	113±12	3215	0.70	10±1	38.7	155±2	205	92	0.73	98±1	36.1
3	115±9	1021	0.45	38±1	37.9	201±3	265	109	0.68	85±1	38.1
4	117±17	2916	0.59	3±1	39.0	130±2	171	102	0.78	94±1	34.6
5	154±10	468	0.47	99±1	39.4	147±2	194	94	0.62	98±1	33.6
6	173±10	2379	0.65	4±1	42.4	241±4	317	139	0.64	80±1	41.1
7	185±9	408	0.47	86±1	41.7	179±3	236	102	0.64	92±1	35.6
8	218±10	394	0.43	74±1	44.0	195±3	257	100	0.69	97±1	36.5

The micronized samples were compacted to prepare panels using a hot plate hydraulic press with accurate control provided by Talleres Remtex (Barcelona, Spain). First, the micronized samples were dried at 60 °C for 30 min in a forced-air high-temperature oven (model 2001405, JP Selecta). Second, the necessary amount of micronized sample was weighted and placed inside a mold with final dimensions of 120×120×15 mm^3. The target apparent density of the compacted samples is

145% of the apparent density of the micronized material. The density was selected to obtain a material that can be handled without breaking it (self-standing panels). Afterward, the mold is placed on the press under pressure at 80 ºC for 30 min. Finally, the sample is removed from the mold obtaining a compacted panel (in the following denoted as C) which is stable and can be handled (**Figure 1**). The panels are used to measure and study the thermal conductivity.

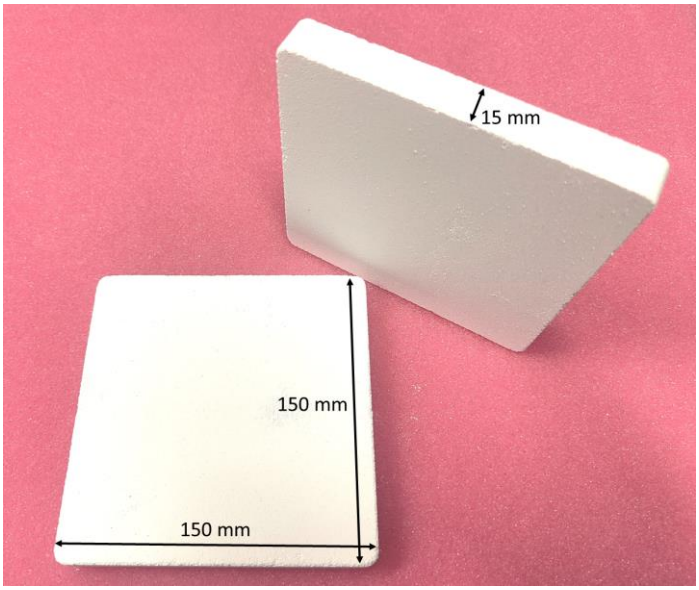

Figure 1. Picture of one of the compacted panels produced in this work showing its dimensions.

2.2. Characterization

2.2.1. Density, particle size, open cell content, and surface morphology

The apparent density of the compacted panels (ρ_{app_C}) was obtained according to UNE-EN 1602[35] by measuring the geometric volume (V) and the mass (m) of the compacted piece ($\rho_{app\_C} = m / V$).

A Scanning Electron Microscope (FlexSEM 1000 VP-SEM) was used to visualize the surface of the micrometric particles and evaluate the effect of the micronization and compaction process (**Supporting Information Section S2 Figure S3**). To allow visualization, the samples were coated with gold using a sputter coater (model SCD 005, Balzers Union).

2.2.2. Thermal conductivity measurements

Thermal conductivity measurements were carried out using a thermal heat flow meter model FOX 200 (TA Instruments / LaserComp, Inc.), which measures according to ASTM C518 and ISO 8301[36,37] (steady-state conditions). For the measurements, the sample was placed between the two plates, promoting a temperature gradient through the material thickness. Measurements were performed at 10 ºC and the temperature gradient was set to 20 ºC (i.e., the temperature goes from 0 ºC in the upper isothermal plate to 20 ºC in the lower one). The active area of the FOX 200 heat flux transducers is 75×75 mm^2, so the samples have larger lateral dimensions than the heat flux

transducers. To fill the remaining volume of the sample cavity a polyurethane foam mask was used to avoid air convection. The absolute thermal conductivity accuracy for this device is 2%.

Measurements were also performed at 10 ºC under vacuum (600, 300, 200, 100, 60, 30, 10, 6, 3, and 0.02 mbar). For these measurements, a set-up consisting of a vacuum pump (RV3, Edwards), a vacuum controller (VacuuSelect + VV-B15C electrovalve + Pirani VacuuWiew extend sensor, Vacuubrand), a vacuum valve (VAC VALVE 425, Matva), and a vacuum bag (Pack-lab) has been used (**Figure 2**). The vacuum controller consists of a device (VacuuSelect) that allows setting and controlling the desired pressure by connecting the electrovalve and the Pirani sensor. The VV-B15C electrovalve opens until the set pressure is reached and then it closes. If the pressure increases overcoming the set value, the electrovalve opens again. The pressure is measured with the Pirani VacuuWiew extend sensor (able to measure pressures from 1100 to 0.001 mbar).

Regarding the methodology to measure the thermal conductivity, first, the material is wrapped in fleece and introduced in a vacuum two layers bag with a composition of metalized poly(ethylene terephthalate) (PET) (thickness of 12 µm) and polyethylene (PE) (sealant, 80 µm in thickness). The vacuum bag is connected to the vacuum devices (pump and vacuum controller) through a vacuum valve and different accessories. Once the wrapped material is inside the vacuum bag the borders of the bag are sealed. Finally, the pump is connected, and the vacuum inside can be controlled with the set-up previously explained.

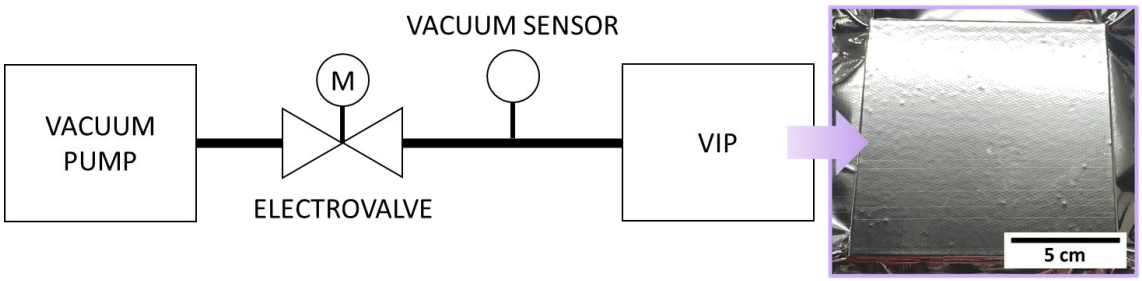

Figure 2. Set-up for measuring the thermal conductivity at different vacuum pressures.

3. Results and discussion

3.1. Sample characterization

Table 2 summarizes the apparent density of the compacted panels (an example of the compacted panels was shown in **Figure 1**). The density of the samples (ρ_{app_C}) ranges between 158 and 357 kg/m^3. After the compaction process, the density of the samples increases by around 45% regarding the micronized material (**Table 1**). Compaction at lower levels results in fragile materials that easily fall apart. After the compaction process, the cellular structure is not noticeably affected, as shown in **Supporting Information Section S2 Figures S3a and S3b**. This was confirmed by measuring the particle size of a dismantled panel. As seen in **Figure S3c**, there are still open cells on the surface of the compacted panels.

Table 2. Apparent density of the compacted samples studied in this work.

	Compacted panel
Sample	ρ_{app_C} (kg/m^3)
1	158
2	223
3	292
4	190
5	201
6	357
7	265
8	282

3.2. Thermal conductivity at ambient pressure: bulk (B) vs. micronized (M) vs. compacted panel (C) samples

Figure 3 shows the experimental thermal conductivity at 10 ºC and ambient pressure (considered as 1013 mbar) of the compacted panels produced in this work in comparison with the initial bulk material and the micronized powder before compaction. Thermal conductivity of compacted samples at ambient pressure ranges between 36.6 and 51.1 mW/(m·K). As observed in **Figure 3a**, despite the higher density of some micronized and compacted materials, their thermal conductivity is close to or even lower than the thermal conductivity of the bulk. For instance, for sample #1, the bulk material (density 105 kg/m^3) presents a thermal conductivity of 37.4 mW/(m·K), meanwhile, the compacted panel (density 158 kg/m^3) is characterized by 36.6 mW/(m·K). This trend can be clearly seen in **Figure 3b**, where the thermal conductivity is presented as a function of the density for the three types of materials. There are two clear trends: on the one hand, the continuous bulk material, and on the other hand, with a much lower thermal conductivity, the discontinuous materials (micronized and compacted panels). The powdered systems follow a similar trend with the density, so the mechanisms affecting these systems may be similar, despite the compaction process, but clearly different than those occurring in the bulk samples. These results reinforce and further confirm that the discontinuity of the solid phase reduces the thermal conductivity by means of new mechanisms not taking place in continuous bulk nanocellular materials. Also, it is observed that the nanocellular samples (#5, #7, and #8, open symbols in **Figure 3b**) present lower thermal conductivity than the microcellular samples, even presenting higher densities.

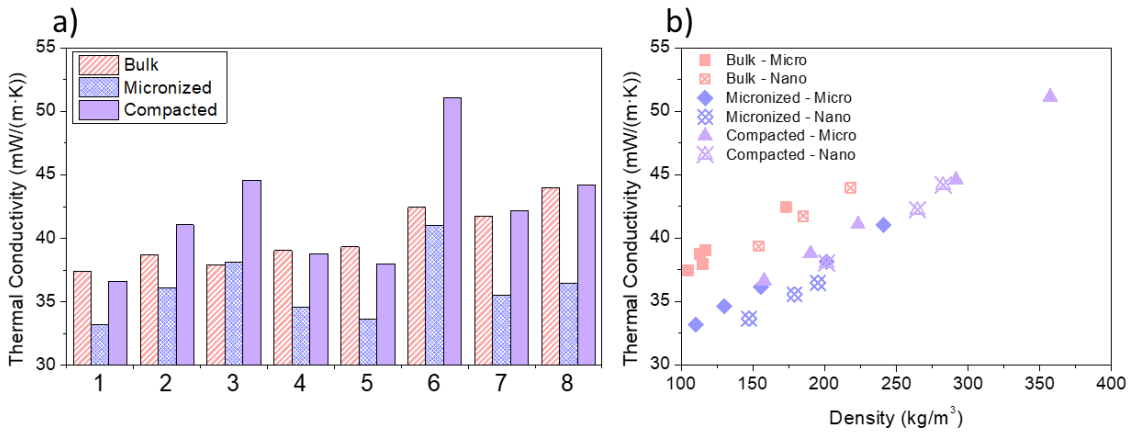

Figure 3. a) Comparison of the thermal conductivity at 10 ºC and ambient pressure of the bulk, micronized, and compacted samples, b) thermal conductivity as a function of the density for the three types of materials. Empty and crossed symbols correspond to the nanocellular samples (#5, #7, and #8).

3.3. Thermal conductivity under vacuum of the compacted panels

Figure 4a shows the thermal conductivity at 10 ºC of the compacted samples at ambient pressure and at maximum vacuum (0.02 mbar). The thermal conductivity of compacted samples at vacuum ranges between 10.7 and 18.1 mW/(m·K). Note that thermal conductivities of VIPs based on silica present thermal conductivities around 4-8 mW/(m·K)[24,26,38,39], so the obtained results are not far away from those values. On the other hand, **Figure 4b** presents the reduction of thermal conductivity (in mW/(m·K)) between the ambient pressure and maximum vacuum conditions at 10ºC as a function of the density along with the maximum vacuum (0.02 mbar) thermal conductivity measurements. The reduction seems to be slightly lower for the nanocellular samples (open symbols in **Figure 4b**). This could be logical, taking into account that nanocellular polymers present a lower fraction of gas phase to be extracted when vacuum is applied. However, the reduction is quite high: it is observed that the thermal conductivity is sharply reduced by more than 25 mW/(m·K) by extracting the gas phase. For instance, for compacted panel #5 the thermal conductivity decreases from 38.0 to 12.8 mW/(m·K), which means a reduction of 25.2 mW/(m·K). This is a surprising result because for a bulk material (continuous structure) with the same characteristics (density and cell size) a reduction of 13 mW/(m·K) is expected taking into account the gas (cells) conduction contribution according to Knudsen effect[7] (see **Supporting Information Section S3**). However, in the panels produced with the micronized material, the reduction is almost twice as high, meaning that there must be some additional heat transfer mechanism associated to the gas phase.

Furthermore, it is also observed that both, the reduction of thermal conductivity and the thermal conductivity at vacuum depend on the density. The higher thermal conductivity at vacuum as density rises is the expected behavior from a theoretical perspective. At vacuum, the active heat

transfer mechanisms are conduction through the solid phase (which increase as density rises) and radiation (which decrease as density rises), but conduction through the solid phase domains over radiation, increasing the overall thermal conductivity. However, the higher reduction between ambient and maximum vacuum thermal conductivity as density rises is unexpected, since from a theoretical perspective at higher density the gas (cells) conduction is lower, so we could expect a lower reduction. Again, this result supports the need for an additional heat transfer mechanism related to the gas phase to explain this behavior. This mechanism, which does not take place in bulk materials, may depend on the density.

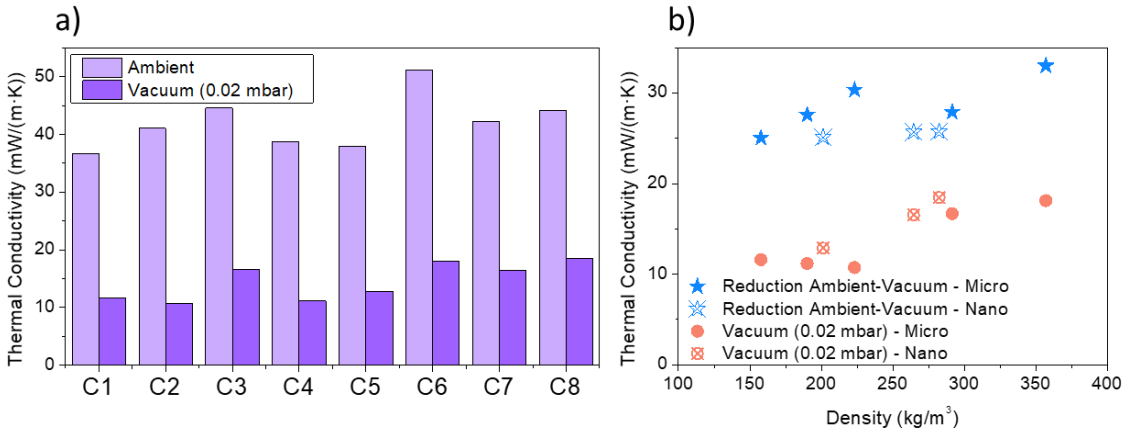

Figure 4. a) Thermal conductivity at 10 ºC of the compacted panels at ambient pressure (1013 mbar) and at maximum vacuum (around 0.02 mbar). b) Thermal conductivity at maximum vacuum (at 10 ºC and 0.02 mbar) and thermal conductivity reduction between ambient and vacuum conditions (at 10ºC) and as a function of the compacted panel density. Empty and crossed symbols correspond to the nanocellular samples (#5, #7, and #8).

The previous discussion is clearer if we perform thermal conductivity measurements at different vacuum pressures. **Figure 5** shows the thermal conductivity at 10 ºC as a function of the pressure for the compacted panel #5 (nanocellular sample with 468 nm of cell size) as a representative example (the curves for the rest of the compacted panels can be found in **Supporting Information Section S4 Figure S4**). The compacted panel (density 201 kg/m^3) is compared with the bulk material (154 kg/m^3). The thermal conductivity of both samples decreases as the pressure is reduced: this is the expected behavior from a theoretical perspective due to the Knudsen effect[18,23,39,40]. As the pressure decreases, the mean free path of the air molecules decreases, so the probability of the gas molecules colliding with each other decreases, reducing the heat conduction through the cells phase. In the bulk sample #5 there is only a drop of the conductivity of approximately 11 mW/(m·K) up to pressures of 10 mbar and then the conductivity remains constant as pressure is reduced. However, the curves of the compacted sample #5 in **Figure 5** (and those included **Figure S4** for the rest of the samples) show a double fall: first, for pressures above 10 mbar, the conductivity drops by around 11 mW/(m·K), and for pressures below this value, there

is a second thermal conductivity decrease of 14 mW/(m·K) (even higher than the first drop). This behavior is unique for the panels produced in this work using the micronized nanocellular polymer. Then, the bulk nanocellular sample and the compacted panel produced with the micronized material present a very different behavior. For pressures lower than 10 mbar, the thermal conductivity of the compacted panel is much lower than that of the bulk sample. For instance, in sample #5, at maximum vacuum, there is a reduction of 12.9 mW/(m·K) between the bulk and the compacted panel thermal conductivities (25.7 vs 12.8 mW/(m·K)). Also, it is important to remark that the compacted panel allows reaching higher evacuation than the bulk material at ultimate vacuum (0.02 vs 0.04 mbar), probably due to the higher interconnectivity of the cells in the powder particles.

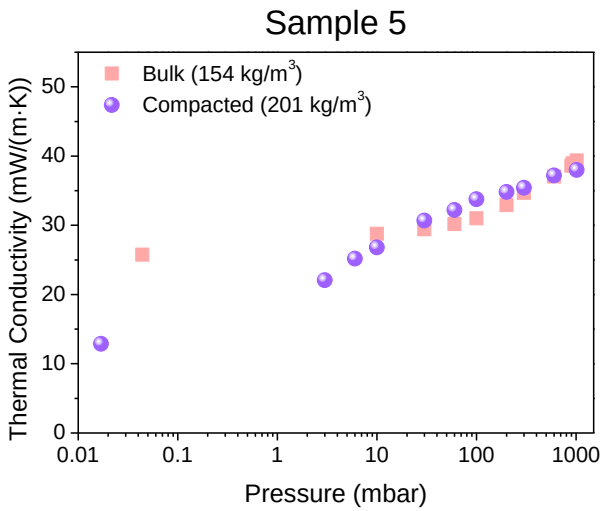

Figure 5. Thermal conductivity at 10 ºC as a function of the pressure of the compacted panel #5. The thermal conductivity at 10ºC as a function of the pressure of bulk sample #5 has been included as a reference.

These results are very interesting and surprising. The single thermal conductivity drop in the bulk sample can be justified due to the Knudsen effect for the material characteristics (density and cell size)[7,27]: the conduction through the gas (cells) phase in the bulk sample is calculated to be 14 mW/(m·K), similar to the reduction measured when applying vacuum[7] (**Supporting Information Section S3**). Meanwhile, for the compacted panel, which presents a higher density (201 kg/m^3), the predicted conduction through the cells phase is 13 mW/(m·K) (calculated using Equation (S4)). This can be associated with the first fall of the thermal conductivity of the compacted panel. But there is still a reduction of 12 mW/(m·K) for pressures below 10 mbar that cannot be justified with the gas (cells) conduction equation. Therefore, it is clear that an additional heat transfer mechanism, which may be related to the presence of the particles and the pressure, is present in the powdered systems.

This additional heat transfer mechanism (named as coupling effect) is well known in systems consisting of contact particles, and it can be a significant contribution to the total thermal

conductivity at ambient pressure, as shown schematically in **Figure 6c**[41–43]. For instance, for powders consisting of hard grains the values of the coupling effect can range between 20-30 mW/(m·K) at atmospheric pressure[44]. The coupling heat transfer takes into account the interaction between the core particles and the gas[25,26]. This additional heat transfer mechanism is negligible for foams with continuous cellular structures because the coupling effect is a result of the heat flow from one solid particle to another through the gas phase (**Figure 6a**). At vacuum, it is negligible due to the lack of gas molecules (**Figure 6b**). The coupling effect arises due to a short circuit for the heat flow from one particle to the other through the gas phase (**Figure 6**) when the heat resistance between two solid phases is lower by passing through the gas phase than the solid path. Thus, if in a material consisting of contact particles we measured a thermal conductivity of 10 mW/(m·K) at vacuum and we do not take into account the coupling effect, we might underpredict the thermal conductivity at ambient pressure, as seen in **Figure 6c**, so the real thermal conductivity exceeds the expected thermal conductivity[45].

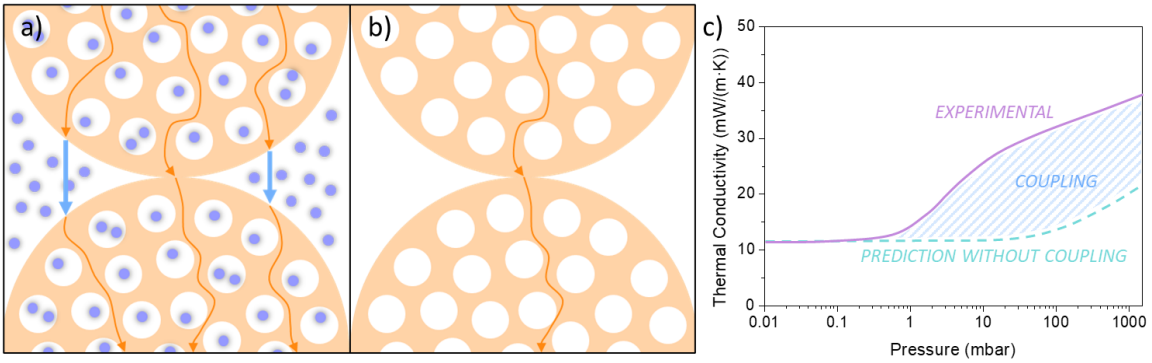

Figure 6. a) Scheme coupling effect at ambient pressure, where the structural thermal resistances are shorted by gas molecules, and additional pathways occur and b) scheme of solid-body conduction in porous powder materials at vacuum (adapted from[41]). c) Scheme of the effect of the coupling on the thermal conductivity as a function of pressure.

Summarizing, in bulk materials the heat transfer mechanisms are conduction through the solid phase, conduction through the cells phase, and radiation. Whereas in the compacted panels, the heat transfer mechanisms are conduction through the solid phase, conduction through the cells phase, radiation, and coupling effect. The radiation and the conduction through the cells phase contribution may be similar for both systems, so the differences are mainly the solid conduction contribution and the coupling effect. The presence of particles generating a discontinuous structure allows for reducing the conduction through the solid phase in the micronized materials, but the appearance of the coupling effect causes an increase in the overall thermal conductivity at ambient pressure. However, when vacuum is applied and the coupling effect is suppressed, the micronized material is proved to be a much better thermal insulator than the bulk material.

4. Conclusions

In this work, compacted self-standing panels with dimensions of 120×120×15 mm^3 are produced from micronized microcellular and nanocellular PMMA. Compacted panels with densities ranging from 160 and 360 kg/m^3 and cell sizes between 400-4000 nm have been studied. Thermal conductivities between 37 and 51 mW/(m·K) are obtained at ambient pressure, whereas at vacuum the thermal conductivities range from 11 to 18 mW/(m·K). The thermal conductivity reduction behavior under vacuum was observed to be different between the bulk materials and the compacted panels, which present higher thermal conductivity reduction (almost doubled) and two drops of thermal conductivity (instead of only one). This is because, an additional heat transfer mechanism arises in systems consisting of contact particles, such as the compacted panels as a result of the heat flow from one solid particle to another through the gas phase: the coupling effect. These results make the compacted panels based on micronized microcellular and nanocellular polymers potential candidates to be used as alternative materials for VIP productions.

Supporting Information

Supporting Information is available.

Acknowledgments

Financial assistance from the Junta of Castile and Leon grant (I. Sánchez-Calderón and VA202P20) is gratefully acknowledged. Financial support from the Spanish Ministry of Science, Innovation, and Universities (RTI2018-098749-B-I00, PID2021-127108OB-I00, TED2021-130965B-I00, PDC2022-133391-I00, and PTQ2019-010560 (Victoria Bernardo-García)) is gratefully acknowledged. Financial support from the European Regional Development Fund of the European Union and the of Castile and Leon ((ICE): R&D PROJECTS IN SMEs: PAVIPEX. 04/18/VA/008 and M-ERA.NET PROJECT: FICACEL. 11/20/VA/0001) is gratefully acknowledged. This work was supported by the Regional Government of Castilla y León (Junta de Castilla y León), by the Ministry of Science and Innovation MICIN, and the European Union NextGenerationEU/PRTR.

References

[1] Directive 2010/31/EU of the European Parliament and of the Council of 19 May 2010 on the energy performance of buildings, (n.d.).

[2] Directive 2012/27/EU of the European Parliament and of the Council of 25 October 2012 on energy efficiency, amending Directives 2009/125/EC and 2010/30/EU and repealing Directives 2004/8/EC and 2006/32/EC, (n.d.).

[3] M. Casini, Smart Buildings, 2016th ed., Elsevier, 2016. https://doi.org/10.1016/C2015-0-00182-4.

[4] European Commission – Department: Energy – In focus. Energy efficiency in buildings, (2020).

[5] J. Wernery, F. Mancebo, W.J. Malfait, M. O'Connor, B.P. Jelle, The economics of thermal superinsulation in buildings, Energy Build. 253 (2021) 111506. https://doi.org/10.1016/j.enbuild.2021.111506.

[6] International Energy Agency. Transition to Sustainable Buildings. Strategies and Opportunities to 2050, (2013).

[7] I. Sánchez-Calderón, V. Bernardo, J. Martín-de-León, M.Á. Rodríguez-Pérez, Thermal conductivity of low-

density micro-and nanocellular poly(methyl-methacrylate) (PMMA): Experimental and modeling, Mater. Des. 221 (2022) 110938. https://doi.org/10.1016/j.matdes.2022.110938.

[8] W. Villasmil, L.J. Fischer, J. Worlitschek, A review and evaluation of thermal insulation materials and methods for thermal energy storage systems, Renew. Sustain. Energy Rev. 103 (2019) 71–84. https://doi.org/10.1016/j.rser.2018.12.040.

[9] S. Schiavoni, F. D'Alessandro, F. Bianchi, F. Asdrubali, Insulation materials for the building sector: A review and comparative analysis, Renew. Sustain. Energy Rev. 62 (2016) 988–1011. https://doi.org/10.1016/j.rser.2016.05.045.

[10] M. Casini, Advanced construction materials, in: Constr. 4.0, Elsevier, 2022: pp. 337–404. https://doi.org/10.1016/B978-0-12-821797-9.00005-2.

[11] F.A. Almeida, J. Corker, N. Ferreira, M.A. Neto, M. Fan, H. Beyrichen, R. Caps, Alternative low cost based core systems for vacuum insulation panels, Cienc. e Tecnol. Dos Mater. 29 (2017) e151–e156. https://doi.org/10.1016/j.ctmat.2016.10.002.

[12] B. Chang, L. Zhong, M. Akinc, Low cost composites for vacuum insulation core material, Vacuum. 131 (2016) 120–126. https://doi.org/10.1016/j.vacuum.2016.05.027.

[13] B. Merillas, J.P. Vareda, J. Martín-de León, M.Á. Rodríguez-Pérez, L. Durães, Thermal Conductivity of Nanoporous Materials: Where Is the Limit?, Polymers (Basel). 14 (2022) 2556. https://doi.org/10.3390/polym14132556.

[14] T. Linhares, M.T. Pessoa de Amorim, L. Durães, Silica aerogel composites with embedded fibres: a review on their preparation, properties and applications, J. Mater. Chem. A. 7 (2019) 22768–22802. https://doi.org/10.1039/C9TA04811A.

[15] H. Maleki, L. Durães, A. Portugal, An overview on silica aerogels synthesis and different mechanical reinforcing strategies, J. Non. Cryst. Solids. 385 (2014) 55–74. https://doi.org/10.1016/j.jnoncrysol.2013.10.017.

[16] B. Merillas, F. Villafañe, M.Á. Rodríguez-Pérez, Super-Insulating Transparent Polyisocyanurate-Polyurethane Aerogels: Analysis of Thermal Conductivity and Mechanical Properties, Nanomaterials. 12 (2022) 2409. https://doi.org/10.3390/nano12142409.

[17] M. Schwan, L. Ratke, Flexibilisation of resorcinol–formaldehyde aerogels, J. Mater. Chem. A. 1 (2013) 13462. https://doi.org/10.1039/c3ta13172f.

[18] F. Almeida, H. Beyrichen, N. Dodamani, R. Caps, A. Müller, R. Oberhoffer, Thermal conductivity analysis of a new sub-micron sized polystyrene foam, J. Cell. Plast. 57 (2021) 493–515. https://doi.org/10.1177/0021955X20943101.

[19] S. Verma, H. Singh, Predicting the conductive heat transfer through evacuated perlite based vacuum insulation panels, Int. J. Therm. Sci. 171 (2022) 107245. https://doi.org/10.1016/j.ijthermalsci.2021.107245.

[20] V. Nemanič, M. Žumer, New organic fiber-based core material for vacuum thermal insulation, Energy Build. 90 (2015) 137–141. https://doi.org/10.1016/j.enbuild.2015.01.012.

[21] C. Li, B. Li, N. Pan, Z. Chen, M.U. Saeed, T. Xu, Y. Yang, Thermo-physical properties of polyester fiber reinforced fumed silica/hollow glass microsphere composite core and resulted vacuum insulation panel, Energy Build. 125 (2016) 298–309. https://doi.org/10.1016/j.enbuild.2016.05.013.

[22] C.-D. Li, M.-U. Saeed, N. Pan, Z.-F. Chen, T.-Z. Xu, Fabrication and characterization of low-cost and green vacuum insulation panels with fumed silica/rice husk ash hybrid core material, Mater. Des. 107 (2016) 440–449. https://doi.org/10.1016/j.matdes.2016.06.071.

[23] M. Alam, H. Singh, S. Brunner, C. Naziris, Experimental characterisation and evaluation of the thermo-physical properties of expanded perlite—Fumed silica composite for effective vacuum insulation panel (VIP) core, Energy Build. 69 (2014) 442–450. https://doi.org/10.1016/j.enbuild.2013.11.027.

[24] S.E. Kalnæs, B.P. Jelle, Vacuum insulation panel products: A state-of-the-art review and future research

pathways, Appl. Energy. 116 (2014) 355–375. https://doi.org/10.1016/j.apenergy.2013.11.032.

[25] S. Fantucci, A. Lorenzati, A. Capozzoli, M. Perino, Analysis of the temperature dependence of the thermal conductivity in Vacuum Insulation Panels, Energy Build. 183 (2019) 64–74. https://doi.org/10.1016/j.enbuild.2018.10.002.

[26] R. Baetens, B.P. Jelle, J.V. Thue, M.J. Tenpierik, S. Grynning, S. Uvsløkk, A. Gustavsen, Vacuum insulation panels for building applications: A review and beyond, Energy Build. 42 (2010) 147–172. https://doi.org/10.1016/j.enbuild.2009.09.005.

[27] B. Notario, J. Pinto, E. Solorzano, J.A. de Saja, M. Dumon, M.A. Rodríguez-Pérez, Experimental validation of the Knudsen effect in nanocellular polymeric foams, Polymer (Guildf). 56 (2015) 57–67. https://doi.org/10.1016/j.polymer.2014.10.006.

[28] B. Notario, J. Pinto, M.A. Rodriguez-Perez, Nanoporous polymeric materials: A new class of materials with enhanced properties, Prog. Mater. Sci. 78–79 (2016) 93–139. https://doi.org/10.1016/j.pmatsci.2016.02.002.

[29] B. Xiang, Y. Jia, Y. Lei, F. Zhang, J. He, T. Liu, S. Luo, Mechanical properties of microcellular and nanocellular silicone rubber foams obtained by supercritical carbon dioxide, Polym. J. 51 (2019) 559–568. https://doi.org/10.1038/s41428-019-0175-6.

[30] J. Martín-de León, V. Bernardo, M.Á. Rodríguez-Pérez, Key Production Parameters to Obtain Transparent Nanocellular PMMA, Macromol. Mater. Eng. 302 (2017) 1700343. https://doi.org/10.1002/mame.201700343.

[31] G.Q. Lu, X.S. Zhao, Nanoporous Materials - An Overview, in: Nanoporous Mater. Sci. Eng., Imperial College Press, 2004: pp. 1–13. https://doi.org/10.1142/9781860946561_0001.

[32] B. Notario, A. Ballesteros, J. Pinto, M.A. Rodríguez-Pérez, Nanoporous PMMA: A novel system with different acoustic properties, Mater. Lett. 168 (2016) 76–79. https://doi.org/10.1016/j.matlet.2016.01.037.

[33] B. Notario, J. Pinto, R. Verdejo, M.A. Rodríguez-Pérez, Dielectric behavior of porous PMMA: From the micrometer to the nanometer scale, Polymer (Guildf). 107 (2016) 302–305. https://doi.org/10.1016/j.polymer.2016.11.030.

[34] I. Sánchez-Calderón, V. Bernardo, D. Cuadra-Rodríguez, J. Martín-de-León, M.Á. Rodríguez-Pérez, Micronization as a solution for enhancing the thermal insulation of nanocellular poly(methyl-methacrylate) (PMMA), Polymer (Guildf). 261 (2022) 125397. https://doi.org/10.1016/j.polymer.2022.125397.

[35] UNE-EN 1602:2013 Thermal insulating products for building applications. Determination of the apparent density., (n.d.).

[36] ASTM C518 Standard Test Method for Steady-State Thermal Transmission Properties by Means of the Heat Flow Meter Apparatus, (2017).

[37] ISO 8301 Thermal insulation - Determination of steady-state thermal resistance and related properties - Heat flow meter, (1991).

[38] R. Caps, U. Heinemann, M. Ehrmanntraut, J. Fricke, Evacuated insulation panels filled with pyrogenic silica powders: Properties and applications, High Temp. - High Press. 33 (2001) 151–156. https://doi.org/10.1068/htwu70.

[39] R. Caps, J. Fricke, Thermal conductivity of opacified powder filler materials for vacuum insulations, Int. J. Thermophys. 21 (2000) 445–452. https://doi.org/10.1023/A:1006691731253.

[40] S. Verma, H. Singh, Vacuum insulation panels for refrigerators, Int. J. Refrig. 112 (2020) 215–228. https://doi.org/10.1016/j.ijrefrig.2019.12.007.

[41] T. Beikircher, M. Demharter, Heat transport in evacuated perlite powders for super-insulated long-term storages up to 300 °c, J. Heat Transfer. 135 (2013) 1–11. https://doi.org/10.1115/1.4023351.

[42] K. Swimm, G. Reichenauer, S. Vidi, H.P. Ebert, Impact of thermal coupling effects on the effective thermal conductivity of aerogels, J. Sol-Gel Sci. Technol. 84 (2017) 466–474. https://doi.org/10.1007/s10971-017-4437-5.

[43] M. Bouquerel, T. Duforestel, D. Baillis, G. Rusaouen, Heat transfer modeling in vacuum insulation panels containing nanoporous silicas - A review, Energy Build. 54 (2012) 320–336. https://doi.org/10.1016/j.enbuild.2012.07.034.

[44] J. Fricke, H. Schwab, U. Heinemann, Vacuum Insulation Panels – Exciting Thermal Properties and Most Challenging Applications, Int. J. Thermophys. 27 (2006) 1123–1139. https://doi.org/10.1007/s10765-006-0106-6.

[45] S. Sonnick, M. Meier, J. Ross-Jones, L. Erlbeck, I. Medina, H. Nirschl, M. Rädle, Correlation of pore size distribution with thermal conductivity of precipitated silica and experimental determination of the coupling effect, Appl. Therm. Eng. 150 (2019) 1037–1045. https://doi.org/10.1016/j.applthermaleng.2019.01.074.

SUPPORTING INFORMATION

Development of new vacuum insulation core panels using micronized nanocellular poly(methyl-methacrylate) (PMMA)

Ismael Sánchez-Calderón[1], Victoria Bernardo[2], Félix Lizalde-Arroyo[1], Judith Martín-de-León[1], Miguel Ángel Rodríguez-Pérez[1,3].

[1]*CellMat Laboratory. Campus Miguel Delibes. Faculty of Science. Condensed Matter Physics Department. University of Valladolid, Paseo de Belén 7, 47011, Valladolid, Spain.*

[2]*CellMat Technologies S.L., Paseo de Belén 9-A, 47011, Valladolid, Spain.*

[3]*BioEcoUVA Research Institute on Bioeconomy, University of Valladolid, 47011, Valladolid, Spain.*

Corresponding author: Ismael Sánchez-Calderón (ismaelsc@fmc.uva.es)

S1. Parameters used to characterize the micronized samples

When a material is micronized, it is now formed by micrometric particles surrounded by air (**Figure S1**). The powder is characterized by its apparent density (ρ_{app_M}). The apparent density of the micronized samples (ρ_{app_M}) was obtained according to ISO 60[1].

Assuming that each particle is characterized by a density ($\rho_{particle\_M}$), it is possible to define a packaging factor, *F*, calculated as Equation (S1).

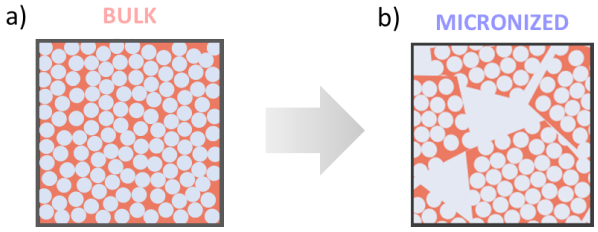

Figure S1. Scheme of a) bulk material and b) micronized material.

$$F = \frac{\rho_{app\_M}}{\rho_{particle\_M}} \quad \text{(S1)}$$

This packaging factor accounts for the fraction of the powder that is occupied by the particles (and not the voids), that is, the fraction of foamed particles in the powder. For random packaging of non-spherical particles, packaging factors as high as 0.77 are expected[2,3]. In our previous work, we obtained a mean experimental packing factor through X-ray tomography of 0.76 for the micronized nanocellular polymers. The packaging factor allows for calculating the density of the powder particles. In this work, we have used a constant packaging factor of 0.76 for all the samples to calculate the particle density ($\rho_{particle\_M}$)[4].

Note that the density of the powder particles is higher than the density of the initial bulk material (**Table 1** in the main manuscript). Therefore, we conclude that the particles suffer some type of densification during the milling process, but the densification did not result in noticeable changes in the cellular structure.

Finally, the open cell content of the micronized materials (OC_M) is calculated using the calculated particle density.

S2. SEM micrographs of the materials produced in this work

Figure S2 shows SEM micrographs at different magnifications of the bulk and micronized microcellular and nanocellular materials. It is observed that the cellular structure is maintained after the micronization.

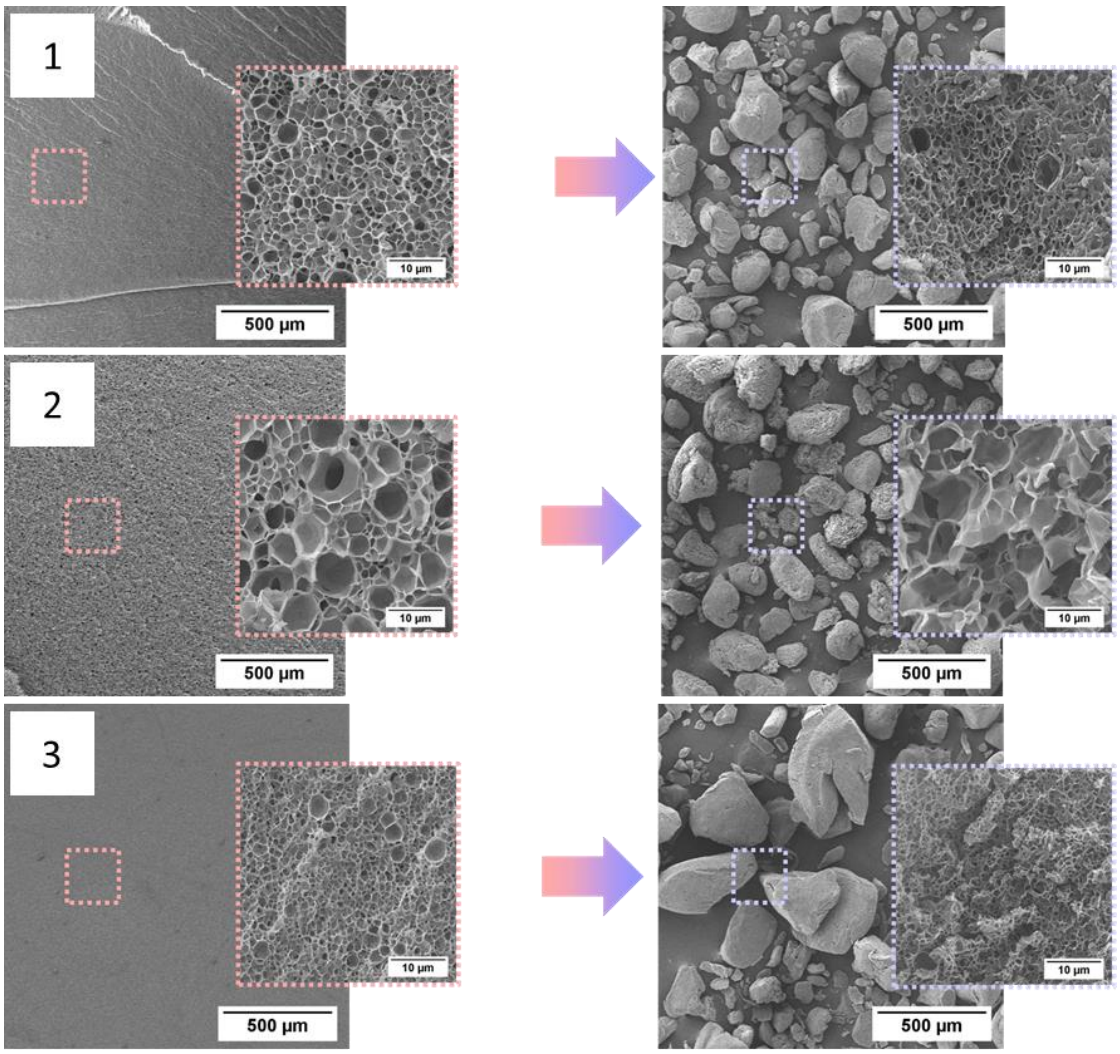

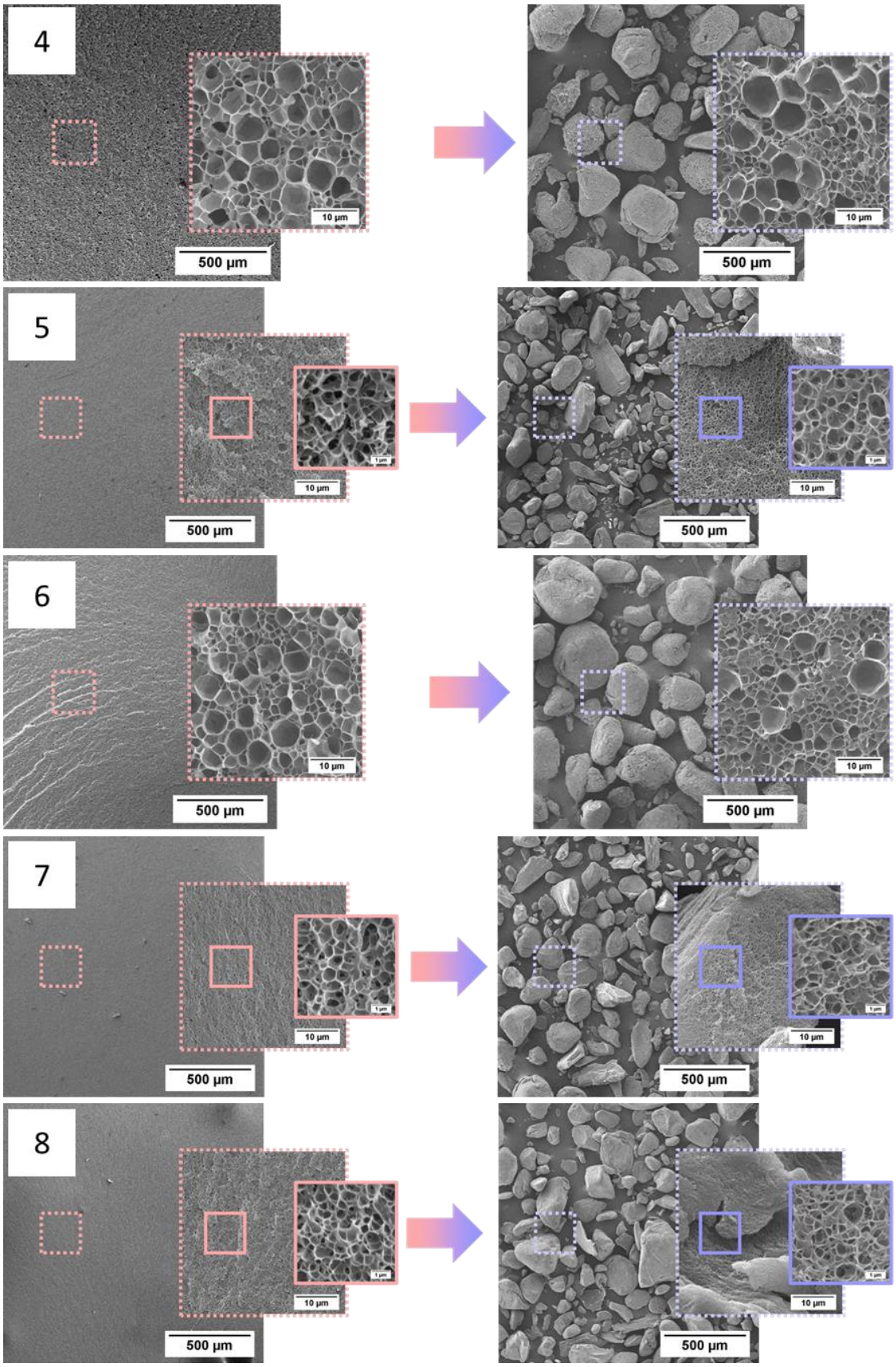

Figure S2. SEM micrographs at different magnifications of the bulk and micronized microcellular and nanocellular materials. The number is referred to the samples summarized in **Table 1** (main manuscript).

Figure S3 shows SEM micrographs at different magnifications of sample 5 before (**Figure S3a**) and after (**Figure S3b**) the compaction process. Also, SEM micrographs at different magnifications of the surface of the compacted sample 5 are shown in **Figure S3c**. It is observed that the cellular structure is maintained after the compaction process.

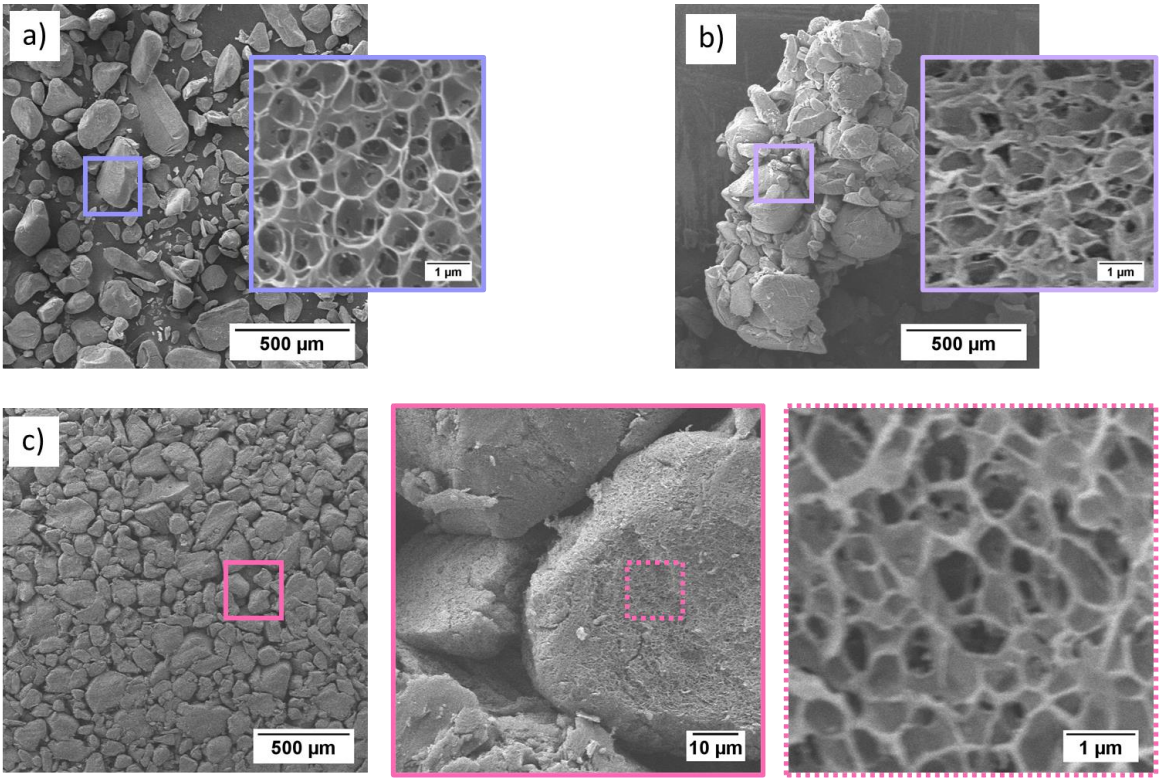

Figure S3. SEM micrographs at different magnifications of sample 5: a) before and b) after the compaction process. c) SEM micrographs at different magnifications of the surface of the compacted sample 5.

S3. Knudsen effect

The conduction through the cell phase depends on the gas volume fraction (X_g), and the thermal conductivity of the gas inside the cells λ'_g[5] (Equation (S2)). In cellular polymers, the gas volume fraction corresponds to the porosity (V_f) (calculated as $V_f = 1 - \rho_r$).

$$\lambda_g = \lambda'_g X_g = \lambda'_g V_f = \lambda'_g (1 - \rho_r) \qquad \text{(S2)}$$

In nanocellular polymers, the appearance of the Knudsen effect reduces the contribution of the thermal conductivity of the cell phase with respect to the equation for conventional materials, as experimentally proved by Notario et al.[6]. This effect implies that when the cell size is comparable to or smaller than the mean free path (i.e. the average distance between collisions) of the gas molecules, they collide more often with the cell walls than among them, reducing the energy transfer[7]. Therefore, the conductivity of the gas inside the cells, λ'_g is reduced (see Equation (S3)). It depends on the thermal conductivity of the free gas, that is without being encapsulated in a cell,

(λ'_{g0}) (which also depends on the temperature), the cell size (ϕ), and the mean free path of the gas molecules (l_g). According to the theory, Knudsen effect starts becoming relevant when the cell size is smaller than 100 times the mean free path, $\phi \leq 100\ l_g$ [8]. At standard ambient temperature and pressure (25 ºC and 101325 Pa) the mean free path of the air is 70 nm. Then, Knusden effect takes place in air-filled nanocellular polymers for $\phi \leq 7$ µm.

$$\lambda'_g = \frac{\lambda'_{g0}}{1 + \frac{2\beta l_g}{\phi}} \tag{S3}$$

β is a dimensionless intrinsic parameter that considers the transfer of energy between the gas molecules and the solid structure. β value varies from 1.5 to 2 for argon and nitrogen[7], being 1.64 the value for air[9,10]. There are several definitions for β in the literature, being a function of at least one of the following parameters: the specific heat ratio, the thermal accommodation coefficient, and the Prandtl number [7,9,11,12]. Meanwhile, the mean free path (l_g) depends on the temperature (T), the pressure (p), and the molecule diameter (d_m) (3.6 Å for air[13]).

So, the conduction through the cell phase can be expressed in terms of the average cell size, the gas characteristics, the pressure, and the temperature, as given in Equation (S4).

$$\lambda_g = \lambda'_g(1-\rho_r) = \frac{\lambda'_{g0}(1-\rho_r)}{1 + \frac{2\beta}{\phi}\frac{RT}{\sqrt{2}\pi d_m^2 N_A p}} \tag{S4}$$

S4. Experimental thermal conductivities of the compacted samples at different pressures

Figure S4 shows the experimental thermal conductivity of the compacted samples at 10 °C and different pressures.

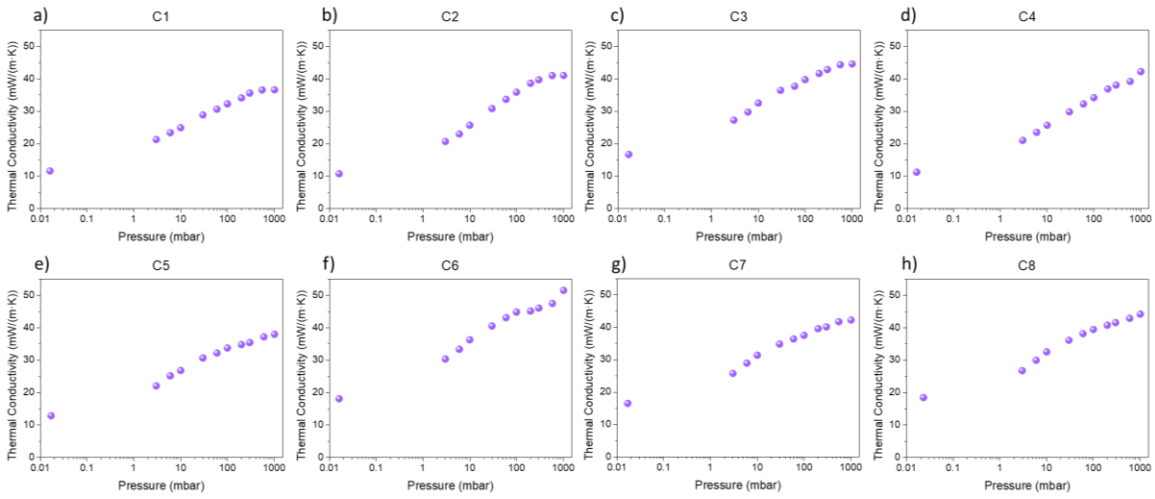

Figure S4. Experimental thermal conductivity of the compacted samples at 10 °C and different pressures: a) C1, b) C2, c) C3, d) C4, e) C5, f) C6, g) C7, and h) C8.

References

[1] ISO 60:1977 Plastics — Determination of apparent density of material that can be poured from a specified funnel, (1977).

[2] X. Chateau, Particle packing and the rheology of concrete, in: Underst. Rheol. Concr., Elsevier, 2012: pp. 117–143. https://doi.org/10.1533/9780857095282.2.117.

[3] A. Averardi, C. Cola, S.E. Zeltmann, N. Gupta, Effect of particle size distribution on the packing of powder beds: A critical discussion relevant to additive manufacturing, Mater. Today Commun. 24 (2020) 100964. https://doi.org/10.1016/j.mtcomm.2020.100964.

[4] I. Sánchez-Calderón, V. Bernardo, D. Cuadra-Rodríguez, J. Martín-de-León, M.Á. Rodríguez-Pérez, Micronization as a solution for enhancing the thermal insulation of nanocellular poly(methyl-methacrylate) (PMMA), Polymer (Guildf). 261 (2022) 125397. https://doi.org/10.1016/j.polymer.2022.125397.

[5] J. Fricke, Thermal Transport in Porous Superinsulations, (1986) 94–103. https://doi.org/10.1007/978-3-642-93313-4_11.

[6] B. Notario, J. Pinto, E. Solorzano, J.A. de Saja, M. Dumon, M.A. Rodríguez-Pérez, Experimental validation of the Knudsen effect in nanocellular polymeric foams, Polymer (Guildf). 56 (2015) 57–67. https://doi.org/10.1016/j.polymer.2014.10.006.

[7] Z.-Y. Li, C.-Y. Zhu, X.-P. Zhao, A theoretical and numerical study on the gas-contributed thermal conductivity in aerogel, Int. J. Heat Mass Transf. 108 (2017) 1982–1990. https://doi.org/10.1016/j.ijheatmasstransfer.2017.01.051.

[8] J. Nassios, Kinetic theory of rarefied gas flows with modern applications, Austms.Org.Au. (2006). https://www.austms.org.au/Publ/Gazette/2013/Mar13/Nassios.pdf.

[9] S. Song, M.M. Yovanovich, F.O. Goodman, Thermal gap conductance of conforming surfaces in contact, J. Heat Transfer. 115 (1993) 533–540. https://doi.org/10.1115/1.2910719.

[10] V. Bernardo, J. Martin-de Leon, J. Pinto, R. Verdejo, M.A. Rodriguez-Perez, Modeling the heat transfer by conduction of nanocellular polymers with bimodal cellular structures, Polymer (Guildf). 160 (2019) 126–137. https://doi.org/10.1016/j.polymer.2018.11.047.

[11] Y.L. He, T. Xie, Advances of thermal conductivity models of nanoscale silica aerogel insulation material, Appl. Therm. Eng. 81 (2015) 28–50. https://doi.org/10.1016/j.applthermaleng.2015.02.013.

[12] S. Sonnick, L. Erlbeck, M. Meier, H. Nirschl, M. Rädle, Methodical selection of thermal conductivity models for porous silica-based media with variation of gas type and pressure, Int. J. Heat Mass Transf. 187 (2022). https://doi.org/10.1016/j.ijheatmasstransfer.2022.122519.

[13] S.E. Kentish, C.A. Scholes, G.W. Stevens, Carbon Dioxide Separation through Polymeric Membrane Systems for Flue Gas Applications, Recent Patents Chem. Eng. 1 (2008) 52–66. https://doi.org/10.2174/1874478810801010052.

4.5. Coupling effect in compacted panels based on micronized nanocellular polymers: modeling of the thermal conductivity

Ismael Sánchez-Calderón[1], Victoria Bernardo[2], Félix Lizalde-Arroyo[1], Judith Martín-de-León[1], Miguel Ángel Rodríguez-Pérez[1,3].

[1]*CellMat Laboratory. Campus Miguel Delibes. Faculty of Science. Condensed Matter Physics Department. University of Valladolid, Paseo de Belén 7, 47011, Valladolid, Spain.*

[2]*CellMat Technologies S.L., Paseo de Belén 9-A, 47011, Valladolid, Spain.*

[3]*BioEcoUVA Research Institute on Bioeconomy, University of Valladolid, 47011, Valladolid, Spain.*

Corresponding author: Ismael Sánchez-Calderón (ismaelsc@fmc.uva.es)

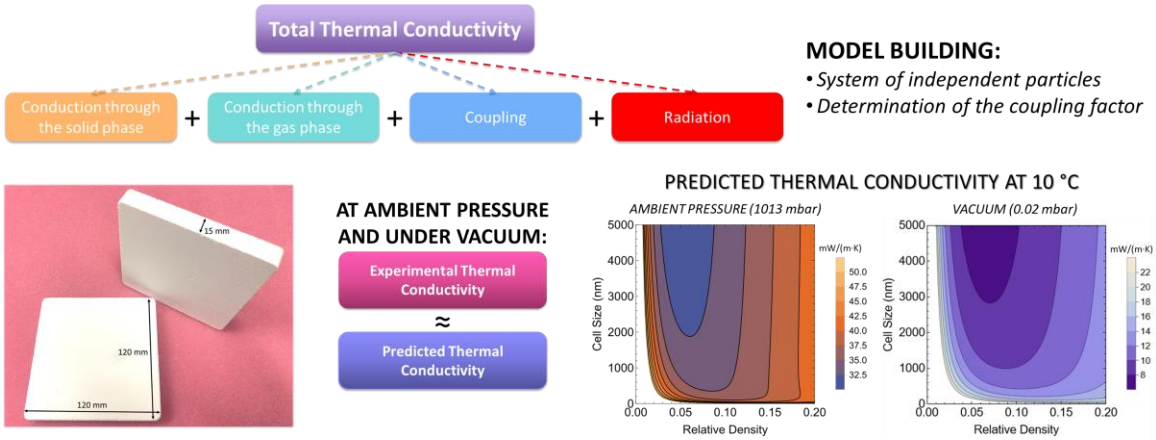

ABSTRACT

Compacted panels based on micronized nanocellular polymers show reduced thermal conductivity in comparison with bulk nanocellular polymers, especially under vacuum, so they are promising materials to be used as vacuum insulation panels (VIP). The discontinuous structure formed by micrometric particles allows for decreasing the conduction through the solid phase since the contact points between the particles act as additional thermal resistances to the heat transmission. However, the discontinuous structure also leads to the appearance of the coupling effect, which cannot be modeled using the typical equations for cellular polymers. In this work, a semi-empirical model able to predict the thermal conductivity of compacted panels based on nanocellular poly(methyl-methacrylate) (PMMA) is developed. The model allows quantifying each heat transfer mechanism contribution (conduction through the solid phase, conduction through the gas phase, radiation, and coupling effect). The model shows that the contribution of the coupling effect in the compacted panels is higher than 50% of the total thermal conductivity for pressures higher than 5 mbar, supporting the need for the model to correctly predict the insulation performance of these materials. The model predicts minimum thermal conductivities of 32.5 mW/(m·K) at ambient pressure and of 10 mW/(m·K) at maximum vacuum.

Keywords: thermal conductivity, poly(methyl-methacrylate), thermal insulation, compacted micronized nanocellular polymer, coupling effect.

1. Introduction

Vacuum insulation panels (VIPs) are one of the most promising high-performance thermal insulation materials[1], exhibiting thermal conductivities between 4-8 mW/(m·K)[2–5]. They can be described as an evacuated open porous material (core) placed inside a gas barrier envelope. The materials usually selected as core materials are based on fumed/precipitated silica, silica aerogel, glass fibers, and open cell rigid polyurethane foams (PUR)[6]. The physics behind their super-thermal insulation behavior is well-known[1,7–11]: the total thermal conductivity (λ_t) can be described as a sum of five heat transfer mechanisms (Equation (1)): conduction through the solid phase (λ_s), conduction through the gas phase (λ_g), radiation (λ_r), convection (λ_c), and coupling (λ_{coup}). From these contributions, convection can be neglected when the cell/pore sizes are lower than 4 mm[12–14]. Thus, when the core is fully evacuated, the conduction through the gas phase and the coupling contribution became null leading to a drastic decrease in the thermal conductivity.

$$\lambda_t = \lambda_s + \lambda_g + \lambda_r + \lambda_c + \lambda_{coup} \quad (1)$$

The coupling term takes into account the interaction between the core particles and the gas[1,7], so it is important for particle-based materials (such as fumed silica) but negligible for materials with continuous structure[1,10,15,16]. As previously commented, at the normal operating conditions of VIPs (vacuum) it becomes null due to the lack of gas molecules, but at ambient pressure, it can have a significant contribution to the total thermal conductivity[8,10,11,17]. For instance, Fricke et al.[10] reported coupling contributions between 20-30 mW/(m·K) for powders consisting of hard grains (perlite and diatomite), leading to a higher thermal conductivity than expected at ambient pressure. Similar behavior was observed by Reichenauer et al.[9] and by Swimm et al.[17] for a system consisting of solid glass spheres of 1 mm diameter and for an organic aerogel (pore size of 600 nm), respectively. However, despite the importance of the coupling effect, only a few authors modeled the coupling due to its complexity. Swimm et al.[18], Zhao et al.[19], and Bi et al.[20] modeled analytically the coupling effect for aerogels. Meanwhile, Verma et al.[21] and Liu et al.[22] developed a numerical model which already takes into account the coupling for perlite-based systems and aerogels, respectively. On the other hand, Swimm et al.[16,17] and Sonnick et al.[15] modeled semi-empirically the coupling for aerogels and precipitated silica, respectively. They show that the coupling depends on the density (the higher density, the higher coupling)[15,17].

In our previous work[23], we produced vacuum insulation panels based on micronized nanocellular poly(methyl-methacrylate) (PMMA). The thermal conductivity results at ambient pressure and under vacuum provided surprising results, obtaining higher thermal conductivity reductions when vacuuming than expected, and this behavior was attributed to the coupling effect. Unlike bulk nanocellular polymers, which are characterized by a continuous cellular structure and whose thermal conductivity has been widely modelized[24–31], micronized nanocellular polymers are

novel materials characterized by a discontinuous cellular structure with the nanocells inside the micrometric particles[32]. Micronized nanocellular polymers rise as an attempt to enhance the thermal insulation behavior of nanocellular polymers[23,32], which present high conduction through the solid phase and radiation as shown by recent theoretical and experimental works[26–29]. Therefore, the modeling of the thermal conductivity of micronized nanocellular polymers is of utmost importance to continue exploring this novel route.

In this work, a semi-empirical model to predict the thermal conductivity of compacted panels based on micronized nanocellular PMMA that only depends on the material characteristics (density, cell size, and particle size) and the measurement conditions (pressure and temperature) is developed. For the first time, the coupling effect is studied in micronized nanocellular polymer systems. Results show that these materials are quite promising for VIP applications since under vacuum it is possible to achieve quite low thermal conductivities, below those obtained with bulk nanocellular polymers.

2. Experimental

Compacted panels of dimensions of 120×120×15 mm^3 were produced from microcellular and nanocellular micronized PMMA. Details about the production of the bulk microcellular and nanocellular PMMA via gas dissolution foaming, the micronization process, the compaction process, and the characterization of these samples can be found in our previous works[23,29,32]. The PMMA grade used was PLEXIGLAS® 7H kindly supplied by Röhm GmbH. This PMMA presents a density of 1190 kg/m^3, a melt flow index of 0.77 g/10 min (measured at 230 ºC and 2.16 kg), and a glass transition temperature of 110.4 ºC measured by DSC (model DSC3+, Mettler).

Table 1 gathers the main features of the compacted samples which are going to be used to develop the semi-empirical model to predict their thermal conductivity. Apparent density (ρ_{app}) was obtained according to UNE-EN 1602[23,33]. Cell size (ϕ_{3D}) was obtained after analyzing the cellular structure from scanning electron microscopy (SEM) micrographs[29,34]. Particle size (D) was obtained through image analysis[32,35]. Open cell content (OC) was measured according to ISO 4590[32,36]. Finally, thermal conductivity under maximum vacuum (0.02 mbar) (λ_{vacuum}) at 10 ºC and thermal conductivities at ambient pressure ($\lambda_{ambient\ pressure}$) at different temperatures (10, 20, 30, and 40 ºC) were measured using a thermal heat flow meter model FOX 200 (TA Instruments / LaserComp, Inc.), which measures according to ASTM C518 and ISO 8301[37,38] (steady-state conditions)[23]. Measurements were also performed under different pressures (600, 300, 200, 100, 60, 30, 10, 6, and 3 mbar) at 10 ºC and used to validate the model. See [23] for details about the characteristics of the FOX 200, the set-up used, the procedure, and the vacuum measurements.

Table 1. Density, cell size, particle size, open cell content, thermal conductivity under vacuum (0.02 mbar) and 10 ºC, and thermal conductivity at ambient pressure at different temperatures (10, 20, 30, and 40 ºC) of the compacted panels.

							λ_{vacuum} (mW/(m·K))	$\lambda_{ambient\ pressure}$ (mW/(m·K))			
Sample	ρ_{app} (kg/m^3)	ϕ_{3D} (nm)	SD/ϕ_{3D_B}	D (µm)	SD/D	OC (%)	*10 ºC*	*10 ºC*	*20 ºC*	*30 ºC*	*40 ºC*
C1	158	1459	0.41	77	0.68	87±1	11.6	36.6	37.5	38.4	39.2
C2	223	3215	0.70	92	0.73	98±1	10.7	41.1	41.9	42.8	43.7
C3	292	1021	0.45	109	0.68	85±1	16.7	44.6	45.4	46.3	47.0
C4	190	2916	0.59	102	0.78	94±1	11.2	38.8	39.8	40.7	41.6
C5	201	468	0.47	94	0.62	98±1	12.9	38.0	38.7	39.5	40.3
C6	357	2379	0.65	139	0.64	80±1	18.1	51.1	52.0	52.9	53.8
C7	265	408	0.47	102	0.64	92±1	16.5	42.2	42.9	43.7	44.4
C8	282	394	0.43	100	0.69	97±1	18.5	44.2	44.7	45.5	46.1

3. Model: Experimental determination of the coupling effect

Our model is based on calculating the contributions of the different heat transfer mechanisms as presented in Equation (1), but with the main novelty of the model is calculating the conduction mechanisms considering a system of independent particles, as described below. Then, the coupling effect can be determined experimentally.

3.1. Conduction mechanisms: association of thermal resistances

On the one hand, the model is based on assuming an infinite association of the powder particles to describe the conduction through the material. The powder particles act as thermal resistances, so the equivalent thermal conductivity of heat transfer by conduction (λ_{eq}) is given by Equation (2) where λ_s and $\lambda_{g,cells}$ are the conduction through the solid and cell phases of each particle, respectively. The term $(1+\sqrt{3})$ is obtained by applying Ohm and Kirchhoff law's (association of infinite resistances in series-parallel configuration[39]). As far as the authors know, this is the first time this hypothesis is used to describe the thermal conductivity of powdered systems.

$$\lambda_{eq} = \frac{\lambda_s + \lambda_{g,cells}}{1+\sqrt{3}} \quad (2)$$

The conduction through the solid phase of each particle (λ_s) depends on its solid volume fraction (X_s), the conductivity of the solid matrix (λ'_s), and a structural factor g (Equation (3)). In the powdered systems, the solid volume fraction is the relative apparent density. The apparent relative density is defined as $\rho_{r,app} = \rho_{app} / \rho_s$, where ρ_{app} is the apparent density and ρ_s is the density of the solid PMMA (1190 kg/m^3). The conductivity of the solid PMMA (λ'_{s_PMMA}) depends on the temperature as shown in **Supporting Information Section S1**. Considering that each particle is a bulk nanocellular polymer, the g factor is considered to be 0.89 (value calculated in our previous work for bulk samples[29]). Note that the effective g factor of the total compacted sample is going

to be 0.33 (because of the dividing term in Equation (2)). This value of g is very low in comparison with the value of the bulk material: this hypothesis implies that the conduction through the solid phase is very much reduced because of the presence of thermal resistances between the powder particles.

$$\lambda_s(mW/(m\cdot K)) = \lambda'_s g X_{s,powder} = \lambda'_{s\_PMMA} 0.89 \rho_{r,app} \quad (3)$$

Meanwhile, the conduction through the cells of each particle ($\lambda_{g,cells}$) depends on the thermal conductivity of the gas ($\lambda'_{g,cells}$) and the cells volume fraction ($X_{g,cells}$) (that can be calculated as 1 – $\rho_{r,app}$) (Equation (4)). The conductivity of the gas is not that of the air, but it is reduced due to the Knudsen effect[40]. Therefore, the conductivity of the gas inside the cells is reduced as the cell size is reduced, and also when pressure is reduced by vacuuming. Thus, the conduction through the cells phase also depends on the conductivity of air (λ'_{g0_air}) (which is a function of the temperature as shown in **Supporting Information Section S1**[41]), the cell size (ϕ), an intrinsic parameter that considers the transfer of energy between the gas molecules and the solid structure (β), the temperature (T), the pressure (p), the molecule diameter (d_m), the ideal gas constant (R) and the Avogadro's number (N_A). All the constants used for the model calculations are also collected in **Supporting Information Section S1**.

$$\lambda_{g,cells}(mW/(m\cdot K)) = \lambda'_{g,cells} X_{g,cells} = \frac{\lambda'_{g\_air}(1-\rho_{r,app})}{1+\frac{2\beta}{\phi}\frac{RT}{\sqrt{2}\pi d_m^2 N_A p}} \quad (4)$$

3.2. Radiation

On the other hand, thermal radiation (λ_r) is supposed to follow the equation obtained for the bulk materials (Equation (5))[29]. We make the hypothesis that the presence of the particle interfaces does not create additional scattering surfaces for radiation, and we assume that the compacted powders behave similarly to bulk materials with the same density as far as the radiation contribution is concerned. The radiation term depends on the temperature (T), the Stefan-Boltzmann constant (σ), the refractive index (n), and the extinction coefficient (K_e). K_e can be calculated with an empirical equation that takes into account the cell size (ϕ) and the relative apparent density ($\rho_{r,app}$) (**Supporting Information Section S1**).

$$\lambda_r(mW/(m\cdot K)) = \frac{16n^2\sigma T^3}{3K_e}\cdot 1000 = \frac{16n^2\sigma T^3}{3(5.6712\cdot 10^6\,\phi^{0.4264})\rho_{r,app}}\cdot 1000 \quad (5)$$

3.3. Coupling effect

There are some models to describe the coupling term (λ_{coup}). In the simplest case, as proposed by Swimm et al.[16], it can be described as a series connection of thermal resistances between the solid (R_s) and the gas (R_g) phases (**Figure 1**). Using the general relation for a thermal resistance ($R = d / \lambda$, where R is the thermal resistance, d is the distance, and λ the thermal conductivity), the following

equation (Equation (6)) can be derived to describe the coupling. Where d_s and d_g are the thickness over which the heat is transferred within the solid and gas phases. The system is described in terms of a unit cell that contains all the information (the unit cell thickness is $d_{unit\ cell}$). In this model, all influencing parameters like the particle surface geometry near the area of particle-to-particle contact or the thermal conductivity of the solid are combined in one-factor *f*, which may be a function of the porosity of the material[15]. As the *f* factor is usually the only unknown parameter, it can be obtained by solving the overall thermal conductivity equation and fitting the calculated data to the experimental data using the method of the least squares[15,17]. For instance, Sonnick et al.[15] obtained that f = -18.68V_f + 17.94 (where V_f is the porosity, which range between 0.92 and 0.76) for a precipitated silica system. Therefore, *f* takes values from 0.75 to 3.74. Meanwhile, Swimm et al.[17] obtained *f* values of 1.73 to 2.25 for two organic aerogels of porosities of 0.78 and 0.76 respectively (if doing a linear fit, f = -26.00 V_f + 22.01). Whereas Heinemann et al.[42] mentioned that for a bed of glass spheres f would be 7.

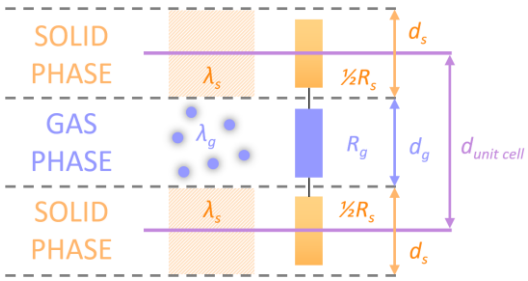

Figure 1. Simple resistance model to describe the coupling of solid and gas heat conduction (adapted from[16]). The violet lines indicate one unit cell.

$$\lambda_{coup} = \frac{d_{unit\ cell}}{R_s + R_g} = \frac{d_s + d_g}{\frac{d_s}{\lambda_s} + \frac{d_g}{\lambda_g}} = \lambda_g \frac{\lambda_s (d_s + d_g)}{\lambda_g d_s + \lambda_s d_g} = \lambda_g \cdot f \qquad (6)$$

Applying Equation (6) to the powdered systems, the thermal conductivity of the gas is that of the air, which is described by the Knudsen effect, depending on the particle size (*D*) because the coupling effect is related to the presence of the particles[15]. So, the coupling effect is described by Equation (7). All terms are known except the *f* factor.

$$\lambda_{coup}(mW/(m \cdot K)) = \frac{\lambda'_{g\_air}}{1 + \frac{2\beta}{D}\frac{RT}{\sqrt{2}\pi d_m^2 N_A p}} \cdot f \qquad (7)$$

3.3.1. Determination of the f factor

The only unknown parameter to predict the thermal conductivity is the *f* factor. It is calculated for each compacted material at different temperatures by solving Equations (7) and (8):

$$\lambda_{coup} = \lambda_t - \lambda_{eq} - \lambda_r \qquad (8)$$

Where λ_t is the experimental thermal conductivity, and λ_{eq} and λ_r are calculated based on Equations (2), (3), (4), and (5). Constants and values used for the calculations are gathered in **Supporting Information Section S1**. Then, the results of the experimental *f* factor at each temperature are fit as a function of the apparent relative density using the method of the last squares[15], as shown in **Figure 2a**. For the samples produced in this work, *f* takes values from 0.75 to 1.09. Note that, the higher the *f* factor, the higher coupling (Equation (7)). As density increases, the *f* factor increases (**Figure 2a**) leading to a higher coupling contribution. It was observed that the fitting parameters were also a function of the temperature as shown in **Figure 2b**. So, the *f* factor has been defined as a function of the apparent density and the temperature. Results of the calculus are summarized in **Supporting Information Section S2**. As far as the authors know, this is the first time that *f* is defined also as a function of the temperature, but, looking at Equation (6), since the thermal conductivity of the solid and gas depends on the temperature, it makes sense for *f* to be also a function of the temperature. As temperature increases, the *f* factor decreases (**Figure 2a**) leading to a lower coupling contribution.

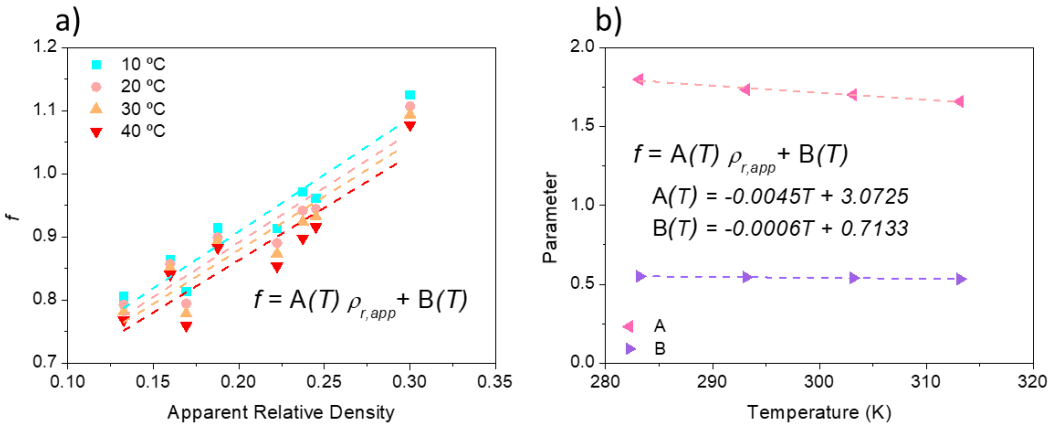

Figure 2. Determination of the *f* factor: a) *f* as a function of the apparent relative density of the compacted samples for different temperatures, and b) fitting parameters as a function of the temperature.

Therefore, the total thermal conductivity (λ_t) of the compacted systems is described by Equation (9).

$$\lambda_t(mW/(m\cdot K)) = \frac{\lambda'_{s\_PMMA}0.89\rho_{r,app} + \frac{\lambda'_{g\_air}(1-\rho_{r,app})}{1+\frac{2\beta}{\phi}\frac{RT}{\sqrt{2}\pi d_m^2 N_A p}}}{1+\sqrt{3}} + \\ + \frac{16n^2\sigma T^3}{3(5.6712\cdot 10^6\,\phi^{0.4264})\rho_{r,app}}\cdot 1000 + \frac{\lambda'_{g\_air}}{1+\frac{2\beta}{D}\frac{RT}{\sqrt{2}\pi d_m^2 N_A p}}\cdot(A\rho_{r,app}+B) \quad (9)$$

4. Model validation and predictions

4.1. Validation: Comparison of the model predictions with the experimental results for the compacted panels

Using Equation (9) it is possible to predict the conductivity of the compacted samples at the different temperatures and at ambient pressure (**Figure 3a**), and at 10 ºC and at maximum vacuum (0.02 mbar) (**Figure 3b**). Regarding the predictions at ambient pressure (**Figure 3a**), the average absolute difference of the predictions at the different temperatures is lower than 0.8 mW/(m·K) (0.7 mW/(m·K) at 10 ºC) (**Figure 3c**). Therefore, the predicted values adjust well to the experimental measurements, with deviations below 3.5%. Meanwhile, at vacuum (**Figure 3b**), the experimental thermal conductivity is in general higher than the predicted thermal conductivity. One possible reason is that, as seen in **Table 1**, the materials are not 100% open cell, so if they cannot be fully evacuated this can cause discrepancies with the model. Nevertheless, the average absolute difference at 10 ºC is lower than 1.0 mW/(m·K) (see **Figure 3d**).

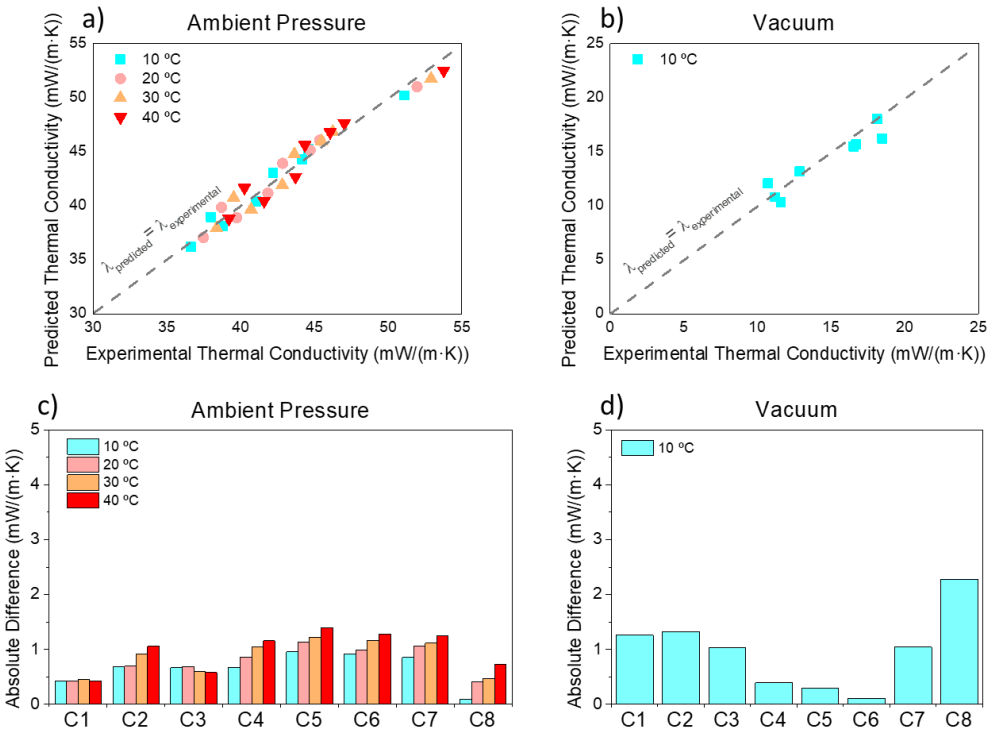

Figure 3. Predicted vs experimental thermal conductivities of the compacted panels at various temperatures and ambient pressure (1013 mbar) (a), and at 10 ºC and maximum vacuum (0.02 mbar) (b). Absolute differences of the predictions of the compacted samples at various temperatures and ambient pressure (a), and at 10 ºC and maximum vacuum (0.02 mbar) (b).

Figure 4 shows the calculated thermal conductivities of the PMMA compacted panels at 10 °C and their contributions from conduction through the gas in the cells and the solid, radiation, and coupling in mW/(m·K) (**Figure 4a**) and in % of the total thermal conductivity (**Figure 4b**). It is observed that the coupling effect represents about 53% (around 20 mW/(m·K)) of the total thermal

conductivity, followed by the conduction through the solid phase (approximately 27%), conduction through the cell phase (which ranges between 10-18%), and radiation (which ranges between 2-9%). Note that the radiation contribution of the nanocellular samples (C5, C7, and C8) is higher, and also C1 presents higher radiation, probably due to its low density. The conduction through the solid phase is quite low in comparison with a bulk nanocellular polymer[29] because the effective *g* factor in this material is 0.33 (2.7 times lower than that of bulk materials). The conduction of the gas inside the cells represents a small fraction of the total due to the assumption of the model of considering this mechanism an association of thermal resistance. Meanwhile, the high fraction represented by the coupling effect remarks the need of the proposed model to understand the thermal conductivity of the micronized nanocellular materials: their behavior cannot be understood without this additional heat transfer mechanism. The coupling effect represents the same fraction in all the materials, regardless the size of the cells and even the density.

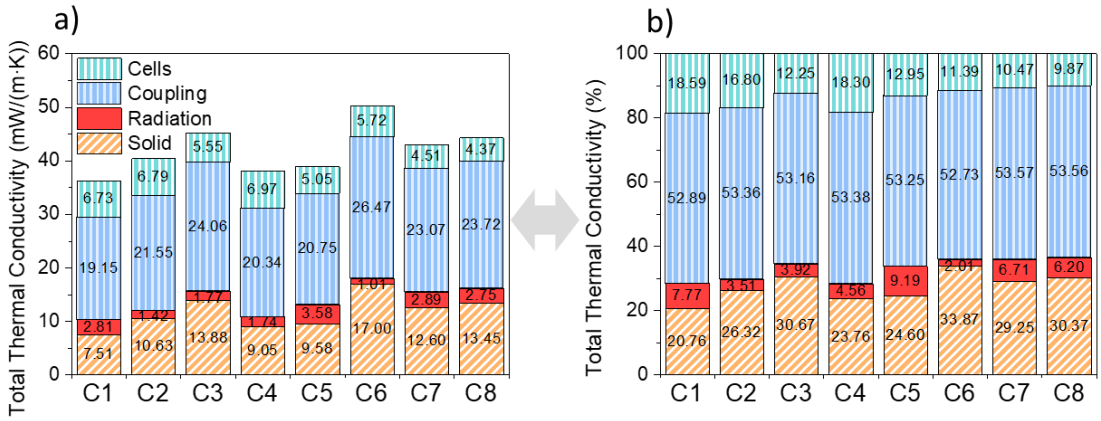

Figure 4. Predicted contribution of each heat transfer mechanism to the total thermal conductivity of the compacted panels at 10 ºC in mW/(m·K) (a) and in % of the total thermal conductivity (b).

Regarding the accuracy of the model to predict the experimental data obtained at different pressures, **Figure 5** shows the experimental and predicted thermal conductivities of the compacted panel #5 at 10 °C as a representative example. It is observed that the prediction of our model adjusts well to the experimental points at different pressures. This accuracy also occurs in the rest of the compacted samples (see **Supporting Information Section S3**) reinforcing the validity of the model. The thermal conductivity at 10 ºC as a function of the pressure of bulk sample #5 and its prediction according to the equation obtained in [29] has also been included in **Figure 5** as a reference. While in the bulk material, there is only one drop of thermal conductivity (due to the Knudsen effect associated with the conduction through the gas phase), in the compacted sample there is a double drop: one due to the Knudsen effect affecting the conduction through the gas in the cells, and the other one due to the coupling effect. The drop due to the Knudsen effect affecting the conduction through the cells phase is governed by the cell size, meanwhile, the drop due to the coupling effect is governed by the particle size.

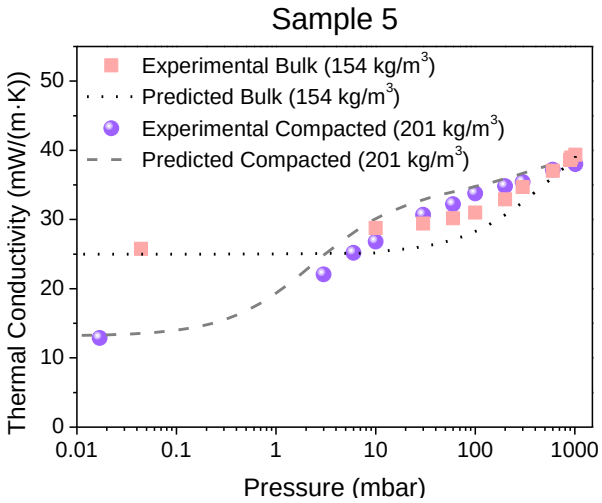

Figure 5. Thermal conductivity at 10 ºC as a function of the pressure of the compacted panel #5 and prediction according to Equation (9). The thermal conductivity at 10 ºC as a function of the pressure of bulk sample #5 and its prediction according to the equation obtained in [29] has been included as a reference.

The good accuracy of the model to predict the experimental results support the validity of the hypothesis used to build the model:

- The effective *g* factor in a compacted panel is as low as 0.33. Then, by means of micronization and compaction, the solid conduction can be reduced 2.7 times.
- There is a coupling effect that is responsible for the highest contribution to the total thermal conductivity at ambient pressure.

Note that the model is developed in a certain range of densities (160-360 kg/m^3) and cell sizes (400-3200 nm). In the next section, the equations developed in the model are going to be used to extrapolate the behavior to densities and cell sizes out of the range of study of this work.

4.2. Effect of the cell size, particle size, pressure, and density on the thermal conductivity

The model can be used to predict trends and study the effect of the different parameters on the thermal conductivity of compacted panels. On the one hand, **Figure 6a**, **6b**, and **6c** show the effect of the particle size on the thermal conductivity at different pressures. The predictions were calculated at 10 ºC, assuming 500 nm of cell size and an apparent density of 150 kg/m^3 (**Figure 6a**), 100 kg/m^3 (**Figure 6b**), and 50 kg/m^3 (**Figure 6c**). Note that since the particle size is not in the nanoscale it does not affect the total thermal conductivity at ambient pressure or at maximum vacuum, only the curve at different pressures. As the particle size is reduced the Knudsen effect occurs at higher pressures (requiring a lower vacuum to fully evacuate the material), so for applications like vacuum insulation panels the smallest the particle size the better. Furthermore, it is observed that as density decreases from 150 kg/m^3 to 100 kg/m^3 the total thermal conductivity

decreases, but at 50 kg/m^3 it increases again. When density decreases the conduction through the solid phase and the coupling decrease, whereas the conduction through the cells phase and the radiation increase (Equation (9)), leading to a compromise between the heat transfer mechanisms that result in an optimum density. On the other hand, **Figure 6d**, **6e**, and **6f** show the effect of the cell size on the thermal conductivity at different pressures for a fixed particle size of 100 µm. The predictions were performed at 10 ºC, assuming an apparent density of 150 kg/m^3 (**Figure 6d**), 100 kg/m^3 (**Figure 6e**), and 50 kg/m^3 (**Figure 6f**). In this case, the cell size is affecting both the conduction through the cells phase and the radiation. Regarding the radiation, the lower the cell size the higher radiation since the material becomes transparent to infrared radiation[27–29], obtaining higher thermal conductivities. Also, when the density is reduced there is less amount of matter to absorb/scatter the thermal radiation, so the radiation rises hugely. This effect can be easily observed at vacuum. With respect to the conduction through the cells phase, it is observed that the first fall of the thermal conductivity as the pressure is reduced is less sharp when the cell size is reduced due to the Knudsen effect. These predictions show that for the compacted panels micrometric cells are promising candidates for this application in VIP panels. However, reaching smaller particle sizes would be more challenging as the cell size increases.

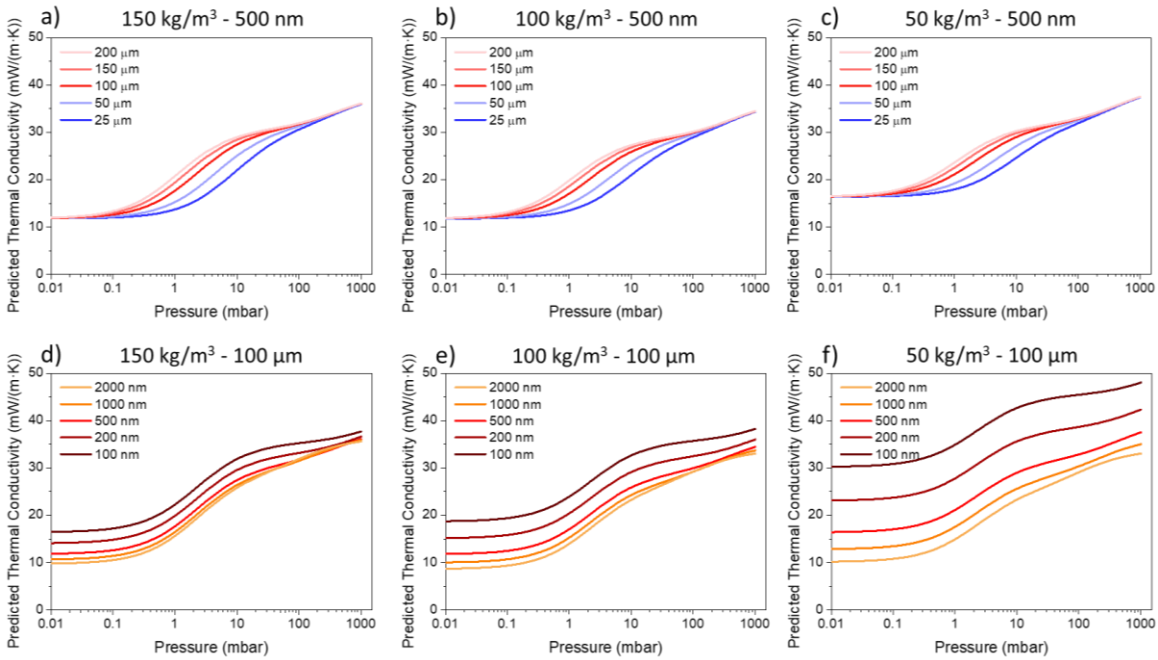

Figure 6. Effect of the particle size on the thermal conductivity at different pressures. Predictions performed at 10 ºC, assuming 500 nm of cell size and an apparent density of 150 kg/m^3 (a), 100 kg/m^3 (b), and 50 kg/m^3 (c). b) Effect of the cell size on the thermal conductivity at different pressures. Predictions performed at 10 ºC, assuming 100 µm of particle size and an apparent density of 150 kg/m^3 (d), 100 kg/m^3 (e), and 50 kg/m^3 (f).

Figure 7 shows the effect of the contributions of each transfer mechanism on the thermal conductivity at different pressures. The predictions were performed at 10 ºC, assuming 500 nm of

cell size, 100 µm of particle size, and an apparent density of 150 kg/m^3 (**Figure 7a** and **6d**), 100 kg/m^3 (**Figure 7b** and **6e**), and 50 kg/m^3 (**Figure 7c** and **6f**). On the one hand, it is observed that since the conduction through the solid phase does not depend on the cell size or the particle size its contribution is constant and becomes more important under vacuum. As density reduces the conduction through the solid phase decreases. On the other hand, radiation depends on the cell size and on the relative density. For a given combination of density and cell size its contribution is also constant and becomes more important under vacuum. As previously commented, as density decreases the amount of matter to absorb/scatter the thermal radiation is reduced, so the radiation rises hugely as observed in **Figure 7a**, **7b**, and **7c**. Therefore, at vacuum for very low density materials, most of the thermal conductivity is due to the radiation contribution (**Figure 7f**). Meanwhile, conduction through the gas phase depends on the density and the cell size. Since the cell size is much smaller than the particle size, the contribution of the conduction through the gas becomes null at higher pressures. Finally, the coupling depends on the density and the particle size. It is noticed that as density increases contribution of the coupling effect rises, being higher than 50% of the total thermal conductivity for pressures higher than 5 mbar for materials with densities higher than 100 kg/m^3 (**Figure 7d** and **7e**).

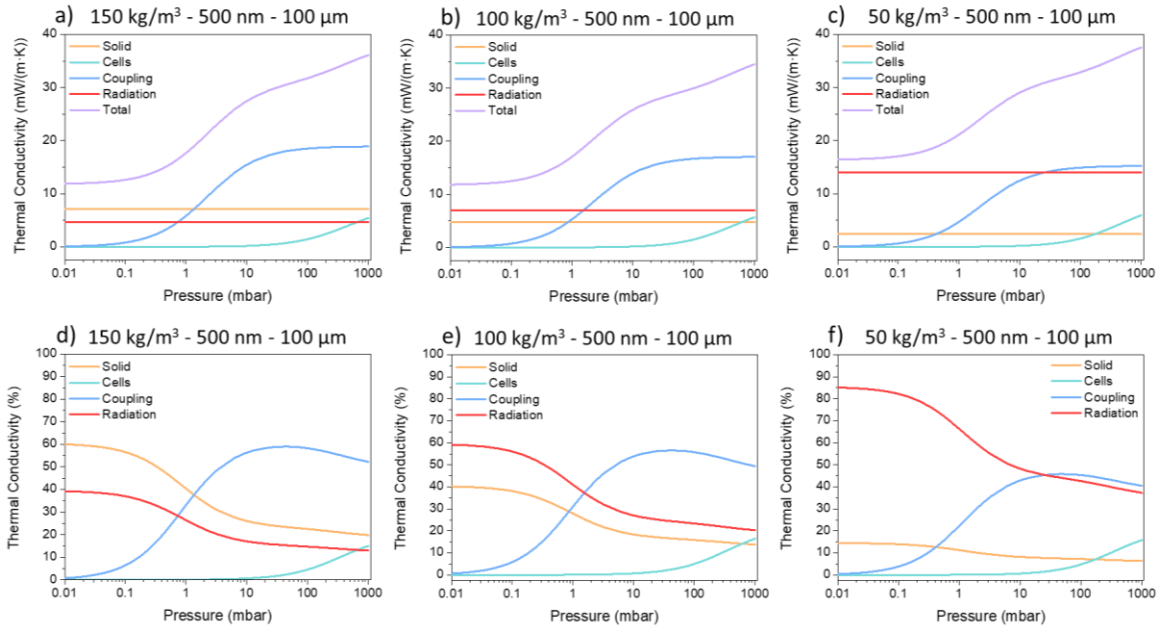

Figure 7. Predicted contribution at 10 ºC of each transfer mechanism to the total thermal conductivity in mW/(m·K) assuming 500 nm of cell size, 100 µm of particle size and density of 150 kg/m^3 (a), 100 kg/m^3 (b), and 50 kg/m^3 (c). Predicted contribution at 10 ºC of each transfer mechanism to the total thermal conductivity in % of the total thermal assuming 500 nm of cell size, 100 µm of particle size and density of 150 kg/m^3 (d), 100 kg/m^3 (e), and 50 kg/m^3 (f).

In **Figure 8** maps of thermal conductivity as a function of the cell size and the relative density are presented, assuming 10 ºC of temperature. **Figure 8a** and **8c** show the thermal conductivity of the

bulk samples at ambient pressure and at vacuum, respectively, whereas **Figure 8b** and **8d** show the thermal conductivity of the compacted panels at ambient pressure and at vacuum, respectively. For the compacted panels, a particle size of 100 µm has been assumed.

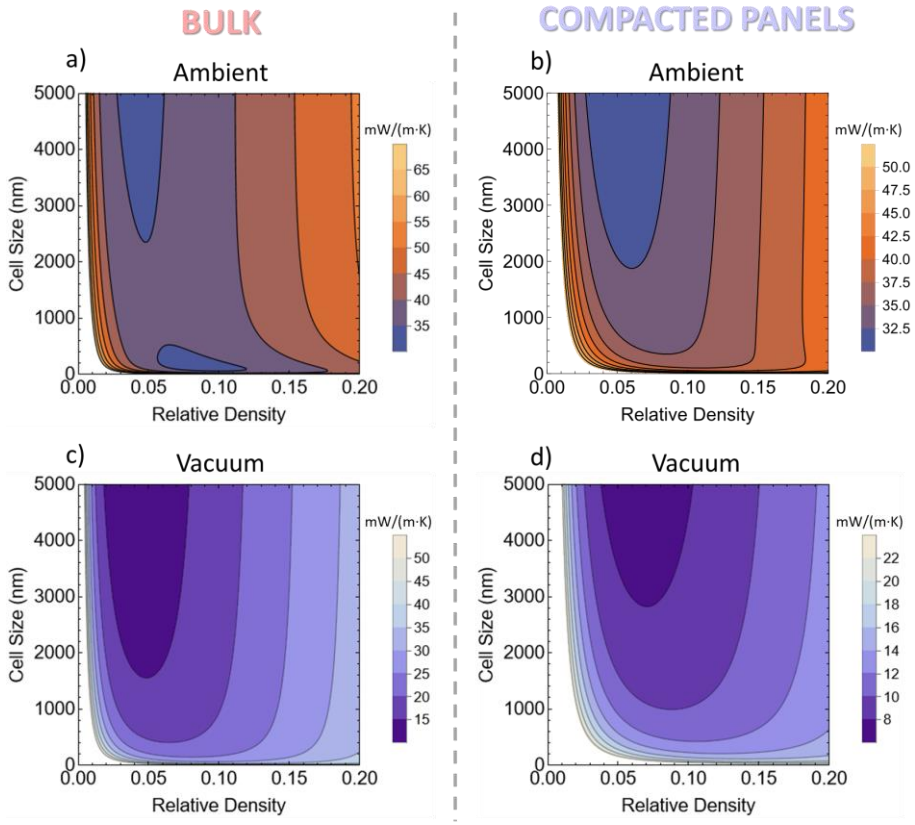

Figure 8. Predictions of thermal conductivity as a function of the cell size and the relative density assuming 10 ºC of temperature based on [29] for the bulk materials and on Equation (9) for the compacted panels: a) bulk at ambient pressure, b) compacted panels at ambient pressure, c) bulk at vacuum, and d) compacted panels at vacuum. For the compacted panels, a particle size of 100 µm was assumed.

Regarding the predictions, the compacted panels present lower thermal conductivity due to their discontinuous cellular structure. At ambient pressure, a minimum (thermal conductivities between 30.0 and 32.5 mW/(m·K)) appear in the region of around 70 kg/m^3 (relative densities of 0.06) and cell sizes higher than 1600 nm for the compacted panels (**Figure 8b**). This minimum is like the one obtained for the bulk material in that region and may be due to the increase in the radiation contribution when the solid volume fraction (which absorbs the radiation) is reduced (**Figure 8a**). However, in the bulk materials, a second region with minimum thermal conductivity was obtained for cell sizes in the nanoscale, whereas this does not appear in the panels. This can be due to the fact that this model assumes a small relevance of the gas inside the cells, so the presence of nanometric cells is not enough to assure a good insulation performance. Meanwhile, at vacuum, the compacted panels (**Figure 8d**) also present lower thermal conductivity than the bulk materials

(**Figure 8c**). For powdered systems based on nanocellular polymers, thermal conductivities higher than 10 mW/(m·K) are predicted, while bulk materials are limited to values over 15 mW/mK. This minimum is again obtained for cell sizes of around 2-3 µm as already discussed in **Figure 6**. Then, microcellular polymers can be suitable for this application as long as the cell size is small enough to assure a good micronization of the material.

In the previous graphs, a solid structure factor of 0.89 has been assumed for the nanocellular polymer (effective solid structure factor of 0.33 for the micronized materials). However, for low-density foams, *g* factors of 0.3-0.6 are usually reported[13,14,43]. To account for the possible configurations of nanocellular polymers that could lead to reduced solid structure factors, **Figure 9** shows a map of the thermal conductivity of compacted panels (100 µm of particle size) as a function of the cell size and the relative density assuming 10 ºC of temperature at ambient pressure (first raw) and at vacuum (second raw) but using different solid structural factors g = 0.7 (**Figure 9a** and **9d**), g = 0.5 (**Figure 9b** and **9e**), and g = 0.3 (**Figure 9c** and **9f**) (effective solid structure factors of 0.26, 0.18, and 0.11, respectively). It is observed that as the solid structure factor decreases, the minimum thermal conductivity that can be reached is reduced. Thus, the reduction of *g* from 0.89 to 0.3 leads to a reduction of 2 mW/(m·K) in compacted panels (from 30 to 28 mW/(m·K)) at ambient pressure. Meanwhile, at vacuum thermal conductivities as low as 4 mW/(m·K) can be obtained (**Figure 9f**).

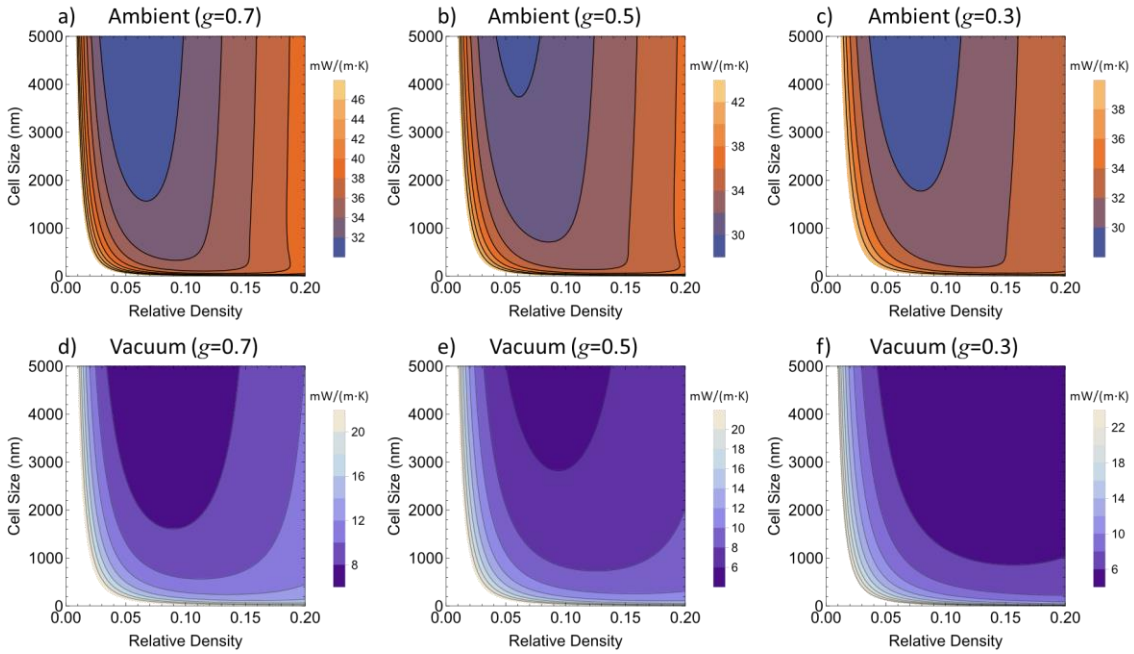

Figure 9. Map of thermal conductivity of compacted panels as a function of the cell size and the relative density assuming 10 °C of temperature and ambient pressure (first row) and under vacuum (second row) using different structure factors: g = 0.7 (a-d), g = 0.5 (b-e), and g = 0.3 (c-f).

Finally, it is important to recall that the present model does not take into account that the contact points between particles may act as radiation scatter points, which may reduce further the radiation,

improving the thermal insulation of these materials. Furthermore, radiation can be reduced by introducing particles that absorb or scatter infrared radiation. Therefore, compacted panels are a new promising eco-friendly, and low-cost alternative materials for the generation of VIP cores.

5. Conclusions

In this work, a model to predict the thermal conductivity of compacted panels based on micronized microcellular and nanocellular PMMA is established. The model is unique in introducing the concept of infinite association of resistances for quantifying the conduction through the powder particles. In addition, a new heat transfer mechanism (the coupling effect) appears due to the discontinuous solid phase and the model is able to quantify this mechanism for the first time in nanocellular polymers. Thus, a semi-empirical model able to predict the thermal conductivity of compacted materials based on microcellular and nanocellular PMMA was developed. The semi-empirical model depends only on the properties of the compacted material (apparent relative density, cell size, and particle size) and the measurement conditions (temperature and pressure). The model presents high accuracy for the compacted panels at ambient pressure, at maximum vacuum, and also at different vacuum pressures. The model also allows analyzing the contribution of each heat transfer mechanism, showing that the contribution of the coupling effect is higher than 50% of the total thermal contribution for pressures higher than 5 mbar. For nanocellular polymers (at 10 ºC), the model predicts minimum thermal conductivities of 32.5 mW/(m·K) at ambient pressure and of 10 mW/(m·K) at maximum vacuum. Furthermore, depending on the solid structure configuration, the model predicts thermal conductivities as low as 4 mW/(m·K) at maximum vacuum. These results make the compacted panels based on micronized microcellular and nanocellular polymers potential candidates to be used as alternative materials for VIP productions.

Supporting Information

Supporting Information is available.

Acknowledgments

Financial assistance from the Junta of Castile and Leon grant (I. Sánchez-Calderón and VA202P20) is gratefully acknowledged. Financial support from the Spanish Ministry of Science, Innovation, and Universities (RTI2018-098749-B-I00, PID2021-127108OB-I00, TED2021-130965B-I00, PDC2022-133391-I00, and PTQ2019-010560 (Victoria Bernardo-García)) is gratefully acknowledged. Financial support from the European Regional Development Fund of the European Union and the of Castile and Leon ((ICE): R&D PROJECTS IN SMEs: PAVIPEX. 04/18/VA/008 and M-ERA.NET PROJECT: FICACEL. 11/20/VA/0001) is gratefully acknowledged. This work was supported by the Regional Government of Castilla y León (Junta de Castilla y León), by the Ministry of Science and Innovation MICIN, and the European Union NextGenerationEU/PRTR.

References

[1] R. Baetens, B.P. Jelle, J.V. Thue, M.J. Tenpierik, S. Grynning, S. Uvsløkk, A. Gustavsen, Vacuum insulation panels for building applications: A review and beyond, Energy Build. 42 (2010) 147–172. https://doi.org/10.1016/j.enbuild.2009.09.005.

[2] M. Casini, Smart Buildings, 2016th ed., Elsevier, 2016. https://doi.org/10.1016/C2015-0-00182-4.

[3] W. Villasmil, L.J. Fischer, J. Worlitschek, A review and evaluation of thermal insulation materials and methods for thermal energy storage systems, Renew. Sustain. Energy Rev. 103 (2019) 71–84. https://doi.org/10.1016/j.rser.2018.12.040.

[4] S. Schiavoni, F. D'Alessandro, F. Bianchi, F. Asdrubali, Insulation materials for the building sector: A review and comparative analysis, Renew. Sustain. Energy Rev. 62 (2016) 988–1011. https://doi.org/10.1016/j.rser.2016.05.045.

[5] M. Casini, Advanced construction materials, in: Constr. 4.0, Elsevier, 2022: pp. 337–404. https://doi.org/10.1016/B978-0-12-821797-9.00005-2.

[6] S.E. Kalnæs, B.P. Jelle, Vacuum insulation panel products: A state-of-the-art review and future research pathways, Appl. Energy. 116 (2014) 355–375. https://doi.org/10.1016/j.apenergy.2013.11.032.

[7] S. Fantucci, A. Lorenzati, A. Capozzoli, M. Perino, Analysis of the temperature dependence of the thermal conductivity in Vacuum Insulation Panels, Energy Build. 183 (2019) 64–74. https://doi.org/10.1016/j.enbuild.2018.10.002.

[8] T. Beikircher, M. Demharter, Heat transport in evacuated perlite powders for super-insulated long-term storages up to 300 °c, J. Heat Transfer. 135 (2013) 1–11. https://doi.org/10.1115/1.4023351.

[9] G. Reichenauer, U. Heinemann, H.P. Ebert, Relationship between pore size and the gas pressure dependence of the gaseous thermal conductivity, Colloids Surfaces A Physicochem. Eng. Asp. 300 (2007) 204–210. https://doi.org/10.1016/j.colsurfa.2007.01.020.

[10] J. Fricke, H. Schwab, U. Heinemann, Vacuum Insulation Panels – Exciting Thermal Properties and Most Challenging Applications, Int. J. Thermophys. 27 (2006) 1123–1139. https://doi.org/10.1007/s10765-006-0106-6.

[11] M. Bouquerel, T. Duforestel, D. Baillis, G. Rusaouen, Heat transfer modeling in vacuum insulation panels containing nanoporous silicas - A review, Energy Build. 54 (2012) 320–336. https://doi.org/10.1016/j.enbuild.2012.07.034.

[12] M. Alvarez-Lainez, M.A. Rodriguez-Perez, J.A. De Saja, Thermal Conductivity of Open-Cell Polyolefin Foams, J. Polym. Sci. Part B Polym. Phys. 46 (2008) 212–221.

[13] P.G. Collishaw, J.R.G. Evans, An assessment of expressions for the apparent thermal conductivity of cellular materials, J. Mater. Sci. 29 (1994) 486–498. https://doi.org/10.1007/BF01162512.

[14] N.C.. Hilyard, A. Cunningham, Low density cellular plastics Physical basis of behaviour, 1994. https://doi.org/10.1007/978-94-011-1256-7.

[15] S. Sonnick, M. Meier, J. Ross-Jones, L. Erlbeck, I. Medina, H. Nirschl, M. Rädle, Correlation of pore size distribution with thermal conductivity of precipitated silica and experimental determination of the coupling effect, Appl. Therm. Eng. 150 (2019) 1037–1045. https://doi.org/10.1016/j.applthermaleng.2019.01.074.

[16] K. Swimm, S. Vidi, G. Reichenauer, H.P. Ebert, Coupling of gaseous and solid thermal conduction in porous solids, J. Non. Cryst. Solids. 456 (2017) 114–124. https://doi.org/10.1016/j.jnoncrysol.2016.11.012.

[17] K. Swimm, G. Reichenauer, S. Vidi, H.P. Ebert, Impact of thermal coupling effects on the effective thermal conductivity of aerogels, J. Sol-Gel Sci. Technol. 84 (2017) 466–474. https://doi.org/10.1007/s10971-017-4437-5.

[18] K. Swimm, G. Reichenauer, S. Vidi, H.-P. Ebert, Gas Pressure Dependence of the Heat Transport in Porous

Solids with Pores Smaller than 10 μm, Int. J. Thermophys. 30 (2009) 1329–1342. https://doi.org/10.1007/s10765-009-0617-z.

[19] J.-J. Zhao, Y.-Y. Duan, X.-D. Wang, B.-X. Wang, Effects of solid–gas coupling and pore and particle microstructures on the effective gaseous thermal conductivity in aerogels, J. Nanoparticle Res. 14 (2012) 1024. https://doi.org/10.1007/s11051-012-1024-0.

[20] C. Bi, G.H. Tang, Z.J. Hu, Heat conduction modeling in 3-D ordered structures for prediction of aerogel thermal conductivity, Int. J. Heat Mass Transf. 73 (2014) 103–109. https://doi.org/10.1016/j.ijheatmasstransfer.2014.01.058.

[21] S. Verma, H. Singh, Predicting the conductive heat transfer through evacuated perlite based vacuum insulation panels, Int. J. Therm. Sci. 171 (2022) 107245. https://doi.org/10.1016/j.ijthermalsci.2021.107245.

[22] J. Liu, P. Buahom, C. Lu, H. Yu, C.B. Park, Microscopic revelation of the solid–gas coupling and Knudsen effect on the thermal conductivity of silica aerogel with inter-connected pores, Sci. Rep. 12 (2022) 21034. https://doi.org/10.1038/s41598-022-24133-5.

[23] I. Sánchez-Calderón, V. Bernardo, F. Lizalde-Arroyo, J. Martín-de-León, M.Á. Rodríguez-Pérez, Development of new vacuum insulation core panels using micronized nanocellular poly(methyl-methacrylate) (PMMA), (n.d.).

[24] H. Yu, H. Zhang, J. Zhao, J. Liu, X. Xia, X. Wu, Thermal conductivity of micro/nano-porous polymers: Prediction models and applications, Front. Phys. 17 (2021). https://doi.org/10.1007/s11467-021-1107-4.

[25] C. Forest, P. Chaumont, P. Cassagnau, B. Swoboda, P. Sonntag, Polymer nano-foams for insulating applications prepared from CO2 foaming, Prog. Polym. Sci. 41 (2015) 122–145. https://doi.org/10.1016/j.progpolymsci.2014.07.001.

[26] G. Wang, C. Wang, J. Zhao, G. Wang, C.B. Park, G. Zhao, Modelling of thermal transport through a nanocellular polymer foam: Toward the generation of a new superinsulating material, Nanoscale. 9 (2017) 5996–6009. https://doi.org/10.1039/c7nr00327g.

[27] V. Bernardo, J. Martin-de Leon, J. Pinto, U. Schade, M.A. Rodriguez-Perez, On the interaction of infrared radiation and nanocellular polymers: First experimental determination of the extinction coefficient, Colloids Surfaces A Physicochem. Eng. Asp. 600 (2020). https://doi.org/10.1016/j.colsurfa.2020.124937.

[28] P. Buahom, C. Wang, M. Alshrah, G. Wang, P. Gong, M. Tran, C.B. Park, Wrong expectation of superinsulation behavior from largely-expanded nanocellular foams, Nanoscale. (2020). https://doi.org/10.1039/d0nr01927e.

[29] I. Sánchez-Calderón, V. Bernardo, J. Martín-de-León, M.Á. Rodríguez-Pérez, Thermal conductivity of low-density micro-and nanocellular poly(methyl-methacrylate) (PMMA): Experimental and modeling, Mater. Des. 221 (2022) 110938. https://doi.org/10.1016/j.matdes.2022.110938.

[30] V. Bernardo, J. Martin-de Leon, J. Pinto, R. Verdejo, M.A. Rodriguez-Perez, Modeling the heat transfer by conduction of nanocellular polymers with bimodal cellular structures, Polymer (Guildf). 160 (2019) 126–137. https://doi.org/10.1016/j.polymer.2018.11.047.

[31] S.S. Sundarram, W. Li, On thermal conductivity of micro- and nanocellular polymer foams, Polym. Eng. Sci. 53 (2013) 1901–1909. https://doi.org/10.1002/pen.23452.

[32] I. Sánchez-Calderón, V. Bernardo, D. Cuadra-Rodríguez, J. Martín-de-León, M.Á. Rodríguez-Pérez, Micronization as a solution for enhancing the thermal insulation of nanocellular poly(methyl-methacrylate) (PMMA), Polymer (Guildf). 261 (2022) 125397. https://doi.org/10.1016/j.polymer.2022.125397.

[33] UNE-EN 1602:2013 Thermal insulating products for building applications. Determination of the apparent density., (n.d.).

[34] J. Pinto, E. Solórzano, M.A. Rodriguez-Perez, J.A. de Saja, Characterization of the cellular structure based on user-interactive image analysis procedures, J. Cell. Plast. 49 (2013) 555–575. https://doi.org/10.1177/0021955X13503847.

[35] http://www.cellmattechnologies.com/en/software-and-methodology-for-the-characterization- of-cellular-structures/, (n.d.).

[36] ISO 4590:2016 Rigid cellular plastics — Determination of the volume percentage of open cells and of closed cells, (2016).

[37] ASTM C518 Standard Test Method for Steady-State Thermal Transmission Properties by Means of the Heat Flow Meter Apparatus, (2017).

[38] ISO 8301 Thermal insulation - Determination of steady-state thermal resistance and related properties - Heat flow meter, (1991).

[39] https://www.beforethebang.org/post/the-infinite-resistance-problem, (n.d.).

[40] Z.-Y. Li, C.-Y. Zhu, X.-P. Zhao, A theoretical and numerical study on the gas-contributed thermal conductivity in aerogel, Int. J. Heat Mass Transf. 108 (2017) 1982–1990. https://doi.org/10.1016/j.ijheatmasstransfer.2017.01.051.

[41] Y.A. Cengel, A.J. Ghajar, Heat and Mass Transfer: Fundamentals & Applications Appendix 1, Fifth Edit, Mc Graw Hill Education, 2006.

[42] U. Heinemann, J. Hetfleisch, R. Caps, J. Kuhn, J. Fricke, Evacuable Guarded Hot Plate for Thermal Conductivity Measurements between-200°C and 800°C, in: Adv. Therm. Insul. Proc. Eurotherm Semin. No.44At Rio Tinto - Port., 1995.

[43] J.A. Reglero Ruiz, C. Saiz-Arroyo, M. Dumon, M.A. Rodríguez-Perez, L. Gonzalez, Production, cellular structure and thermal conductivity of microcellular (methyl methacrylate)-(butyl acrylate)-(methyl methacrylate) triblock copolymers, Polym. Int. 60 (2011) 146–152. https://doi.org/10.1002/pi.2931.

SUPPORTING INFORMATION

Coupling effect in compacted panels based on micronized nanocellular polymers: modeling of the thermal conductivity

Ismael Sánchez-Calderón[1], Victoria Bernardo[2], Félix Lizalde-Arroyo[1], Judith Martín-de-León[1], Miguel Ángel Rodríguez-Pérez[1,3].

[1]*CellMat Laboratory. Campus Miguel Delibes. Faculty of Science. Condensed Matter Physics Department. University of Valladolid, Paseo de Belén 7, 47011, Valladolid, Spain.*

[2]*CellMat Technologies S.L., Paseo de Belén 9-A, 47011, Valladolid, Spain.*

[3]*BioEcoUVA Research Institute on Bioeconomy, University of Valladolid, 47011, Valladolid, Spain.*

Corresponding author: Ismael Sánchez-Calderón (ismaelsc@fmc.uva.es)

S1. Constants and values for calculations

Table S1 shows the constants and values used in the calculations of thermal conductivity.

Table S1. Constants and values used in the calculations of the thermal conductivity.

	Parameter	Value	Units
Model Variables	$\rho_{r,app}$	Variable for each material	-
	ϕ	Variable for each material	m
	D	Variable for each material	m
	T	283.15 → 313.15	K
	p	0.01 → 101325	Pa
Model Parameters	λ'_{s_PMMA}	$0.2060T + 115.5811$	mW/(m·K)
	g	0.89	-
	λ'_{g0_air}	$0.0741T + 3.4029$	mW/(m·K)
	d_m	$3.6 \cdot 10^{10}$	m
	β	1.64	-
	n	1	-
	K_e	$(5.6712 \cdot 10^6\ \phi^{0.4264})\ \rho_{r,app}$	m^{-1}
	A	$-0.0045T + 3.0725$	-
	B	$0.0006T + 0.7133$	-
Universal Constants	R	8.31446	$(Pa \cdot m^3)/(mol \cdot K)$
	N_A	$6.022 \cdot 10^{23}$	molecules/mol
	σ	$5.67 \cdot 10^{-8}$	$W/(m^2 \cdot K^4)$

S2. Determination of the *f* factor

Table S2 summarizes the obtained parameters and correlation coefficient (r^2) in the first and second fitting (**Figure 8a** and **8b** in the manuscript respectively) for the calculus of the *f* factor. *A* is the slope and *B* is the y-intercept in the first fitting for each temperature (*f* factor as a function of the apparent relative density). Whereas *A'* is the slope and *B'* is the y-intercept in the second fitting (calculated parameters (slopes and y-intercepts) in the first fitting as a function of the temperature). It is observed that the correlation coefficient obtained on both adjustments is high (over 0.9).

Table S2. Obtained parameters and correlation coefficient (r^2) in the first and second fitting (**Figure 8a** and **8b** in the manuscript respectively) for the calculus of the *f* factor.

	FIRST FITTING		
T (K)	*A*	*B*	r^2
283.15	1.797545	0.549126	0.952901
293.15	1.733235	0.544920	0.937960
303.15	1.699849	0.539262	0.924714
313.15	1.657692	0.531779	0.907308

	SECOND FITTING		
Parameter	*A'*	*B'*	r^2
A(T)	-0.004529	3.072536	0.990322
B(T)	-0.000577	0.713306	0.992014

S3. Comparison between the experimental and predicted thermal conductivities of the micronized samples at ambient pressure

Figure S1 shows the experimental thermal conductivity of the compacted samples at 10 °C and different pressures and the prediction of the thermal conductivity as a function of pressure. It is observed that the predicted thermal conductivity curve fits very well with the experimental data.

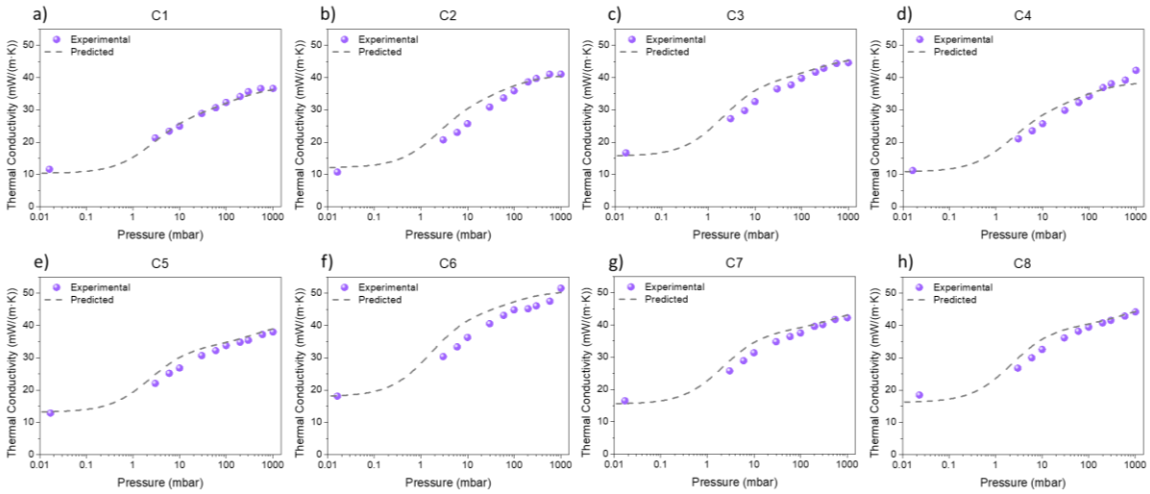

Figure S1. Experimental thermal conductivity of the compacted samples at 10 °C and different pressures and prediction of the thermal conductivity as a function of pressure: a) C1, b) C2, c) C3, d) C4, e) C5, f) C6, g) C7, and h) C8.

References

[1] ISO 60:1997 Plastics — Determination of apparent density of material that can be poured from a specified funnel, (1997).

[2] X. Chateau, Particle packing and the rheology of concrete, in: Underst. Rheol. Concr., Elsevier, 2012: pp. 117–143. https://doi.org/10.1533/9780857095282.2.117.

[3] A. Averardi, C. Cola, S.E. Zeltmann, N. Gupta, Effect of particle size distribution on the packing of powder beds: A critical discussion relevant to additive manufacturing, Mater. Today Commun. 24 (2020) 100964. https://doi.org/10.1016/j.mtcomm.2020.100964.

[4] I. Sánchez-Calderón, V. Bernardo, D. Cuadra-Rodríguez, J. Martín-de-León, M.Á. Rodríguez-Pérez, Micronization as a solution for enhancing the thermal insulation of nanocellular poly(methyl-methacrylate) (PMMA), Polymer (Guildf). 261 (2022) 125397. https://doi.org/10.1016/j.polymer.2022.125397.

[5] J. Fricke, Thermal Transport in Porous Superinsulations, (1986) 94–103. https://doi.org/10.1007/978-3-642-93313-4_11.

[6] B. Notario, J. Pinto, E. Solorzano, J.A. de Saja, M. Dumon, M.A. Rodríguez-Pérez, Experimental validation of the Knudsen effect in nanocellular polymeric foams, Polymer (Guildf). 56 (2015) 57–67. https://doi.org/10.1016/j.polymer.2014.10.006.

[7] Z.-Y. Li, C.-Y. Zhu, X.-P. Zhao, A theoretical and numerical study on the gas-contributed thermal conductivity in aerogel, Int. J. Heat Mass Transf. 108 (2017) 1982–1990. https://doi.org/10.1016/j.ijheatmasstransfer.2017.01.051.

[8] J. Nassios, Kinetic theory of rarefied gas flows with modern applications, Austms.Org.Au. (2006). https://www.austms.org.au/Publ/Gazette/2013/Mar13/Nassios.pdf.

[9] S. Song, M.M. Yovanovich, F.O. Goodman, Thermal gap conductance of conforming surfaces in contact, J. Heat Transfer. 115 (1993) 533–540. https://doi.org/10.1115/1.2910719.

[10] V. Bernardo, J. Martin-de Leon, J. Pinto, R. Verdejo, M.A. Rodriguez-Perez, Modeling the heat transfer by conduction of nanocellular polymers with bimodal cellular structures, Polymer (Guildf). 160 (2019) 126–137. https://doi.org/10.1016/j.polymer.2018.11.047.

[11] Y.L. He, T. Xie, Advances of thermal conductivity models of nanoscale silica aerogel insulation material, Appl. Therm. Eng. 81 (2015) 28–50. https://doi.org/10.1016/j.applthermaleng.2015.02.013.

[12] S. Sonnick, L. Erlbeck, M. Meier, H. Nirschl, M. Rädle, Methodical selection of thermal conductivity models for porous silica-based media with variation of gas type and pressure, Int. J. Heat Mass Transf. 187 (2022). https://doi.org/10.1016/j.ijheatmasstransfer.2022.122519.

[13] S.E. Kentish, C.A. Scholes, G.W. Stevens, Carbon Dioxide Separation through Polymeric Membrane Systems for Flue Gas Applications, Recent Patents Chem. Eng. 1 (2008) 52–66. https://doi.org/10.2174/1874478810801010052.

4.6. Improvement of the thermal conductivity of micronized nanocellular poly(methyl-methacrylate) (PMMA) by adding infrared blockers

Ismael Sánchez-Calderón[1], Victoria Bernardo[2], Félix Lizalde-Arroyo[1], Judith Martín-de-León[1], Miguel Ángel Rodríguez-Pérez[1,3].

[1]*CellMat Laboratory. Campus Miguel Delibes. Faculty of Science. Condensed Matter Physics Department. University of Valladolid, Paseo de Belén 7, 47011, Valladolid, Spain.*

[2]*CellMat Technologies S.L., Paseo de Belén 9-A, 47011, Valladolid, Spain.*

[3]*BioEcoUVA Research Institute on Bioeconomy, University of Valladolid, 47011, Valladolid, Spain.*

Corresponding author: Ismael Sánchez-Calderón (ismaelsc@fmc.uva.es)

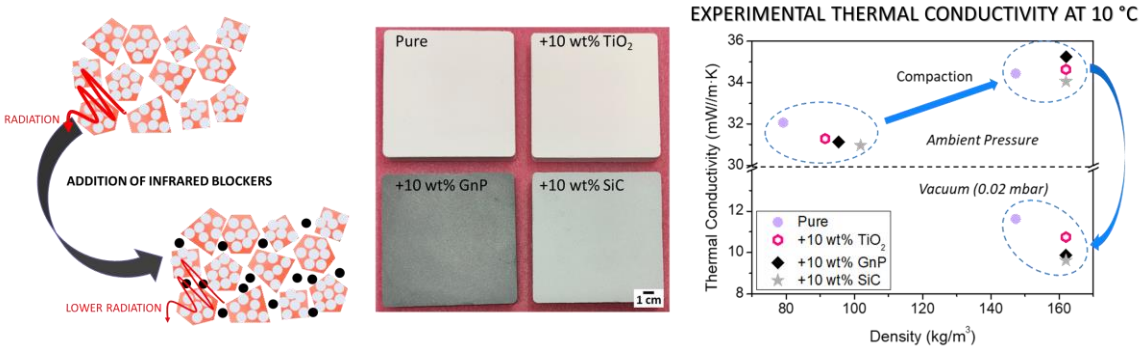

ABSTRACT

Micronized nanocellular polymers show great potential to be used as core materials for vacuum insulation panels due to their reduced thermal conductivity under vacuum. However, as a result of their nanocellular structure, these materials are characterized by thermal radiation contributions higher than 4 mW/(m·K). In this work, a way to further enhance their thermal insulation behavior is studied through the addition of infrared blockers to reduce the thermal radiation contribution. Three different opacifiers (titanium(IV) oxide, graphene nanoplatelets, and silicon carbide) are used in different contents (2.5, 5, 10, 15, and 20 wt%). The obtained powders are characterized to determine the apparent density, the particle size distribution, and the thermal conductivity. The addition of infrared blockers leads to an increase in the apparent density which is also related to the opacifier's particle size. For each infrared blocker, there is an optimum concentration to achieve the minimum thermal conductivity. Finally, compacted panels are produced to analyze their behavior as VIP cores by measuring the thermal conductivity under vacuum conditions. A minimum thermal conductivity of 9.6 mW/(m·K) is obtained for the compacted panel containing 10 wt% of silicon carbide, a reduction of 2 mW/(m·K) regarding the sample without opacifier.

Keywords: thermal conductivity, poly(methyl-methacrylate), micronized nanocellular polymer, infrared blockers.

1. Introduction

Nowadays, Recently, micronization of nanocellular polymers has been shown as a method to enhance the thermal insulation of nanocellular polymers[1]. Due to their discontinuous structure, these materials present lower thermal conductivity than their bulk counterparts, especially under vacuum. Thus, micronized nanocellular polymers are expected to have thermal conductivities as low as 10 mW/(m·K) at vacuum, showing a great potential to be used as a low-cost and eco-friendly core material for vacuum insulation panels (VIPs)[2]. The core is the inner part of a VIP, which is fabricated from an open porous material and whose function is to physically support the VIP envelope and provide superinsulation performance. The materials usually selected as core materials are based on silica (fumed/precipitated silica or silica aerogel with densities around 200 kg/m^3) because, due to their nanostructure, they require a lower vacuum to fully evacuate[3,4]. Nevertheless, the main drawback of nanoscale silica materials is their high price[5,6].

VIPs are characterized by ultimate thermal conductivities between 4-8 mW/(m·K)[7–10]. This conductivity is the sum of two main contributions, once the gas phase is evacuated: the conduction through the solid phase and the radiation contribution. Radiation in silica-based core materials is usually high (it can be higher than 4 mW/(m·K) at 300 K[11]) due to their nanostructure. When the pore size reduces to the nanoscale, radiation is not scattered in the structure[12]. Then, to boost the performance of the VIP core, opacifiers or infrared blockers (IR-blockers) are also usually added[3,11,13–16]. An opacifier is a material that strongly absorbs or scatters infrared radiation, increasing the extinction coefficient and thus reducing heat transfer by radiation. Graphite, titanium(IV) oxide (TiO_2), and silicon carbide (SiC) are usually used[11,13–17]. Such materials attenuate radiation via different mechanisms; for instance, carbon-based opacifiers reduce radiation mainly by absorption, whereas TiO_2 or SiC particles both scatter and absorb radiation[13]. The addition of opacifiers, physically dispersed in the silica-based material as powder mixtures, can reduce the thermal conductivity of fumed silica core by 1-3 mW/(m·K) [13,14,16]. The amount of IR-blocker should be high enough to reduce radiation, but an excess can lead to higher conduction through the solid phase since opacifiers present a high thermal conductivity. Hence, there is an optimum opacifier mass proportion to achieve a minimum thermal conductivity in VIP cores. For instance, Singh et al.[15] studied the radiation of fumed silica VIPs containing different contents (from 10 wt% to 40 wt%) of several opacifiers (carbon black, TiO_2, and SiC), observing a linear reduction of the thermal radiation with an increase in the proportion of opacifier. Carbon black showed the best performance, while TiO_2 showed the worst. Meanwhile, Davraz et al.[17] studied the optimum SiC content in fumed silica VIPs. Results showed that 15 wt% of SiC was the optimum. Also, there is an optimum opacifier size to maximize the IR extinction which also depends on the temperature[18–20]. This was also observed by Wang et al.[19]: they reported that the optimum opacifier particle size for SiC changes from 6 to 4 μm when temperature increases

from 300 to 800 K, while for carbon black the optimum particle size varies from 4 to 2 μm in the same temperature range [19].

This strategy can also be applied to reduce the radiation contribution of micronized nanocellular polymers, which can be higher than 4 mW/(m·K)[1,21]. One possibility could be adding the IR-Blockers to the polymer matrix as an additive before the foaming process, as it is done for conventional cellular polymers[11,22]. Some examples of IR-blockers used in the literature for cellular polymers are carbon-based materials (multi-walled nanotubes, carbon black nanoparticles, graphite), TiO_2, or aluminum oxide (Al_2O_3)[11,23–26]. The previously mentioned works are mainly related to the production of microcellular or conventional polymer foams since the incorporation of these additives in nanocellular polymers is not so straightforward. Firstly, the IR-Blockers need to be in the nanometric range if they are incorporated into the solid formulation to prevent the appearance of large cells. It is a challenge to achieve a good dispersion of the nanometric particles without agglomeration, especially at high loads, which could also affect the foaming process[27]. The second option for micronized nanocellular polymers is dispersing the IR-blockers in the form of powder particles, as is done for fumed silica. This second strategy allows high loads without compromising the structure and foaming process of the nanocellular polymer.

In the present work, this concept is proved by preparing powder mixtures of micronized nanocellular PMMA and infrared blockers. The materials are studied to be used as core materials for VIPs. Three different types of opacifiers are used in several contents. The obtained powders are characterized to determine the apparent density, the particle size distribution, and the thermal conductivity. Finally, compacted panels are produced and their thermal conductivity is measured at ambient pressure and under different vacuum pressures.

2. Experimental

2.1. Materials and sample preparation

A low-density nanocellular material based on PMMA was produced by gas dissolution foaming. The PMMA grade used was PLEXIGLAS® 7H supplied by Röhm GmbH. This PMMA presents a density of 1190 kg/m^3, a melt flow index of 0.77 g/10 min (measured at 230 ºC and 2.16 kg), and a glass transition temperature of 110.4 ºC measured by DSC (model DSC3+, Mettler). Details of the gas dissolution foaming equipment used and the two-step foaming process can be found elsewhere[28]. To produce the nanocellular material, the saturation conditions were 31 MPa and 40 ºC, while the foaming parameters were 90 ºC and 5 min.

The main features of the bulk nanocellular material produced with the aforementioned conditions were: 100 kg/m^3 of density (ρ), 800 nm of cell size in three dimensions (ϕ_{3D}), and 0.5 of normalized standard deviation of the cell size distribution (SD/ϕ_{3D}). Then, the material was micronized using a rotor beater mill SR 300 (Retsch). After the milling process, the resultant material was a

homogeneous powder characterized by an apparent density of 80 kg/m^3, micrometric particles with a mean particle size of 146 µm (obtained by laser diffraction), 100% of open cell content (*OC*), and a similar cell size to the bulk nanocellular material. Details of the procedure to produce and characterize the micronized nanocellular material can be found in our previous works[1].

To study the effect of the addition of IR-Blockers, three different types of opacifiers were added and physically mixed with the low-density nanocellular powder in different contents (2.5, 5, 10, 15, and 20 wt%). The IR-Blockers used in this work were: titanium dioxide (TiO_2) supplied by Riedel-de Haën (product code: 14027), graphite nanoplatelets (GnP) PLAT7 provided by Avanzare, and silicon carbide (SiC) F1000 supplied by Navarro SiC. **Figure 1** shows the appearance of the powders and their particles visualized with scanning electron microscopy (SEM). TiO_2 is a white powder of spherical particles, GnP is a black powder of lamellar particles, and SiC is a gray powder of polyhedral particles. **Table 1** summarizes the particle size of the opacifiers (obtained from the technical datasheets).

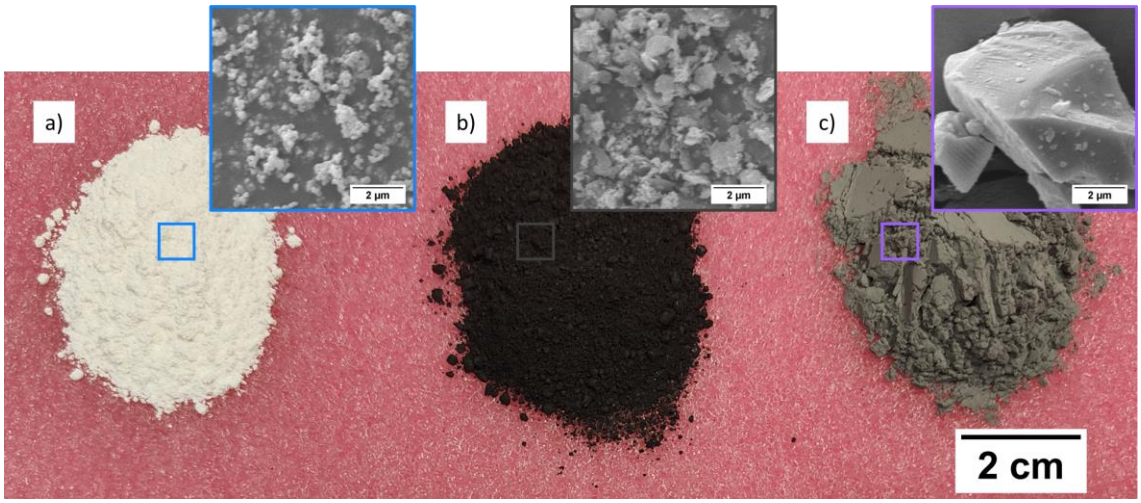

Figure 1. Photograph and SEM micrographs of the opacifiers used in this work: a) TiO_2, b) GnP, and c) SiC.

Table 1. Particle size of the opacifiers used in this work (from the technical datasheets).

IR-Blocker	Particle Size
TiO_2	100-150 nm of diameter
GnP	7 µm of lateral size 2-3 nm of thickness
SiC	5 µm of diameter

Finally, the pure sample and the samples containing 10 wt% of each IR-Blocker were compacted to prepare panels using a hot plate hydraulic press with accurate control provided by Talleres Remtex (Barcelona, Spain). First, the micronized samples were dried at 60 °C for 30 min in a forced-air high-temperature oven (model 2001405, JP Selecta). Second, the necessary amount of

sample was weighed and placed inside a mold with final dimensions of 120×120×15 mm^3. The target apparent density of the compacted samples is 147 kg/m^3 for the pure sample and 162 kg/m^3 for the samples containing an additional amount of 10 wt% IR-Blocker. The density was selected to obtain self-standing panels and to properly analyze the effect of the addition of opacifiers to the pure sample, keeping the same amount of pure nanocellular polymer in all the samples. Afterward, the mold is placed on the press under 20 tons at 80 ºC for 30 min. Finally, the sample is removed from the mold obtaining a compacted panel.

2.2. Characterization

2.2.1. Density

The apparent density (ρ_{app_M}) of the powder mixtures was obtained according to ISO 60[29]. Meanwhile, the apparent density of the compacted panels (ρ_{app_C}) was obtained according to UNE-EN 1602[30] by measuring the geometric volume (V) and the mass (m) of the compacted piece ($\rho_{app\_C} = m / V$).

2.2.2. Surface morphology (SEM)

A Scanning Electron Microscope (FlexSEM 1000 VP-SEM) was used to visualize the IR-blockers and the surface of the micrometric nanocellular particles with and without opacifiers. To allow visualization, the samples were coated with gold using a sputter coater (model SCD 005, Balzers Union).

2.2.3. Volume particle size distribution (laser diffraction)

Laser diffraction measurements were performed to study the particle size distribution of the micronized nanocellular polymer and the mixtures containing 10 wt% content of opacifier. Experiments were carried out at CENIEH (Burgos, Spain) using a LS13 320 Particle Size Analyzer (Beckman Coulter). The powder particles are dispersed for one minute in ethanol with ultrasounds. Then, they are analyzed in the ULM module. This technique assumes spherical particles and provides the particle size distribution in percentage of volume (%volume), from which it is possible to calculate the average particle size. Note that in volume distributions, the larger particles have a higher weight than the smaller ones. The mean volume particle size, also known as De Brouckere's mean diameter, is provided by the analysis software[31,32].

2.2.4. Thermal conductivity measurements (Heat Flow Meter)

Thermal conductivity measurements were performed using a thermal heat flow meter model FOX 200 (TA Instruments / LaserComp, Inc.), which measures according to ASTM C518 and ISO 8301[33,34]. The absolute thermal conductivity accuracy for this device is 2%. Both micronized materials and compacted panels were characterized with this technique. For the measurements, samples have larger dimensions than the FOX 200 heat flux transducers (120×120 mm^2 vs 75×75 mm^2). Measurements were performed in steady-state conditions at ambient pressure and under

vacuum using the same procedure as in our previous works[1]. The ambient pressure measurements were performed at different mean temperatures 10, 20, 30, and 40 ºC. Meanwhile, measurements at vacuum were performed at 10 ºC.

3. Results and discussion

3.1. Effect of the addition of IR-Blockers on the apparent density and the surface of the micrometric particles

The powder mixtures obtained are homogeneous, with the opacifiers well-dispersed through the micronized nanocellular PMMA. **Figure 2** shows the density of the powder blends (**Figure 2a**) and the surface of the micrometric nanocellular PMMA particles with 10 wt% of each IR-blocker (**Figure 2b**). It is observed that as the IR-Blocker content increases, the apparent density of the resultant powder mixture increases because the opacifier is characterized by a much higher density (**Figure 2a**). TiO_2 and GnP show a similar trend, with the density of the GnP blends being slightly higher. However, the apparent density of the SiC mixtures is much higher. The SiC blends show quite different behavior, with a significant density increase even for low contents of SiC. For instance, for an IR-Blocker content of 10 wt%, the apparent density goes from 91 kg/m^3 (TiO_2) to 102 kg/m^3 (SiC). In comparison to the pure polymer, this represents an increase of 15% and 29%, respectively. The different behaviors can be related to the opacifier's particle size (**Table 1**) and how it is distributed on the surface of the nanocellular PMMA micrometric particles (**Figure 2b**). As observed in **Figure 2b**, TiO_2 and GnP particles are distributed inside the exposed superficial cells (diameter of the cells 800 nm) due to their reduced size, while SiC particles (size 5 μm) are too large to enter the nanometric structure. This change in the packaging of the powders influences density, leading to higher densities when the particles are much larger than the pore size.

Laser diffraction measurements were conducted to study the size of the particles in the blends. Due to the measurement procedure (dispersion of the powder in EtOH), the opacifier particles leave the nanocellular PMMA surface being dispersed together with the micronized nanocellular PMMA particles in the solvent. **Figure 4** shows the particle size distribution of the reference sample (pure), and the powder blends containing 10 wt% of each opacifier. All the samples present a similar mean particle size (*D*) to the original size of the PMMA micrometric particles (146 μm) (**Table 2**). However, the normalized standard deviation of the particle size (*SD/D*) of the samples containing opacifiers is slightly higher since the blend contains also smaller particles. In the pure polymer, there is a small fraction of particles with sizes below 10 μm (**Figure 4b**). GnP increases the fraction of these small particles. Then, the presence of TiO_2 particles generates an extra peak at around 400 nm, corresponding to TiO_2 particles and particle aggregates. Meanwhile, SiC particles generate a shoulder around 5 μm, which is the size of these particles.

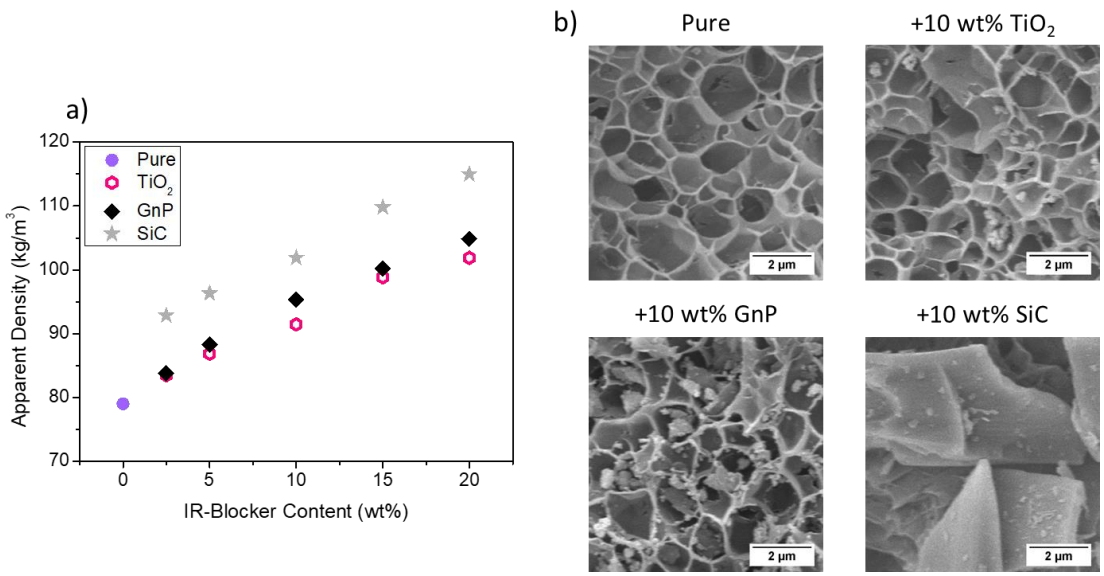

Figure 2. a) Apparent density of the samples as a function of the type and content of IR-Blocker and b) SEM micrographs of the reference sample (pure) and the samples with 10 wt% of each IR-Blocker.

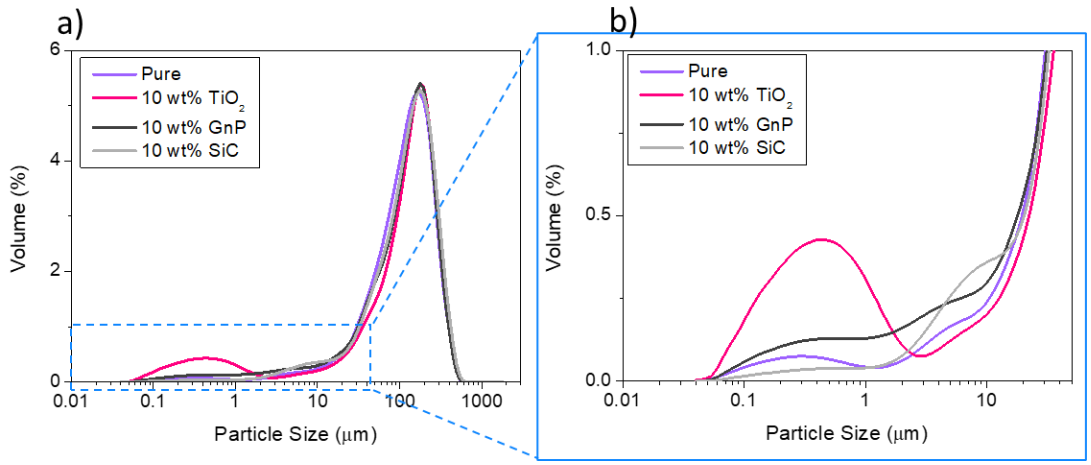

Figure 3. Dynamic laser diffraction %volume particle size distributions of the reference sample (pure) and the samples containing 10 wt% of each IR-blocker: a) full distribution and b) zoom in the region < 50 µm.

Table 2. Mean particle size (*D*) and normalized standard deviation of the particle size distribution (*SD/D*) results of the reference sample (pure) and the samples containing 10 wt% of IR-blocker obtained by laser diffraction.

IR-Blocker	*D* (µm)	*SD/D* (µm)
Pure	146	0.68
+10 wt% TiO_2	143	0.75
+10 wt% GnP	144	0.71
+10 wt% SiC	153	0.70

3.2. Effect of the addition of IR-Blockers on the thermal conductivity

3.2.1. Powder mixtures

Figure 4a, 5b, and **5c** show the thermal conductivity as a function of the IR-Blocker content at different temperatures (10, 20, 30, and 40 ºC) for TiO_2, GnP, and SiC, respectively. The reference sample (pure) is found at the point of 0 wt% of IR-blocker in every graph. In general, as the amount of opacifier in the mixture increases the thermal conductivity is reduced until reaching a minimum, then the thermal conductivity raises again. When adding IR-Blockers there is a compromise between radiation reduction and conduction through the solid phase rise. As the amount of opacifiers increases, the highly conductive particles are more in touch with one another, increasing the heat transfer by conduction through the solid opacifier particles. This explains the presence of the minimum observed in the different systems: for low IR-blocker contents, radiation is reduced, but at high concentrations, there is higher conduction through the solid phase. On the other hand, as the temperature increases, the thermal conductivity increases. The minimum thermal conductivies obtained are 30.8 mW/(m·K) for 15 wt% TiO_2 (99 kg/m^3), 30.8 mW/(m·K) for 5 wt% GnP (88 kg/m^3), and 31.0 mW/(m·K) for 10 wt% SiC (102 kg/m^3). Thus, the IR-blockers used in this work lead to reductions of thermal conductivity of around 1.2 mW/(m·K) regarding the reference sample (pure) at ambient pressure. However, the optimum amount of opacifier varies, meaning different infrared radiation-blocking behaviors. The IR-blocker leading to the minimum thermal conductivity at lower content (GnP in this case) is the one with the highest infrared radiation blocking behavior.

The gap between the thermal conductivity measurements performed at 10 ºC and 40 ºC ($\Delta\lambda$) is shown in **Figure 4d**. The difference between measurements at two temperatures is directly related to the radiation contribution. The radiation term depends on the temperature cube[35,36], so slight variations in the temperature affect significantly this contribution. The reduction of $\Delta\lambda$ when the opacifier content increases mean that indeed the IR-blockers are decreasing the radiation contribution. It is observed that the gap is lower when using GnP followed closely by SiC and finally TiO_2. From these measurements, we can distinguish between the effects on the radiation and conduction through the solid phase terms. For TiO_2, $\Delta\lambda$ reduces continuously for all the concentrations tested up to 20 wt%, so there is a radiation reduction in all the range. However, the optimum TiO_2 content was 15 wt% and the conductivity was measured to increase later on. Then, for 20 wt% of TiO_2, there is an increase in the solid conduction that compensates the reduction in the radiation contribution. Meanwhile, for GnP, $\Delta\lambda$ reduces until 10 wt% and then remains constant. The optimum GnP content was 5 wt% meaning that for higher contents there is an increase in the solid conduction that compensates the reduction in the radiation contribution. Also, it is observed that $\Delta\lambda$ at 5 wt% for GnP is lower than in the other systems at the different concentrations, meaning that, as previously commented, GnP has higher infrared radiation-blocking behavior than SiC and

TiO_2. Finally, for SiC, $\Delta\lambda$ reduces until 15 wt% and then maintains constant. Since the optimum SiC content was 10 wt%, for higher contents there is an increase in the solid conduction that compensates the reduction in the radiation contribution.

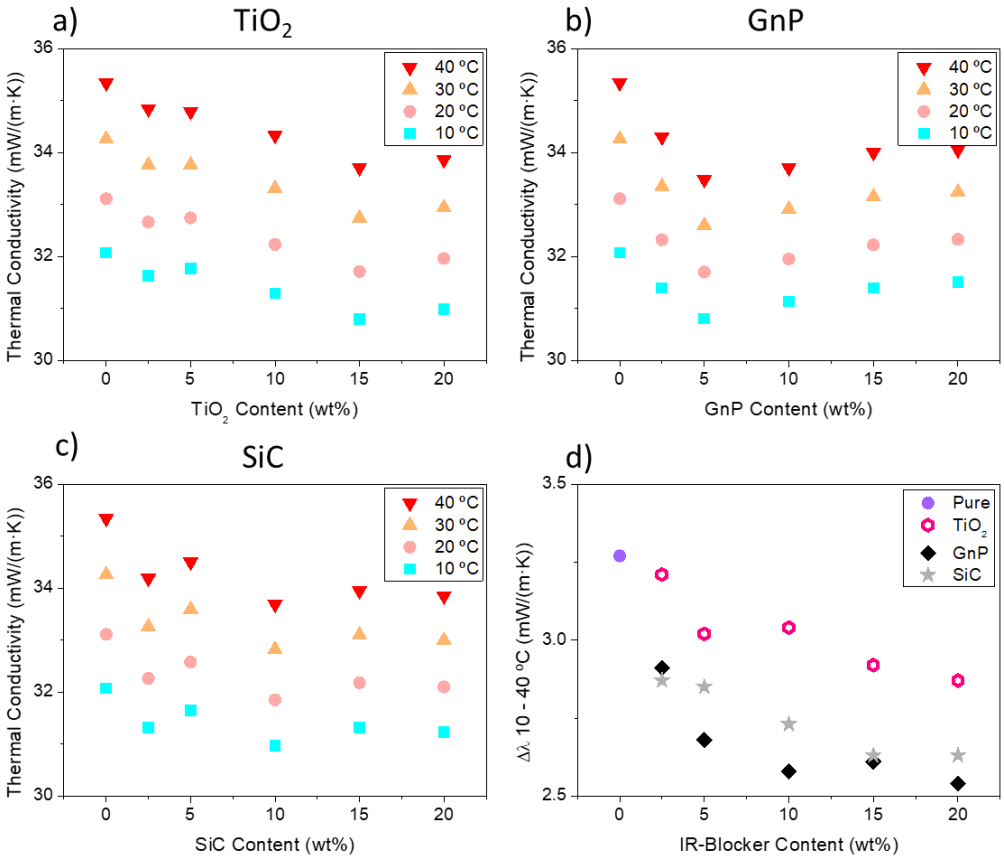

Figure 4. Thermal conductivity as a function of the IR-Blocker content at different temperatures for TiO_2 (a), GnP (b), and SiC (c). d) Thermal conductivity gap between the measurements performed at 10 ºC and at 40 ºC as a function of the type and content of each IR-Blocker.

These results prove that adding IR-blockers can help to reduce the conductivity of the micronized nanocellular PMMA powder in 1.2 mW/(m·K) (3.7%). In the next section, compacted panels are produced and their thermal conductivity is studied at ambient pressure and under vacuum.

3.2.2. Compacted panels

The samples containing 10 wt% of opacifiers were compacted to the same final density (162 kg/m^3), obtaining self-standing panels of dimensions 120×120×15 mm^3 (**Figure 5a**). The reference sample (pure) was also compacted to a final density of 147 kg/m^3 for sake of comparison (same amount of PMMA as the opacified samples). The results of the thermal conductivity as a function of the density for the measurements performed at 10 ºC under ambient pressure and ultimate vacuum (0.02 mbar) are shown in **Figure 5b**. Due to the compaction process, the thermal conductivity increases between 2-4 mW/(m·K) with respect to the powder since the compacted samples are characterized by a higher amount of material per unit volume (higher conduction through the solid phase).

Regarding the compacted samples at ambient pressure, the sample with SiC presents the lowest thermal conductivity (34.0 mW/(m·K)), 0.4 mW/(m·K) lower than the reference (pure) sample. Meanwhile, the GnP sample presents higher thermal conductivity (35.3 mW/(m·K)), probably due to percolation between the GnP particles, resulting in higher conduction through the solid phase. In comparison with the pure sample the conductivity with GnP and TiO_2 is higher.

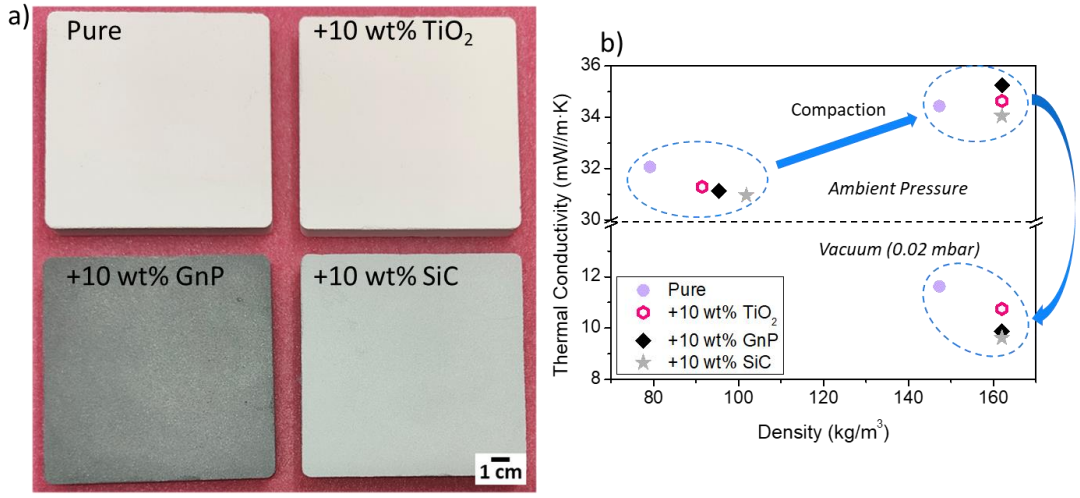

Figure 5. a) Photograph of the compacted panels produced in this work. b) Thermal conductivity at 10 ºC of the reference sample and the samples with 10 wt% of opacifiers as a function of the density of the compacted samples produced in this work at ambient pressure and at vacuum (0.02).

When vacuuming, the thermal conductivity is sharply reduced (**Figure 6**). This is because, in systems based on contact particles, a coupling effect between the particles and the gas surrounding the particles arises[37–40]. When the sample is fully evacuated it is negligible due to the lack of gas molecules, however, at ambient pressure, it can represent around 55% of the total thermal conductivity[21]. Thus, at maximum vacuum, the only heat transfer mechanisms affecting the system are the conduction through the solid phase and the radiation. As shown in **Figure 6b**, the difference between the measurements under ambient and vacuum conditions was more significant in the samples with IR-blockers. The reason is that the coupling effect contribution depends on the density (the higher density, the higher coupling)[21,39,41]. Also, differences in the thermal conductivity reduction when vacuuming between the compacted panels containing opacifiers may be due to the influence of each type of particle on the coupling mechanism. All the samples with opacifiers present lower thermal conductivity than the reference (pure) compacted panel (11.6 (mW/(m·K)) (**Figure 6b**). For instance, the thermal conductivity of the TiO_2 sample is 10.8 mW/(m·K), almost 1 mW/(m·K) lower than the reference despite the higher density. The GnP sample presents 9.9 mW/(m·K), meanwhile, the SiC sample shows the lowest thermal conductivity (9.6 mW/(m·K)), which is 2 mW/(m·K) lower than the thermal conductivity of the reference (pure) compacted panel.

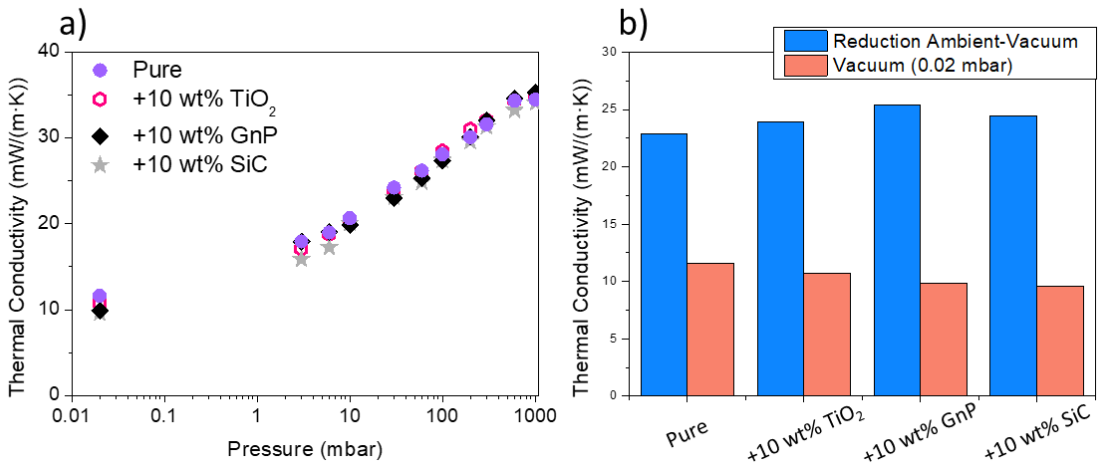

Figure 6. a) Thermal conductivity at 10 ºC of the compacted panels produced in this work at different vacuum pressures. b) Thermal conductivity at maximum vacuum (at 10 ºC and 0.02 mbar) and thermal conductivity reduction between ambient and vacuum conditions (at 10ºC) of the compacted panels produced in this work.

These last results confirm that adding IR-blockers helps to reduce the thermal conductivity of the compacted panels based on micronized nanocellular PMMA, boosting their performance as VIP core material. Thermal conductivities below 10 mW/(m·K) can be obtained under vacuum. The findings of this work are promising and pave the way for even further improvements by a fine tune of the content of the opacifier and the density of the compacted panel.

4. Conclusions

In this work, the effect of the addition of infrared blockers to micronized nanocellular PMMA has been analyzed. Three different opacifiers (TiO_2, GnP, and SiC) have been added to the reference (pure) sample in different contents (2.5, 5, 10, 15, and 20 wt%). On the one hand, regarding the powder mixtures, as the amount of IR-Blocker increases the density increases. Depending on the size of the opacifier particles the packaging changes, affecting the final density. Furthermore, the addition of opacifiers reduces thermal conductivity. For each IR-Blocker there is an optimum amount that leads to the minimum of thermal conductivity (a compromise between reducing the radiation and increasing the conduction through the solid phase). On the other hand, regarding the compacted panels, when compacting the thermal conductivity increases because of the density increase (higher conduction through the solid phase). When extracting the gas phase under vacuum, the thermal conductivity sharply decreases to 9.6 mW/(m·K) for the sample containing 10 wt% of SiC, which is 2 mW/(m·K) lower than the thermal conductivity of the reference (pure) compacted panel despite the higher density of the sample with SiC. These results confirm these materials as potential candidates to be used as alternative, low-cost, and eco-friendly VIP cores.

Acknowledgments

Financial support from the Junta of Castile and Leon grant (I. Sánchez-Calderón and VA202P20) is gratefully acknowledged. Financial assistance from the Spanish Ministry of Science, Innovation, and Universities (PID2021-126046OB-C22, PDC2022-133391-I00, TED2021-129419B-C22 and PTQ2019-010560 (Victoria Bernardo)) is gratefully acknowledged. Financial assistance from the European Regional Development Fund of the European Union and the of Castile and Leon ((ICE): R&D PROJECTS IN SMEs: PAVIPEX. 04/18/VA/008 and M-ERA.NET PROJECT: FICACEL. 11/20/VA/0001) is gratefully acknowledged. This work was supported by the Regional Government of Castilla y León (Junta de Castilla y León) and by the Ministry of Science and Innovation MICIN and the European Union NextGenerationEU/PRTR. We would also like to thank Leticia Miguens (CENIEH) for the laser diffraction measurements.

References

[1] I. Sánchez-Calderón, V. Bernardo, D. Cuadra-Rodríguez, J. Martín-de-León, M.Á. Rodríguez-Pérez, Micronization as a solution for enhancing the thermal insulation of nanocellular poly(methyl-methacrylate) (PMMA), Polymer (Guildf). 261 (2022) 125397. https://doi.org/10.1016/j.polymer.2022.125397.

[2] I. Sánchez-Calderón, V. Bernardo, F. Lizalde-Arroyo, J. Martín-de-León, M.Á. Rodríguez-Pérez, Development of new vacuum insulation core panels using micronized nanocellular poly(methyl-methacrylate) (PMMA), (n.d.).

[3] S.E. Kalnæs, B.P. Jelle, Vacuum insulation panel products: A state-of-the-art review and future research pathways, Appl. Energy. 116 (2014) 355–375. https://doi.org/10.1016/j.apenergy.2013.11.032.

[4] J. Fricke, H. Schwab, U. Heinemann, Vacuum Insulation Panels – Exciting Thermal Properties and Most Challenging Applications, Int. J. Thermophys. 27 (2006) 1123–1139. https://doi.org/10.1007/s10765-006-0106-6.

[5] F.A. Almeida, J. Corker, N. Ferreira, M.A. Neto, M. Fan, H. Beyrichen, R. Caps, Alternative low cost based core systems for vacuum insulation panels, Cienc. e Tecnol. Dos Mater. 29 (2017) e151–e156. https://doi.org/10.1016/j.ctmat.2016.10.002.

[6] B. Chang, L. Zhong, M. Akinc, Low cost composites for vacuum insulation core material, Vacuum. 131 (2016) 120–126. https://doi.org/10.1016/j.vacuum.2016.05.027.

[7] W. Villasmil, L.J. Fischer, J. Worlitschek, A review and evaluation of thermal insulation materials and methods for thermal energy storage systems, Renew. Sustain. Energy Rev. 103 (2019) 71–84. https://doi.org/10.1016/j.rser.2018.12.040.

[8] M. Casini, Smart Buildings, 2016th ed., Elsevier, 2016. https://doi.org/10.1016/C2015-0-00182-4.

[9] S. Schiavoni, F. D'Alessandro, F. Bianchi, F. Asdrubali, Insulation materials for the building sector: A review and comparative analysis, Renew. Sustain. Energy Rev. 62 (2016) 988–1011. https://doi.org/10.1016/j.rser.2016.05.045.

[10] M. Casini, Advanced construction materials, in: Constr. 4.0, Elsevier, 2022: pp. 337–404. https://doi.org/10.1016/B978-0-12-821797-9.00005-2.

[11] F. Almeida, H. Beyrichen, N. Dodamani, R. Caps, A. Müller, R. Oberhoffer, Thermal conductivity analysis of a new sub-micron sized polystyrene foam, J. Cell. Plast. 57 (2021) 493–515. https://doi.org/10.1177/0021955X20943101.

[12] L.W. Hrubesh, R.W. Pekala, Thermal properties of organic and inorganic aerogels, J. Mater. Res. 9 (1994) 731–

738. https://doi.org/10.1557/JMR.1994.0731.

[13] R. Caps, J. Fricke, Thermal conductivity of opacified powder filler materials for vacuum insulations, Int. J. Thermophys. 21 (2000) 445–452. https://doi.org/10.1023/A:1006691731253.

[14] M. Davraz, M. Koru, H.C. Bayrakçi, Y. Yusufoğlu, O. Ipek, The effect of opacifier properties on thermal conductivity of vacuum insulation panel with fumed silica, J. Therm. Anal. Calorim. 142 (2020) 1377–1386. https://doi.org/10.1007/s10973-020-09277-8.

[15] H. Singh, M. Geisler, F. Menzel, Experimental investigations into thermal transport phenomena in vacuum insulation panels (VIPs) using fumed silica cores, Energy Build. 107 (2015) 76–83. https://doi.org/10.1016/j.enbuild.2015.08.004.

[16] M. Davraz, H.C. Bayrakci, Performance properties of vacuum insulation panels produced with various filling materials, Sci. Eng. Compos. Mater. 21 (2014) 521–527. https://doi.org/10.1515/secm-2013-0162.

[17] M. Davraz, H.C. Bayrakçi, Y. Yusufoğlu, The Effect of Fiber, Opacifier Ratios and Compression Pressure on the Thermal Conductivity of Fumed Silica Based Vacuum Insulation Panels, Arab. J. Sci. Eng. 41 (2016) 4263–4272. https://doi.org/10.1007/s13369-016-2031-8.

[18] V. Napp, R. Caps, H. Ebert, Optimization of the Thermal Radiation Extinction of Silicon Carbide in a Silica Powder Matrix, J. Therm. Anal. Calorim. 56 (1999) 77–85. https://doi.org/10.1023/A:1010131324100.

[19] X.D. Wang, D. Sun, Y.Y. Duan, Z.J. Hu, Radiative characteristics of opacifier-loaded silica aerogel composites, J. Non. Cryst. Solids. 375 (2013) 31–39. https://doi.org/10.1016/j.jnoncrysol.2013.04.058.

[20] C.-Y. Zhu, Z.-Y. Li, H.-Q. Pang, N. Pan, Design and optimization of core/shell structures as highly efficient opacifiers for silica aerogels as high-temperature thermal insulation, Int. J. Therm. Sci. 133 (2018) 206–215. https://doi.org/10.1016/j.ijthermalsci.2018.07.032.

[21] I. Sánchez-Calderón, V. Bernardo, F. Lizalde-Arroyo, J. Martín-de-León, M.Á. Rodríguez-Pérez, Coupling effect in compacted panels based on micronized nanocellular polymers: modeling of the thermal conductivity, (n.d.).

[22] P. Buahom, P. Gong, C. Wang, H. Yu, J. Liu, C.B. Park, Carbon as a solution for nanocellular foam superinsulation, Carbon N. Y. 189 (2022) 319–338. https://doi.org/10.1016/j.carbon.2021.11.041.

[23] P. Gong, P. Buahom, M.-P. Tran, M. Saniei, C.B. Park, P. Pötschke, Heat transfer in microcellular polystyrene/multi-walled carbon nanotube nanocomposite foams, Carbon N. Y. 93 (2015) 819–829. https://doi.org/10.1016/j.carbon.2015.06.003.

[24] P. Gong, G. Wang, M.P. Tran, P. Buahom, S. Zhai, G. Li, C.B. Park, Advanced bimodal polystyrene/multi-walled carbon nanotube nanocomposite foams for thermal insulation, Carbon N. Y. 120 (2017) 1–10. https://doi.org/10.1016/j.carbon.2017.05.029.

[25] T. Li, G. Zhao, G. Wang, L. Zhang, J. Hou, Thermal-Insulation, Electrical, and Mechanical Properties of Highly-Expanded PMMA/MWCNT Nanocomposite Foams Fabricated by Supercritical CO2 Foaming, Macromol. Mater. Eng. 304 (2019) 1–14. https://doi.org/10.1002/mame.201800789.

[26] C. V. Vo, F. Bunge, J. Duffy, L. Hood, Advances in thermal insulation of extruded polystyrene foams, Cell. Polym. 30 (2011) 137–156. https://doi.org/https://doi.org/10.1177/026248931103000303.

[27] Y. Li, Z. Chen, C. Zeng, Poly(Methyl Methacrylate) (PMMA) Nanocomposite Foams, in: Polym. Nanocomposite Foam., 2018.

[28] I. Sánchez-Calderón, V. Bernardo, J. Martín-de-León, M.Á. Rodríguez-Pérez, Thermal conductivity of low-density micro-and nanocellular poly(methyl-methacrylate) (PMMA): Experimental and modeling, Mater. Des. 221 (2022) 110938. https://doi.org/10.1016/j.matdes.2022.110938.

[29] ISO 60:1977 Plastics — Determination of apparent density of material that can be poured from a specified funnel, (1977).

[30] UNE-EN 1602:2013 Thermal insulating products for building applications. Determination of the apparent

density., (n.d.).

[31] ISO 9276-2:2014 Representation of results of particle size analysis — Part 2: Calculation of average particle sizes/ diameters and moments from particle size distributions, (2014).

[32] A. Rawle, Basic of principles of particle size analysis, Surf. Coatings Int. Part A, Coatings J. (2003). https://www.atascientific.com.au/basic-principles-of-particle-size-analysis/%0Ahttps://www.atascientific.com.au/.

[33] ASTM C518 Standard Test Method for Steady-State Thermal Transmission Properties by Means of the Heat Flow Meter Apparatus, (2017).

[34] ISO 8301 Thermal insulation - Determination of steady-state thermal resistance and related properties - Heat flow meter, (1991).

[35] L. Glicksman, M. Schuetz, M. Sinofsky, Radiation heat transfer in foam insulation, Int. J. Heat Mass Transf. 30 (1987) 187–197. https://doi.org/10.1016/0017-9310(87)90071-8.

[36] R.J.J. Williams, C.M. Aldao, Thermal conductivity of plastic foams, Polym. Eng. Sci. 23 (1983) 293–298. https://doi.org/10.1002/pen.760230602.

[37] S. Fantucci, A. Lorenzati, A. Capozzoli, M. Perino, Analysis of the temperature dependence of the thermal conductivity in Vacuum Insulation Panels, Energy Build. 183 (2019) 64–74. https://doi.org/10.1016/j.enbuild.2018.10.002.

[38] R. Baetens, B.P. Jelle, J.V. Thue, M.J. Tenpierik, S. Grynning, S. Uvsløkk, A. Gustavsen, Vacuum insulation panels for building applications: A review and beyond, Energy Build. 42 (2010) 147–172. https://doi.org/10.1016/j.enbuild.2009.09.005.

[39] S. Sonnick, M. Meier, J. Ross-Jones, L. Erlbeck, I. Medina, H. Nirschl, M. Rädle, Correlation of pore size distribution with thermal conductivity of precipitated silica and experimental determination of the coupling effect, Appl. Therm. Eng. 150 (2019) 1037–1045. https://doi.org/10.1016/j.applthermaleng.2019.01.074.

[40] K. Swimm, S. Vidi, G. Reichenauer, H.P. Ebert, Coupling of gaseous and solid thermal conduction in porous solids, J. Non. Cryst. Solids. 456 (2017) 114–124. https://doi.org/10.1016/j.jnoncrysol.2016.11.012.

[41] K. Swimm, G. Reichenauer, S. Vidi, H.P. Ebert, Impact of thermal coupling effects on the effective thermal conductivity of aerogels, J. Sol-Gel Sci. Technol. 84 (2017) 466–474. https://doi.org/10.1007/s10971-017-4437-5.

Chapter 5

Conclusions & Future Work

"Not all treasure is silver and gold, mate."

Captain Jack Sparrow – Pirates of the Caribbean

INDEX

5. Conclusions & Future Work

5.1. Conclusions

This thesis has investigated in detail the thermal conductivity of nanocellular polymers. The objectives of the thesis are schematically shown in **Figure 5.1** together with the main accomplishments related to each one. It was possible to measure the thermal conductivity of nanocellular polymers using reliable techniques and use the results to understand in detail the heat transfer mechanisms in the bulk materials and model their thermal conductivity. Then, the thermal insulation behavior was enhanced using the main novelty of this thesis: the micronization of nanocellular polymers to give rise to a new material, that can be compacted in self-standing panels too. The micronized and compacted materials were studied in detail to understand the heat transfer mechanisms and develop models to predict their behavior. Quite promising results were obtained in the compacted panels, with minimum conductivities of 10.7 mW/(m·K) under vacuum and as low as 9.6 mW/(m·K) when infrared blockers were added.

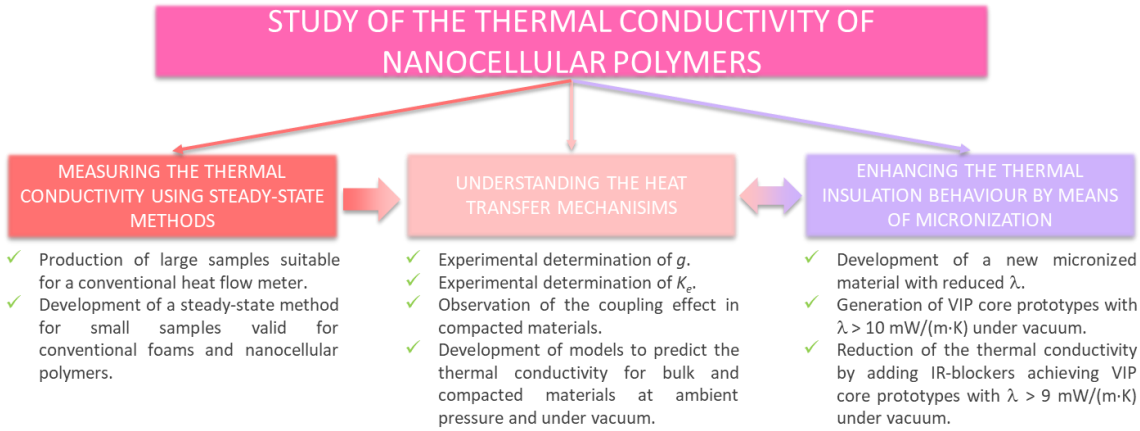

Figure 5.1. Objectives and main accomplishments achieved in this thesis.

Then, the results presented in the previous chapters of this thesis (**Chapter 3** and **Chapter 4**) have reported several important conclusions in the field of nanocellular polymers. These conclusions are summarized in more detail in the following paragraphs:

5.1.1. Bulk nanocellular polymers: measurement of the thermal conductivity

A collection of low-density microcellular and nanocellular poly(methyl methacrylate) (PMMA) (relative densities ranging from 0.09 to 0.18 and cell sizes between 400–4000 nm) were produced by gas dissolution foaming using CO_2 as a physical blowing agent. After cutting and polishing, bulk samples with dimensions of 50×50×7 mm^3 were obtained.

- Then, the samples were stacked forming a stack of large dimensions (150×150×14 mm^3) to properly measure their thermal conductivity at different temperatures using a commercial heat flow meter (HFM) (**Chapter 4** Section 4.2). The bulk microcellular and nanocellular

PMMA samples filled new regions in terms of relative density - cell size - thermal conductivity regarding the results of the state-of-the-art[1–8], as shown in **Figure 5.2**. Thermal conductivities between 37.4 and 46.6 mW/(m·K) at 10 °C were obtained for the bulk samples. It is important to remark that most of the literature data was obtained from samples with small dimensions using a transient technique (transient plane source (TPS)), which accuracy for characterizing the thermal conductivity of thermal insulators is not clear[9–11]. Then, the obtained results are one of the few reliable data points in the literature together with the steady-state measurements of Zhou et al.[6] (using a homemade guarded hot plate (GHP*)) and Almeida et al.[4] (using external sensors (ES)).

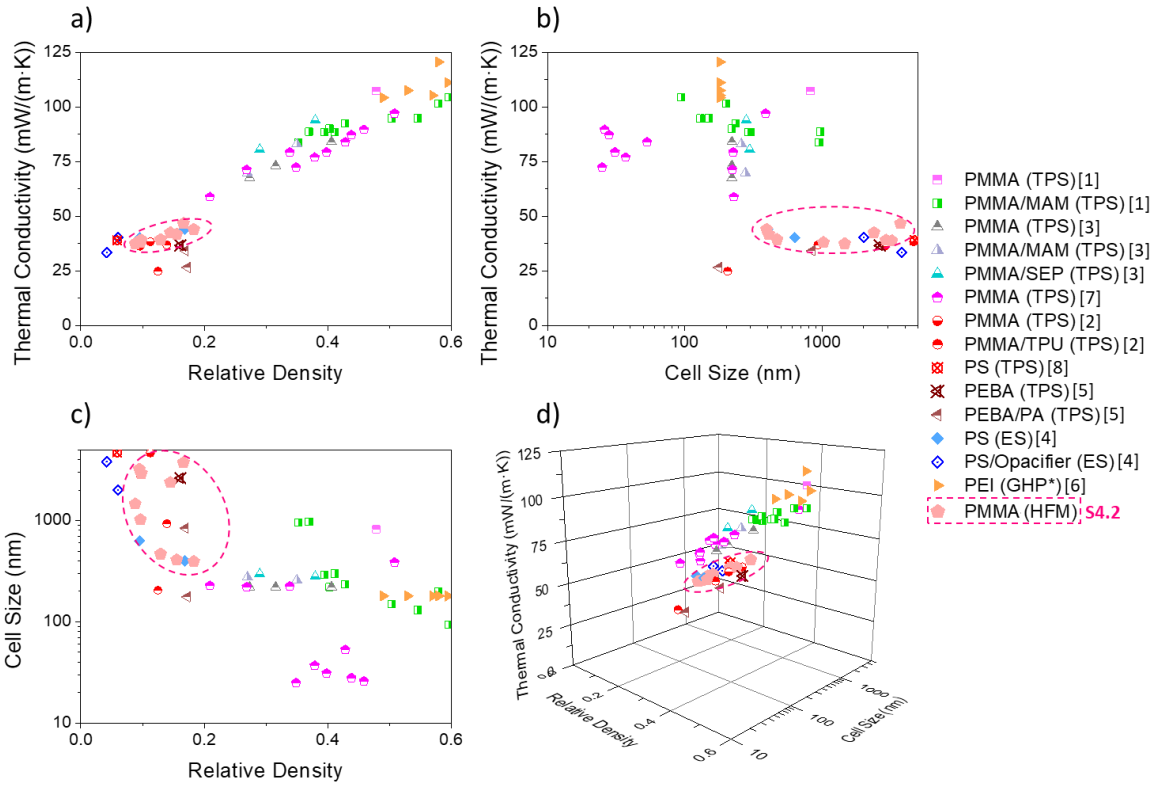

Figure 5.2. Experimental research on the thermal conductivity of bulk nanocellular polymers (state-of-the-art data + results of this thesis): a) thermal conductivity – relative density, b) thermal conductivity – cell size, c) cell size – relative density, and d) Thermal conductivity – cell size – relative density 3D map.

- In parallel to the HFM measurements of the large samples, two steady-state-based methods able to measure small dimensions samples were developed and validated, showing accurate results (**Figure 5.3**): the use of a mask of lower thermal conductivity (M) and the use of external sensors (ES) (**Chapter 3** Section 3.4 and Section 3.5).

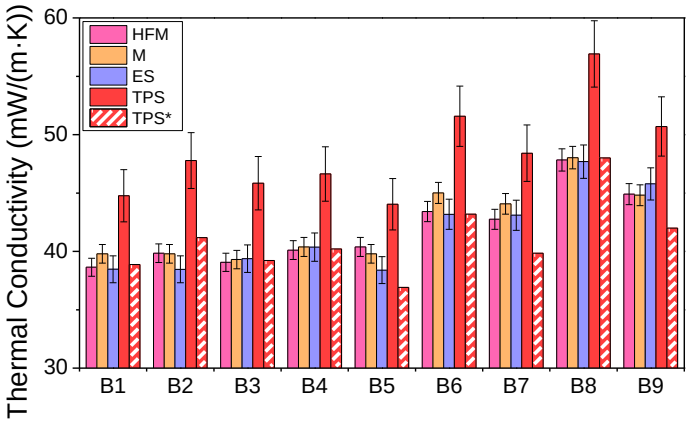

Figure 5.3. Thermal conductivity of bulk nanocellular PMMA obtained through the commercial heat flow meter (HFM), the mask method (M), the external sensors method (ES), the TPS method, and applying the TPS correction proposed by Zheng et al.[10]. Extracted from **Chapter 3** Section 3.5.

- Mask (M) method: The mask fills the area of the heat flux transducer of the commercial HFM that the sample cannot cover. Thus, the resulting total heat flow in the transducers is a sum of the heat flux through the sample and the mask. This method allows measuring comfortably and precisely the thermal conductivity of small insulating samples using a conventional heat flow meter without any additional investment. However, the main drawback of this method is that the thermal conductivity of the mask must be necessarily lower than the sample to provide accurate results. This fact may complicate using this method for super-insulating samples like aerogels, characterized by thermal conductivities of around 14 mW/(m·K)[12,13].
- External sensors (ES) method: The heat flow and the temperature are measured on both sides of the sample with external heat flux sensors and thermocouples, respectively. Also, two rubber pieces, placed between the sample and the HFM plates, are needed to minimize the fluctuations of the registered heat flux. This methodology, developed in this thesis, was described and validated for different conventional foams (**Chapter 3** Section 3.4) and for nanocellular polymers (**Chapter 3** Section 3.5). In this case, the conventional HFM needs to be modified, but the main advantage of this method is that it can be used for any type of material, even for super-insulating materials. In fact, Merillas et al.[13–16] use this method to measure the thermal conductivity of aerogels characterized by thermal conductivities as low as 12 mW/(m·K).

- Finally, the thermal conductivity of the bulk samples was also measured through TPS, obtaining high deviations regarding the reference HFM measurements, even when applying a correction developed by Zheng et al.[10] (TPS*)(**Chapter 3** Section 3.5), as shown in **Figure 5.3**. Therefore, TPS, despite allowing measuring samples with small dimensions, is not a reliable technique for characterizing nanocellular polymers.

5.1.2. Bulk nanocellular polymers: thermal conductivity modeling

The thermal conductivity of the bulk microcellular and nanocellular PMMA was deeply analyzed to study the contribution of each heat transfer mechanism (conduction through the solid phase, conduction through the gas phase, and radiation) (**Chapter 4** Section 4.2).

- The experimental data were used to calculate the structural factor and the extinction coefficient of nanocellular polymers and learn about their behavior in these novel systems:
    - A novel method to determine the solid structure factor from the slope of the thermal conductivity versus the temperature cube curve was introduced. Solid structure factors *g* around 0.89 were obtained. Those values are high compared with other super-thermal insulators such as aerogels presenting values around 0.05[17,18]. The reason for that different behavior is related to the solid phase structure: nanocellular polymers present a continuous solid phase, whereas aerogels present a discontinuous structure characterized by particles in contact. Furthermore, the increase of the solid structure factor in comparison with low-density conventional cellular materials (where *g* ranges between 1/3 and 2/3 for open and close cell foams, respectively[19]), may be associated with an increment of the polymer's thermal conductivity when it is confined in the walls and struts of the cell. Thus, instead of being randomly distributed, the polymer chains are oriented toward the structure and this could facilitate the phonon (thermal) transport.
    - From the analysis of the thermal conductivity vs. temperature curve, it is also possible to determine, the extinction coefficient (including both the absorption and scattering mechanisms). This is the first time that the extinction coefficient of PMMA-based nanocellular polymers is obtained using thermal conductivity measurements. An empirical equation relating the cell size and the density with the extinction coefficient is obtained. As the cell size is reduced, the extinction coefficient decreases sharply due to reduced cell scattering of infrared radiation. These achievements match the results obtained, both theoretically and experimentally, for nanocellular polymers[20,21].
- A semi-empirical model able to predict the thermal conductivity of low-density microcellular and nanocellular PMMA was developed. The semi-empirical model depends only on the properties of the polymer foam (relative density and cell size) and the measurement conditions (temperature and pressure). The model allows understanding the influence of each parameter on the total conductivity, as well as the expected minimum conductivities that can be reached depending on the solid polymer configuration. A reduction of the solid structure factor *g* leads to lower thermal conductivities. Also, the region where the minimum appears changes. For instance, at ambient pressure and

assuming g = 0.89, the minimum thermal conductivity predicted is 34 mW/(m·K) for relative densities of 0.08 and cell sizes around 140 nm. Meanwhile, if assuming g = 0.3 the minimum thermal conductivity predicted is 22 mW/(m·K) for relative densities of 0.18 and cell sizes around 70 nm. At maximum vacuum and assuming g = 0.89, the model predicts minimum thermal conductivities higher than 17 mW/(m·K) for bulk nanocellular PMMA.

- In general, thermal conductivity increases with density. However, when the cell size is reduced below the micron the Knudsen effect plays a key role, leading to a drastic reduction of the conduction through the gas phase, decreasing the overall thermal conductivity. As a counterpart, the reduction of the cell size below the micron implies an increase in the radiation contribution for low-density foams. Therefore, there is a compromise between these two factors (relative density and cell size) to produce an optimum material with minimum thermal conductivity (**Figure 5.4**).

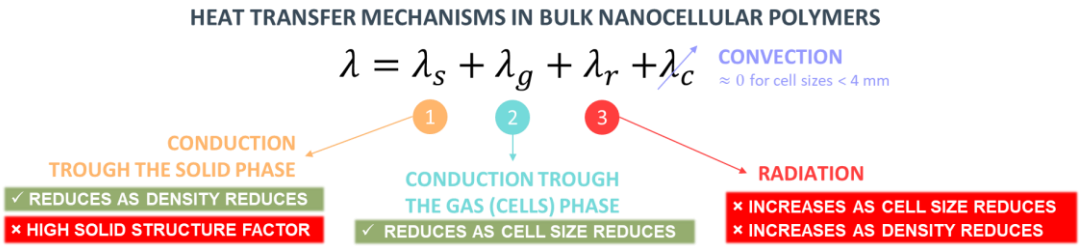

Figure 5.4. Heat transfer mechanisms in nanocellular polymers.

5.1.3. Micronized systems based on nanocellular polymers

Micronization was explored as a way to further enhance the thermal insulator behavior of nanocellular polymers by decreasing the conduction through the solid phase, as a route to scale-up nanocellular polymers, and as an approach to ease the addition of opacifiers (infrared blockers). By means of micronization, it is possible to transform a continuous solid phase in the cellular structure into a discontinuous solid phase with the nanocells inside the micrometric particles. Micronized samples (M) were produced (**Chapter 4** Section 4.3) and then compacted to obtain self-standing panels (C) (**Chapter 4** Section 4.4) with dimensions of 120×120 ×15 mm^3. A mold with dimensions similar to those of the bulk materials was used for the sake of comparison, but the process could be valid for larger molds too.

- In general, after micronization, the density (apparent density) is reduced due to the presence of voids between the powder particles. However, the densification of the powder particles during the micronization process could lead to higher apparent densities. The increase in density can be due to the forces involved in the milling process, that is, the material can be partially compressed and thus densified. Densification is lower in nanocellular samples than in microcellular samples. Then, nanocellular cell sizes allow a more efficient micronization process with lower densification and a significant reduction of the density.

- Micronization results in polyhedral particles where the cellular structure is visible on the surface of the particles. Therefore, the micronization process maintains the cellular structure and helps to interconnect the cellular structure, increasing the open cell content. This is a key factor in order to evacuate the inner cellular structure to produce vacuum insulation panels (VIP).

- Micronization allows obtaining particles of about 100 µm size (obtained through image analysis). The size of the particles depends on the sieve used for micronizing. The particle size distribution is monomodal, but it covers a wide range of particle sizes.

- A densification of 145% (under pressure and temperature) of the apparent density of the micronized material is necessary to obtain self-standing compacted panels. The nanocellular structure is still visible in the panels, meaning that the compaction process does not modify significantly the structure and it maintains the interconnectivity of the cells.

- Micronization leads to a reduction of thermal conductivity due to a change in the heat transfer mechanisms because of the solid phase discontinuity. Thus, micronized samples (M) and compacted panels (C) present lower thermal conductivity at ambient pressure than bulk materials (B), even presenting higher densities, as shown in **Figure 5.5**.

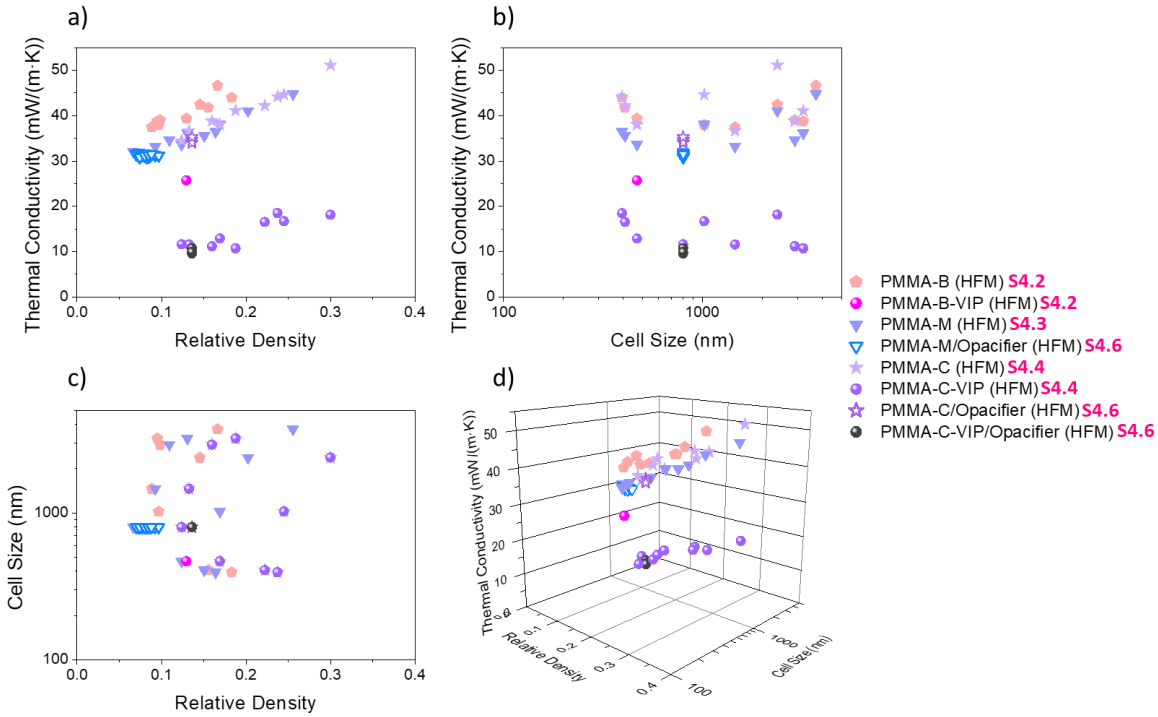

Figure 5.5. Experimental thermal conductivity of the materials produced in this thesis (B-Bulk, M-micronized, C-compacted panels, and VIP-vacuum insulation panels): a) thermal conductivity – relative density, b) thermal conductivity – cell size, c) cell size – relative density, and d) Thermal conductivity – cell size – relative density 3D map.

- The study of the micronized samples using a simple model based on the models usually used to describe nanocellular polymers (**Chapter 4** Section 4.3), which includes, in a first approximation, conduction through the solid phase, conduction through the cells phase, conduction through the voids phase, and radiation, showed that:
    - The solid structure factor is calculated to be reduced by about 29% (from 0.89 to 0.63). So, the conduction through the solid phase decreases thanks to the micronization process (the powder particles act as additional thermal resistances).
    - The extinction coefficient increases since the presence of particles may act as additional scattering points. Therefore, the thermal radiation is reduced.

- The thermal conductivity behavior under vacuum (VIP) was observed to be different between the bulk materials (B) and the compacted panels (C) (**Chapter 4** Section 4.4), which present lower thermal conductivity (almost half, as shown in **Figure 5.5**) and two drops of thermal conductivity (instead of only one) (**Figure 5.6a**). The drops of thermal conductivity when evacuating the compacted panel correspond to the Knudsen effect applied to the conduction through the cells phase and to the coupling effect, which depends on the cell size and the particle size, respectively. Also, the thermal conductivity reduction under vacuum was higher than expected if only Knudsen effect is considered. Thus, the study of compacted panels under vacuum provided new insights about the powdered systems. A new heat transfer mechanism called the coupling effect arises. The coupling thermal conductivity takes into account the interaction between the core particles and the gas in systems formed by contact particles[22,23]. This additional heat transfer mechanism is negligible for foams with continuous solid phase because the coupling effect is a result of the heat flow from one solid particle to another through the gas phase.

- A semi-empirical model able to predict the thermal conductivity of compacted panels based on microcellular and nanocellular PMMA was developed (**Chapter 4** Section 4.5). The model included conduction through the solid phase, conduction through the cells phase, radiation, and coupling effect. Due to the compaction process, the fraction of voids was supposed to be null. The model presents the main novelty of considering a system of independent particles to calculate the conduction mechanisms. The semi-empirical model depends only on the properties of the compacted material (apparent relative density, cell size, and particle size) and the measurement conditions (temperature and pressure). The model presents high accuracy for the compacted panels at ambient pressures, at maximum vacuum, and also at different vacuum pressures, allowing analyzing the contribution of each heat transfer mechanism.

- The model is unique in introducing the concept of infinite association of resistances for quantifying the conduction through the powder particles. The model assumes that the radiation in the compacted panel is like that of a bulk material (it is assumed that the presence of the particle interfaces does not create additional scattering surfaces for radiation).
- The model showed that the reduction of the solid structure factor could be higher than expected based on the results of the simple model for the micronized material, decreasing from 0.89 to 0.33.
- The coupling factor f (which depends on the density and the temperature) was determined and the model showed that the coupling effect represents about 55% of the total thermal conductivity at ambient pressure.

- For compacted panels made of nanocellular polymers, the model predicts minimum thermal conductivities of 32.5 mW/(m·K) at ambient pressure and of 10 mW/(m·K) at maximum vacuum.

- **Figure 5.6** collects a comparison between bulk and compacted samples with similar characteristics (150 kg/m^3 and 500 nm of cell size, being 100 µm the particle size of the compacted panel) using the semi-empirical model developed in this thesis for each system to make the predictions. **Figure 5.6a** shows that the compacted panel presents lower thermal conductivity at ambient pressure than the bulk sample (36.1 vs. 39.0 mW/(m·K), respectively) and also under vacuum where the gap between the two conductivities is much higher (11.8 vs. 24.2 mW/(m·K)). Meanwhile, **Figure 5.6b** and **5.6c** show that due to the micronization the conduction through the solid phase is reduced from 19.5 mW/(m·K) for the bulk sample to 7.1 mW/(m·K) for the compacted panel, the contribution in the total thermal conductivity being reduced by 60% (from 50% to 20%). Also, it is observed that in the compacted panels the contribution of the coupling effect represents more than half of the thermal conductivity. Thermal radiation is equal since both models use the same equation to determine it.
- Micronization allows the introduction of opacifiers (infrared blockers) by making powder mixtures. The addition of infrared blockers reduces thermal conductivity, as shown in **Figure 5.5**. For each opacifier, there is an optimum amount that leads to a minimum thermal conductivity because there is a compromise between reducing the radiation and increasing the conduction through the solid phase. For compacted panels with equal characteristics, under vacuum, the addition of opacifiers reduced the thermal conductivity from 11.6 mW/(m·K) to 9.6 mW/(m·K) (**Chapter 4** Section 4.6).

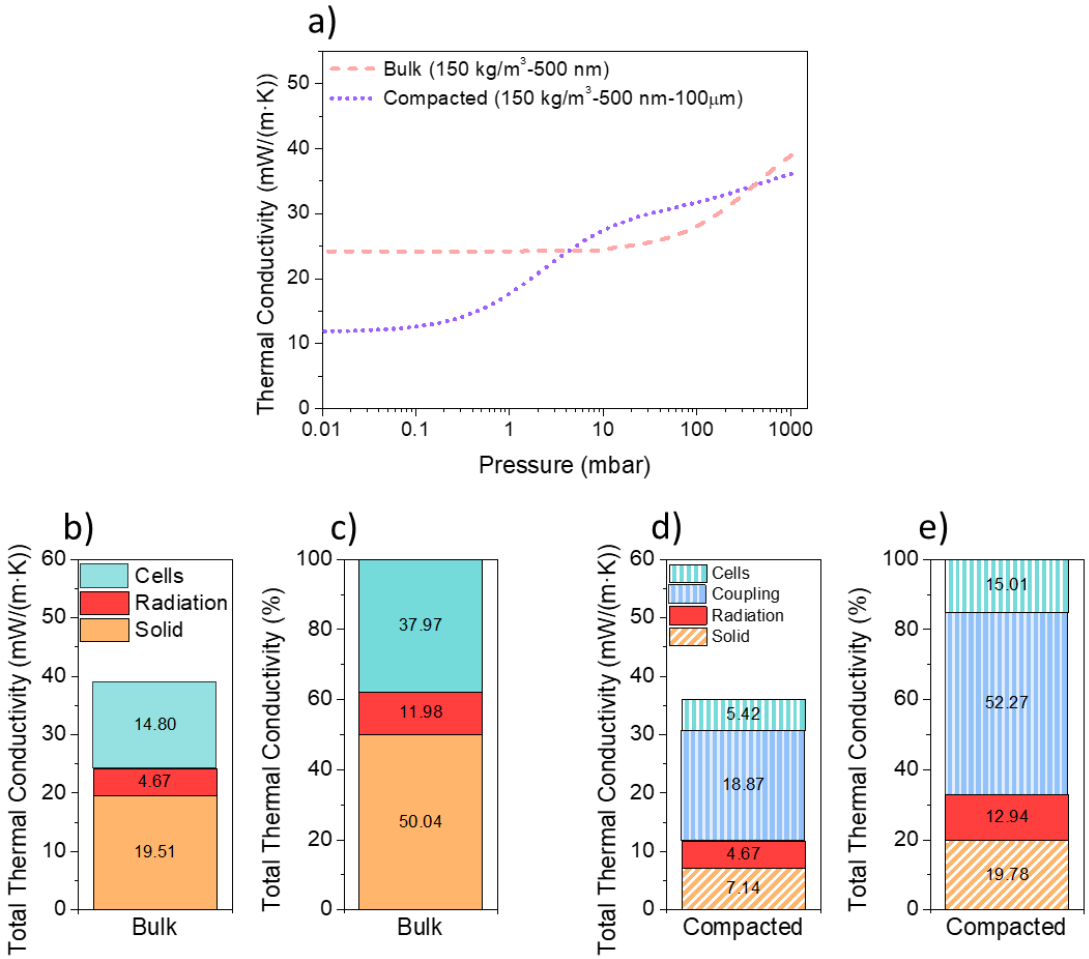

Figure 5.6. Comparison between bulk and compacted samples with similar characteristics (150 kg/m^3 and 500 nm of cell size; the compacted sample particle size is 100 μm). a) Prediction of the thermal conductivity at 10ºC as a function of the pressure of bulk and compacted samples according to the equation obtained in **Chapter 4** Section 4.2 and in **Chapter 4** Section 4.5, respectively. Predicted contribution of each heat transfer mechanism to the total thermal conductivity of the bulk material at ambient pressure in mW/(m·K) (b) and in % of the total thermal conductivity (c). Predicted contribution of each heat transfer mechanism to the total thermal conductivity of the compacted panels at ambient pressure in mW/(m·K) (d) and in % of the total thermal conductivity (e). At maximum vacuum cells and coupling contributions become null.

5.2. Future Work

The knowledge gained with the development of this thesis in the field of microcellular and nanocellular polymers opens many possibilities for further studies. Thus, different investigation lines are proposed:

- *Further exploring the production routes and parameters to obtain optimum micro/nanocellular materials (bulk, micronized, and compacted panels) in terms of cell size and density for thermal insulation*. The thermal conductivity models developed in this

thesis for PMMA have shown that there is a minimum of thermal conductivity that can be achieved for a certain combination of cell size and density. However, these optimum materials do not exist yet, therefore, their production would allow further verification of the predictions and refining of the models.

- *Production and thermal conductivity characterization of micro/nanocellular materials (bulk, micronized, and compacted panels) based on different polymers*. This thesis has been developed around PMMA, but there are a lot of polymer matrices like polystyrene (PS), polycarbonate (PC), or poly(lactic acid) (PLA), which may be lead to micro/nanocellular polymers with interesting thermal insulator behavior. Also, the production and characterization of these materials would help to extend the models developed for PMMA to other polymer matrices.

- *Study of the sound speed of micro/nanocellular materials (bulk, micronized, and compacted panels)*. It is well known that the sound speed through a material is related to the thermal conduction through the solid phase, as commented in **Chapter 2**. In this thesis, the solid structure factor was determined with thermal conductivity measurements but using the sound speed will help to verify and refine the models. Measuring the sound speed independently would allow to build a more robust model and to finally distinguish between the effect of the structure (in the g factor) and the effects on the solid phase (that we considered to be constant so far, but we know it can vary due to confinement and/or orientation of the polymeric phase).

- *Measurement of the extinction coefficient using infrared spectroscopy.* Although it is quite challenging for the micronized materials, measuring this coefficient independently on the thermal conductivity measurements would allow to build a more robust understanding of the insulation behavior of these materials.

- *Characterization of the mechanical properties of micro/nanocellular materials ((bulk, micronized, and compacted panels)*. Also, the mechanical properties are related to thermal conduction through the solid phase. So, the characterization of the mechanical properties will help to verify and refine the models developed in this thesis as well as understanding the mechanical properties of the VIP core prototypes developed in this thesis.

- *Sieving.* The model developed in this thesis proves the relevance of the particle size in the thermal conductivity of the compacted panels. The study of micronized samples and compacted panels made of powders with different mean particle sizes would allow further understanding of the coupling effect. Also, the particle size is probably related to the radiation, existing an optimum particle size that leads to a minimum thermal conductivity.

Therefore, this study will help to further improve the model regarding the thermal conductivity of compacted panels. This study is currently ongoing.

- *Refining the thermal conductivity model developed to compacted panels to extend the predictions to the micronized samples.* The model developed for compacted panels could be used to predict the overall thermal conductivity of micronized samples. However, it fails at determining the contribution of each heat transfer mechanism, particularly the conduction through the cells phase. This is because the model does not include the contribution through the voids phase. Then, it is important to extend the model to properly describe the heat transfer mechanisms of the powdered systems.

- *Addition of opacifiers.* This thesis has analyzed the effect of the addition of different opacifiers to micronized nanocellular PMMA. However, there are multiple mixtures, like combinations of different infrared blockers in different contents, that have not been studied yet. Also, the production of opacified compacted panels based on different opacifiers contents is necessary to determine the optimum amount in these systems.

- *Production of commercial-like VIP*. This thesis has studied the thermal conductivity of opacified and non-opacified VIPs based on nanocellular PMMA. However, commercial VIPs also present fibers, getters, and desiccants, to improve the mechanical properties and extend the service life, respectively. The introduction of these materials may affect the thermal conductivity.

- *VIP characterization.* This thesis has studied the thermal conductivity of VIPs. However, there are other relevant properties like thermal stability and aging that have not been analyzed.

- *Proper characterization of the thermal conductivity of powders (small dimensions).* In this thesis, a method to characterize the thermal conductivity of thermal insulators (in bulk form) with small dimensions has been developed and validated. However, the method has not been tested for micronized or compacted materials. Therefore, validating the method or tuning the method to properly characterize those samples is of utmost importance for the future.

References

[1] B. Notario, J. Pinto, E. Solorzano, J.A. de Saja, M. Dumon, M.A. Rodríguez-Pérez, Experimental validation of the Knudsen effect in nanocellular polymeric foams, Polymer (Guildf). 56 (2015) 57–67. https://doi.org/10.1016/j.polymer.2014.10.006.

[2] G. Wang, J. Zhao, L.H. Mark, G. Wang, K. Yu, C. Wang, C.B. Park, G. Zhao, Ultra-tough and super thermal-insulation nanocellular PMMA/TPU, Chem. Eng. J. 325 (2017) 632–646. https://doi.org/10.1016/j.cej.2017.05.116.

[3] V. Bernardo, J. Martin-de Leon, J. Pinto, R. Verdejo, M.A. Rodriguez-Perez, Modeling the heat transfer by conduction of nanocellular polymers with bimodal cellular structures, Polymer (Guildf). 160 (2019) 126–137. https://doi.org/10.1016/j.polymer.2018.11.047.

[4] F. Almeida, H. Beyrichen, N. Dodamani, R. Caps, A. Müller, R. Oberhoffer, Thermal conductivity analysis of a new sub-micron sized polystyrene foam, J. Cell. Plast. 57 (2021) 493–515. https://doi.org/10.1177/0021955X20943101.

[5] J. Zhao, G. Wang, Z. Xu, A. Zhang, G. Dong, G. Zhao, C.B. Park, Ultra-elastic and super-insulating biomass PEBA nanoporous foams achieved by combining in-situ fibrillation with microcellular foaming, J. CO2 Util. 57 (2022) 101891. https://doi.org/10.1016/j.jcou.2022.101891.

[6] C. Zhou, N. Vaccaro, S.S. Sundarram, W. Li, Fabrication and characterization of polyetherimide nanofoams using supercritical CO2, J. Cell. Plast. 48 (2012) 239–255. https://doi.org/10.1177/0021955X12437984.

[7] J. Martin-de Leon, Understanding The Production Process Of Nanocellular Polymers Based On Pmma Driven By A Homogeneous Nucleation. (October 2019), n.d. https://pdfs.semanticscholar.org/a3d2/2c024e3c550652f34f510769ad3d84e6020d.pdf.

[8] P. Gong, P. Buahom, M.-P. Tran, M. Saniei, C.B. Park, P. Pötschke, Heat transfer in microcellular polystyrene/multi-walled carbon nanotube nanocomposite foams, Carbon N. Y. 93 (2015) 819–829. https://doi.org/10.1016/j.carbon.2015.06.003.

[9] O. Almanza, M.A. Rodríguez-Pérez, J.A. De Saja, Applicability of the Transient Plane Source Method To Measure the Thermal Conductivity of Low-Density Polyethylene Foams, J. Polym. Sci. Part B Polym. Phys. 42 (2004) 1226–1234. https://doi.org/10.1002/polb.20005.

[10] Q. Zheng, S. Kaur, C. Dames, R.S. Prasher, Analysis and improvement of the hot disk transient plane source method for low thermal conductivity materials, Int. J. Heat Mass Transf. 151 (2020) 119331. https://doi.org/10.1016/j.ijheatmasstransfer.2020.119331.

[11] R.C. Kerschbaumer, S. Stieger, M. Gschwandl, T. Hutterer, M. Fasching, B. Lechner, L. Meinhart, J. Hildenbrandt, B. Schrittesser, P.F. Fuchs, G.R. Berger, W. Friesenbichler, Comparison of steady-state and transient thermal conductivity testing methods using different industrial rubber compounds, Polym. Test. 80 (2019) 106121. https://doi.org/10.1016/j.polymertesting.2019.106121.

[12] B. Merillas, J.P. Vareda, J. Martín-de León, M.Á. Rodríguez-Pérez, L. Durães, Thermal Conductivity of Nanoporous Materials: Where Is the Limit?, Polymers (Basel). 14 (2022) 2556. https://doi.org/10.3390/polym14132556.

[13] B. Merillas, F. Villafañe, M.Á. Rodríguez-Pérez, Super-Insulating Transparent Polyisocyanurate-Polyurethane Aerogels: Analysis of Thermal Conductivity and Mechanical Properties, Nanomaterials. 12 (2022) 2409. https://doi.org/10.3390/nano12142409.

[14] B. Merillas, F. Villafañe, M.Á. Rodríguez-Pérez, Improving the Insulating Capacity of Polyurethane Foams through Polyurethane Aerogel Inclusion: From Insulation to Superinsulation, Nanomaterials. 12 (2022) 2232. https://doi.org/10.3390/nano12132232.

[15] B. Merillas, A. Lamy-Mendes, F. Villafañe, L. Durães, M.Á. Rodríguez-Pérez, Silica-Based Aerogel Composites Reinforced with Reticulated Polyurethane Foams: Thermal and Mechanical Properties, Gels. 8 (2022) 1–18. https://doi.org/10.3390/gels8070392.

[16] B. Merillas, A. Lamy-Mendes, F. Villafañe, L. Durães, M. Rodríguez-Pérez, Polyurethane foam scaffold for silica aerogels: effect of cell size on the mechanical properties and thermal insulation, Mater. Today Chem. 26 (2022). https://doi.org/10.1016/j.mtchem.2022.101257.

[17] P. Scheuerpflug, M. Hauck, J. Fricke, Thermal properties of silica aerogels between 1.4 and 330 K, J. Non. Cryst. Solids. 145 (1992) 196–201. https://doi.org/10.1016/S0022-3093(05)80455-7.

[18] L.W. Hrubesh, R.W. Pekala, Thermal properties of organic and inorganic aerogels, J. Mater. Res. 9 (1994) 731–

738. https://doi.org/10.1557/JMR.1994.0731.

[19] N.C.. Hilyard, A. Cunningham, Low density cellular plastics Physical basis of behaviour, 1994. https://doi.org/10.1007/978-94-011-1256-7.

[20] V. Bernardo, J. Martin-de Leon, J. Pinto, U. Schade, M.A. Rodriguez-Perez, On the interaction of infrared radiation and nanocellular polymers: First experimental determination of the extinction coefficient, Colloids Surfaces A Physicochem. Eng. Asp. 600 (2020). https://doi.org/10.1016/j.colsurfa.2020.124937.

[21] P. Buahom, C. Wang, M. Alshrah, G. Wang, P. Gong, M. Tran, C.B. Park, Wrong expectation of superinsulation behavior from largely-expanded nanocellular foams, Nanoscale. (2020). https://doi.org/10.1039/d0nr01927e.

[22] S. Fantucci, A. Lorenzati, A. Capozzoli, M. Perino, Analysis of the temperature dependence of the thermal conductivity in Vacuum Insulation Panels, Energy Build. 183 (2019) 64–74. https://doi.org/10.1016/j.enbuild.2018.10.002.

[23] R. Baetens, B.P. Jelle, J.V. Thue, M.J. Tenpierik, S. Grynning, S. Uvsløkk, A. Gustavsen, Vacuum insulation panels for building applications: A review and beyond, Energy Build. 42 (2010) 147–172. https://doi.org/10.1016/j.enbuild.2009.09.005.